Generation and Detection Schemes for Laser-Induced Coherent Terahertz Radiation at the Electron Storage Ring DELTA

Dissertation
zur Erlangung des Grades eines
Doktors der Naturwissenschaften
(Dr. rer. nat.)

vorgelegt
der Fakultät Physik
der Technischen Universität Dortmund

von
Peter Ungelenk
geb. am 16.06.1988 in Münster

2015

Tag der mündlichen Prüfung: 07.12.2015

Vorsitzender der Prüfungskommission:
Prof. Dr. Markus Betz (Technische Universität Dortmund)

1. Gutachter:
Prof. Dr. Shaukat Khan (Technische Universität Dortmund)

2. Gutachterin:
Prof. Dr. Anke-Susanne Müller (Karlsruher Institut für Technologie)

3. Gutachter:
Prof. Dr. Metin Tolan (Technische Universität Dortmund)

Vertreter der wissenschaftlichen Mitarbeiter:
Dr. Christian Sternemann (Technische Universität Dortmund)

für Lisa, Dieter und Christel

„denn nichts wirkt, auch ohne daß wir es gewahr werden, auf unser jugendliches Gemüth mehr, als das Beispiel derer, mit denen wir leben.“

Johann Gottfried von Herder
Vorrede zu den Palmblättern, 1786 [1]

Abstract

At DELTA, a 1.5-GeV electron storage ring operated as a synchrotron light source by the TU Dortmund University, a short-pulse facility for vacuum-ultraviolet and terahertz (THz) radiation was established in 2011. Here, a laser-induced modulation of the electron energy followed by energy-dependent path length differences in the magnetic lattice leads to the formation of a sub-picosecond electron density modulation. In a subsequent bending magnet, ultrashort coherent radiation pulses in the THz regime are emitted, which are extracted by a dedicated THz beamline and are detected by a hot-electron bolometer with a response time in the microsecond regime.

Within the scope of this thesis, the evacuated THz beamline at DELTA was optimized and extended. A Fourier transform infrared spectrometer and ultrafast detectors with response times in the picosecond regime were installed, which allowed studying the spectrum of the laser-induced THz radiation as well as the temporal evolution of the density modulation over several revolutions after the initial laser-electron interaction. The laser-electron interaction, the formation of the density modulation, and the generation of the THz radiation were modeled in detail. The simulation results are in good agreement with the experimental findings and enable a deeper understanding of the underlying physics.

Characterization measurements of the laser-induced THz radiation intensity and spectrum confirmed theoretical expectations and numerical results. Based on a variation of laser and storage ring parameters and of the longitudinal and transverse laser-electron overlap, optimized parameters and improvements for the operation of the DELTA short-pulse facility are presented. By scanning the delay between laser pulse and electron bunch, the longitudinal bunch profile was studied, while a Fourier transform of the THz spectra was used to determine the profile of the laser-induced density modulation. Results from turn-by-turn resolved measurements give insight into the longitudinal beam dynamics. In cooperation with a group from the University Lille 1, France, narrow-band THz pulses were generated based on the so-called chirped-pulse beating technique, which extended previous results from the UVSOR storage ring in Japan from the sub-THz range to frequencies up to 5.5 THz.

Zusammenfassung

Bei DELTA, einem von der Technischen Universität Dortmund als Synchrotronstrahlungsquelle betriebenen 1,5-GeV-Elektronenspeicherring, wurde 2011 eine Kurzpulsquelle für Vakuum-Ultraviolett- und Terahertz-(THz-)Strahlung errichtet. Durch eine Laser-induzierte Modulation der Elektronenenergie und energieabhängige Weglängenunterschiede in der nachfolgenden Magnetstruktur entsteht eine Elektronendichtemodulation mit Strukturlängen von unter einer Pikosekunde. Als Konsequenz werden in einem Ablenkmagneten ultrakurze kohärente Strahlungspulse im THz-Bereich emittiert, durch eine dedizierte THz-Strahllinie nach außen geführt und mit Hilfe eines sogenannten „hot-electron“ Bolometers detektiert, welches eine Zeitauflösung im Mikrosekunden-Bereich bietet.

Im Rahmen dieser Arbeit wurde die bei DELTA bestehende Vakuum-THz-Strahllinie optimiert und erweitert. Durch die Installation eines Fourier-Transformations-Infrarot-Spektrometers und ultraschneller Detektoren mit Zeitauflösungen im Pikosekunden-Bereich konnten das Spektrum der Laser-induzierten THz-Strahlung sowie die Weiterentwicklung der Dichtemodulation über mehrere Umläufe im Speicherring nach der ursprünglichen Laser-Elektronen-Wechselwirkung untersucht werden. Für die Laser-Elektronen-Wechselwirkung, die Entstehung der Dichtemodulation und die Erzeugung der THz-Strahlung wurde ein detailliertes Computermodell erstellt. Die Simulationsergebnisse weisen eine gute Übereinstimmung mit den experimentellen Daten auf und ermöglichen ein tieferes Verständnis der zugrunde liegenden Physik.

Durch Messungen der Intensität und des Spektrums der Laser-induzierten THz-Strahlung wurden theoretische Vorhersagen und numerische Ergebnisse bestätigt. Basierend auf der Variation von Laser- und Speicherring-Parametern sowie des longitudinalen und transversalen Laser-Elektronen-Überlapps werden optimierte Parameter-Einstellungen und Verbesserungen für den Betrieb der Kurzpulsquelle beschrieben. Die longitudinale Ladungsverteilung im Elektronenpaket wurde durch Abtasten mit dem zeitlich verzögerten Laserpuls untersucht, während das Profil der Laser-induzierten Dichtemodulation durch die Fourier-Transformation von THz-Spektren bestimmt wurde. Die Ergebnisse von umlaufaufgelösten Messungen gewähren einen Einblick in die longitudinale Strahldynamik. In Zusammenarbeit mit einer Gruppe der Universität Lille 1 in Frankreich wurden schmalbandige THz-Pulse basierend auf der sogenannten „chirped-pulse beating“-Methode erzeugt. Der bei vorherigen Experimenten am Speicherring UVSOR in Japan auf unter 1 THz limitierte Frequenzbereich wurde dabei mit bis zu 5,5 THz deutlich erweitert.

Contents

3. Simulation of Laser-Induced THz Radiation 51

4. Laser-Induced THz Radiation at DELTA 59

5. Experimental and Simulation Results 71

List of Abbreviations

AC	alternating current
ACO	Anneau de collision d'Orsay (former storage ring in Orsay, France)
AlGaAs	aluminium gallium arsenide
ALS	Advanced Light Source (synchrotron radiation facility at the Lawrence Berkeley National Laboratory in Berkeley, USA)
ANKA	Angströmquelle Karlsruhe (synchrotron radiation facility at the KIT)
ARPES	angle-resolving photoemission spectrometer
BBO	β-barium borate
BESSY	Berliner Elektronen-Speicherring Gesellschaft für Synchrotronstrahlung (synchrotron radiation facility at the Helmholtz-Zentrum Berlin, Germany)
BL	beamline
BNC	Bayonet Neill–Concelman (coaxial cable/connector standard)
BoDo	Booster Dortmund (booster synchrotron at DELTA)
BoPET	biaxially-oriented polyethylene terephthalate
BPM	beam position monitor
BPP	beam parameter product
BWO	backward-wave oscillator
CCD	charge-coupled device
CDR	coherent diffraction radiation
CHG	coherent harmonic generation
CPA	chirped-pulse amplification
CPB	chirped-pulse beating
CSR	coherent synchrotron radiation
CTR	coherent transition radiation
CW	continuous wave
DC	direct current
DCCT	DC current transformer
DELTA	Dortmund Electron Accelerator (synchrotron light source at TU Dortmund University, Germany)
DESY	Deutsches Elektronen-Synchrotron (national research center in Hamburg, Germany)
DLaTGS	deuterated L-α-Alanine doped TGS
DORIS	Doppel-Ring-Speicher (former storage ring at DESY)
DSO	digital storage oscilloscope
EEHG	echo-enabled harmonic generation
Elettra	Elettra Sincrotrone Trieste (national research center in Trieste, Italy, and name of its electron storage ring)
EPICS	Experimental Physics and Industrial Control System
ESD	electrostatic discharge
FEL	free-electron laser
FERMI	Free-Electron Radiation and Matching Instrumentation (FEL at Elettra)
FFT	fast Fourier transform
FIR	far-infrared
FLASH	Free-Electron Laser in Hamburg (FEL at DESY)
FODO	focusing, drift, defocusing, drift (quadrupole magnetic lattice)
FROG	frequency-resolved optical gating
FTIR	Fourier transform infrared spectroscopy
FWHM	full width at half maximum
GaAs	gallium arsenide
GDD	group delay dispersion
Ge	germanium
GVD	group velocity dispersion
HEB	hot-electron bolometer
HeNe	helium-neon [laser]
Hg	mercury
iCCD	intensified CCD
IMS	Institute of Micro- and Nanoelectronic Systems (institute of the KIT)
InGaAs	indium gallium arsenide
InSb	indium antimonide
IR	infrared
KBr	potassium bromide
KIT	Karlsruhe Institute of Technology (national research center in Karlsruhe, Germany)
KLM	Kerr-lens mode-locking
LCLS	Linac Coherent Light Source (FEL at SLAC)
LHe	liquid helium
LN2	liquid nitrogen

MIR	mid-infrared
MLS	Metrology Light Source (synchrotron light source operated by the Physikalisch-Technische Bundesanstalt in Berlin, Germany)
MPI	Martin-Puplett interferometer
Mylar	brand name for BoPET
NbN	niobium nitride
Nd:YLF	neodymium-doped yttrium lithium fluoride
Nd:YVO$_4$	neodymium-doped yttrium orthovanadate
NEP	noise-equivalent power
PhLAM	Laboratoire de Physique des Lasers, Atomes et Molécules (institute at the University Lille 1, France)
PSI	Paul Scherrer Institute (national research institute in Villigen, Switzerland)
QCL	quantum cascade laser
RF	radio frequency
RGA	regenerative amplifier
rms	root mean square
SACLA	SPring-8 Angstrom Compact Free Electron Laser (FEL near SPring-8)
SAW	superconducting asymmetric wiggler
SBD	Schottky-barrier diode
SHG	second-harmonic generation
Si	silicon
SLAC	Stanford Linear Accelerator Center (national laboratory in Menlo Park, USA)
SLS	Swiss Light Source (synchrotron radiation facility at the PSI)
SPA	single-pass amplifier
SPIDER	spectral phase interferometry for direct electric-field reconstruction
SPring-8	Super Photon ring-8 GeV (synchrotron radiation facility in Sayo-cho, Japan)
SVD	singular value decomposition
T1	transfer line 1 (at DELTA)
T2	transfer line 2 (at DELTA)
TES	transition edge sensor
TGS	triglycine sulfate
THG	third-harmonic generation
THz	terahertz (10^{12} hertz)
THzSMe	‘THz Simulation with MATLAB and `elegant`’ (computer code)
Ti:sapphire	titanium-sapphire (titanium-doped sapphire (Al_2O_3))
U250	electromagnetic undulator at DELTA
U55	permanent magnet undulator at DELTA
UHV	ultrahigh vacuum
USA	United States of America
UV	ultraviolet
UVSOR	Ultraviolet Synchrotron Orbital Radiation Facility (synchrotron radiation facility in Okazaki, Japan)
VUV	vacuum-ultraviolet
YBCO	$YBa_2Cu_3O_7$ (yttrium barium copper oxide)
ZFF	zero-filling factor

Introduction

In 1947, a group of scientists and technicians led by H. C. Pollock observed "a small spot of brilliant white light" [2] when looking into the transparent vacuum chamber of the 70-MeV electron synchrotron at General Electric, Schenectady, NY. Then identified as the radiation predicted by Ivanenko and Pomeranchuk in 1944 [3] and Schwinger in 1945 [4][1], the radiation emitted by relativistic charged particles on a circular trajectory is known today as 'synchrotron radiation' due to the type of particle accelerator at which it was observed for the first time. Theoretical considerations about the radiation emitted by accelerated charges and its basic properties date back even further to Schott in 1912 [6], Wiechert in 1900 [7], Liénard in 1898 [8], and Larmor in 1897 [9].

First experiments with synchrotron radiation were based on the parasitic use of light from bending (dipole) magnets of electron or positron storage rings mainly built for high-energy physics [5]. Soon it was realized that synchrotron radiation offers outstanding properties – high intensity, a broad and continuous spectrum, and analytical calculability of the spectrum and spatial distribution – with a potential value for, e.g., the study of matter and as a precise radiation standard [10]. This led to the construction of storage rings designed exclusively for operation as a synchrotron radiation facility. Later versions introduced optimized magnetic lattices for a low emittance (i.e., small electron beam size and divergence) as well as so-called insertion devices to further increase the photon flux or to narrow the emission spectrum of the synchrotron radiation, e.g., by using periodic sequences of alternating dipole magnets ('wigglers' and 'undulators'). Today, about 50 synchrotron light sources around the world [11] deliver brilliant radiation ranging from the hard X-ray to the far-infrared (FIR) regime for a huge and ever growing variety of applications. With the so-called high-gain free-electron lasers (FELs), at which linear accelerators deliver short electron bunches with high peak currents to produce ultrashort, coherent, and high-brilliance light pulses in a long undulator section, a new generation of light sources has emerged in recent years.

Ultrashort and coherent light pulses from FELs, particularly at short wavelengths in the vacuum-ultraviolet (VUV) or X-ray regime, have become of increasing interest for several fields of fundamental research, e.g., for time-resolved studies of ultrafast chemical processes or magnetization dynamics. However, only four high-gain FELs with wavelengths in the VUV regime or shorter are currently being operated as a user facility[2] as opposed to almost 50 storage rings. In recent years, several strategies have been devised to shorten the pulse length and thereby extend the scientific possibilities of the well-established storage ring-based light sources. One of these strategies, based on the interaction of ultrashort laser pulses with electron bunches in an undulator section, is the so-called coherent harmonic generation (CHG) principle, which is ex-

---

[1] Although not published until 1949 [4], Schwinger communicated his results to interested parties starting in 1945 [5].

[2] In historical order: FLASH at DESY (Hamburg, Germany), LCLS at SLAC (Menlo Park, USA), SACLA near SPring-8 (Sayo-cho, Japan), and FERMI at Elettra (Trieste, Italy).

plained in detail together with its implementation at the electron storage ring DELTA in Dortmund, Germany, in Ch. 1.3.

Caused by the laser-electron interaction, energy-dependent path length differences in the subsequent magnetic lattice lead to a modulation of the longitudinal electron density. When these sub-picosecond structures pass through a bending magnet, coherent pulses in the terahertz (THz) regime are emitted, corresponding to the Fourier transform of the density modulation. The THz radiation can be used as a diagnostics tool for the laser-electron interaction as well as for studies of general storage ring parameters and electron beam dynamics. Furthermore, THz radiation itself has become a highly demanded instrument for experiments in fundamental research (Ch. 1.1).

After the installation and commissioning of a dedicated THz beamline at the electron storage ring DELTA in 2011 (Ch. 1.3 and 4.1; [12,13]), the goals of this thesis were to extend the scientific capabilities of this beamline by introducing ultrafast THz detectors and a high-resolution spectrometer, and to employ these instruments for

- diagnostics and optimization of the laser-electron overlap,
- studies of the charge distribution in the electron bunches,
- studies of the beam dynamics in the storage ring, and
- intensity and spectral optimization of the laser-induced THz pulses for application in future user experiments.

The following Ch. 1 gives an overview of the THz frequency range, available sources and detectors, the synchrotron radiation source DELTA in Dortmund, and its short-pulse facility. Chapter 2 covers the theoretical aspects of laser-induced THz radiation, including the laser-electron interaction and the emission process. As a basis for later comparison to experimental results, different approaches to simulating the THz generation are discussed in Ch. 3. Chapter 4 describes the THz setup at DELTA including the different detector types that have been employed at the THz beamline. The experimental and simulation results (Ch. 5) cover time-resolved turn-by-turn observations of laser-induced THz pulses as well as the detection and manipulation of their spectrum. The final Ch. 6 gives a conclusion and outlook. Further information can be found in the appendices.

1. Basic Concepts

1.1. The Terahertz Frequency Range

This section will give an overview of radiation properties and applicable technologies in the terahertz (THz) frequency range. The information presented here is mainly based on the books by E. Bründermann et al. [14] and X.-C. Zhang and J. Xu [15].

1.1.1. Properties and Challenges

The THz frequency range is usually defined as the section of the electromagnetic spectrum between 0.3 and 10 THz, corresponding to a wavelength range of 1 mm to 0.03 mm (Fig. 1.1), and is also referred to as the far-infrared (FIR) or sub-millimeter range.

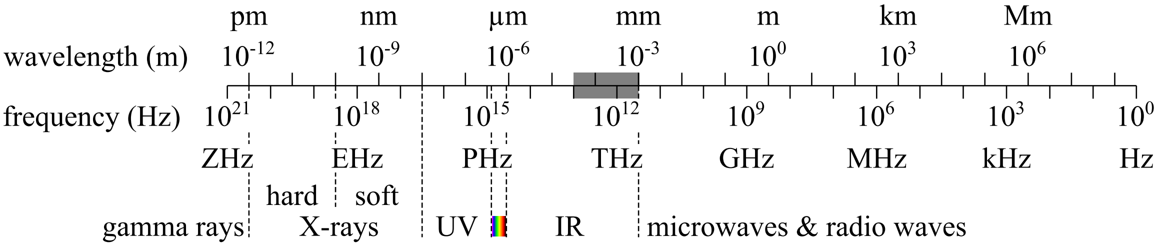

Figure 1.1.: Electromagnetic spectrum ranging from gamma rays over X-rays, ultraviolet radiation (UV), visible light (colored section), infrared radiation (IR), and microwaves down to radio waves (spectral ranges according to [16]). The THz frequency range is marked as a grey section on the wavelength/frequency axis.

THz radiation occurs in nature mainly as part of thermal or black-body radiation, which is emitted by matter with a temperature above absolute zero, and as part of the cosmic background radiation. With limited intensity and coherence, these sources are of little value for laboratory experiments, but have their applications for astronomic studies as well as for the security industry, e.g., as part of passive full-body scanners.

Far into the 20th century, the electromagnetic spectrum between microwaves and infrared light was often referred to as the 'THz gap'. Neither efficient detectors nor suitable sources existed due to the fact that THz radiation falls into the 'gap' between the well-established radio frequency (RF) technology on the one hand and optics on the other hand. For example, the low photon energy (1 THz corresponds to 4 meV) is easily obscured by thermal motion ($k_\mathrm{B}T \approx 26$ meV at room temperature $T = 300$ K)[1], making it difficult to use optical sources or detectors based on quantum transitions. Furthermore, as the wavelength of THz radiation approaches the macroscopic dimensions of typical optical components, approximations used in optics may no longer apply,

---

[1] Boltzmann constant $k_\mathrm{B} \approx 1.381 \cdot 10^{-23}$ J/K $\approx 8.617 \cdot 10^{-5}$ eV/K.

and diffraction losses become dominant. Classic RF sources and detectors based on circuits and antennas are equally problematic, as the charge carriers cannot follow oscillations above several hundred GHz. The same applies to waveguides, where the resistance is drastically increased due to the skin effect at these high frequencies. Despite these difficulties, first ventures into the THz range date back into the late 19th century, e.g., with H. Rubens and E. F. Nichols using reflective quartz- or fluorite-based filters behind a heat lamp to generate almost monochromatic light down to a frequency of 12 THz (25 µm) [17], or with J. C. Bose using waveguides, horn antennas, and even semiconductors at frequencies up to 60 GHz (5 mm) [18].

In recent decades, THz radiation has become of major interest to a growing number of applications, e.g., in biology, medicine, astronomy, plasma physics, chemistry, nondestructive testing, security, and the defense sector. Only a few examples shall be mentioned here, related to the unique properties of this frequency range [14, 15]:

- Many molecules offer strong and characteristic absorption lines at THz frequencies, related to their vibrational and rotational modes. Therefore, THz radiation can be employed to study and identify molecules, whether in space, chemistry labs, or at a security checkpoint.
- Dry dielectric materials like cloth, paper, wood, and plastic are transparent to THz radiation, which has its applications in nondestructive testing, process control, and security.
- With sub-millimeter wavelengths, THz radiation is still suitable to reach moderate resolutions at two- and three-dimensional imaging applications, but also has a sufficiently low frequency to directly sample the electric field, which is used, e.g., for the phase-sensitive time-domain spectroscopy.
- With ultrashort THz pulses, time-resolved measurements are possible, e.g., for studies of plasma dynamics or insulator-conductor transitions [19].

These properties and applications have led to the development of a huge variety of sources and detectors, some of which will be discussed briefly in the following sections with emphasis on the devices employed at the DELTA THz beamline.

1.1.2. Table-Top Sources

The above-mentioned thermal or black-body emission does not only occur as a natural THz radiation source, but is also vastly used as a dedicated continuous wave (CW) laboratory source for many applications which do not require ultrashort pulses or coherence, e.g., Fourier transform infrared spectroscopy (FTIR) (Ch. 2.7). Ideal black bodies emit a continuous spectrum following Planck's law [14]. Practical thermal sources offer a reduced emissivity, which is the ratio of emitted thermal radiation to the radiation from an ideal black body at the same temperature. As an example for solid-state thermal sources, the so-called Globar, a rod made of silicon carbide and heated to 1 350 K to 1 500 K, provides a sufficiently high emissivity above a few THz [14]. Operating at much higher temperatures and with their emissivity increasing towards lower frequencies, plasma sources are better suited for the THz range. One example is the mercury (Hg) arc lamp, usually operated around 1 bar, at which the emission spectrum is a combination of the 5 000-K arc and the surrounding quartz tube, which reaches up to 1 000 K [14]. Both, a Globar and an Hg arc lamp, serve as an internal reference source in the FTIR spectrometer employed at the DELTA THz beamline (Ch. 4.3).

Table 1.1.: Table-top THz sources and their parameters [14].

source	**frequency range** (THz, typ.)	**tunability**	**power** (max.)	**pulse length** (min.)	**coherent**
Globar	> 1	broad spectrum	-	CW	no
Hg arc lamp	> 0.3	broad spectrum	-	CW	no
electrically ex. gas laser	1 to 40	fixed lines	600 mW (CW)	µs	yes
optically ex. gas laser	0.15 to 8	fixed lines	$\sim$ 100 mW	µs	yes
Si/Ge laser	1 to 7	limited	40 W (peak)	ps	yes
QCL	0.8 to 4.9	fixed lines	140 mW (CW)	ns	yes
photomixing	0.3 to 9	yes	µW	ps	yes
harm. generator	< 2	yes	µW to mW	CW	yes
BWO	< 1.4	yes	1 mW to 100 mW	CW	yes
gyrotron	< 1	partially	mW to W	CW	yes
photo-conductive antenna	< 70	broad spectrum	µW to mW	ps	yes

Not employed within the scope of this thesis, the following selection of other common sources for THz radiation [14] is listed for comparison. Their key parameters are given in Tab. 1.1.

- Electrically excited or optically pumped gas lasers use population inversions between rotational levels of vibrational states.
- Silicon (Si) and germanium (Ge) THz lasers are based on impurity energy levels or Landau levels introduced by external magnetic fields.
- The quantum cascade laser (QCL) is based on a series of artificially created quantum wells (usually a GaAs/AlGaAs superlattice) exposed to an external electric field. Electrons drop down the resulting ‘potential staircase’ and emit one photon per step.
- Harmonic generators use high-power microwave sources in the GHz regime and a series of frequency doublers or triplers to convert the initial frequency up into the THz band.
- The backward-wave oscillator (BWO) is an electron tube in which an electron beam travels through a slow-wave structure generating and amplifying a continuously tunable electromagnetic wave.
- The gyrotron is an electron tube in which the beam passes through a resonant cavity while under the influence of an external longitudinal magnetic field, which leads to relativistic instabilities and the emission of radiation.
- Photomixing (or optical-rectification) sources employ non-linear diodes or crystals to generate radiation at the sum and difference frequency of two visible, infrared (IR), or microwave sources.
- At photoconductive antennas, a voltage is applied to two metal electrodes patterned as an antenna structure on a semiconductor substrate. An ultrashort laser

pulse focused onto the gap between the electrodes leads to the emission of a short and broad-band THz pulse.

1.1.3. Accelerator-Based Sources

As mentioned before, synchrotron radiation emitted by relativistic charges forced on a circular trajectory offers a broad and continuous spectrum reaching from the X-ray into the FIR or THz regime. In this section, the basic spectral properties shall be sketched through the example of the electron storage ring BESSY II at the Helmholtz-Zentrum Berlin, Germany. Figure 1.2 shows its synchrotron radiation spectrum at the nominal beam energy of 1.7 GeV [20]. The so-called critical frequency (see Eq. 2.99), which divides the power spectrum into two areas of equal size, is $6.0 \cdot 10^{17}$ Hz. Towards lower frequencies ν, the spectral power decreases according to $\mathrm{d}P/\mathrm{d}\nu \propto \nu^{1/3}$ (Eq. 2.102). As a consequence, the spectral power at $\nu = 1$ THz is reduced by two orders of magnitude as compared to that at the critical frequency, and the spectral power integrated over a relative bandwidth of 0.1% by more than seven orders of magnitude.

Several methods have been devised to enhance the spectral power of synchrotron radiation at THz frequencies, which are mostly based on an emission process leading to coherent synchrotron radiation (CSR). Due to the quadratic dependence of the coherent emission power on the number of electrons involved – rather than just linear in case of incoherent emission – several orders of magnitude in emission power can be gained (Eq. 2.107).

CSR occurs when structures of the electron beam become shorter than the emission wavelength. For the THz regime, corresponding to a (sub-)picosecond time scale, this can be achieved using very short electron bunches, either from photo-cathode electron sources and linear accelerators, or by operating a storage ring in a so-called low-α

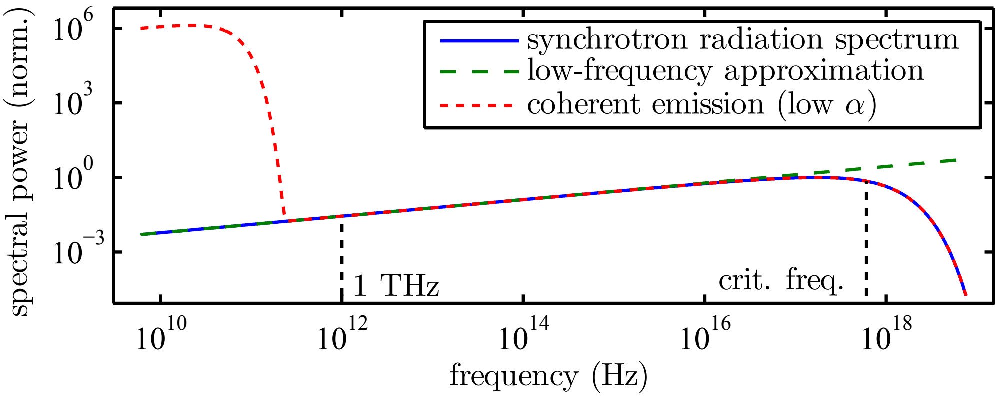

Figure 1.2.: Angle-integrated spectrum (Eq. 2.101) of the synchrotron radiation from a bending magnet at the electron storage ring BESSY II operated at its nominal beam energy of 1.7 GeV [20], normalized to maximum spectral power (blue). The low-frequency approximation (green, dashed) is given by Eq. 2.102. The spectral powers at 1 THz and at the critical frequency are indicated by the vertical dashed lines. The coherent emission spectrum during low-α operation (red, dotted) is given by Eq. 2.107. Here, a bunch length of 3 ps (rms) and a bunch current of 40 µA were assumed [21].

Table 1.2.: Accelerator-based THz sources and their parameters [14, 28, 29].

source	**peak frequency** (THz, typ.)	**tunability/ spectrum**	**power/ energy** (max.)	**pulse length** (min.)	**repetition rate**
low-α CSR (stable)	0.4	broad spectrum	$\sim$ 10 mW	few ps	$\sim$ 100 MHz
low-α CSR (burst.)	0.6	broad spectrum	$\sim$ 10 mW	few ps	$\sim$ 100 MHz
laser-induced CSR	1.5 to 2.5	broad spectrum	$\sim$ 10 nJ	(sub-)ps	few kHz
linac-based CSR	few THz	broad spectrum	$\sim$ 1 nJ	sub-ps	$\sim$ 10 kHz
THz FEL	0.1 to 100	narrow, tunable	$\sim$ 1 µJ	(sub-)ps	$\sim$ 10 MHz
CTR	1 to 3	broad spectrum	mJ	(sub-)ps	$\sim$ 10 MHz
CDR	1 to 3	broad spectrum	µJ	(sub-)ps	$\sim$ 10 MHz

mode, at which the typical bunch length of a few ten to hundred picoseconds (about 15 ps (rms) at BESSY II) is reduced to the few-picosecond regime by applying different magnet optics. The low-α user operation at BESSY II offers a typical bunch length of 3 ps (rms) and a bunch current of 40 µA [21], resulting in a strong coherent emission in the sub-THz regime (Fig. 1.2). Other facilities in Germany offering a low-α user operation are the MLS in Berlin and ANKA in Karlsruhe.

Sub-picosecond structures on top of longer electron bunches lead to coherent emission in the THz regime as well. These structures can occur naturally as part of the so-called microbunching instability, at which an initial random density fluctuation radiates coherently with the radiation acting back on the electron bunch, thereby amplifying the density modulation. This instability and the corresponding THz radiation bursts happen above a certain current threshold [22] and have been observed at several storage rings (see, e.g., [23, 24]) especially during low-α operation, where the bunches are short and the peak current is high.

Alternatively to this spontaneous process, sub-picosecond structures can also be imprinted using a laser-induced energy modulation, which leads to a (sub-)picosecond longitudinal density modulation due to energy-dependent path length differences in the storage ring lattice. This process together with its implementation at DELTA is explained in detail in Chs. 1.3 and 2. Laser-induced THz radiation has been generated at several other storage rings as well, including BESSY II [25], the SLS at the Paul Scherrer Institute (PSI) in Villigen, Switzerland [26], and the ALS at the Lawrence Berkeley National Laboratory in Berkeley, USA [27].

Listed for comparison, other accelerator-based THz sources are

- undulators, which provide a narrow emission spectrum with high peak power at a tunable frequency given by the period length and field strength of the undulator (Eq. 2.78),
- THz FELs, at which spontaneous undulator radiation acts back on the electron beam using an optical cavity, leading to a bunching of the electron beam at the undulator wavelength and a coherent emission,
- coherent transition radiation (CTR), which is emitted when an ultrashort electron bunch experiences a change of the dielectric constant, e.g., by passing through a thin metal screen [28, 30], and

- coherent diffraction radiation (CDR) [29], occurring when an ultrashort electron bunch passes alongside an inhomogeneous medium or a non-planar surface. In case of a periodically structured surface, e.g., a metal grating, radiation with a narrow and well-defined spectrum is emitted and is often called Smith-Purcell radiation [31].

An overview of the above-mentioned accelerator-based sources is given in Tab. 1.2.

1.1.4. Detectors

In principle, detector types can be divided into incoherent (or direct) detectors, measuring only the amplitude or intensity of a signal, and coherent detectors, which also measure the phase.

Thermal detectors are an example for direct detectors and are vastly applied throughout most THz research fields and corresponding applications. They can be schematically described by Fig. 1.3. Incoming radiation is absorbed by a sensor, which might include the actual sensor material and a separated absorber material for the desired frequency range. The temperature of the sensor rises, which is measured and transformed into an electrical signal. Due to a defined thermal coupling to a heat reservoir, the sensor then returns to the reservoir temperature. For a high sensitivity, the sensor should have a high absorptivity close to one (over the desired frequency range), a low heat capacitance, and a low thermal coupling. The ratio between thermal coupling G (in W/K) and heat capacitance C (in J/K) determines a high-frequency cutoff, or a minimum time constant of $\tau = C/G$. For room temperature detectors, typical time constants are of the order of seconds to milliseconds. Reducing C, e.g., by reducing the sensor size, would reveal a faster response, but might be prohibited in order to maintain a high absorptivity especially at low frequencies [14].

The three most common room-temperature thermal detectors are Golay cells [32], thermopiles [14], and pyroelectric detectors. Pyroelectric detectors use the permanent electric dipole moment which is present along a certain axis of some materials. If the temperature of the material changes due to an incoming radiation pulse, the spacing of the atomic lattice changes and a charge or voltage can be measured at electrodes attached to opposite ends of the detector chip [14]. A common and sensitive pyroelectric material is deuterated L-α-Alanine doped TGS (DLaTGS). The FTIR spectrometer employed at the DELTA THz beamline (Ch. 4.3) is equipped with two DLaTGS detectors, optimized for the mid-infrared (MIR) (> 10 THz) and FIR (> 0.5 THz) regime, respectively [33].

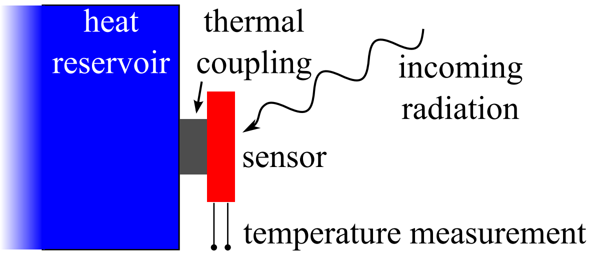

Figure 1.3.: Schematic principle of a thermal THz detector (source: [13], modified).

Bolometers are thermal detectors based on a temperature-dependent change of electrical resistance, which is usually measured as a change in voltage while applying a fixed bias current. Bolometers are often cooled to liquid nitrogen (77 K) or liquid helium (4.2 K) temperatures, which helps to overcome some of the above-mentioned difficulties when trying to increase sensitivity and speed by decreasing the sensor's heat capacity C without diminishing absorption. Furthermore, the temperature coefficient of the electrical resistance is increased, offering a much higher responsivity[2], while thermal noise is greatly reduced. A common type of bolometers are those based on doped semiconductors like Ge or Si usually bonded or glued to a separate absorber material like painted sapphire or diamond ('composite bolometer') [14]. Such an Si bolometer with a response time in the millisecond regime is used as the most sensitive detector at the FTIR spectrometer employed at the DELTA THz beamline (Ch. 4.3), and it also provides sensitivity at slightly lower frequencies than achievable with the above-mentioned FIR DLaTGS detector. Bolometers based on thin-film superconducting metals exploit the strong dependence of resistivity on temperature near the superconducting transition temperature and are often called transition edge sensors (TES) [14].

If the change of resistivity is not based on a change of temperature of the atomic lattice, but instead on a direct absorption of photons by electrons, the detector is no longer a classical bolometer but a photoconductive detector. One example is the photoconductive antenna, at which a voltage is induced by the electric field of the THz pulse, and probing the antenna with a laser pulse then delivers a current proportional to the incoming THz field [14].

In some photoconductors, when cooled to very low temperatures of 4.2 K (normal boiling point of helium) or below, the so-called hot electron effect occurs [34]. Here, radiation is absorbed by free carriers causing intraband transitions, thereby generating so-called hot electrons at a thermal equilibrium above the lattice temperature. This significantly changes the electron mobility and, therefore, the conductivity of the detector. Such photoconductive detectors are called hot-electron bolometers (HEBs), as it is a change of the electron temperature which is detected through a change of conductivity, whereas the lattice of the sensor presents the heat reservoir. A commercial semiconductor HEB based on InSb [35] operated at 4.2 K serves as the standard THz detector at DELTA (Ch. 4.2) with a response time in the µs regime. A superconducting HEB based on NbN offering a response time of less than 160 ps [36,37] was temporarily employed at the DELTA THz beamline for time-resolved experiments (Ch. 4.2).

Furthermore, a detector based on the high-temperature superconductor $YBa_2Cu_3O_7$ (YBCO) was tested and is now permanently installed at the DELTA THz beamline (Ch. 4.2). It was developed by the Institute of Micro- and Nanoelectronic Systems (IMS) at the Karlsruhe Institute of Technology (KIT) and shows a frequency-dependent change of its detection mechanism [38, 39]:

- For photon energies above the superconducting energy gap (corresponding to a few THz), it works as a superconducting HEB with a fast response component of a few picoseconds based on electron heating and electron-phonon cooling, and a nanosecond relaxation component based on the energy transfer from phonons in the YBCO lattice to the detector substrate (phonon escape time).
- For THz pulses with photon energies below the superconducting energy gap, an increase by one order of magnitude in responsivity has been measured, the

---

[2] The voltage responsivity is defined as output voltage over incoming radiation power.

nanosecond bolometric component is no longer visible, and a signal can be measured without applying any bias current ('zero-bias response') [40]. Further studies based on switching the polarity of an incoming THz pulse have shown that for these frequencies the detector directly responds to the electric field of the pulse rather than just to its intensity. It is suggested that the detection is based on the movement of magnetic vortices within this type-II superconductor [40].

As a final example for a direct detector, the Schottky-barrier diode (SBD) is based on a metal-semiconductor junction leading to a potential barrier and a region depleted of electrons. If a voltage is applied, thermionic emission over the barrier or tunneling through the barrier can occur (depending on the temperature and doping of the semiconductor) with a highly non-linear current-voltage curve. Embedded into an antenna structure, this non-linear junction resistance serves as the actual THz detector [14]. A commercial zero-bias SBD based on InGaAs [41, 42] was employed at DELTA in 2015 (Ch. 4.2).

When combined with a local oscillator in a mixer setup, SBDs are also widely used as coherent detectors. Another example for coherent detectors is electro-optical crystals, at which a laser pulse is used to sample the time-dependent birefringence induced by the incoming THz field [14].

An overview of the above-mentioned direct detectors with a comparison of the achievable frequency ranges, sensitivities, and response times is given in Tab. 1.3.

Table 1.3.: THz detectors and their parameters [14, 35–42].

detector	**frequency range** (THz, typ.)	**sensitivity/ NEP**[3] ($\mathrm{W}/\sqrt{\mathrm{Hz}}$)	**response time** (min.)
Golay cell	> 0.3	$2 \cdot 10^{-10}$	100 ms
thermopile	> 0.3	µW	> 1 s
pyroelectric detector	> 0.5	10^{-9} to 10^{-10}	sub-ns
Si composite bolometer	0.15 to 15	10^{-13}	10 µs
supercond. bolometer	antenna-dependent	10^{-17}	sub-ns
InSb HEB	0.06 to 0.5	$5 \cdot 10^{-13}$	µs
NbN HEB	0.16 to 3	$6 \cdot 10^{-9}$	< 160 ps
YBCO detector	antenna-dependent	$1.2 \cdot 10^{-11}$	< 17 ps
Schottky diode (SBD)	antenna-dependent	$8.5 \cdot 10^{-10}$	< 20 ps

---

[3] The noise-equivalent power (NEP) is the power of the incoming signal required to achieve a signal-to-noise ratio of one at an output bandwidth of one hertz (corresponding to an integration time of 0.5 s).

1.2. The Synchrotron Radiation Source DELTA

The experiments discussed in this thesis were carried out at DELTA, a 1.5-GeV electron storage ring operated as a synchrotron light source by the Center for Synchrotron Radiation of the TU Dortmund University in Dortmund, Germany [44–47].

A schematic layout of DELTA is shown in Fig. 1.4. The electron source is a thermionic triode gun with dispenser cathode and an anode voltage of 90 kV [48,49]. Its mode of operation can be switched online, allowing for a multi-bunch, a single-bunch, or a combined filling pattern (hybrid filling). Following a 4-MeV buncher cavity, an S-band linear accelerator increases the particle energy to 75 MeV [50]. These components are driven by a 3-GHz pulsed klystron, leading to a bunched structure with about 0.3 ns spacing.

The booster synchrotron BoDo consists of C-shaped dipole magnets and alternating focusing and defocusing quadrupole magnets (Fig. 1.5) forming a so-called FODO lattice with a circumference of 50.4 m [51]. Acceleration is provided by a three-cell DESY-type cavity operated at 500 MHz, leading to a bunch spacing of 2 ns. Electrons with 75 MeV from the linac are injected into BoDo via transfer line T1 and a set of fast injection kicker magnets. In a 7-second cycle, the magnets are ramped up to 1.5 T, which increases the particle energy to the nominal beam energy of 1.5 GeV, the electrons are transferred to the storage ring via transfer line T2 and corresponding extraction and injection kickers (full energy injection), and the magnets are ramped down again.

The dipole and quadrupole magnets in the storage ring DELTA are arranged in a triplet lattice. The circumference amounts to 115.2 m, resulting in a revolution

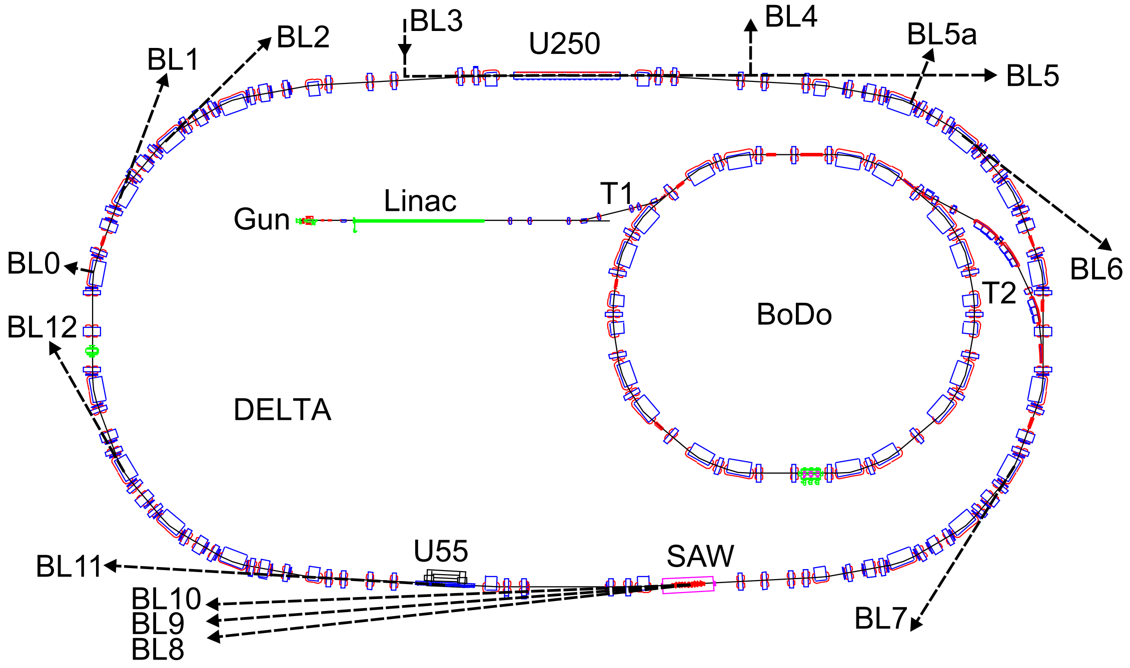

Figure 1.4.: Layout of DELTA with the electron source (Gun), the linear accelerator (Linac), the booster synchrotron BoDo, the electron storage ring including its three insertion devices (SAW, U55, U250), and the beamlines BL0 to BL12 (see text for details; source: [43], modified, courtesy of D. Schirmer).

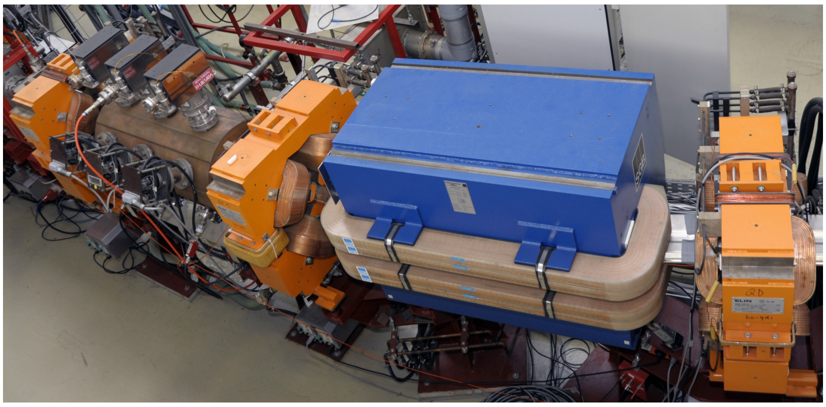

Figure 1.5.: Section of the booster synchrotron BoDo with a dipole magnet (blue), three quadrupole magnets (orange), and the three-cell RF cavity.

frequency of 2.6 MHz and a revolution time of 384 ns. DELTA has been operated temporarily at 550 MeV for a storage-ring FEL experiment [52]. However, the standard beam energy for delivering synchrotron radiation to the user community as well as for operation of the new short-pulse facility (Ch. 1.3) is the maximum energy of 1.5 GeV. Beam energy lost due to the emission of synchrotron radiation is replenished by a single-cell DORIS-type cavity operated at 500 MHz, which leads to a number of 192 possible bunches (‘RF buckets’).

During standard user operation, a multi-bunch train with approximately 144 bunches is accumulated up to a total beam current of 130 mA. The beam current then decreases with a lifetime of about 12 h (at 100 mA) until the next injection process is started, usually after 8 to 10 hours. For the commissioning of the new short-pulse facility (Ch. 1.3), the standard filling pattern is a single bunch with up to 20 mA. Short-pulse operation using a hybrid filling pattern with a 144-buckets multi-bunch train and a high-current single bunch within the 48-buckets gap has been demonstrated and is the preferred mode for a future short-pulse user operation.

Given by the beam energy, the magnetic lattice, and the accelerating RF gradient, the bunch length at DELTA is about 100 ps (FWHM). A low-α lattice for short-bunch operation has not been implemented. The position-dependent transverse beam size is given by the emittances and beta functions (see Ch. 2.2 for details).

Beam diagnostics and feedback is provided by a beam current monitor based on a DC current transformer (DCCT), 54 button-type beam position monitors (BPMs), 56 steering magnets controlled by a slow singular value decomposition (SVD)-based orbit correction [53], a transverse tune measurement and feedback system, and a digital bunch-by-bunch feedback system suppressing multi-bunch instabilities [54, 55]. The control system is based on EPICS [56].

Synchrotron radiation is generated in the 1.5-T dipole magnets offering a broad and continuous spectrum (Fig. 1.2) with a critical energy of 2.18 keV for the dipole magnet beamlines BL1, BL2, BL5a, BL7, and BL12 (Fig. 1.4). BL5a is the THz beamline and will be described in detail in Chs. 1.3 and 4.1. Furthermore, synchrotron radiation is provided by three insertion devices. The superconducting asymmetric wiggler (SAW) with a magnetic field of up to 5.3 T and critical photon energies from 4.2 keV to 7.9 keV serves as the source for the hard X-ray beamlines BL8, BL9, and

BL10. Providing soft X-ray photon energies from 55 eV to 1.5 keV, the U55 is a mechanically tunable permanent-magnet undulator serving BL11. During standard user operation, the electromagnetic undulator U250 delivers soft X-ray photon energies from 5 eV to 400 eV to BL5. Configured as an optical klystron (see Ch. 1.3 for details), it was part of the storage ring FEL [52] and is now a central element of the new short-pulse facility, which also includes the laser beamline BL3 and diagnostics beamline BL4.

An overview of the storage ring parameters is given in Tab. 1.4.

Table 1.4.: Parameters of the electron storage ring DELTA as of September 2015.

parameter	**value**
nominal beam energy	1.49 GeV
RF frequency	499.819 MHz
bunch spacing	2.0 ns
harmonic number	192
circumference	115.2 m
revolution frequency	2.60 MHz
revolution time	384.1 ns
bunch length	100 ps FWHM
multi-bunch current	130 mA (max.)
single-bunch current	10 to 20 mA (typ.)
lifetime (multibunch)	$\approx$ 12 h (at 100 mA)
lifetime (single bunch)	$\approx$ 2 h to 3 h (at 10 mA)
momentum compaction factor α	$5 \cdot 10^{-3}$
horizontal beam emittance	15 nm rad
vertical beam emittance	1.5 nm rad
relative energy spread	$6.8 \cdot 10^{-4}$

1.3. The Short-Pulse Facility at DELTA

The pulse length of synchrotron radiation emitted from dipole magnets and insertion devices is given by the electron bunch length of about 100 ps (FWHM). Modern, commercially available short-pulse laser systems offer pulse lengths in the femtosecond regime, however, only at wavelengths near the visible spectrum. In order to provide ultrashort radiation pulses in the sub-picosecond regime at shorter wavelengths, e.g., for time-resolved studies of ultrafast chemical reactions, phase transitions, or magnetization dynamics, a short-pulse facility based on the so-called coherent harmonic generation (CHG) principle has been established at DELTA since 2011 [57, 58]. Here, the idea is to convert ultrashort laser pulses in the visible frequency range to radiation pulses at harmonics of the original laser frequency using a laser-electron interaction within the electromagnetic undulator U250 of the DELTA storage ring. As a second consequence of the laser-electron interaction, coherent THz radiation pulses are emitted in a following dipole magnet.

1.3.1. Basic Principle and Setup

Ultrashort laser pulses (approx. 40 fs FWHM) co-propagate with an electron bunch (approx. 100 ps FWHM) in a first undulator, called modulator, which is tuned to the laser wavelength (Fig. 1.6). Caused by the transversely oscillating motion of the electrons in the undulator and the transverse electric field of the laser pulse, electrons gain or lose energy depending on their phase relative to the laser pulse, resulting

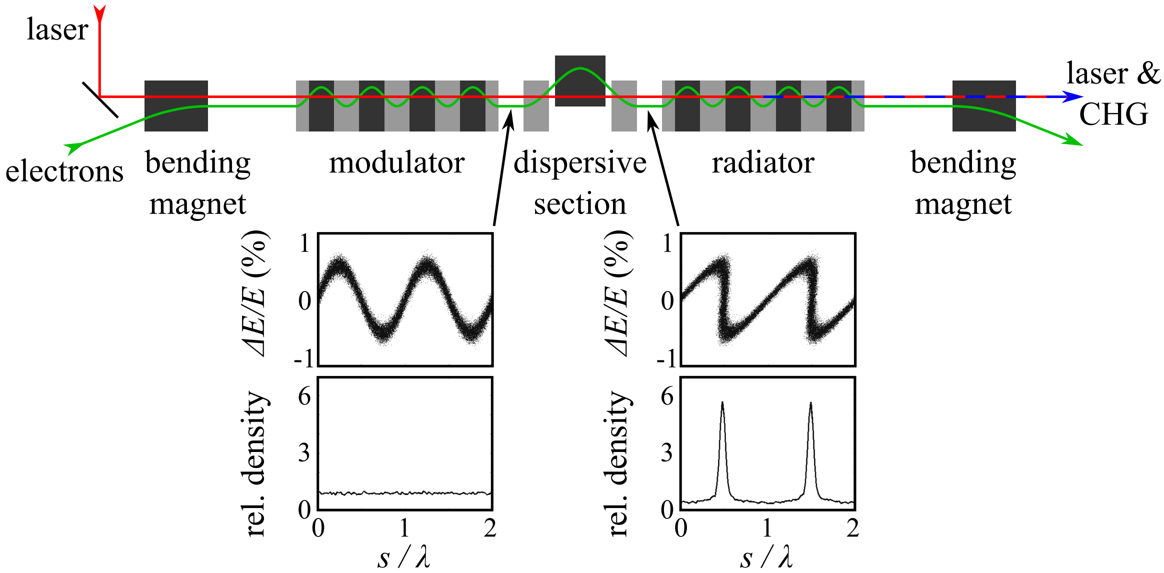

Figure 1.6.: Schematic sketch of the CHG setup including the incoming laser (red) and electron beam (green), two undulators (modulator and radiator) and a dispersive section (chicane), and the generated VUV (blue) radiation (source: [13], modified). The plots below show the electron distribution in longitudinal phase space (energy deviation ΔE from nominal beam energy E vs. longitudinal position s; top) and the corresponding longitudinal electron density (bottom) before and after passing the chicane.

in a sinusoidal energy modulation (Ch. 2.3). Due to energy-dependent path length differences in a magnetic chicane, electrons with more energy move ahead and electrons with less energy lag behind, which leads to a density modulation in the form of a series of so-called microbunches within the interaction range. A second undulator, called radiator, is tuned to a harmonic of the laser wavelength. Here, radiation from the periodically spaced microbunches overlaps coherently, resulting in an ultrashort and coherent radiation pulse on top of the incoherent 100-ps pulse emitted by the electrons which have not interacted with the laser pulse.

Due to further path length differences in the subsequent magnetic lattice of the storage ring, the off-energy electrons move out of the laser-affected slice, leaving a dip at the center of the electron bunch (Fig. 1.7). In one of the following dipole magnets, this sub-ps modulation of the longitudinal electron density leads to the emission of a coherent radiation pulse in the THz regime ('turn-0' signal; see below). The spectrum, given by the Fourier transform of the dip in the longitudinal electron density, is similar to that of a sub-picosecond electron bunch (Ch. 1.1.3). The modulation of the longitudinal electron density persists for several revolutions of the electron bunch in the storage ring, giving rise to a series of subsequent THz radiation pulses ('turn 1', 'turn 2', etc.). The THz radiation pulses (and their turn-by-turn evolution) can be used as a diagnostics instrument for the laser-electron overlap, as a tool to study general parameters and dynamics of the storage ring, and for time-resolved THz experiments.

The CHG principle was proposed in 1982 by R. Coisson and F. De Martini [59], who called it 'coherent relativistic scatterer' (CORSCAT). It was then demonstrated at the ACO storage ring in Orsay, France, in 1984 [60]. More recently, CHG has been implemented at the Elettra storage ring in Trieste, Italy [61], at the UVSOR storage ring in Okazaki, Japan [62], and at DELTA. While CHG experiments at Elettra have been discontinued in order to concentrate on the FEL project FERMI, CHG at UVSOR is still being investigated, but only during a few specialized shifts per year, as the undulators cannot be tuned to the laser wavelength at full beam energy. In contrast to Elettra and UVSOR, the CHG-based short-pulse facility at DELTA is operated on a regular basis, benefiting from two factors. Firstly, the CHG undulator can be tuned to the fundamental laser wavelength of 800 nm at the nominal beam energy of 1.5 GeV, thereby allowing CHG operation during standard operation for synchrotron radiation users. Secondly, DELTA offers 1000 hours per year of dedicated machine time for

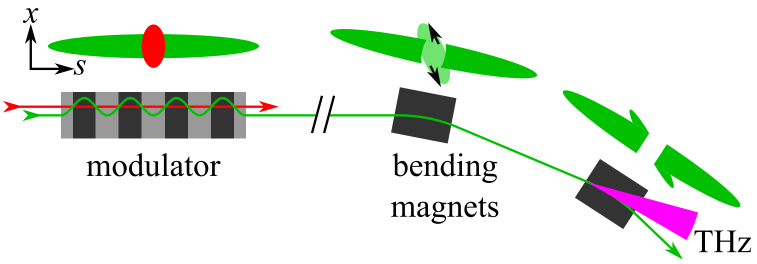

Figure 1.7.: Schematic sketch of the THz generation principle. An on-top view (horizontal coordinate x vs. longitudinal coordinate s, not to scale) of the electron bunch is sketched together with the interacting laser pulse (left), with the modulated electrons leaving the interaction range (center), and with a central gap (right) leading to the emission of THz radiation (magenta).

studies in accelerator physics, and about half of this time is being used to characterize and optimize the CHG source.

The layout of the DELTA short-pulse facility is shown in Fig. 1.8. The laser laboratory houses an 800-nm titanium-sapphire (Ti:sapphire) laser system with a mode-locked oscillator operating at a repetition rate of 83 MHz and a chirped-pulse amplifier providing a maximum pulse energy of 8 mJ and a minimum pulse length of 40 fs FWHM at a repetition rate of 1 kHz (see Chs. 2.1.1 and A.1.1). The laser pulses are coupled into BL3, focused by a refractive telescope embedded in a vacuum tank, and then sent into the electromagnetic undulator U250. Due to problems with mirror degradation at pre-vacuum conditions, the first section of BL3 including the telescope tank is presently operated at ambient pressure. The telescope tank is followed by a viewport marking the entrance to the storage-ring ultrahigh vacuum (UHV). Alternatively to 800-nm seeding, the wavelength can be converted to 400 nm using a second-harmonic generation (SHG) unit based on a non-linear crystal (BBO), which is followed by a reflective telescope in the laser laboratory and a bypass of the 800-nm telescope. A third-harmonic generation (THG) unit is installed but has not been used for seeding yet. For diagnostic purposes, a fraction of each laser pulse can be coupled out behind the telescopes and sent back into the laser lab, thereby allowing a ‘virtual waist’ to be observed at a distance to the telescopes equal to that of the modulator center. Two commercial instruments, a SPIDER [64] and a FROG [65], can be used for temporal pulse characterization.

The coils of the electromagnetic undulator U250 (250 mm period length, 19 periods) are grouped into three sections with independent power supplies. As part of a storage ring FEL [52], it was configured as an optical klystron – two undulators tuned to the desired FEL wavelength and a central dispersive section. For the new short pulse facility, the first seven periods serve as the modulator, the central three periods as the chicane, and the final seven periods as the radiator. Both, the modulator and radiator, can be tuned to a maximum wavelength of 800 nm at 1.5 GeV.

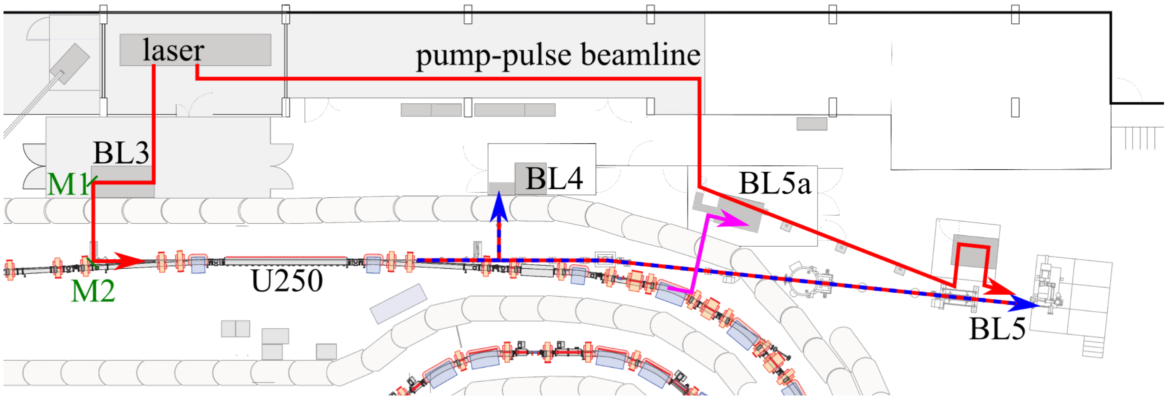

Figure 1.8.: Layout of the short-pulse facility at DELTA including the laser laboratory, the laser beamline BL3 with its motorized mirrors M1 and M2 (see Ch. 5.2.1), the northern section of the storage ring with the electromagnetic undulator U250, the diagnostics beamline BL4, the VUV beamline BL5, the THz beamline BL5a, and the pump-pulse beamline (source: [63], modified, courtesy of T. Schulte-Eickhoff).

The CHG and laser pulses can be sent into BL4 using a retractable in-vacuum mirror. BL4 serves as a diagnostics beamline for the short pulse facility and is equipped with CCD cameras, photodiodes, and a streak camera for finding the transverse and longitudinal overlap between the laser pulses and electron bunches. A Czerny-Turner-type monochromator [66] followed by an avalanche photodiode, and a fast-gated intensified CCD (iCCD) camera are used to study the spectral, spatial, and coherence properties of the CHG radiation. As BL4 is operated at ambient pressure, only radiation with a wavelength down to 200 nm can be detected.

Time-resolved pump-probe experiments will be performed at the evacuated VUV beamline BL5 operated by the Forschungszentrum Jülich, which is equipped with a plane-grating monochromator and an angle-resolving photoemission spectrometer (ARPES). A fraction of each laser pulse is sent directly to BL5 via the evacuated pump-pulse beamline and will be used for exciting a sample, which will then be probed by the CHG pulses with a variable delay ('pump-probe experiments').

The third dipole downstream of the U250 serves as the source for the evacuated THz beamline BL5a, which guides and focuses the THz radiation over the radiation shielding wall into an experimental hutch. Here, the THz pulses are studied using an InSb HEB, a YBCO detector, or an FTIR spectrometer with DLaTGS detectors and a Si composite bolometer. Details on the beamline setup and detector technology are given in Chs. 1.1.4 and 4.

1.3.2. Brief History and Overview of Recent Results

The construction of the short-pulse facility started in 2010 with most of the then preassembled components being installed in the Easter shutdown of 2011. The electromagnetic undulator U250 – however, with new power supplies – and the corresponding vacuum chamber as well as parts of the diagnostics beamline BL4 have been adopted from the previous storage-ring FEL setup. The seeding beamline BL3, including the vacuum system, laboratory infrastructure, and the laser system, as well as the THz beamline BL5a, were built from scratch [12,13,67]. Commissioning began in May 2011 and the first successful laser-electron overlap was achieved on June 29, 2011, verified by the detection of coherent THz pulses arriving with the 1-kHz laser repetition rate at the InSb bolometer at BL5a. The next day, first CHG pulses (400 nm, second harmonic of the 800-nm seeding laser) were detected at BL4 using a fast photodiode.

Until the end of 2011, seeding with 800 nm continued and experiments concentrated on characterizing and optimizing the short pulse facility. CHG radiation could be detected up to the fourth harmonic (200 nm) in BL4 and basic properties, e.g., the quadratic dependence of the coherent ultraviolet (UV) and THz intensity on the bunch current (number of electrons), were verified ([57,58,67–69], Ch. 5.1.3). In addition to the usual single-bunch filling of DELTA during operation of the short-pulse facility, CHG and THz radiation could successfully be generated using a hybrid filling pattern.

In 2012, the seeding wavelength was switched to 400 nm using the SHG unit and characterization and optimization experiments continued [70,71]. The availability and stability of the short-pulse facility were increased, e.g., by partially automatizing the search and optimization of the laser-electron overlap, and by covering huge sections of the in-air laser path [72]. After slight modifications to the electron orbit and laser path in the U250 section and further optimization of hybrid filling patterns, first CHG and

THz experiments were performed during standard user operation of DELTA. Coherent THz pulses from several subsequent revolutions of a single bunch after a single laser-electron interaction were detected for the first time ([73], Ch. 5.4) using a fast NbN HEB provided by the ANKA THz group of the KIT. Furthermore, an FTIR spectrometer was installed at BL5a (Ch. 4.3) and the pump-pulse beamline from the laser laboratory to the VUV beamline BL5 was constructed [74].

In 2013, the vacuum system at BL5a was modified and extended to include the vacuum FTIR spectrometer, and first measurements of the coherent THz spectrum followed in spring ([73,75], Ch. 5.1.3). Using a prototype of the ultrafast YBCO detector developed at the KIT-IMS, Karlsruhe, a better understanding of the turn-by-turn evolution of the dip in the longitudinal electron density as well as of the YBCO detection mechanism was achieved [76]. By rewiring the central periods of the U250, the chicane strength[4] was significantly increased from $r_{56} = 11$ μm to $r_{56} = 130$ μm, thereby allowing much higher CHG intensities [77, 78]. Using a double-slit and Michelson-interferometer setup in conjunction with a fast gated iCCD camera at BL4, the coherence properties of the CHG pulses were investigated [75,79]. The detector at the VUV beamline BL5 was upgraded to a better temporal resolution in order to distinguish between the CHG pulses arriving at 1 kHz and the spontaneous undulator radiation arriving at 2.6 MHz. Now, CHG radiation up to the fifth harmonic of 400 nm (80 nm or 15.5 eV) was detected [75,78,79]. Pulses from the pump beamline were focused onto a sample at BL5 for the first time and a temporal overlap between seed and pump laser was achieved [80, 81]. Finally, air-conditioned hutches were constructed at BL4 and BL5a, thereby providing a cleaner environment and more stable conditions.

A modification of the laser path at BL3 allows for quick switching between 800- and 400-nm seeding since 2014. In cooperation with the Laboratoire de Physique des Lasers, Atomes et Molécules (PhLAM) at the University Lille 1, France, narrow-band THz pulses were generated by seeding with longer, intensity-modulated laser pulses ([76], Ch. 5.5). As a first user experiment, the frequency dependence of YBCO detectors was investigated by the KIT-IMS group [82]. Since summer 2014, a YBCO detector is permanently installed at the DELTA THz beamline. The characterization of CHG continued, e.g., by studying the intensity and spectrum under variation of the laser chirp [79], or while a phase modulation was applied to the storage ring RF ([81], Ch. 5.2.3), which leads to a modification of the electron bunch shape.

As of 2015, preparations for a first pump-probe experiment with CHG radiation at BL5 continue in cooperation with groups from the Forschungszentrum Jülich and the University of Duisburg-Essen. Investigations of the turn-by-turn evolution and spectral characteristics of the THz radiation pulses continue with a new spectrometer for the sub-THz regime currently under construction [83]. For the years to come, an upgrade of the short-pulse facility to implement the echo-enabled harmonic generation (EEHG) principle [84] is being planned [85–89]. Here, a second modulator and second chicane create a more complex density modulation with higher harmonic content in order to generate ultrashort radiation pulses at much shorter wavelengths.

---

[4] The r_{56} parameter indicates the path length difference or longitudinal offset Δs which occurs when an electron with a relative energy offset $\Delta E/E = \Delta p/p$ of one (100%) travels through the corresponding element (e.g., a chicane): $\Delta s \approx r_{56} \cdot \Delta p/p$.

2. Theory of Laser-Induced THz Radiation

This chapter will introduce the theoretical framework for the generation and detection of laser-induced THz radiation. The subsections follow the chronological sequence of the experimental setup from the generation of ultrashort laser pulses to the detection of THz radiation. Besides the basic theory of these processes, preliminary studies based on numerical simulations are presented.

2.1. Ultrashort Laser Pulses

2.1.1. Short-Pulse Laser Systems and Properties of Ultrashort Laser Pulses

The 800-nm Ti:sapphire laser oscillator installed at the DELTA short-pulse facility is based on an optical cavity with a Ti:sapphire crystal as the gain medium and a frequency-doubled Nd:YVO$_4$ CW pump laser [90]. Ti:sapphire offers a broad emission spectrum (670 nm to 1070 nm). Therefore, a large number of longitudinal modes – standing waves with slightly different frequencies – fulfill the condition that the length L of the resonator has to be an integer multiple q of half the mode wavelength λ_q. With the speed of light c, the corresponding mode frequencies are then given by [91]

$$\nu_q = \frac{c}{\lambda_q} = q\frac{c}{2L}. \tag{2.1}$$

In general, each of the modes would oscillate independently (with random phase, Fig. 2.1 a), leading to a multi-mode CW emission with some random intensity fluctuations (c). However, by introducing a fixed phase relationship ('phase-locking' or 'mode-locking', Fig. 2.1 b), constructive interference leads to a train of ultrashort pulses with a repetition rate f given by the inverse round-trip time in the resonator (d), which is equal to the mode frequency separation $\delta\nu = \nu_q - \nu_{q-1}$ [92]:

$$f = \delta\nu = \frac{c}{2L}. \tag{2.2}$$

In case of the Ti:sapphire oscillator installed at DELTA, mode-locking is achieved using the passive technique of Kerr-lens mode-locking (KLM) [93].

The shape and length of the laser pulses are determined by the emission spectrum, the spectral reflectivity of the cavity optics, and dispersion inside the cavity. Assuming a Gaussian pulse shape and spectrum, the electric field of a laser pulse with amplitude E_0 and central angular frequency $\omega_0 = 2\pi\nu_0$ can be described by [92]

$$E(t) = E_0 \cdot e^{-\Gamma t^2} \cdot e^{i\omega_0 t} = E_0 \cdot e^{-at^2} \cdot e^{i\omega_0 t + ibt^2} = E_0 \cdot e^{-at^2} \cdot e^{i\phi(t)}, \tag{2.3}$$

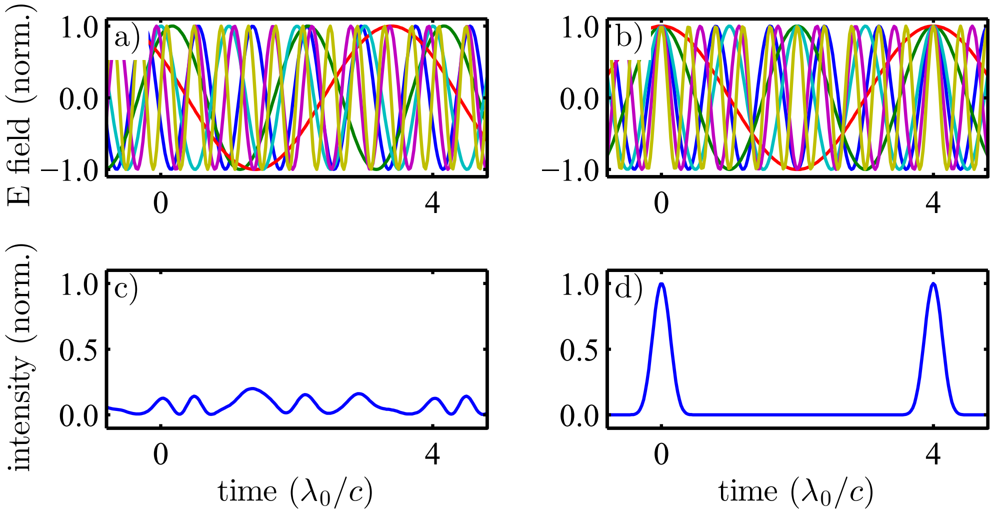

Figure 2.1.: Principle of mode-locking through the unrealistic but illustrative example of an oscillator with central wavelength λ_0, resonator length $L = 2\lambda_0$, and an emission bandwidth (FWHM) of $1.5\lambda_0$ (see text for details).

where $\Gamma = a - ib$ and $\phi(t) = \omega_0 t + bt^2$. Comparing the pulse intensity $I(t) \propto |E(t)|^2$ to a Gaussian intensity distribution, the parameter $a = 1/(4\sigma_t^2)$ can be identified as an inverse measure of the rms pulse length σ_t or the FWHM $\Delta t = 2\sqrt{2\ln 2}\,\sigma_t$. The parameter b is a measure of the so-called chirp – a variation of the instantaneous frequency depending on the longitudinal position within the laser pulse. The instantaneous frequency is given by the time-derivative of the phase (see Eq. 2.3)

$$\omega(t) = \dot{\phi}(t) = \omega_0 + 2bt, \tag{2.4}$$

which shows a linear increase of the instantaneous frequency along the pulse as depicted in Fig. 2.2.

Calculating the Fourier transform of the electric field (Eq. 2.3) and the corresponding intensity $\tilde{I}(\omega) \propto |\tilde{E}(\omega)|^2$ reveals the rms bandwidth of the intensity [92]

$$\sigma_\nu = \frac{1}{2\pi}\sqrt{a\left(1 + \frac{b^2}{a^2}\right)}. \tag{2.5}$$

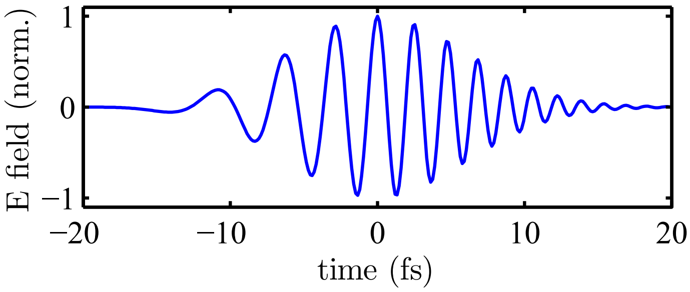

Figure 2.2.: Electric field of a chirped pulse according to Eq. 2.3 with $\lambda_0 = 800$ nm, $\Delta t = 10$ fs, and $b = 0.059$ fs^{-2}. The instantaneous frequency increases from 0 to $2\omega_0$ over the plot range of $4\Delta t$.

The so-called time-bandwidth product, using the FWHM bandwidth $\Delta\nu = 2\sqrt{2\ln 2}\,\sigma_\nu$ and the pulse length $\Delta t = 2\sqrt{2\ln 2}/\sqrt{4a}$, is then given by

$$\Delta t \cdot \Delta\nu = \frac{2\ln 2}{\pi}\sqrt{1+\frac{b^2}{a^2}} \approx 0.441\sqrt{1+\frac{b^2}{a^2}}. \tag{2.6}$$

The pulses depicted in Fig. 2.1 do not have a chirp ($b = 0$). Such pulses are called bandwidth- or Fourier-limited, as they provide the minimum possible pulse length of

$$\Delta t_{\mathrm{min}} = \frac{2\ln 2}{\pi\Delta\nu} \approx \frac{0.441}{\Delta\nu} \tag{2.7}$$

for a given bandwidth $\Delta\nu$. The value of 0.441 is only valid for the time-bandwidth product of a Gaussian-shaped pulse, while other pulse shapes offer slightly different values (e.g., approx. 0.315 for hyperbolic secant-shaped pulses).

A chirp is usually introduced by dispersion, which is the frequency-dependence of the refractive index $n(\omega)$ in a medium. A laser pulse in frequency domain $\tilde{E}(\omega, 0)$ propagating through a medium of thickness z will undergo a phase modulation according to [91]

$$\tilde{E}(\omega, z) = \tilde{E}(\omega, 0) \cdot e^{-ik(\omega)z}, \tag{2.8}$$

where the wavenumber is given by

$$k(\omega) = \frac{2\pi}{\lambda(\omega)} = \frac{2\pi}{\lambda_0} n(\omega). \tag{2.9}$$

Expanding $k(\omega)$ into a Taylor series,

$$k(\omega) = k(\omega_0) + k'(\omega_0)\cdot(\omega-\omega_0) + \frac{k''(\omega_0)}{2}(\omega-\omega_0)^2 + \frac{k'''(\omega_0)}{6}(\omega-\omega_0)^3 + ..., \tag{2.10}$$

the coefficients can be identified with the phase velocity at the central (mean) frequency

$$v_{\mathrm{p}}(\omega_0) = \frac{\omega_0}{k(\omega_0)}, \tag{2.11}$$

the group velocity

$$v_{\mathrm{g}}(\omega_0) = \left.\frac{\partial\omega}{\partial k}\right|_{k_0} = \frac{1}{k'(\omega_0)} = v_{\mathrm{p}}(\omega_0) + k\left.\frac{\partial v_{\mathrm{p}}}{\partial k}\right|_{k_0} = v_{\mathrm{p}}(\omega_0) - \lambda\left.\frac{\partial v_{\mathrm{p}}}{\partial\lambda}\right|_{\lambda_0}, \tag{2.12}$$

the so-called group velocity dispersion (GVD)

$$D(\omega_0) = \left.\frac{\partial}{\partial\omega}\frac{1}{v_{\mathrm{g}}}\right|_{\omega_0} = k''(\omega_0) = \frac{\lambda_0^3}{2\pi c^2}\left.\frac{\mathrm{d}^2 n}{\mathrm{d}\lambda^2}\right|_{\lambda_0}, \tag{2.13}$$

and a cubic term (see Ch. 2.1.2)

$$\beta(\omega_0) = \frac{k'''(\omega_0)}{6}. \tag{2.14}$$

The GVD is a measure for the frequency-dependence of the group velocity, and $D \neq 0$ will change the shape of the envelope introducing a chirp. Sometimes it is more practical to use the so-called group delay dispersion (GDD) $D_2 = D \cdot z$, where z is the length of the dispersive material.

The bulk materials and coatings in an optical setup are usually chosen to present a low and uniform absorption for the desired frequency range. Thus, there are only minor influences on the spectrum of a pulse and a dispersion-induced chirp will primarily increase the pulse length. Transforming Eq. 2.8 back into the time domain and taking dispersion into account only up to the second order, it can be shown that the length of a previously Fourier-limited pulse after passing through a material of thickness z will increase according to [92]

$$\Delta t(z) = \Delta t_{\min} \sqrt{1 + \left(\frac{z}{z_0}\right)^2}, \quad \text{with } z_0 = \frac{\Delta t_{\min}^2}{4|D| \ln 2} \tag{2.15}$$

being the so-called dispersion length, and $\Delta t_{\min}$ being the Fourier-limited pulse length.

A chirp can also be generated in order to increase or decrease the pulse length intentionally. This is the case for the Ti:sapphire amplifier installed at DELTA [94]. It is based on the so-called chirped-pulse amplification (CPA) (Fig. 2.3), at which the lower peak intensity of stretched pulses avoids damage to the gain medium inside a regenerative amplifier (RGA) [95] and a single-pass amplifier (SPA).

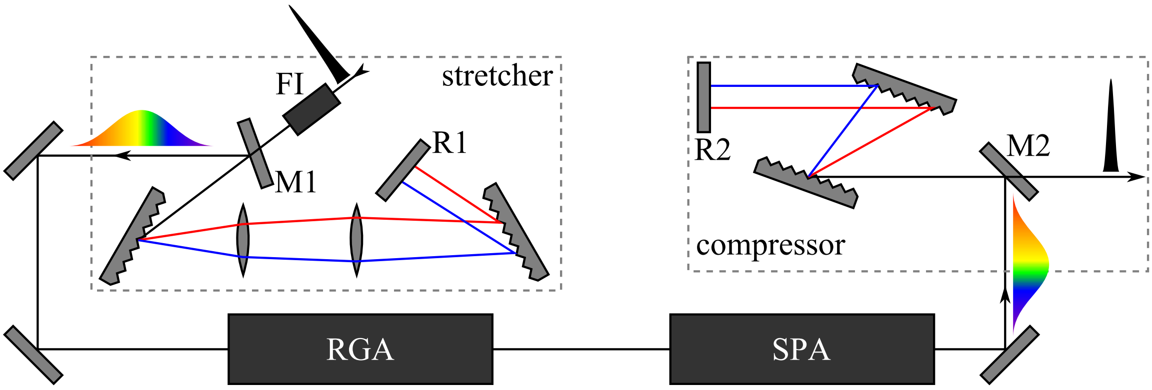

Figure 2.3.: Schematic sketch of a Ti:sapphire laser amplifier based on chirped-pulse amplification (CPA). Ultrashort pulses with high peak intensity (black) enter the stretcher through a Faraday isolator (FI) in order to prevent unwanted feedback into the oscillator and pass above mirror M1. The arrangement of optical gratings, lenses, and a vertical retroreflector (R1) presents a longer path for high-frequency light (blue) than for low-frequency light (red). Thus, pulses receive a positive GVD resulting in a chirp (colored pulse). The pulses then pass through an RGA and an SPA (see text for details). The arrangement of optical gratings and a vertical retroreflector (R2) in the compressor now presents a shorter path for high-frequency light (blue). Here, pulses receive a negative GVD and the chirp is eliminated. The pulses then leave the amplifier passing over mirror M2.

2.1.2. Chirped-Pulse Beating

As mentioned in Ch. 1.3.1, the interaction of an ultrashort laser pulse with an electron bunch leads to a sub-ps dip in the electron density, which results in a broad coherent THz emission spectrum. Using the so-called chirped-pulse beating (CPB) technique, a periodic density modulation leading to a narrow coherent emission spectrum is achieved. CPB-based THz generation was first implemented with photoconductive antennas in the mid-1990s [96, 97]. More recently, a group from PhLAM, University Lille 1, France, has used CPB at the UVSOR storage ring in Okazaki, Japan [98, 99]. In cooperation with PhLAM, a temporary CPB setup was established at DELTA in 2014 (Ch. 5.5).

The principle of CPB is shown in Fig. 2.4. The internal compressor of the Ti:sapphire amplifier (Fig. 2.3) is slightly detuned, leaving a remaining chirp in the output pulse. The chirped pulse travels through a Michelson interferometer, where it splits and then recombines with a variable delay. The interference of two chirped pulses with a small delay leads to a beating effect (see below), resulting in a periodic intensity modulation. In the modulator, the intensity-modulated laser pulse imprints a periodic energy modulation onto the electron bunch, which is converted into a periodic density modulation by the subsequent dispersive magnetic lattice. A multi-cycle coherent THz pulse with a narrow spectrum is emitted at the THz beamline, as opposed to a single-cycle pulse

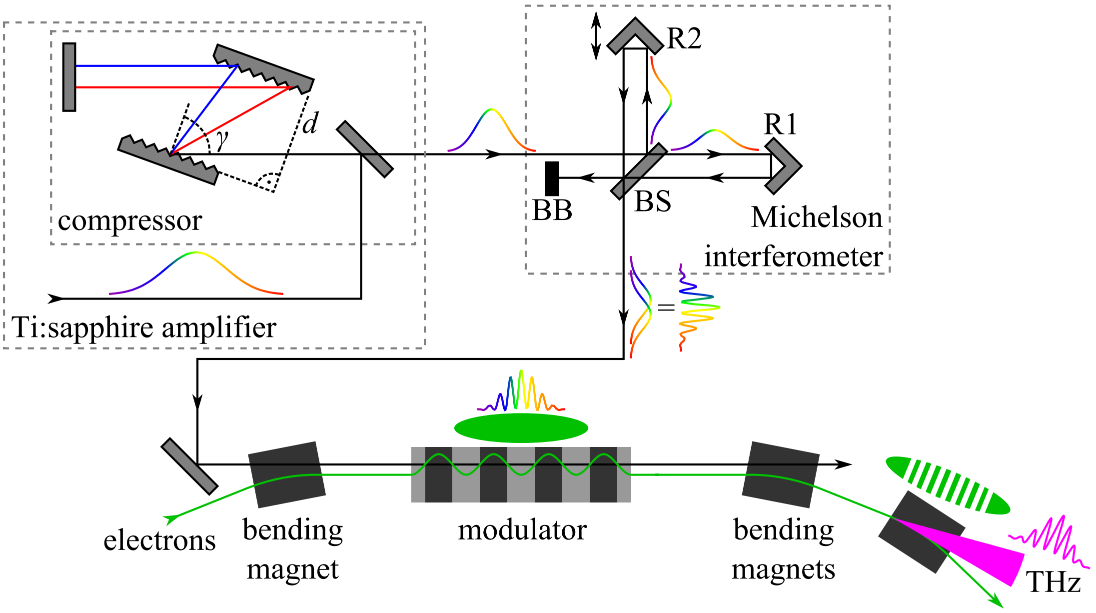

Figure 2.4.: Schematic sketch of a chirped-pulse beating (CPB) setup used to generate narrow-band coherent THz radiation at a storage ring, including the internal compressor of the Ti:sapphire amplifier (Fig. 2.3) with an angle of incidence γ and a perpendicular grating separation d, a Michelson interferometer with a beam splitter (BS), two retroreflectors (R1, fixed, R2, movable), and a beam block (BB), and a section of the storage ring with the modulator and the subsequent magnetic lattice. The colored waveforms indicate the chirp and intensity of the laser and THz pulse, the top view of the electron bunch (green ellipse) illustrates the density modulation.

when seeding with one ultrashort laser pulse. By changing the delay in the Michelson interferometer, the central emission frequency can be tuned continuously. The following paragraphs will discuss the theory of CPB in more detail.

A grating compressor as depicted in Fig. 2.4 introduces a GDD according to [97,100][1]

$$D_2 = D \cdot z = -2 \cdot \frac{4\pi^2 c\, d}{\omega_0^3 g^2} \left\{ 1 - \left[\frac{2\pi c}{\omega_0 g} - \sin\gamma \right]^2 \right\}^{-\frac{3}{2}}, \tag{2.16}$$

where d is the perpendicular grating separation, g is the grating constant (line distance), and γ is the angle of incidence.

For simplicity, a Fourier-limited laser pulse (Eq. 2.3 with $b_{\text{in}} = 0$) is assumed to enter the compressor[2]:

$$E_{\text{in}}(t) = E_0 \cdot e^{-a_{\text{in}} t^2} \cdot e^{i\omega_0 t}. \tag{2.17}$$

Taking dispersion into account only up to the second order, the electric field of the outgoing pulse is given by

$$E_{\text{out}}(t) = E_0 \sqrt{\frac{\Delta t_{\text{in}}}{\Delta t_{\text{out}}}} \cdot e^{-a_{\text{out}} t^2} \cdot e^{i\omega_0 t + i b_{\text{out}} t^2}, \tag{2.18}$$

with $\sqrt{\Delta t_{\text{in}} / \Delta t_{\text{out}}}$ accounting for the lower peak intensity of the elongated pulse and $a_{\text{out}} = 2\ln 2 / \Delta t_{\text{out}}^2$. The chirp parameter b_{out} can be calculated by comparing Eqs. 2.6 and 2.15 and by assuming a fixed bandwidth $\Delta\nu_{\text{out}} = \Delta\nu_{\text{in}} = \Delta\nu$:

$$|b_{\text{out}}| = a_{\text{out}} \sqrt{\frac{\Delta t_{\text{out}}^2}{\Delta t_{\text{in}}^2} - 1} \approx \frac{2\ln 2}{\Delta t_{\text{out}} \Delta t_{\text{in}}} \quad \text{for } \Delta t_{\text{out}} \gg \Delta t_{\text{in}}. \tag{2.19}$$

The sign of b_{out} depends on the sign of D_2. The incoming pulse length is given by the time-bandwidth product (Eq. 2.7) and the outgoing pulse length by Eqs. 2.15 and 2.16. In Eq. 2.18, the frequency-independent phase advance given by the zero- and first-order terms in Eq. 2.10 has been neglected, as it does not affect the pulse shape.

The intensity of the recombined laser pulse after passing the Michelson interferometer, which is set to introduce a path length difference of τ/c, is given by [97]

$$I_{\text{tot}} \propto \frac{1}{2} \left| E_{\text{out}}\left(t + \frac{\tau}{2}\right) + E_{\text{out}}\left(t - \frac{\tau}{2}\right) \right|^2 \tag{2.20}$$

$$= \frac{E_0^2}{2} \frac{\Delta t_{\text{in}}}{\Delta t_{\text{out}}} \left[e^{-2a_{\text{out}}\left(t+\frac{\tau}{2}\right)^2} + e^{-2a_{\text{out}}\left(t-\frac{\tau}{2}\right)^2} + 2e^{-2a_{\text{out}}\left(t^2+\frac{\tau^2}{4}\right)} \cdot \cos(\omega_0\tau + 2b_{\text{out}}\tau t) \right] \tag{2.21}$$

$$= E_0^2 \frac{\Delta t_{\text{in}}}{\Delta t_{\text{out}}} e^{-2a_{\text{out}}\left(t^2+\frac{\tau^2}{4}\right)} \left[\cosh(2a_{\text{out}}\tau t) + \cos(\omega_0\tau + 2b_{\text{out}}\tau t) \right]. \tag{2.22}$$

---

[1] The exponent $-3/2$ is given by [97] Eq. 7, while [100] Eqs. 5b and 8 provide an exponent of -1. A careful revision of the derivation, which is based on geometric relations and the derivative of the frequency-dependent time to pass through the compressor, confirmed the exponent $-3/2$.

[2] In principle, the internal compressor of the amplifier is designed to fully compensate the chirp of the incoming pulses for a given grating separation d_0. Furthermore, the GDD is linear in d. Therefore, assuming zero chirp for incoming pulses and regarding d as a relative measure to d_0 is equivalent to the actual setup with chirped incoming pulses and an absolute measure of d.

A detailed derivation for this formula is given in Eqs. A.1 ff.. The first two terms in Eq. 2.21 represent the slowly varying pulse envelopes of the two pulse copies created in the Michelson interferometer. The third term represents the interference between the two pulse copies and allows defining the modulation frequency

$$f_{\mathrm{mod}} = \frac{|b_{\mathrm{out}}|\tau}{\pi} = \frac{2\ln 2 \cdot \tau}{\pi \Delta t_{\mathrm{out}} \Delta t_{\mathrm{in}}} \approx \frac{\tau}{2\pi |D_2|} \tag{2.23}$$

applying the approximation derived in Eqs. A.7 ff.. The bandwidth of the intensity modulation can be determined by a Fourier transform of Eq. 2.21, leading to a FWHM of

$$\Delta f_{\mathrm{mod}} = \frac{2}{\pi}\sqrt{2\ln 2 \cdot a_{\mathrm{out}}} = \frac{4\ln 2}{\pi \Delta t_{\mathrm{out}}} = 2\Delta\nu \frac{\Delta t_{\mathrm{in}}}{\Delta t_{\mathrm{out}}} \approx \frac{\Delta t_{\mathrm{in}}}{\pi |D_2|} \tag{2.24}$$

based on Eq. 2.7 and the same approximation as above. Therefore, the bandwidth of the intensity modulation is given by two times the optical bandwidth of the laser scaled down by the stretching ratio $\Delta t_{\mathrm{in}}/\Delta t_{\mathrm{out}}$.

So far, the third-order dispersion ($k'''(\omega_0)/6 = \beta(\omega_0)$ in Eq. 2.10) has been neglected. However, a grating compressor as depicted in Fig. 2.4 introduces a cubic term [97,101]

$$\beta \cdot z = -\frac{D_2}{2\omega_0} \cdot \frac{1 + \frac{2\pi c}{\omega_0 g}\sin\gamma - \sin^2\gamma}{1 - \left[\frac{2\pi c}{\omega_0 g} - \sin\gamma\right]^2}, \tag{2.25}$$

which results in a quadratic chirp of the outgoing pulse (Eq. 2.18) [97]

$$E_{\mathrm{out}}(t) \propto e^{i\alpha t^3} \tag{2.26}$$

and a linear chirp of the intensity modulation (Eq. 2.21) [97]

$$I_{\mathrm{tot}} \propto \cos(2\pi f_{\mathrm{mod}} t + 3\alpha\tau t^2), \tag{2.27}$$

where $\alpha(\Delta\nu, \beta)$ is a cubic phase coefficient.

In order to gain a better understanding of the effects of the third-order dispersion, a simulation of the CPB process has been implemented in MATLAB [102] based on Eqs. 2.17, 2.8, and 2.10. Starting with an initially Fourier-limited pulse (Fig. 2.5, a), a fast Fourier transform (FFT) and a phase modulation are performed numerically. The pulse then undergoes an inverse FFT (Fig. 2.5, b) and is numerically split, delayed, and recombined as it would happen in the Michelson interferometer in order to retrieve the intensity-modulated pulse (Fig. 2.5, c). A final FFT is used to obtain the spectrum of the intensity modulation (Fig. 2.5, d). The parameters for the simulation are $\lambda_0 = 800$ nm, $\Delta t_{\mathrm{in}} = 40$ fs, $\Delta t_{\mathrm{out}} = 11$ ps, $g = 1500^{-1}$ mm, and $\gamma = 51.3°$. The GDD $D_2 = Dz$ is extracted from Eq. 2.15, while g and γ, which are the actual values from the compressor installed at DELTA, are used to calculate βz according to Eq. 2.25.

Figure 2.6 shows the theoretical dependence of f_{mod} and Δf_{mod} on the interferometer delay τ based on Eqs. 2.23 and 2.24 (‘analyt.’), which do not include third-order dispersion. The numerical results (‘num.’) are extracted from the simulated spectrum of the intensity modulation (Fig. 2.5, d). The internal compressor of the Ti:sapphire system installed at DELTA is optimized to eliminate third-order dispersion at the minimum

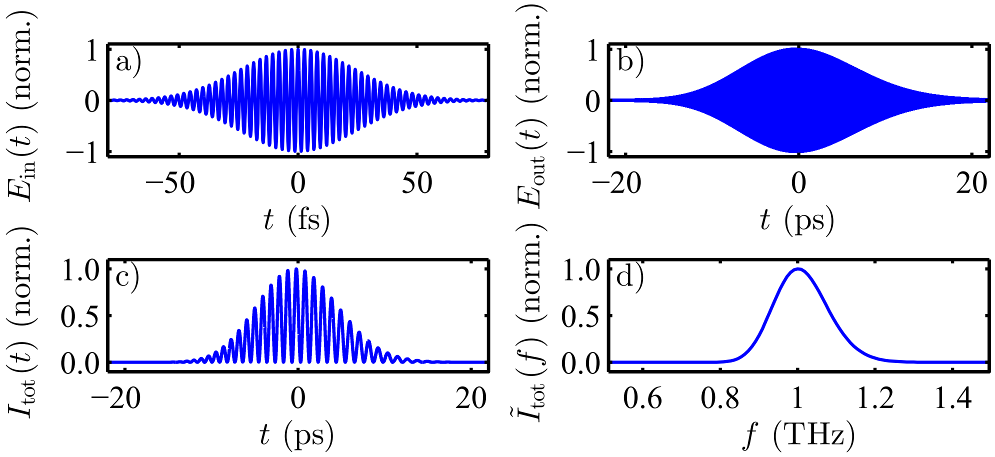

Figure 2.5.: Simulation of a CPB process, including the incoming Fourier-limited pulse (a), the phase-modulated pulse (b, after compressor, note the different time scale), the intensity-modulated pulse (after Michelson interferometer, c), and the spectrum of the intensity modulation (d) for $\tau = 1$ ps (see text for details).

pulse length of approximately 40 fs. When detuned to approximately 11 ps, a third-order term is present ($\beta z \neq 0$). The third-order term neither affects the pulse length during compression or stretching, nor does it change the linear dependence of f_{mod} on τ (Fig. 2.6, black circles). However, the modulation bandwidth Δf_{mod} increases with an asymptotically linear dependence on τ (blue squares), which decreases the efficiency of the CPB process.

It is possible to design an external compressor which eliminates third-order dispersion for a pulse length of 11 ps. Based on the parameters of the internal compressor at full compression, $\Delta t_{\text{min}} \approx 40$ fs, $d \approx 0.265$ m, $\gamma \approx 51.3°$, and $g = 1500^{-1}$ mm, it introduces $D_2 = -1.45$ ps^2 and $\beta z = 4.95 \cdot 10^{-4}$ ps^3. Thus, the uncompressed pulse, which can be

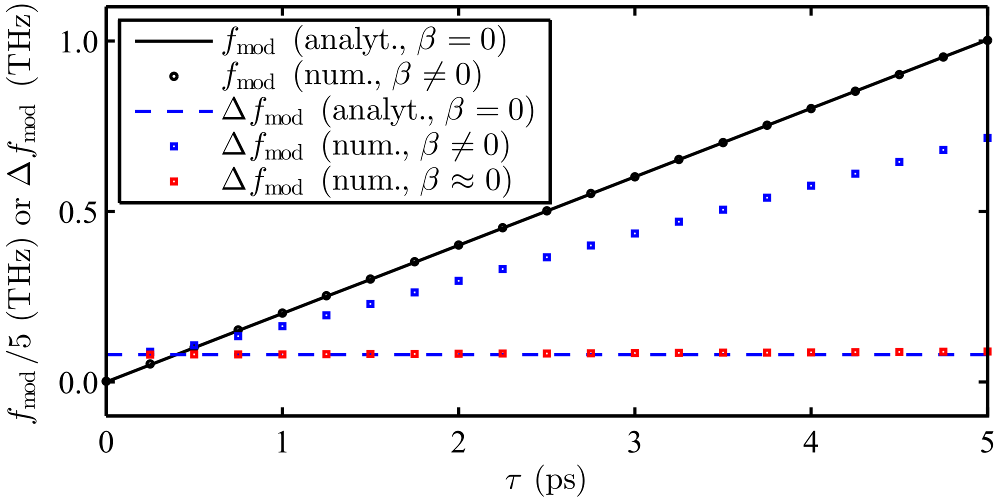

Figure 2.6.: Modulation frequency f_{mod} and bandwidth Δf_{mod} as function of the interferometer delay τ (see text for details).

coupled out of the amplifier directly before the internal compressor, has a D_2 value of 1.45 ps^2, a βz value of $-4.95 \cdot 10^{-4}$ ps^3, and a pulse length of 100 ps. Using an external compressor with a parameter set of, e.g., $d = 0.2027$ m, $\gamma = 44°$, and $g = 1500^{-1}$ mm, a pulse length of 11 ps can be generated with $\beta z \approx 0$ and, therefore, no broadening of the THz spectra (Fig. 2.6, red squares). However, an independent tuning of both, D_2 (or the pulse length) and βz, is not possible with this simple geometrical setup. If a pulse length other than 11 ps is desired, different compressor parameters for $\beta z \approx 0$ can again be found and must be incorporated in the setup.

2.1.3. Gaussian Beam Optics

The three-dimensional properties of a laser pulse or beam can be described by the solution of the paraxial approximation (or small-angle approximation) of the wave equation [92]

$$\vec{E}(x, y, z, t) = \vec{E}_0 e^{i(\omega t - kz)} \frac{w_0}{w(z)} e^{i\zeta(z)} e^{-ik\frac{r^2}{2R(z)}} e^{-\frac{r^2}{w^2(z)}}, \tag{2.28}$$

with $r^2 = x^2 + y^2$ and z being the distance from the so-called waist (the point of narrowest beam size). The beam radius ($1/e$ radius of the field, $1/e^2$ radius or two times the rms width of the intensity) is given by

$$w(z) = w_0 \sqrt{1 + \frac{z^2}{z_\mathrm{R}^2}}, \tag{2.29}$$

with the waist radius $w_0 \equiv w(0)$. The so-called Gouy phase is given by

$$\zeta(t) = \arctan\left(\frac{z}{z_\mathrm{R}}\right), \tag{2.30}$$

the radius of curvature of the wavefronts by

$$R(z) = z\left(1 + \frac{z_\mathrm{R}^2}{z^2}\right), \tag{2.31}$$

and the so-called Rayleigh length by

$$z_\mathrm{R} = \frac{\pi w_0^2}{\lambda}. \tag{2.32}$$

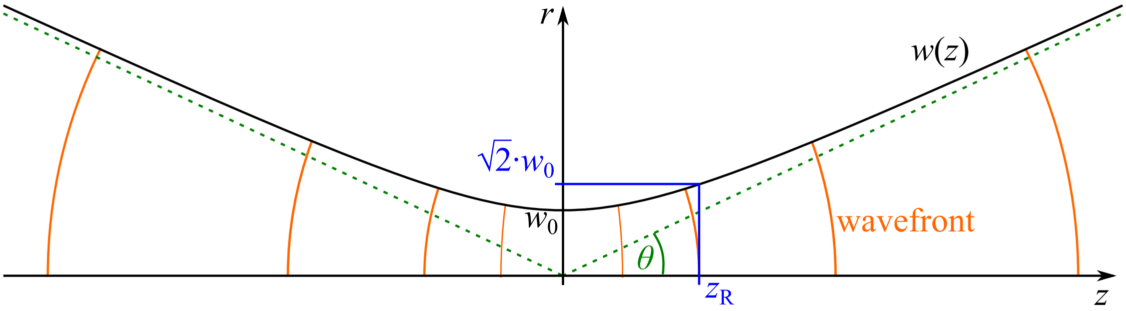

Figure 2.7.: Sketch of a Gaussian beam waist showing the beam radius $w(z)$, the Rayleigh length z_R, the divergence θ, and a selection of wavefronts.

For large distances $z \gg z_\mathrm{R}$ the radius is linearly dependent on z, $w(z) \approx z \cdot w_0/z_\mathrm{R}$, and the divergence can be defined:

$$\theta = \arctan\left(\frac{w_0}{z_\mathrm{R}}\right) = \arctan\left(\frac{\lambda}{\pi w_0}\right) \approx \frac{\lambda}{\pi w_0}. \tag{2.33}$$

The behavior of these parameters near a beam waist is illustrated in Fig. 2.7.

Using a complex beam parameter [92]

$$q(z) = z + q_0 = z + iz_\mathrm{R} \tag{2.34}$$

$$\Rightarrow \quad \frac{1}{q(z)} = \frac{1}{R(z)} - i\frac{\lambda}{\pi w^2(z)}, \tag{2.35}$$

it is possible to transform a Gaussian beam through a setup of optical elements with the matrix formalism known from geometrical or ray optics. Here, a light ray is characterized by its distance $r(z)$ from the optical axis and its angle $r'(z)$, and is transformed from z_1 to z_2 through an optical element with transfer matrix $\mathbf{T}$ according to

$$\begin{pmatrix} r(z_2) \\ r'(z_2) \end{pmatrix} = \begin{pmatrix} A & B \\ C & D \end{pmatrix} \cdot \begin{pmatrix} r(z_1) \\ r'(z_1) \end{pmatrix} = \mathbf{T} \cdot \begin{pmatrix} r(z_1) \\ r'(z_1) \end{pmatrix}. \tag{2.36}$$

For Gaussian beam optics, the complex beam parameter transforms according to [92]

$$q_2 = \frac{Aq_1 + B}{Cq_1 + D}. \tag{2.37}$$

In addition to the transverse Gaussian beam profile discussed above, there are also higher-order transverse modes which solve the paraxial wave equation. These higher-order modes can be described by the product of a Gaussian profile with Hermite polynomials, or, in case of a cylindrical symmetry, with Laguerre polynomials [92]. Any real laser beam is given by a superposition of these modes. As an approximation, a laser beam can be described by a single Gaussian mode and the so-called beam quality factor M^2, which is defined as the ratio of the beam parameter product (BPP) of the beam to that of an ideal Gaussian beam at the same wavelength. The BPP is the product of the beam divergence and the waist radius, which amounts to $\theta w_0 \approx \lambda/\pi$ for an ideal Gaussian beam. Replacing $\lambda \to M^2\lambda$, Eqs. 2.28 to 2.33 remain valid [92].

2.2. Properties of an Electron Bunch

This chapter will briefly introduce the transverse and longitudinal particle and beam dynamics of storage rings. The discussion is limited to ultra-relativistic electrons with velocity $v = \beta c \approx c$ and charge $q = -e$, where e is the elementary charge. A more detailed derivation can be found in, e.g., [103, 104].

The motion of electrons in a storage ring is determined by the Lorentz force

$$\vec{F} = -e\left(\vec{E} + \vec{v} \times \vec{B}\right), \tag{2.38}$$

where $\vec{E}$ is the electric field and $\vec{B}$ is the magnetic field. Magnetic fields are usually employed for transverse deflection and focusing, and electrostatic or electrodynamic fields for longitudinal acceleration.

Given by the magnetic lattice of the storage ring, there is an 'ideal' closed path through the center of all magnets, called orbit. The path of individual electrons is described by deviations from an 'ideal' particle position using the coordinate system explained in Fig. 2.8. In addition to the spatial coordinates x, y, and s, the transverse angles $x' = \mathrm{d}x/\mathrm{d}s$, $y' = \mathrm{d}y/\mathrm{d}s$, and a relative energy or momentum deviation $\Delta E/E \approx \Delta p/p$ from the ideal particle energy or momentum E or p, respectively, are considered in order to define a six-dimensional phase space [103].

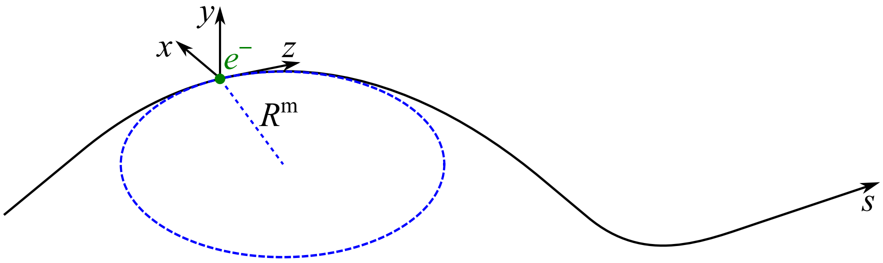

Figure 2.8.: Sketch of an arbitrary orbit section and a moving coordinate system attached to an 'ideal' electron e^-. The position of the ideal electron along the orbit is given by the coordinate s, whereas the single-particle positions relative to the ideal electron are measured in the moving coordinate system with horizontal coordinate x, vertical coordinate y, and longitudinal coordinate z. For a given position s, the orbit is characterized by a local curvature with radius R^{m}.

2.2.1. Transverse Beam Dynamics

Equating the Lorentz and centripetal force, the local transverse bending radius $R^{\mathrm{m}}_{x,y}$ is given by the transverse magnetic field $B_{y,x}$, which can be expanded into a Taylor series, e.g., for B_y [103]

$$\frac{1}{R^{\mathrm{m}}_x} = \frac{e}{p}B_y = \frac{e}{p}B_{y0} + \frac{e}{p}\frac{\mathrm{d}B_y}{\mathrm{d}x}x + \frac{1}{2}\frac{e}{p}\frac{\mathrm{d}^2B_y}{\mathrm{d}x^2}x^2 + \ldots \tag{2.39}$$

$$\equiv \frac{1}{R_x} + k_x x + \frac{1}{2}mx^2 + \ldots\ . \tag{2.40}$$

Here, p is the electron momentum, and different types of magnets are characterized by the dipole bending radius R_x, the quadrupole strength k_x, and the sextupole strength m. An analogous expression exists for B_x. Dipole magnets are used to deflect the beam, quadrupole magnets (de-)focus the beam in analogy to lenses used in light optics, and sextupoles are employed to compensate the energy-dependent focusing strength of quadrupole magnets. A quadrupole always acts like a focusing lens in one plane and like a defocusing lens in the perpendicular plane, requiring a combination of alternating quadrupoles for an overall focusing effect.

For small deviations from the ideal particle, the electron motion in a linear magnetic lattice including only quadrupoles and horizontally deflecting dipoles is described by the differential equations of linear beam optics [103]

$$x''(s) + \left[\frac{1}{R(s)} - k(s)\right] x(s) = \frac{1}{R(s)}\frac{\Delta p}{p} \tag{2.41}$$

$$y''(s) + k(s)y(s) = 0 \tag{2.42}$$

with $k < 0$ for horizontally focusing quadrupoles and $k > 0$ for vertically focusing quadrupoles. Real magnets with continuously in-/decreasing fringe fields are usually approximated by an effective length of constant field (hard-edge approximation), resulting in constant values for $1/R$ or k inside the magnet and $1/R = k = 0$ otherwise. In case of a periodic magnetic lattice, i.e., $k(s + L) = k(s)$ and $R(s + L) = R(s)$, Eqs. 2.41 and 2.42 are so-called Hill equations.

The differential equations 2.41 f. can be solved piecewise analytically, leading to the transfer matrices $\mathbf{M} \equiv \{r_{ij}\}$ of linear beam optics, which act on the six-dimensional phase space vector

$$\begin{pmatrix} x_1 \\ x'_1 \\ y_1 \\ y'_1 \\ z_1 \\ \Delta p/p \end{pmatrix} = \begin{pmatrix} r_{11} & r_{12} & 0 & 0 & 0 & r_{16} \\ r_{21} & r_{22} & 0 & 0 & 0 & r_{26} \\ 0 & 0 & r_{33} & r_{34} & 0 & 0 \\ 0 & 0 & r_{43} & r_{44} & 0 & 0 \\ r_{51} & r_{52} & 0 & 0 & 1 & r_{56} \\ 0 & 0 & 0 & 0 & 0 & 1 \end{pmatrix} \begin{pmatrix} x_0 \\ x'_0 \\ y_0 \\ y'_0 \\ z_0 \\ \Delta p/p \end{pmatrix}. \tag{2.43}$$

A complete list of transfer matrices is given in [104]. The elements $r_{ij} \neq 0$ characterize the focusing properties as well as energy-dependent deflections and path length differences. Several matrix elements are zero due to the decoupling of the respective pair of coordinates i and j.

The energy-dependent effects of a magnetic lattice are referred to as dispersion. Solving Eq. 2.41 with $\Delta p/p = 1$ leads to the so-called dispersion function $D(s)$ and its derivative $D'(s)$, which transform with the same matrix elements as x and x'. The horizontal displacement $x(s)$ of an electron is then described by [103]

$$x(s, \Delta p/p) = x(s, 0) + D(s)\frac{\Delta p}{p}. \tag{2.44}$$

The previously mentioned momentum compaction factor α describes the energy-dependent path length differences over the entire storage ring and is defined as [103]

$$\alpha \equiv \frac{\Delta L_\mathrm{c}/L_\mathrm{c}}{\Delta p/p} = \frac{1}{L_\mathrm{c}} \oint \frac{D(s)}{R(s)} \mathrm{d}s, \tag{2.45}$$

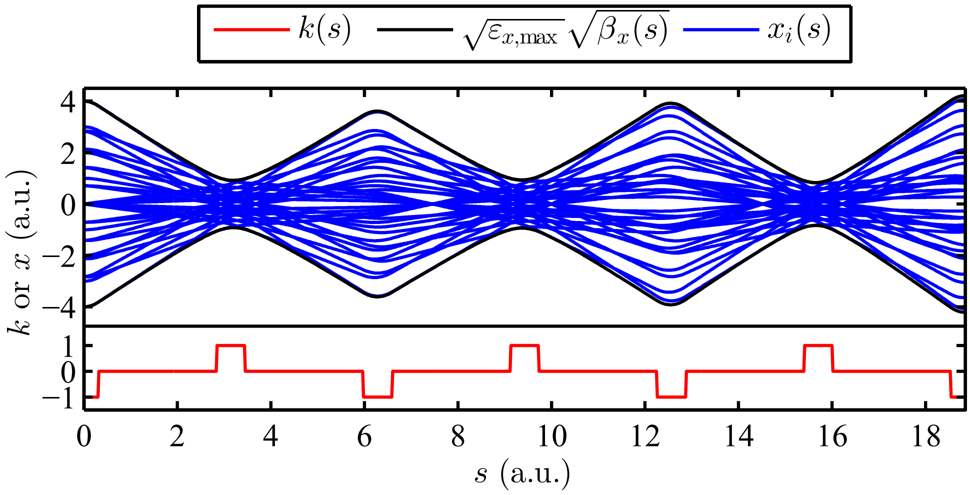

Figure 2.9.: Quadrupole strength $k(s)$ (red), beam envelope $\sqrt{\varepsilon_{x,\max}}\sqrt{\beta_x(s)}$ (black), and individual particle traces $x_i(s)$ (blue) with $\varepsilon_{x,i} \in [0, \varepsilon_{x,\max}]$ and $\phi_{x,i} \in [0, 2\pi]$ for an arbitrary magnetic lattice.

where $\Delta L_\mathrm{c}/L_\mathrm{c}$ is the relative change of the storage ring circumference.

Alternatively to the matrix formalism, Hill's equations of linear beam optics can be solved for the case of $\Delta p/p = 0$ by a continuous function [103]

$$x_i(s) = \sqrt{\varepsilon_{x,i}}\sqrt{\beta_x(s)}\cos[\Psi_x(s) + \phi_{x,i}], \tag{2.46}$$

with $\varepsilon_{x,i}$ being the so-called single-particle emittance or Courant-Snyder invariant [105], which is a constant along the storage ring, $\beta_x(s)$ being the so-called beta function, which is the same for all electrons and is determined by the magnetic lattice (see below), and with the phase advance

$$\Psi_x(s) = \int_0^s \frac{1}{\beta_x(s')}\mathrm{d}s' \tag{2.47}$$

and an individual start phase $\phi_{x,i}$. The same considerations are valid for the vertical plane. Thus, each electron performs so-called betatron oscillations with the individual and position-dependent amplitude $\sqrt{\varepsilon_{x,i}}\sqrt{\beta_x(s)}$, start phase $\phi_{x,i}$, and non-linear phase advance $\Psi_x(s)$. An ensemble of electrons with a certain $\varepsilon_{x,\max} = \max(\{\varepsilon_{x,i}\})$ is then characterized by a beam envelope $\sqrt{\varepsilon_{x,\max}}\sqrt{\beta_x(s)}$ as shown in Fig. 2.9.

Eliminating the phase advance $\Psi_x(s)$, Eq. 2.46 and its derivative $x_i'(s)$ can be transformed into [103]

$$\gamma_x(s)x_i^2(s) + 2\alpha_x(s)x_i(s)x_i'(s) + \beta_x(s)x_i'^2(s) = \varepsilon_{x,i}, \tag{2.48}$$

where

$$\alpha_x(s) \equiv -\frac{\beta_x'(s)}{2} \quad \text{and} \tag{2.49}$$

$$\gamma_x(s) \equiv \frac{1+\alpha_x^2(s)}{\beta_x(s)}. \tag{2.50}$$

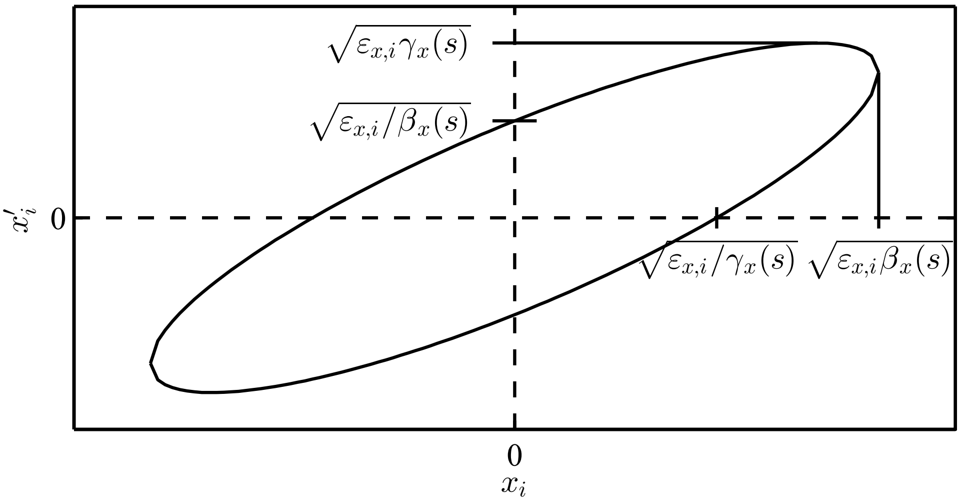

Figure 2.10.: Phase space ellipse for an arbitrarily chosen set of optical functions with the x_i and x'_i intercepts and maximum extents marked accordingly.

The three optical functions $\beta_{x,y}(s)$, $\alpha_{x,y}(s)$, and $\gamma_{x,y}(s)$, also called Twiss parameters, together with $D(s)$ and $D'(s)$ for the horizontal plane fully describe the linear beam optics. Equation 2.48 defines an ellipse in horizontal phase space with area $\pi\varepsilon_{x,i}$ (Fig. 2.10). The ellipse changes its shape along the storage ring, while its area remains constant. For a fixed position s and $D(s) = D'(s) = 0$, all electrons are positioned on concentric ellipses characterized by different areas $\pi\varepsilon_{x,i}$. Also, as the phase advance Ψ_x usually is not equal to an integer multiple of 2π for a complete revolution in the storage ring, an electron moves along discrete points of the ellipse from revolution to revolution for a given position s. Again, the same considerations are valid for the vertical plane, but without a vertical dispersion function due to the lack of vertically deflecting dipole magnets.

The optical functions can be transformed along the lattice using the same 2×2 submatrices $\mathbf{M}_{x,x'}$ as for the phase-space vectors (x, x') (and (y, y') accordingly), however, employing the modified rule [103]

$$\mathbf{B}_{x,1} = \mathbf{M}_{x,x'}\mathbf{B}_{x,0}\mathbf{M}^T_{x,x'} \tag{2.51}$$

with the so-called beta matrix

$$\mathbf{B}_x = \begin{pmatrix} \beta_x & -\alpha_x \\ -\alpha_x & \gamma_x \end{pmatrix}. \tag{2.52}$$

2.2.2. Longitudinal Beam Dynamics

The longitudinal beam dynamics is dominated by the accelerating RF system on the one hand, and the energy-dependent path length differences and synchrotron radiation losses on the other hand. Taking both effects into account, the equations of motion in longitudinal phase space are given by [103]

$$\Delta\dot{E} = \frac{eV_0}{T_0}\left[\sin(\Psi_\mathrm{s} + \Delta\Psi) - \sin(\Psi_\mathrm{s})\right] - \frac{1}{T_0}\frac{\mathrm{d}W}{\mathrm{d}E}\Delta E \tag{2.53}$$

$$\Delta\dot{\Psi} = \frac{2\pi q\alpha}{T_0 E_0}\Delta E. \tag{2.54}$$

Here, ΔE is the energy deviation from the ideal particle energy E_0, T_0 is the revolution time of the ideal particle, Ψ_s is the so-called synchronous phase in the RF field (see below), and $\Delta\Psi$ is the phase difference to Ψ_s (corresponding to a longitudinal offset $\Delta z = c\Delta\Psi/\omega_\mathrm{RF}$). The energy dependence of the synchrotron radiation losses is described by $\mathrm{d}W/\mathrm{d}E$, $q = T_0/T_\mathrm{RF} = T_0 f_\mathrm{RF}$ is the so-called harmonic number, $f_\mathrm{RF} = \omega_\mathrm{RF}/(2\pi)$ is the RF frequency, and α is the momentum compaction factor.

Acceleration is usually provided by a standing electromagnetic wave inside an RF resonator or cavity. The maximum effective accelerating voltage V_0 which is seen by an electron passing through the cavity is given by [106]

$$V_0 = \tau_\mathrm{TTF}\sqrt{2P_\mathrm{RF}R_\mathrm{s}} \tag{2.55}$$

with the average RF power P_RF, the so-called shunt impedance R_s accounting for the ohmic losses due to the RF current flows in the resistive cavity walls, and the so-called transit-time factor

$$\tau_\mathrm{TTF} = \frac{\sin\left(\pi L_\mathrm{RF}/\lambda_\mathrm{RF}\right)}{\pi L_\mathrm{RF}/\lambda_\mathrm{RF}}, \tag{2.56}$$

which is related to the change of the accelerating voltage during the passage time of the electron. Here, L_RF is the length of the cavity and $\lambda_\mathrm{RF} = c/f_\mathrm{RF}$ is the RF wavelength. For the synchronous phase Ψ_s of the ideal electron ($\Delta\Psi = 0$), the energy gain exactly compensates the synchrotron radiation losses,

$$eV_0\sin(\Psi_\mathrm{s}) = W. \tag{2.57}$$

For small phase deviations $\Delta\Psi \ll \Psi_\mathrm{s}$, Eqs. 2.53 f. can be simplified and combined to [103]

$$\Delta\ddot{E} + 2a_\mathrm{s}\Delta\dot{E} + \Omega^2\Delta E = 0 \quad \text{with} \tag{2.58}$$

$$a_\mathrm{s} = \frac{1}{2T_0}\frac{\mathrm{d}W}{\mathrm{d}E}, \tag{2.59}$$

$$\Omega = \omega_0\sqrt{-\frac{eV_0 q\alpha\cos\Psi_\mathrm{s}}{2\pi E_0}}, \tag{2.60}$$

and the revolution frequency $\omega_0 = 2\pi/T_0$. Thus, for small amplitudes $\Delta\Psi$, the electrons perform a damped harmonic oscillation with the so-called synchrotron oscillation frequency $\Omega \ll \omega_0$. In case of DELTA, the synchrotron frequency is approximately 15 kHz, while the revolution frequency is approximately 2.6 MHz.

The synchrotron oscillation is caused by the energy-dependent change of circumference (Eq. 2.45). Electrons with $\Delta\Psi = 0$ but a positive energy deviation $\Delta E > 0$ travel on a dispersive orbit with larger circumference and, after one revolution, arrive at a later phase with $\Delta\Psi > 0$. Here, the electrons experience a smaller voltage, which reduces their energy and phase deviation for the next turn. This process is also called ‘phase focusing’.

As the entire ensemble of electrons within a bunch perform incoherent synchrotron oscillations, the appearance of an overall steady rms bunch length σ_z and energy spread σ_E is given with [104]

$$\sigma_z = \frac{c\alpha}{\Omega}\frac{\sigma_E}{E_0}. \tag{2.61}$$

2.2.3. Bunch Profile and Dimensions

Due to the damping and heating effect of synchrotron radiation emission, the transverse and longitudinal bunch profiles within the betatron and synchrotron oscillation potentials can usually be described by Gaussian distributions. Thus, instead of the maximum particle emittance $\varepsilon_{\mathrm{max}}$ (Fig. 2.9), the horizontal and vertical beam emittances $\varepsilon_{x,y}$ are defined via [103]

$$\sigma_{x,y}(s) = \sqrt{\varepsilon_{x,y}\beta_{x,y}(s)} \tag{2.62}$$

for the case of $D(s) = 0$ and with $\sigma(s)$ being the standard deviation of the Gaussian distribution and $\beta(s)$ being the beta function. The natural horizontal beam emittance can be calculated by considering the overall damping effect of synchrotron radiation emission (Eq. 2.59) and the heating effect due to the stochastic quantum mechanical emission of single photons [107]. As synchrotron radiation is primarily emitted by the horizontal deflection in bending magnets, the finite vertical emittance is caused by an x-y coupling due to fringe fields and magnetic field errors.

With the Twiss parameters, dispersion function, and beam emittances known, the normalized transverse charge distribution at any position along the storage ring is given by

$$\rho_{\mathrm{t}}(x,y,s) = \frac{1}{2\pi\sigma_x(s)\sigma_y(s)} \exp\left(-\frac{x^2}{2\sigma_x^2(s)} - \frac{y^2}{2\sigma_y^2(s)}\right) \quad \text{with} \tag{2.63}$$

$$\sigma_{x,y}(s) = \sqrt{\varepsilon_{x,y}\beta_{x,y}(s) + D_{x,y}^2(s)\frac{\sigma_E^2}{E^2}}, \tag{2.64}$$

and σ_E being the natural rms energy spread. Also the transverse angular distribution is given by a Gaussian distribution with (see maximum x' extent in Fig. 2.10)

$$\sigma_{x',y'}(s) = \sqrt{\varepsilon_{x,y}\gamma_{x,y}(s) + {D'}_{x,y}^{2}(s)\frac{\sigma_E^2}{E^2}}. \tag{2.65}$$

The longitudinal bunch profile can be described by a normalized Gaussian distribution

$$\rho_{\mathrm{l}} = \frac{1}{\sqrt{2\pi}\sigma_z} \exp\left(-\frac{z^2}{2\sigma_z^2}\right), \tag{2.66}$$

where the natural bunch length σ_z is defined by Eq. 2.61 and the natural energy spread is determined by the particle energy and dipole bending radii [104].

2.3. The Laser-Electron Interaction

With knowledge of the distribution and propagation of laser pulses (Ch. 2.1) and electron bunches (Ch. 2.2), the next step is to describe the laser-electron interaction.

2.3.1. The Path of an Electron Bunch in an Undulator

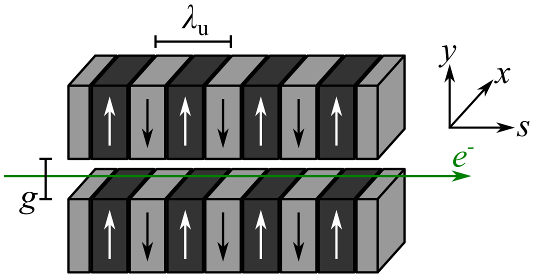

Figure 2.11.: Schematic sketch of an undulator with pole gap g and period length λ_u.

An undulator is a periodic sequence of alternating dipole magnets (Fig. 2.11). The on-axis ($y = 0$) vertical magnetic field can be described by [103]

$$B_y(s) = B_0 \cos(k_\mathrm{u} s) \quad \text{with} \tag{2.67}$$

$$k_\mathrm{u} = \frac{2\pi}{\lambda_\mathrm{u}}, \tag{2.68}$$

where λ_u is the undulator period, and B_0 is the field amplitude.

Solving the equations of motion given by the Lorentz force (Eq. 2.38) and the on-axis field including several approximations ($v_y \approx 0$, $v_x \ll c$, $1/\gamma^2 \ll 1$) leads to [103]

$$x(t) = -\frac{K}{k_\mathrm{u}\gamma} \cos(\omega_\mathrm{u} t) \quad \text{and} \tag{2.69}$$

$$s(t) = \beta^* ct + \frac{K^2}{8k_\mathrm{u}\gamma^2} \sin(2\omega_\mathrm{u} t) \quad \text{with} \tag{2.70}$$

$$K = \frac{\lambda_\mathrm{u} e B_0}{2\pi m_\mathrm{e} c} \quad \text{and} \tag{2.71}$$

$$\beta^* = 1 - \frac{1}{2\gamma^2}\left(1 + \frac{K^2}{2}\right), \tag{2.72}$$

where m_e is the electron mass at rest, and $\omega_\mathrm{u} = k_\mathrm{u}\beta^* c$. The electrons move on a horizontally sinusoidal path with a slightly reduced longitudinal average velocity $\beta^* c$ due to the transverse excursions and a modulation of the longitudinal speed with frequency $2\omega_\mathrm{u}$.

2.3.2. The Process of Energy Exchange

The energy ΔW gained by an electron moving through an undulator under influence of a horizontal electric field $\vec{E}_\mathrm{L}(t) = (E_\mathrm{L}(t), 0, 0)$ is given by [103]

$$\Delta W = -e \int \vec{E}_\mathrm{L} \mathrm{d}\vec{s} = -e \int \vec{v}\vec{E}_\mathrm{L} \mathrm{d}t = -e \int v_x E_\mathrm{L} \mathrm{d}t \tag{2.73}$$

with (Eq. 2.69)

$$v_x = \dot{x} = \frac{\beta^* c K}{\gamma} \sin(\omega_\mathrm{u} t), \tag{2.74}$$

and, as a first approximation, a plane wave for the laser field

$$E_\mathrm{L} = E_{\mathrm{L},0} \cos(k_\mathrm{L} s - \omega_\mathrm{L} t + \phi_\mathrm{L}) \tag{2.75}$$

with amplitude $E_{\mathrm{L},0}$, wavenumber $k_\mathrm{L} = 2\pi/\lambda_L = \omega_\mathrm{L}/c$ and a start phase ϕ_L. The energy change then becomes

$$\Delta W = -\frac{ceE_{\mathrm{L},0}K}{2\gamma} \int [\sin(\Psi_+) - \sin(\Psi_-)] \mathrm{d}t \quad \text{with} \tag{2.76}$$

$$\Psi_\pm = (k_\mathrm{L} \pm k_\mathrm{u}) s - \omega_\mathrm{L} t + \phi_\mathrm{L}. \tag{2.77}$$

For a net energy change $\Delta W \neq 0$, either both phases Ψ_+ and Ψ_- must be constant, or one of them must be constant while the other one oscillates. The latter case with only $\Psi_+ = \text{const.}$ is fulfilled by the resonance condition [103]

$$\lambda_\mathrm{L} = \frac{\lambda_\mathrm{u}}{2\gamma^2} \left(1 + \frac{K^2}{2}\right), \tag{2.78}$$

which is identical to the expression for the fundamental emission wavelength λ_0 of an undulator. Here, the electron lags behind one laser period per undulator period ('slippage'), always experiencing the same sign of $E_\mathrm{L} v_x$ (Fig. 2.12). As the oscillating motion of the electrons starts and stops abruptly at the beginning and end of the undulator, the spectral shape of the undulator line, identical to the resonance curve of the laser-electron interaction, is given by the Fourier transform of a boxcar function [103]

$$I(\omega) \propto \left\{ \frac{\sin\left[\frac{\pi N_\mathrm{u}(\omega - \omega_0)}{\omega_0}\right]}{\frac{\pi N_\mathrm{u}(\omega-\omega_0)}{\omega_0}} \right\}^2 \tag{2.79}$$

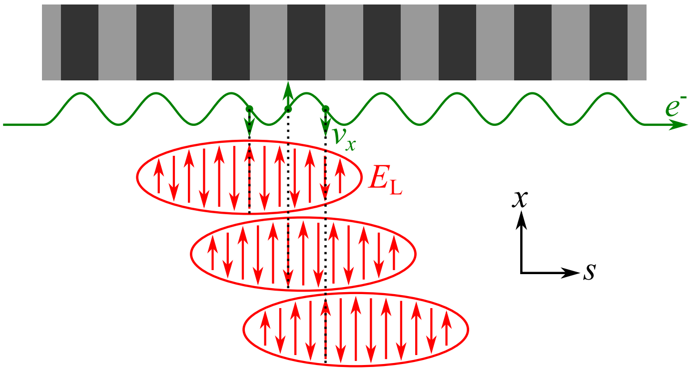

Figure 2.12.: Schematic sketch of an electron (green dot) and a laser pulse (red ellipse) passing through an undulator at resonance condition. The electron lags behind one laser period per undulator period. As a consequence, the horizontal electron velocity v_x and electric laser field vector E_L are always oriented anti-parallel, leading to a net energy gain of the electron.

with N_u being the number of undulator periods and $\omega_0 = 2\pi c/\lambda_0$ being the fundamental frequency.

The absolute amount of positive or negative energy exchange depends on the phase ϕ between electron and laser field. With the resonance condition (Eq. 2.78), the energy change (Eq. 2.76) becomes

$$\Delta W = -\frac{ceE_{\mathrm{L},0}K}{2\gamma}\int[\underbrace{\sin(\phi)}_{\text{const.}} - \underbrace{\sin(\phi - 2k_\mathrm{u}s)}_{\text{fast oscillation}}]\mathrm{d}t \tag{2.80}$$

$$= -\frac{ceE_{\mathrm{L},0}K}{2\gamma}\frac{N_\mathrm{u}\lambda_\mathrm{u}}{c}\sin\phi \tag{2.81}$$

with $\Psi_+ = \text{const.} \equiv \phi$ and $\Psi_- = \Psi_+ - 2k_\mathrm{u}s$. The result is a sinusoidal energy modulation within the slice overlapping with the laser pulse.

2.3.3. Influence of Storage Ring and Laser Parameters

Due to the finite transverse and longitudinal dimensions and Gaussian shapes of the laser pulse and electron bunch, not all electrons experience the full electric field amplitude as assumed in the derivation of Eq. 2.81. Instead, off-axis electrons see a reduced electric field, and in case of a laser pulse much smaller than the electron bunch, electrons far off the laser pulse center are not modulated at all. Furthermore, the energy modulation amplitude depends on the transverse and longitudinal overlap between laser pulse and electron bunch, and on the beta functions of the storage ring and the Rayleigh length of the laser beam, as both may lead to a significant change of bunch or pulse size, respectively, inside the undulator.

These effects are included in the numerical simulations discussed in Ch. 3. As an example, Fig. 2.13 shows a central slice of an electron bunch after experiencing an energy modulation in an undulator, which has been simulated with the code THzSMe (see Ch. 3.2) using the parameters of the CHG setup at DELTA (Tab. A.9). The effect of a finite natural energy spread leading to an overall broadened trace is observed. Furthermore, the limited laser beam size results in less affected electrons ‘filling’ the maxima and minima.

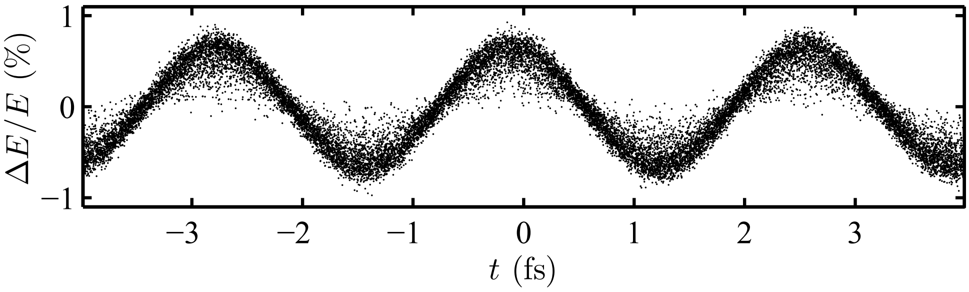

Figure 2.13.: Simulated slice of an electron bunch after experiencing an interaction with an 800-nm laser pulse in an undulator (see text for details).

2.4. Evolution of the Longitudinal Electron Density

As shown later in Ch. 2.5, the longitudinal electron density $\rho_\mathrm{l}(z)$ must feature (sub-)ps structures in order to generate coherent radiation in the THz regime. These structures are caused by energy-dependent path length differences of the laser-affected electrons in the magnetic lattice of the storage ring.

2.4.1. Energy-Dependent Path Length Differences

The longitudinal position change induced by a series of magnets with the combined transfer matrix $\mathbf{M} = \{r_{ij}\}$ (Eq. 2.43) is given by

$$\Delta z = z_1 - z_0 = r_{51}x_0 + r_{52}x_0' + r_{56}\frac{\Delta E}{E}, \tag{2.82}$$

where the energy-dependent path length difference is proportional to the r_{56} parameter of the transfer matrix. Although only dipole magnets offer a significant r_{56} value, the combination of several elements leads to an overall r_{56} value which depends also on the horizontal deflection and focusing properties of the lattice.

The evolution of a sub-ps modulation of the longitudinal electron density is illustrated in Fig. 2.14. Here, an energy-modulated slice is tracked through the section of the DELTA lattice between the modulator and the THz beamline. The simulation of the energy modulation as well as the particle tracking have been performed with the code THzSMe (see Ch. 3.2) using the parameters of the CHG setup at DELTA (Tab. A.9). Electrons with a positive energy deviation lag behind and electrons with a negative energy deviation move ahead. Thus, the central section of the slice is vacated leaving a dip in the electron density, while the laser-affected electrons cause two density maxima at the edges of the dip.

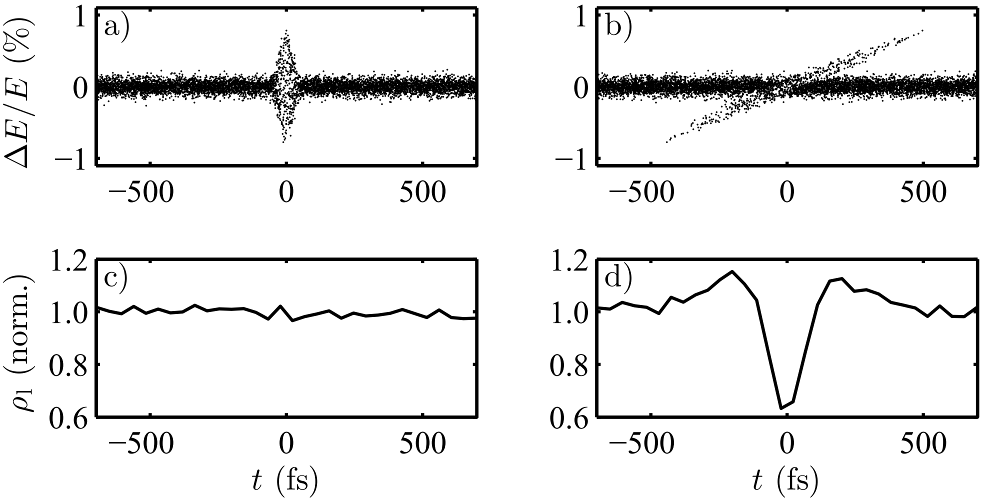

Figure 2.14.: Single particle positions in longitudinal phase space (a, b), and longitudinal electron density ρ_l for the central slice of an electron bunch modulated by a 40-fs laser pulse before (a, c) and after (b, d) passing through a section of the DELTA lattice. The coordinate t indicates the arrival time, i.e., particles with $t > 0$ lag behind.

2.4.2. Analytical Treatment

For the simplified case of an ideal transverse, longitudinal, and spectral laser-electron overlap and using several approximations (see below), an analytical treatment of the electron density modulation is possible, which allows a useful relation for chirped-pulse beating (CPB) at storage rings to be derived.

The following considerations and equations are based on [99]. For the purpose of a compact notation, the coordinates are normalized to the rms bunch dimensions, i.e., $x/\sigma_x \to \hat{x}$, $x'/\sigma_{x'} \to \hat{x}'$, $z/\sigma_z \to \hat{z}$, and $\Delta E/\sigma_E \to \Delta\hat{E}$. The vertical plane $(y,\, y')$ is neglected, as it is not relevant for the energy-dependent path length differences.

The electron density before the laser-electron interaction is assumed to be Gaussian,

$$\rho(\hat{x}, \hat{x}', \hat{z}, \Delta\hat{E}) = \frac{1}{4\pi^2} e^{-\frac{1}{2}(\hat{x}^2+\hat{x}'^2+\hat{z}^2+\Delta\hat{E}^2)}. \tag{2.83}$$

The laser pulse is assumed to be a transverse plane wave with normalized wavelength $2\pi\lambda/\sigma_z \to \hat{\lambda}$, which leads to the modulated electron density

$$\rho(\hat{x}, \hat{x}', \hat{z}, \Delta\hat{E}) = \frac{1}{4\pi^2} e^{-\frac{1}{2}(\hat{x}^2+\hat{x}'^2+\hat{z}^2)} e^{-\frac{1}{2}\left[\Delta\hat{E}-a(\hat{z})\sin(\hat{z}/\hat{\lambda})\right]}, \tag{2.84}$$

where $a(\hat{z})$ is the longitudinal energy modulation amplitude in units of the natural energy spread σ_E.

Using normalized transfer matrix elements, i.e., $r_{51} \cdot \sigma_x/\sigma_z \to \hat{r}_{51}$, $r_{52} \cdot \sigma_{x'}/\sigma_z \to \hat{r}_{52}$, and $r_{56} \cdot \sigma_E/\sigma_z \to \hat{r}_{56}$, integrating over $\hat{x}$, $\hat{x}'$, and $\Delta\hat{E}$ to calculate the longitudinal electron density $\rho_\mathrm{l}(\hat{z})$, and performing a Fourier transform

$$\tilde{\rho}_\mathrm{l}(k) = \int \rho_\mathrm{l}(\hat{z}) e^{-ik\hat{z}} \mathrm{d}\hat{z} \tag{2.85}$$

to retrieve the spectral content of the modulated electron density, leads to

$$\tilde{\rho}_\mathrm{l}(k) = e^{-\frac{1}{2}k^2(\hat{r}_{51}^2+\hat{r}_{52}^2+\hat{r}_{56}^2)} \psi(k) \quad \text{with} \tag{2.86}$$

$$\psi(k) = \frac{1}{\sqrt{2\pi}} \int e^{-ik\hat{z}} e^{-\hat{z}^2/2} e^{ik\hat{r}_{56} a(\hat{z}) \sin(\hat{z}/\hat{\lambda})} \mathrm{d}\hat{z}. \tag{2.87}$$

Applying the so-called slowly-varying-envelope approximation, i.e., $a(\hat{z})$ varies slowly compared to the optical oscillation $\sin(\hat{z}/\hat{\lambda})$, a simplified expression is retrieved,

$$\tilde{\rho}_\mathrm{l}(k) = e^{-\frac{1}{2}k^2(\hat{r}_{51}^2+\hat{r}_{52}^2+\hat{r}_{56}^2)} \frac{1}{\sqrt{2\pi}} \int e^{-ik\hat{z}} e^{-\hat{z}^2/2} J_0[k\hat{r}_{56} a(\hat{z})] \mathrm{d}\hat{z}, \tag{2.88}$$

with J_0 being the Bessel function of the first kind.

For small laser intensities, i.e., $|a(\hat{z})| \ll 1/|k\hat{r}_{56}|$, the Bessel function can be expanded into a second-order Taylor series. Assuming an infinitely long laser pulse with an intensity modulation $\propto [1 + \cos(k_\mathrm{mod}\hat{z})]$ based on CPB (Ch. 2.1.2), and, thus, an energy modulation amplitude $a(\hat{z}) = \sqrt{P}\cos(k_\mathrm{mod}\hat{z}/2)$, Eq. 2.88 becomes

$$\tilde{\rho}_\mathrm{l}(k) = 2\pi\delta(k) - e^{-\frac{1}{2}k^2(\hat{r}_{51}^2+\hat{r}_{52}^2+\hat{r}_{56}^2)} \frac{k^2\hat{r}_{56}^2 P\pi}{8} [\delta(k_\mathrm{mod} - k) + \delta(k_\mathrm{mod} + k)]. \tag{2.89}$$

The Dirac delta functions are a consequence of the infinite pulse length with continuous modulation. For a finite pulse and modulation length, these peaks are broadened to a finite width.

A more important implication can be drawn from the factor in front of the Dirac delta functions. This factor tells which ratio of coherent and incoherent THz emission power can be expected for a given modulation wavenumber k_{mod},

$$\frac{P_{\mathrm{coh.}}}{P_{\mathrm{inc.}}} \propto \tilde{\rho}_1^2(k_{\mathrm{mod}}) \propto \hat{r}_{56}^4 P^2 k_{\mathrm{mod}}^4 e^{-k^2(\hat{r}_{51}^2+\hat{r}_{52}^2+\hat{r}_{56}^2)}, \tag{2.90}$$

or, expressed in terms of the original variables,

$$\frac{P_{\mathrm{coh.}}}{P_{\mathrm{inc.}}} \propto \left(r_{56}\frac{\sigma_E}{E}\right)^4 P^2 \left(\frac{2\pi f_{\mathrm{mod}}}{c}\right)^4 e^{-\left(\frac{2\pi f_{\mathrm{mod}}}{c}\right)^2\left(r_{51}^2\sigma_x^2+r_{52}^2\sigma_{x'}^2+r_{56}^2\frac{\sigma_E^2}{E^2}\right)}, \tag{2.91}$$

with f_{mod} being the modulation frequency of the laser intensity. This so-called gain curve is a measure for the efficiency of the CPB process for a given set of storage ring parameters.

Figure 2.15 shows the gain curve for DELTA calculated according to Eq. 2.91 using the bunch properties (σ_x, $\sigma_{x'}$, and σ_E/E) at the modulator and the elements of the transport matrix from the modulator to the THz beamline ('turn 0'), including a one-turn matrix starting at the THz beamline ('turn 1'), and including further revolutions ('turn 2', 'turn 3'). These properties and matrix elements have been extracted from a numerical simulation of the storage ring lattice (Ch. 3.2). As a result, the CPB technique can be employed to generate coherent narrow-band THz radiation with a tuning range of about 1 to 7 THz when looking at the signal directly after the laser-electron interaction, or with a tuning range of about 10 to 300 GHz when looking at the signal after one ore more revolutions.

It is important to remember that an assumption of small laser intensities, i.e., $|a(\hat{z})| \ll 1/|k\hat{r}_{56}|$ was used to derive the gain curve, which translates in terms of the original variables to $r_{56}\Delta E/E \ll \lambda_{\mathrm{mod}}/(2\pi)$. Thus, the path length differences of the off-energy electrons are much smaller than the intensity modulation period of the CPB pulse. As a consequence, the curve only depends on the properties of the undisturbed bunch (σ_x, $\sigma_{x'}$, and σ_E/E) and the storage ring (r_{51}, r_{52}, and r_{56}). In principle, the limited tuning range is caused by the laser-unaffected electrons obscuring the periodic dip structure due to naturally occurring path length differences.

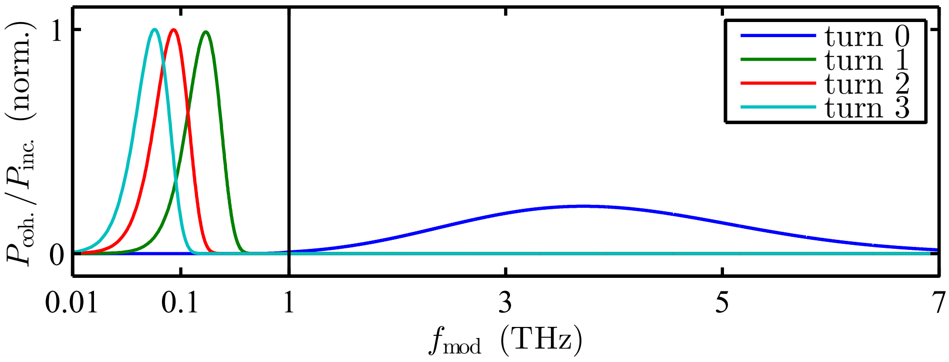

Figure 2.15.: Gain curve according to Eq. 2.91 for turn 0 to 3 (see text for details).

2.5. Emission of THz Radiation

2.5.1. Theory of Synchrotron Radiation

The electrostatic field of charged particles at rest or when moving linearly can be described by field lines originating at the particle position and extending radially outwards. If the particle is accelerated, the information about the change in velocity travels radially outwards with the finite speed of light. For example, the effect of an instantaneous acceleration from zero to a constant velocity can be seen in Fig. 2.16 in the form of small 'kinks' in the field lines. When these kinks pass by a stationary observer, an electric field with a time-dependent transverse component can be detected. In principle, this is an electromagnetic wave. The mathematical derivation of the synchrotron radiation power, spectrum, spatial and angular distribution, etc. is based on a similar consideration. Here, only the most significant steps shall be mentioned.

The magnetic and electric fields $\vec{B}$ and $\vec{E}$ can be described by [104]

$$\vec{B} = \vec{\nabla} \times \vec{A} \quad \text{and} \quad \vec{E} = -\frac{\partial \vec{A}}{\partial t} - \vec{\nabla}\varphi \tag{2.92}$$

with a vector and scalar potential $\vec{A}$ and φ and the Lorenz gauge $\vec{\nabla}\vec{A} + c^{-2}\partial\varphi/\partial t = 0$. Using Maxwell's equations, two wave equations for $\vec{A}$ and φ can be derived. Considering only a single point charge q, these wave equations are solved by the so-called Liénard-Wiechert potentials [104]

$$\vec{A}(x,y,z,t) = \frac{\mu_0}{4\pi}\,\frac{q}{r}\,\frac{\vec{\beta}}{1+\vec{n}\vec{\beta}}\bigg|_{t_\mathrm{r}} \quad \text{and} \tag{2.93}$$

$$\varphi(x,y,z,t) = \frac{1}{4\pi\varepsilon_0}\,\frac{q}{r}\,\frac{\vec{1}}{1+\vec{n}\vec{\beta}}\bigg|_{t_\mathrm{r}}\,, \tag{2.94}$$

where μ_0 is the vacuum permeability, ε_0 is the vacuum permittivity, r is the distance between the observer and the charge, $\vec{n}$ is the normalized vector pointing from the observer to the charge, and $\vec{\beta}$ is the velocity of the charge. Due to the finite speed of light, the expressions must be evaluated at a retarded time $t_\mathrm{r} = t - r(t_\mathrm{r})/c$.

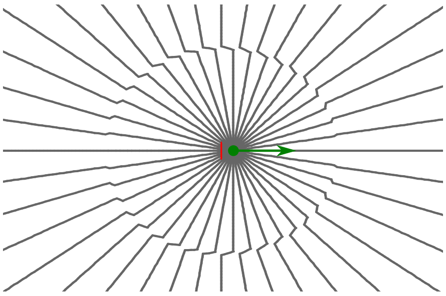

Figure 2.16.: Electric field lines (gray) of a point charge (green) formerly at rest (position indicated by red marker) shortly after acceleration to a constant velocity. The sketch is based on a graphic which was generated with 'Radiation 2D' [108, 109].

Using Eq. 2.92 and the Liénard-Wiechert potentials under consideration of the retarded time, the electric field at the observer is calculated to be [104]

$$\frac{4\pi\varepsilon_0}{q}\vec{E} = \frac{1-\beta^2}{r^2}(\vec{n}+\vec{\beta}) + \frac{1}{cr}\left\{\vec{n}\times\left[(\vec{n}+\vec{\beta})\times\frac{\mathrm{d}\vec{\beta}}{\mathrm{d}t_\mathrm{r}}\right]\right\}\Bigg|_{t_\mathrm{r}} . \tag{2.95}$$

The first term falls off quickly with $1/r^2$ and depends only on the particle velocity β. This is the Coulomb field and will not be considered further. The second term, however, falls off only with $1/r$ and depends on the particle acceleration $\mathrm{d}\vec{\beta}/\mathrm{d}t_\mathrm{r}$. The following considerations will focus on this radiation term.

With the magnetic field calculated accordingly and found to be $\vec{B} = c^{-1}\vec{E}\times\vec{n}$, the energy flux density is given by the Poynting vector $\vec{S} = -\varepsilon_0 c E^2 \vec{n}$. The total radiation power is calculated integrating the Poynting vector over a closed surface around the charge. Assuming a circular trajectory with bending radius ρ, and transforming the acceleration $\mathrm{d}\vec{\beta}/\mathrm{d}t_\mathrm{r}$ into the laboratory system, this leads to [104]

$$P_\mathrm{e} = \frac{2}{3} r_\mathrm{c} m_\mathrm{e} c^3 \frac{\beta^4\gamma^4}{\rho^2} = \frac{e^2 c}{6\pi\varepsilon_0}\frac{\beta^4\gamma^4}{\rho^2} \quad \text{with} \quad r_c = \frac{e^2}{4\pi\varepsilon_0 m_\mathrm{e} c^2} \tag{2.96}$$

for an electron with charge e and rest mass m_e. For a storage ring without insertion devices, i.e., synchrotron radiation is only emitted in the bending magnets, the total energy loss per revolution is then given by

$$\Delta E = P_\mathrm{e}\frac{2\pi\rho}{\beta c} = \frac{e^2}{3\varepsilon_0}\frac{\beta^3\gamma^4}{\rho} = \frac{e^2}{3\varepsilon_0 (m_\mathrm{e}c^2)^4}\frac{E^4}{\rho} \approx 88.5\ \mathrm{keV}\frac{E^4[\mathrm{GeV}^4]}{\rho[\mathrm{m}]} \tag{2.97}$$

with $\beta \approx 1$ and E being the particle energy.

A Fourier transform of the Poynting vector $\vec{S}$ is performed to obtain the angular and frequency dependence or spectrum of the synchrotron radiation. Assuming a vertical angle θ between the observer and the electron path, this results in [104]

$$\frac{\mathrm{d}^2 P_\mathrm{e}}{\mathrm{d}\Omega\mathrm{d}\omega}(\omega,\theta) = \frac{3 r_\mathrm{c} m_\mathrm{e} c^2}{8\pi^3\rho}\gamma^2\left(\frac{\omega}{\omega_\mathrm{c}}\right)^2(1+\gamma^2\theta^2)^2\left[\underbrace{K_{2/3}^2(\xi)}_{\sigma} + \underbrace{\frac{\gamma^2\theta^2 K_{1/3}^2(\xi)}{1+\gamma^2\theta^2}}_{\pi}\right] \tag{2.98}$$

with K_i being the modified Bessel functions of the second kind,

$$\xi = \frac{1}{2}\frac{\omega}{\omega_\mathrm{c}}(1+\gamma^2\theta^2)^{3/2}, \quad \text{and} \quad \omega_\mathrm{c} = \frac{3}{2}\gamma^3\frac{c}{\rho}. \tag{2.99}$$

The term marked with σ is horizontally polarized, the term marked with π is polarized perpendicularly to the line between source point and observer (vertically, in case of $\theta = 0$). There is no dependence on the horizontal angle φ due to the assumed circular trajectory.

An angular or frequency integration of Eq. 2.98 leads to [104]

$$\frac{\mathrm{d}P_\mathrm{e}}{\mathrm{d}\Omega}(\theta) = \frac{7 r_c m_\mathrm{e} c^3}{32\pi\rho^2}\frac{\gamma^5}{(1+\gamma^2\theta^2)^{5/2}}\left(1+\frac{5}{7}\frac{\gamma^2\theta^2}{1+\gamma^2\theta^2}\right) \quad \text{or} \tag{2.100}$$

$$\frac{\mathrm{d}P_\mathrm{e}}{\mathrm{d}\omega}(\omega) = \frac{P_\mathrm{e}}{\omega_\mathrm{c}} S\left(\frac{\omega}{\omega_\mathrm{c}}\right) \quad \text{with} \quad S(\chi) = \frac{9\sqrt{3}}{8\pi}\chi\int_\chi^\infty K_{5/3}(x)\mathrm{d}x. \tag{2.101}$$

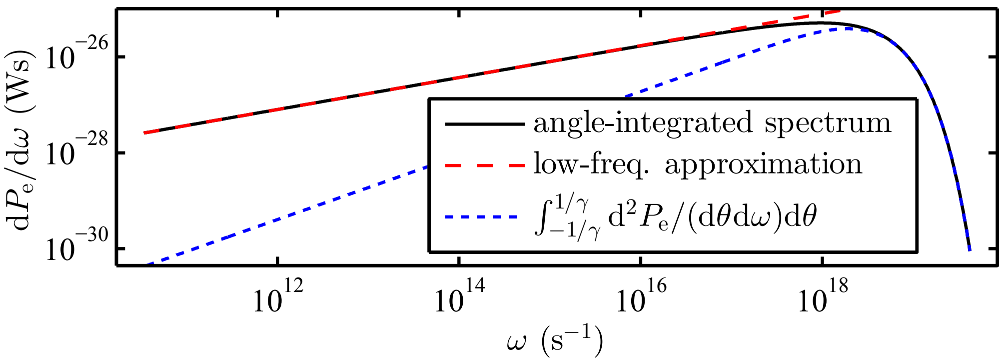

Figure 2.17.: Angle-integrated bending-magnet power spectrum (Eq. 2.101) from a single electron at DELTA, low-frequency approximation (Eq. 2.102), and angle-resolved spectrum (Eq. 2.98) integrated from $\theta_1 = -1/\gamma$ to $\theta_2 = 1/\gamma$.

The so-called critical frequency ω_c divides the power spectrum into two areas of equal size. The function $S(\chi)$ is normalized, thus, a spectral integration of Eq. 2.101 results in P_e in accordance with Eq. 2.96. For small frequencies $\omega \ll \omega_c$ an asymptotic solution for Eq. 2.101 is found [104],

$$\frac{dP_e}{d\omega} \approx 1.333 \left(\frac{\omega}{\omega_c}\right)^{1/3} \frac{P_e}{\omega_c}. \tag{2.102}$$

Figure 2.17 shows the angle-integrated spectrum and the asymptotic solution based on DELTA parameters (Tab. 1.4). Furthermore, the angle-resolved spectrum integrated over an angle of $\pm 1/\gamma$ is shown. The high-frequency domain is clearly dominated by the $\pm 1/\gamma$ radiation cone.

The angular power distribution is shown in Fig. 2.18 (a). At an opening angle of $\pm 1/\gamma$, the power has dropped to about 1/4 of the peak power at $\theta = 0$. Thus, the opening angle of synchrotron radiation from a bending magnet is usually considered to be $\pm 1/\gamma$. However, in the THz regime (Fig. 2.18, b), the power is distributed over a much wider opening angle.

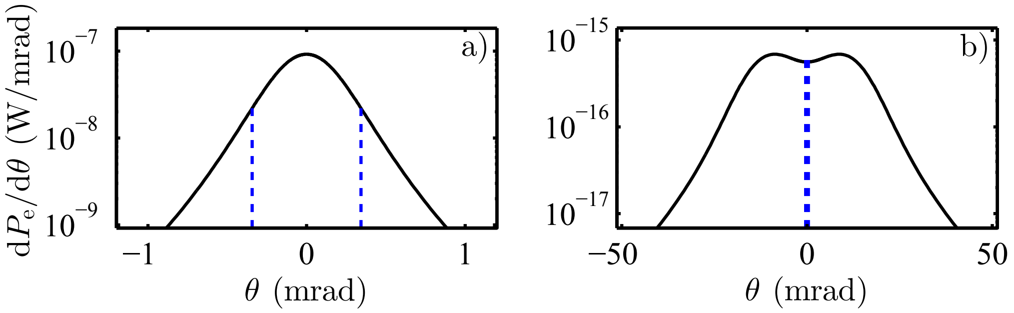

Figure 2.18.: Angular power distribution (Eq. 2.100) from a single electron passing through a DELTA bending magnet (a) and angle-resolved spectrum (Eq. 2.98) integrated over a frequency range of 10 GHz to 10 THz (b; note the different angular scale). The blue dashed lines indicate an opening angle of $\pm 1/\gamma$.

2.5.2. Coherent Emission Process

Coherence is the property of two or more waves (or parts of a spatially or temporally extended wave pattern) to have a fixed phase relation to each other. By definition, those waves must have the same frequency. For example, different transverse sections of a plane wave are transversely coherent, which causes the well-known stationary interference pattern after passing through a double slit. If each slit would have been illuminated by two independent light sources, the spherical waves originating from each slit would have a random phase relation and – on average – no interference pattern would be detected. Synchrotron radiation is emitted by single electrons. Therefore, the coherence properties of synchrotron radiation from an ensemble of electrons are determined by the transverse and longitudinal electron distribution in the bunch.

Regarding the transverse plane, a photon beam emittance can be defined in analogy to the electron beam emittance as the product of beam size (Eq. 2.29) and divergence (Eq. 2.33). The so-called diffraction-limited photon beam emittance [104]

$$\varepsilon_{\mathrm{ph,min}} = \frac{\lambda}{4\pi} \tag{2.103}$$

is the minimum possible emittance for a given wavelength λ, resulting from $M^2 = 1$ in Ch. 2.1.3. If the electron beam emittance is smaller than the diffraction-limited photon beam emittance, the synchrotron radiation is transversely fully coherent. At DELTA, this is the case for radiation with a wavelength larger than approximately 190 nm, which includes the THz regime.

For a discussion of the longitudinal coherence, the electric field emitted by each electron can be described by

$$E_k(\omega, t) = E_{\mathrm{e}}(\omega) e^{i(\omega t + \varphi_k)}, \tag{2.104}$$

with $E_{\mathrm{e}}(\omega)$ being the Fourier transform of the single-particle electric field $E_{\mathrm{e}}(t)$ and φ_k being an individual phase. The total electric field from the entire bunch and the corresponding power are then given by

$$E_{\mathrm{tot}}(\omega, t) = \sum_k E_k(\omega, t) = E_{\mathrm{e}}(\omega) \sum_k e^{i(\omega t + \varphi_k)} \quad \text{and} \tag{2.105}$$

$$P_{\mathrm{tot}}(\omega, t) = P_{\mathrm{e}}(\omega) \left| \sum_k e^{i(\omega t + \varphi_k)} \right|^2 = P_{\mathrm{e}}(\omega) \left[N_{\mathrm{e}} + \sum_k \sum_{l \neq k} e^{i(\varphi_k - \varphi_l)} \right], \tag{2.106}$$

with $P_{\mathrm{e}}(\omega)$ being the single-particle spectrum (Eq. 2.101) and N_{e} being the number of electrons in the bunch. Introducing the longitudinal particle position z_k via $\varphi_k = 2\pi z_k/\lambda = \omega z_k/c$ and a continuous normalized particle distribution $\rho(z)$, the sums can be replaced by integrals leading to (see Eqs. A.11 ff. for details)

$$P_{\mathrm{tot}}(\omega) = P_{\mathrm{e}}(\omega) N_{\mathrm{e}} \left[1 + (N_{\mathrm{e}} - 1) g^2(\omega) \right] \tag{2.107}$$

with the so-called form factor

$$g^2(\omega) = \left| \int \rho(t) e^{i\omega t} \mathrm{d}t \right|^2, \tag{2.108}$$

which is the squared Fourier transform of the normalized longitudinal electron density $\rho(t)$. The first term in Eq. 2.107 is the incoherent radiation power $P_{\mathrm{inc}}(\omega) = P_{\mathrm{e}}(\omega) N_{\mathrm{e}}$, the second term the coherent power $P_{\mathrm{coh}}(\omega) = P_{\mathrm{e}}(\omega) N_{\mathrm{e}} (N_{\mathrm{e}} - 1) g^2(\omega)$. With $N_{\mathrm{e}} \gg 1$, the form factor can be approximated by $g^2(\omega) \approx P_{\mathrm{coh}}(\omega)/(N_{\mathrm{e}} P_{\mathrm{inc}}(\omega))$.

2.6. THz Optics and Beam Transport

After the emission of THz radiation in a dipole magnet of the storage ring, the radiation has to be transported to the experimental setup using mirrors and focusing optics, vacuum pipes, and windows to exit the storage ring vacuum.

2.6.1. Gaussian Beam Optics II

In analogy to a laser beam, the THz beam transport can be described by Gaussian beam optics (Ch. 2.1.3). The horizontal radiation fan of the dipole magnet and the vertical synchrotron radiation cone (Fig. 2.18 b) are cut off by an aperture in the DELTA THz beamline (see Ch. 4.1 for details) with a diameter of 38 mm at a distance of 1133 mm to the source point. This results in a round beam with a waist radius (Eq. 2.33)

$$w_0 = \frac{\lambda}{\pi \tan\theta_0} \quad \text{and} \quad \theta_0 = \frac{1}{2}\frac{38\ \text{mm}}{1133\ \text{mm}} = 16.77\ \text{mrad}. \tag{2.109}$$

The optics of the THz beamline must be designed to transport radiation with a broad spectrum ranging from several 10 GHz to at least 10 THz. In general, however, the final waist position depends on the frequency, which is illustrated in Fig. 2.19 (left) and would prevent a broad-band detection at a fixed detector position (see [12] for an analytical derivation). This problem is solved using a so-called Gaussian telescope comprising two lenses with focal lengths f_1 and f_2 placed at a distance $d = f_1 + f_2$. As a consequence, the new waist position becomes independent of the frequency (Fig. 2.19, right) even when cascading several Gaussian telescopes.

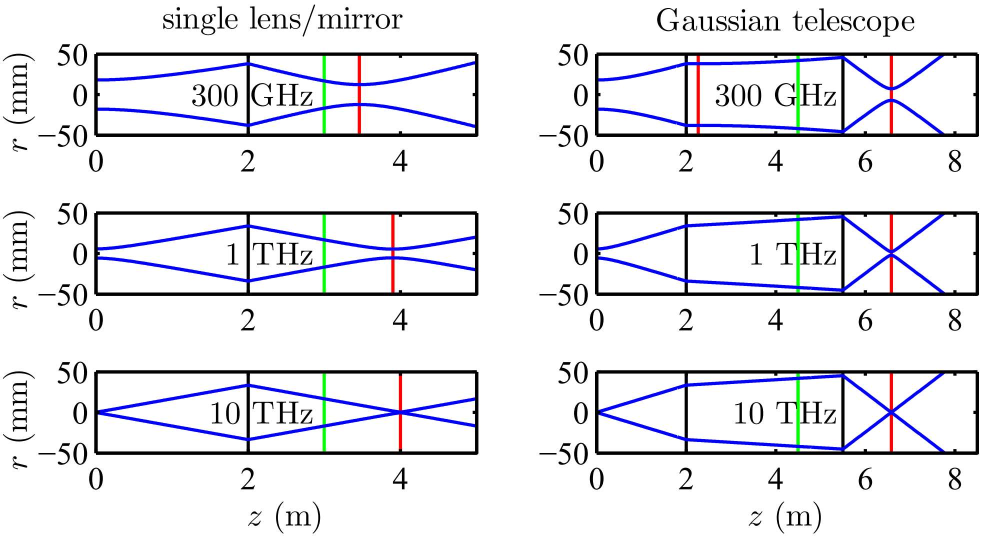

Figure 2.19.: Beam diameter (blue), lenses (black), focal lengths (distance between lenses and green lines), and waist positions (red) for a beam with three different frequencies (top to bottom) passing through a single lens (left) and passing through a Gaussian telescope (right). The plots are obtained using a numerical code for Gaussian beam propagation based on the equations in Ch. 2.1.3.

2.6.2. Guiding and Focusing Mirrors

In paraxial approximation and for an angle of incidence $\alpha = 0°$, the focal length of a spherical mirror with radius R is $f = R/2$. At the DELTA THz beamline, the mirrors of the focusing optics also guide the beam through the right-angled beamline resulting in $\alpha = 45°$. For $\alpha \neq 0°$, however, the focal length f_m for meridional rays (rays in the optical plane defined by the incoming and outgoing optical axis and the mirror normal) becomes shorter and the focal length f_s for sagittal rays (rays in the optical plane perpendicular to the meridional plane) becomes larger [12]. As a consequence, to achieve a symmetrical optics with $f = f_\mathrm{m} = f_\mathrm{s}$ for $\alpha = 45°$, toroidal mirrors with different radii of curvature

$$R_\mathrm{m} = \sqrt{2}f \quad \text{and} \quad R_\mathrm{s} = 2\sqrt{2}f \tag{2.110}$$

must be chosen.

2.6.3. Absorption and Reflection of THz Radiation

With the direct current (DC) conductance σ_DC, the reflectance R of metals at low frequencies $\nu \ll \sigma_\mathrm{DC}/\varepsilon_0$ is given by [14, 110]

$$R = 1 - 2\sqrt{\frac{4\pi\varepsilon_0\nu}{\sigma_\mathrm{DC}}}. \tag{2.111}$$

Thus, the reflectivity decreases with increasing frequency. For the gold and aluminium[3] mirrors used at the DELTA THz beamline, this results in $R_\mathrm{Au} = 98.99\%$ and $R_\mathrm{Al} = 98.90\%$ for $\nu = 10$ THz, which is in good agreement with experimental results showing reflectances around 99% [111].

Absorption in (semi-)transparent material follows the Lambert-Beer law [14]

$$\frac{I(\lambda)}{I_0(\lambda)} = e^{-\alpha(\lambda)d}, \tag{2.112}$$

where I_0 is the incoming intensity with wavelength λ, $\alpha(\lambda)$ is the absorption coefficient, and d is the material thickness. The surface reflectance [14]

$$R(\lambda) = \frac{[n(\lambda) - 1]^2 + \kappa^2(\lambda)}{[n(\lambda) + 1]^2 + \kappa^2(\lambda)}, \tag{2.113}$$

depends on the refractive index $n(\lambda)$ and the extinction coefficient $\kappa(\lambda) = \lambda\alpha(\lambda)/(4\pi)$. Consequently, the overall transmission through a window is described by

$$T(\lambda) = [1 - R(\lambda)]^2 e^{-\alpha(\lambda)d}. \tag{2.114}$$

Figure 2.20 shows the refractive index (a) and the absorption coefficient (b) of z-cut quartz based on experimental data, and the overall transmission calculated via Eq. 2.114 for three different thicknesses. At DELTA, in order to separate the storage ring UHV from the beamline and spectrometer vacuum, the THz radiation passes through a 4.5 mm thick z-cut quartz window. For in-air detection, e.g., with the InSb

---

[3] $\sigma_\mathrm{DC,Au} = 44.0 \cdot 10^6$ S/m, $\sigma_\mathrm{DC,Al} = 36.6 \cdot 10^6$ S/m.

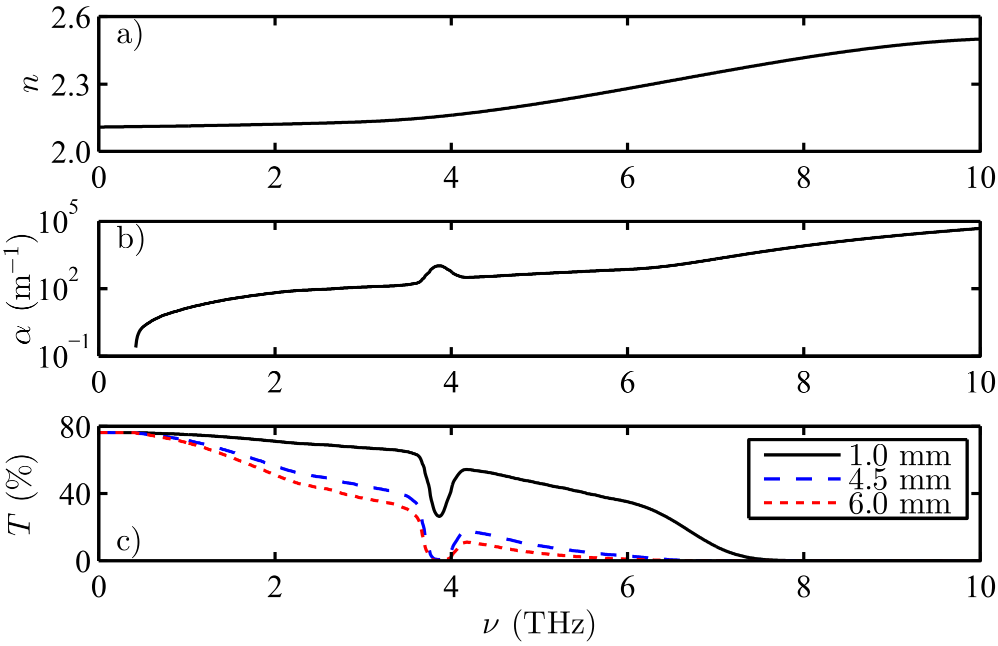

Figure 2.20.: Refractive index (a), absorption coefficient (b), and transmission (c) for three different thicknesses of z-cut quartz. The data for (a) and (b) is based on [14, 112, 113].

bolometer, one of two beam ports with an additional 4.5 mm or a 6 mm thick z-cut quartz window is passed at the end of the beamline (see Ch. 4.1 for details), resulting in a high-frequency cut-off at about 6 to 7 THz. In general, quartz crystal is birefringent, i.e., the refractive index n depends on the polarization of the incoming light. However, 'z-cut' implies that the window surfaces are cut perpendicular to the optical axis of the crystal. Here, all incoming light independent of its polarization experiences the same refractive index leading to the same reflectance and absorption.

A further limitation results from the diameter of the beamline vacuum tubing. For very low frequencies in the GHz regime, the radiation can no longer be assumed to travel in free space. Instead, the metal tubing acts as a waveguide with a cut-off frequency, below which the electromagnetic waves decay exponentially instead of propagating further. The cut-off frequency of the fundamental TE_{11} mode in a round waveguide with radius a is given by [114]

$$\lambda_\mathrm{c} \approx \frac{2\pi a}{1.8412} \quad \Rightarrow \quad f_\mathrm{c} = \frac{c}{\lambda_\mathrm{c}} \approx 1.8412 \frac{c}{2\pi a} \tag{2.115}$$

with $x = 1.8412$ being the first zero of $J_1'(x)$, the first derivative of the Bessel function of the first kind of order 1. With the narrowest beam pipe diameter at the DELTA THz beamline being 38 mm, the cut-off frequency is approximately 4.6 GHz. However, the beamline later opens up to about 80 mm and is then lined with an absorber. The radiation emanating from the end of the 38-mm 'wave guide' is no longer matched to the beamline optics and is mostly absorbed. As a consequence, only radiation with frequencies above several ten GHz reaches the experimental setup.

2.7. Fourier Transform Infrared Spectroscopy

At DELTA, a so-called Fourier transform infrared (FTIR) spectrometer is employed for spectroscopic studies (Ch. 4.3).

2.7.1. Basic Principle

An FTIR spectrometer is based on an interferometer (Fig. 2.21), in which an incoming pulse is split and later recombined with a relative path length difference $2x$. The incoming signal can be described by the sum of weighted monochromatic waves, i.e., its Fourier transform $\tilde{E}_0(\omega)$:

$$E_{\text{in}}(t) = \int \tilde{E}_0(\omega) e^{i\omega t}\,\mathrm{d}\omega. \tag{2.116}$$

The recombined signal will comprise two copies of the original signal, one of which experienced an additional phase advance of $k \cdot 2x$ with $k = \omega/c$:

$$E_{\text{out}}(t,x) = \frac{1}{2}\int \tilde{E}_0(\omega) e^{i\omega t}\,\mathrm{d}\omega + \frac{1}{2}\int \tilde{E}_0(\omega) e^{i[\omega t - 2k(\omega)x]}\,\mathrm{d}\omega. \tag{2.117}$$

The interferogram $I_{\text{out}}(x) \propto |E_{\text{out}}(t,x)|^2$ is then given by [115]

$$\begin{aligned} I_{\text{out}}(x) &= \frac{1}{2}\int \tilde{I}_0(\omega)\{1 + \cos[2k(\omega)x]\}\,\mathrm{d}\omega & (2.118)\\ &= \frac{1}{2}I_{\text{tot}} + \frac{1}{2}\int \tilde{I}_0(\omega)\cos[2k(\omega)x]\,\mathrm{d}\omega. & (2.119)\end{aligned}$$

The first term is the spectrally integrated intensity. As only the second term contains the spectral information of the signal, the constant first term is usually neglected, and an interferogram function [115]

$$I(x) = \int B(\omega)\cos[2k(\omega)x]\,\mathrm{d}\omega \tag{2.120}$$

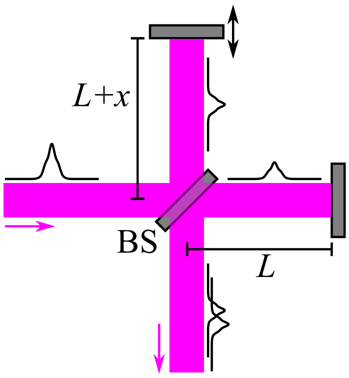

Figure 2.21.: Interferometer with a beam splitter (BS) and two mirrors (one fixed at distance L to be beam splitter, one movable at distance $L + x$). The THz beam (magenta) and longitudinal pulse profiles (black) are shown as well.

is defined with $B(\omega) = H(\omega)\tilde{I}_0(\omega)/2$. Here, a correction factor $H(\omega)$ has been included, which accounts for the frequency-dependent efficiency of the beam splitter and the detector sensitivity. For a broad-band signal, there is always partial destructive interference except for $x = 0$, where perfect constructive interference occurs. Therefore, the typical interferogram has a strong central peak at $x = 0$ and decreases rapidly for $|x| > 0$.

Inverting Eq. 2.120, the signal spectrum can be extracted from the Fourier cosine transform of the recorded interferogram:

$$B(\omega) = \int I(x)\cos[2k(\omega)x]\,\mathrm{d}x. \tag{2.121}$$

It should be noted that, in general, a complete Fourier transform is equivalent to the sum of the cosine and sine transform. However, as it makes no difference which of the two pulse copies is the first to arrive at the beam splitter again, $I(x) = I(-x)$ is an even function, for which the sine transform is zero.

2.7.2. Truncation, Apodization, Zero-Filling, and Phase Correction

In principle, the integration in Eq. 2.121 has to be performed over the interval $[-\infty, \infty]$. In reality, the path length difference is limited to a certain x_{max} due to the mechanical design of the interferometer, which can be described by a boxcar function $f(x) = 1$ for $x \in [-x_{\mathrm{max}}, x_{\mathrm{max}}]$ and $f(x) = 0$ otherwise. The measured interferogram then transforms into a spectrum

$$G(\omega) = \int f(x)I(x)\cos[2k(\omega)x]\,\mathrm{d}x = B(\omega) * \tilde{f}(\omega) \quad \text{with} \tag{2.122}$$

$$\tilde{f}(\omega) = 2x_{\mathrm{max}}\,\mathrm{sinc}(2kx_{\mathrm{max}}). \tag{2.123}$$

Here, the sinc function is defined as $\mathrm{sinc}(\chi) \equiv \sin(\pi\chi)/(\pi\chi)$. Thus, a monochromatic signal $B(\omega) = \delta(\omega-\omega_0)$ will be seen as $G(\omega) = \tilde{f}(\omega-\omega_0) = 2x_{\mathrm{max}}\,\mathrm{sinc}(2(\omega-\omega_0)x_{\mathrm{max}}/c)$ with a peak FWHM of

$$\Delta\omega \approx 1.896\frac{c}{x_{\mathrm{max}}} \quad \text{or} \quad \Delta\nu \approx 0.302\frac{c}{x_{\mathrm{max}}}, \tag{2.124}$$

which is the theoretical frequency resolution of an FTIR spectrometer.

In order to reduce the sinc ringing caused by the boxcar truncation, i.e., the finite interferogram length, the interferogram is usually multiplied by a so-called apodization function which is symmetrical (like $I(x)$), has its maximum at $x = 0$, and continuously decreases to zero at $x = \pm x_{\mathrm{max}}$. Although the ringing is reduced, the peak width increases, resulting in a lower resolution.

The interferogram function $I(x)$ measured by a detector is usually sampled and digitized at discrete mirror positions $x_i \in [-x_{\mathrm{max}}, x_{\mathrm{max}}]$ with spacing Δx. The spectrum $\{G_i\} = \{G(\nu_i)\}$ is then computed using the discrete Fourier cosine transform of $\{I_i\} = \{I(x_i)\}$. With a sampling frequency of $\nu_{\mathrm{s}} = 1/T_{\mathrm{s}} = c/(2\Delta x)$, the Nyquist-Shannon sampling theorem [116,117] states that the maximum detectable frequency is given by

$$\nu_{\mathrm{max}} = \nu_{\mathrm{s}}/2 = c/(4\Delta x). \tag{2.125}$$

The frequency coordinates ν_i are then defined on the interval $[0, \nu_{\max}]$ with spacing

$$\Delta\nu_i = \frac{\Delta x}{2x_{\max}}\nu_{\max} = \frac{c}{8x_{\max}} = 0.125\frac{c}{x_{\max}}. \tag{2.126}$$

However, the spectral resolution is still $\Delta\nu$ according to Eq. 2.124.

In order to increase the number of frequency sampling points $n_\nu = \nu_{\max}/\Delta\nu_i = 2x_{\max}/\Delta x$, the digitized interferogram can be expanded by adding zeros at the end ('zero filling') before performing the Fourier transform, thereby virtually increasing the maximum path length difference $x_{\max}$. Of course, the physical resolution can and will not be increased; instead this acts as a spectral interpolation, resulting in a smoother spectrum. Furthermore, if the maximum (or minimum) of a spectral feature occurs between two spectral sampling points ν_i, the amplitude of the feature can appear reduced by up to 36%. Using zero filling, this so-called picket-fence effect is reduced [118]. The number of zeros added to the interferogram is usually specified by the so-called zero-filling factor (ZFF).

As mentioned before, Eq. 2.121 is only valid if $I(x)$ is an even function. However, due to the discrete sampling at $\{x_i\}$, the interferogram might be slightly shifted and no sample is taken at exactly $x = 0$. Furthermore, frequency-dependent phase shifts might occur in the spectrometer optics or electronics. In principle, this leads to a complex Fourier transform of $I(x)$ or a non-zero Fourier sine transform. In this case, a phase correction signal can be calculated using the imaginary part of an FFT [119].

3. Simulation of Laser-Induced THz Radiation

The numerical simulation of the laser-electron interaction (Chs. 2.1, 2.2 and 2.3), the propagation of the electron distribution through the magnetic lattice of the storage ring (Chs. 2.2 and 2.4), and the emission of coherent THz radiation (Ch. 2.5) is an important step towards understanding the principle of laser-induced THz radiation and for interpreting the experimental results (Ch. 5).

3.1. Previous Simulation Efforts at DELTA

The THz beamline at DELTA was designed, constructed, and commissioned within the scope of two diploma theses [12,13]. As part of the design phase in 2010, a simulation of the laser-induced THz generation was performed in order to find a suitable position for the THz beamline at which the density modulation is most prominent, i.e., deepest and narrowest. The simulation was based on

- an in-house C++ program called LASEEM [12] to generate a random DELTA-compliant particle distribution and calculate the energy modulation induced by a laser pulse,
- a so-called tracking simulation [13] based on MATLAB [102] and the Accelerator Toolbox [120] to compute the path of each particle through the magnetic lattice, and
- the calculation [13] of the THz spectrum (Eq. 2.107) using the single-particle spectrum (Eq. 2.101) and a Fourier transform of the density profile performed with Mathematica [121].

With the simulated electron propagation limited to a quarter of the DELTA lattice starting at the U250, only an estimate of the first ('turn-0') coherent signal at the source point of the THz beamline was given.

A first multi-turn simulation was performed as part of a bachelor's thesis in 2013 [122]. An in-house C++ code was used to generate the particle distribution (similar to LASEEM) and to calculate the density profiles. The energy modulation and particle tracking were performed using '`elegant`' – a versatile accelerator physics code [123, 124] – which allows for several tracking methods, including the direct numerical solution of the equations of motion to take into account non-linear effects. A set of MATLAB scripts was used for pre- and post-processing.

3.2. A New Multi-Turn and Chirped-Pulse-Beating Simulation Code

Within the scope of this thesis, a more extensive simulation code called ‘THz Simulation with MATLAB and `elegant`’ (THzSMe) has been newly developed in order to study the laser-induced THz intensity and spectrum under variation of several laser and storage ring parameters. It is based on a combination of MATLAB scripts for particle generation, laser-electron interaction, longitudinal profile, and spectral calculations, and `elegant` for particle tracking.

THzSMe offers an interactive routine for defining simulation parameters. A complete list of parameters, their description, and their default values is given in Tab. A.9. The parameters are stored in a configuration file and can be used for multiple independent simulation runs. As an alternative to manual input, THzSMe can extract several parameters, e.g., the Twiss parameters at the start of the modulator, from the storage ring lattice using `elegant`.

In addition, an `elegant`-compatible description file of the storage ring lattice has to be provided. The simulations performed in the scope of this thesis use a slightly modified version of the ‘del008’ `elegant` lattice file [125], which is based on the original design optics of DELTA [126].

The algorithm for particle generation is based on the considerations described in Ch. 2.2.3. To save computation time, only a short longitudinal slice of the electron bunch centered on the laser pulse may be generated.

The program then loops over a set of discrete time steps. At each step, the position of each particle traveling through the modulator (according to Ch. 2.3.1), the electric field of the laser pulse at each particle position (according to Ch. 2.1.3), and the energy exchange (according to Ch. 2.3.2) are calculated. The simulated laser pulse may include a spatial, angular, and timing offset to the electron bunch, a linear and quadratic chirp (according to Chs. 2.1.1 and 2.1.2), and a numerically simulated intensity modulation (according to Ch. 2.1.2). The sum of energy change from all time steps reveals the overall induced energy deviation per particle. Afterwards, the six-dimensional coordinates of all particles are saved to disk twice – once with and once without energy modulation.

Next, THzSMe executes `elegant` using the particle positions from disk as start values and the predefined lattice file including dipole, quadrupole, and sextupole magnets. The tracking simulation starts at the end of the modulator, continues for a user-defined number of revolutions, and saves the 6-d particle positions at the THz-beamline source point during each passage. Instead of the matrix formalism, magnets are simulated using a series of discrete kicks, which allows the statistical emission of synchrotron radiation and the corresponding energy losses to be included. A simulated RF cavity provides the sinusoidal acceleration field and correctly reproduces the longitudinal beam dynamics (Ch. 2.2.2).

Finally, the particle positions with and without energy modulation are read back into MATLAB for each revolution. A histogram of the longitudinal electron density is calculated, and a difference histogram from the runs with and without energy modulation is generated. This difference histogram contains the information about the laser-induced density modulation and can be scaled and added to a Gaussian bunch profile using the previously stored number of electrons per macro particle to obtain an absolute measure of the total electron density. An FFT is used to calculate the form factor and the total coherent emission spectrum (Ch. 2.5).

3.2.1. Example 1: Multi-Turn Simulation

As an example for the step-by-step simulation sequence, and to gain a better descriptive and qualitative understanding of the energy modulation and particle dynamics, the results from THzSMe for an energy modulation with a short laser pulse (as opposed to a CPB setup, see Ch. 3.2.2) shall be presented. The simulation is based on the default parameters given in Tab. A.9, but with an increased number of particles of $2 \cdot 10^5$ and including 200 revolutions of the electron bunch after the laser-electron interaction. The parameters model the default setup of the DELTA short-pulse facility with the exception of the RF voltage and bunch length, which had to be modified to result in consistent longitudinal dynamics.

Figure 3.1 shows the longitudinal phase space distribution within the simulated slice directly after the laser-electron interaction. The sinusoidal energy modulation described by Eq. 2.81 is modulated with a Gaussian envelope due to the longitudinal laser pulse profile, and the width of this envelope is slightly larger than the laser pulse length (40 fs FWHM) due to the slippage (the electrons lag behind one laser period per undulator period; see Ch. 2.3.2).

The turn-by-turn evolution of the longitudinal phase space distribution is shown in Fig. 3.2. As mentioned before, particles with a positive energy deviation (red) travel on a dispersive orbit with increased path length and exhibit a delayed arrival time t at the THz source point. Particles with a longitudinal offset experience a reduced or increased accelerating RF field and, after half a synchrotron oscillation period (at about turn 83), the particles with an initial positive energy modulation now have a negative energy deviation and vice versa. The spiral-like shape of the particle distribution is caused by the non-linear RF field, which leads to an increased synchrotron oscillation period for particles with a large amplitude.

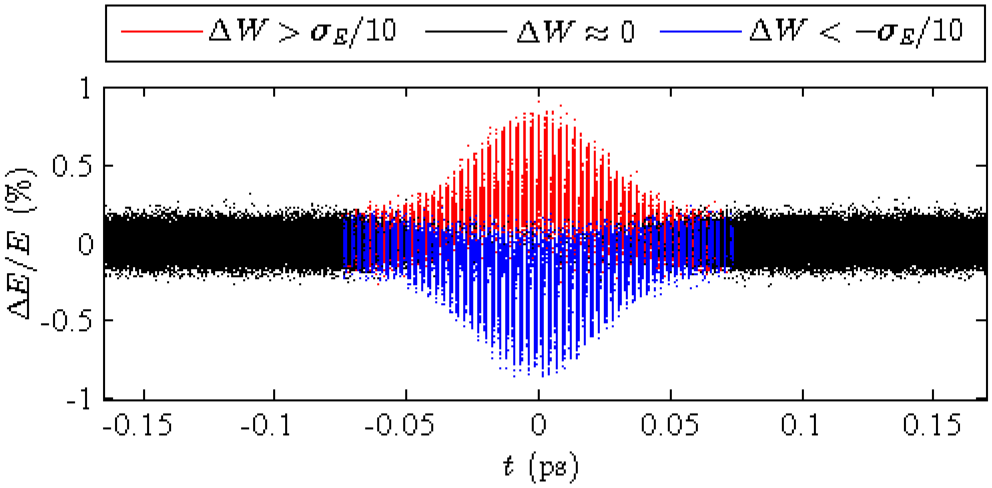

Figure 3.1.: Longitudinal phase space distribution of particles within the generated slice after simulation of the energy modulation.

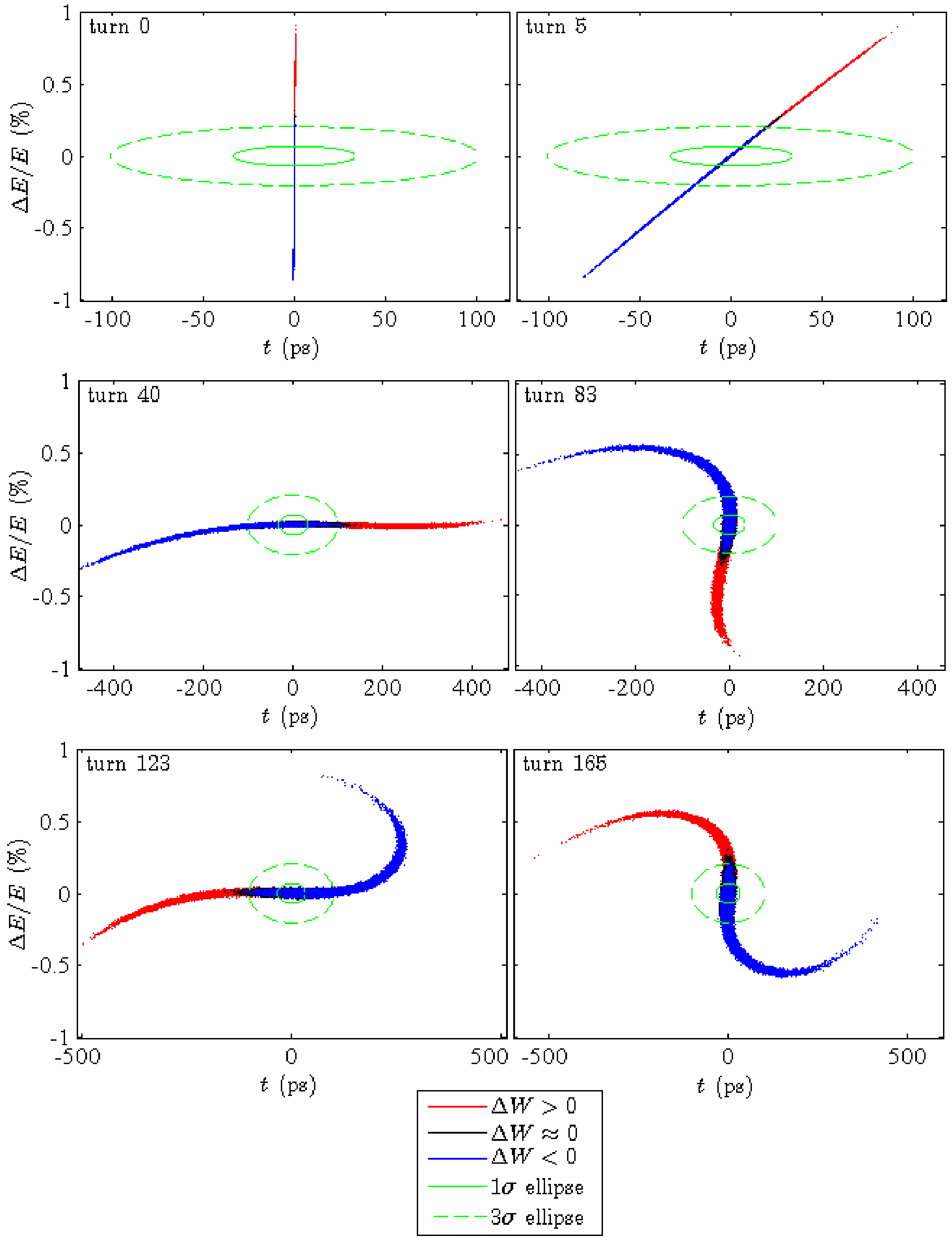

Figure 3.2.: Longitudinal phase space distribution at the THz source point for turn 0 (directly after the laser-electron interaction), turn 5, turn 40 (approx. 1/4 of a synchrotron oscillation period T_S), turn 83 ($\approx T_\mathrm{S}/2$), turn 123 ($\approx 3T_\mathrm{S}/4$), and turn 165 ($\approx T_\mathrm{S}$). The particle colors indicate the initial energy deviation (Fig. 3.1). As only a short slice has been simulated, the 1σ and 3σ ellipses of the longitudinal phase space distribution of the entire bunch are shown for reference. Note the different time scales.

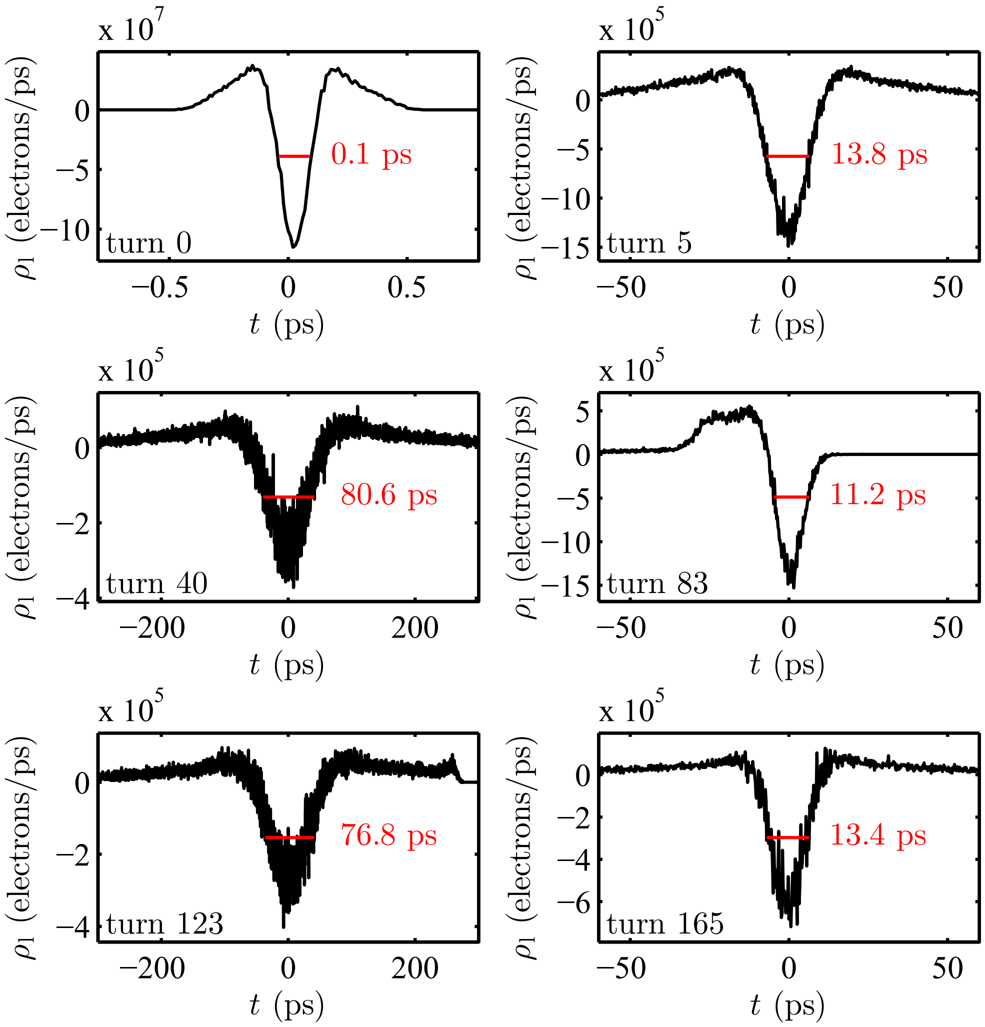

Figure 3.3.: Longitudinal electron density modulation (difference histogram) for the same turns as shown in Fig. 3.2. Note the different scales.

Figure 3.3 shows the difference histograms for the same turns as in Fig. 3.2. The typical dip with corresponding density maxima (see Fig. 2.14) can be seen with a width increasing from turn 0 to turn 40. Here, the broadening of the density maxima is caused by the spread in energy modulation leading to an extended range of path length differences, while the broadening of the dip is mainly caused by the natural energy spread of all electrons in the bunch, which slowly smear out and fill up the dip (see Ch. 5.2.3 for details).

Corresponding to the evolution of the density modulation, the form factors (Fig. 3.4, squared Fourier transform of the difference histogram) are shifted to lower frequencies. However, after half a synchrotron oscillation period, the (already partially washed out) structure has rotated in phase space by 180°, the dip becomes more narrow (Fig. 3.3, turn 83), and the form factor is shifted to higher frequencies again (Fig. 3.4, turn 83). This is reproduced after another half synchrotron oscillation period (turn 165). The strong asymmetry of the turn-83 density is caused by the asymmetry of the RF potential. As can be seen in Fig. 3.2 for turn 83, the synchrotron motion of the particles with initial energy loss (blue) was slowed down more than the motion of the particles

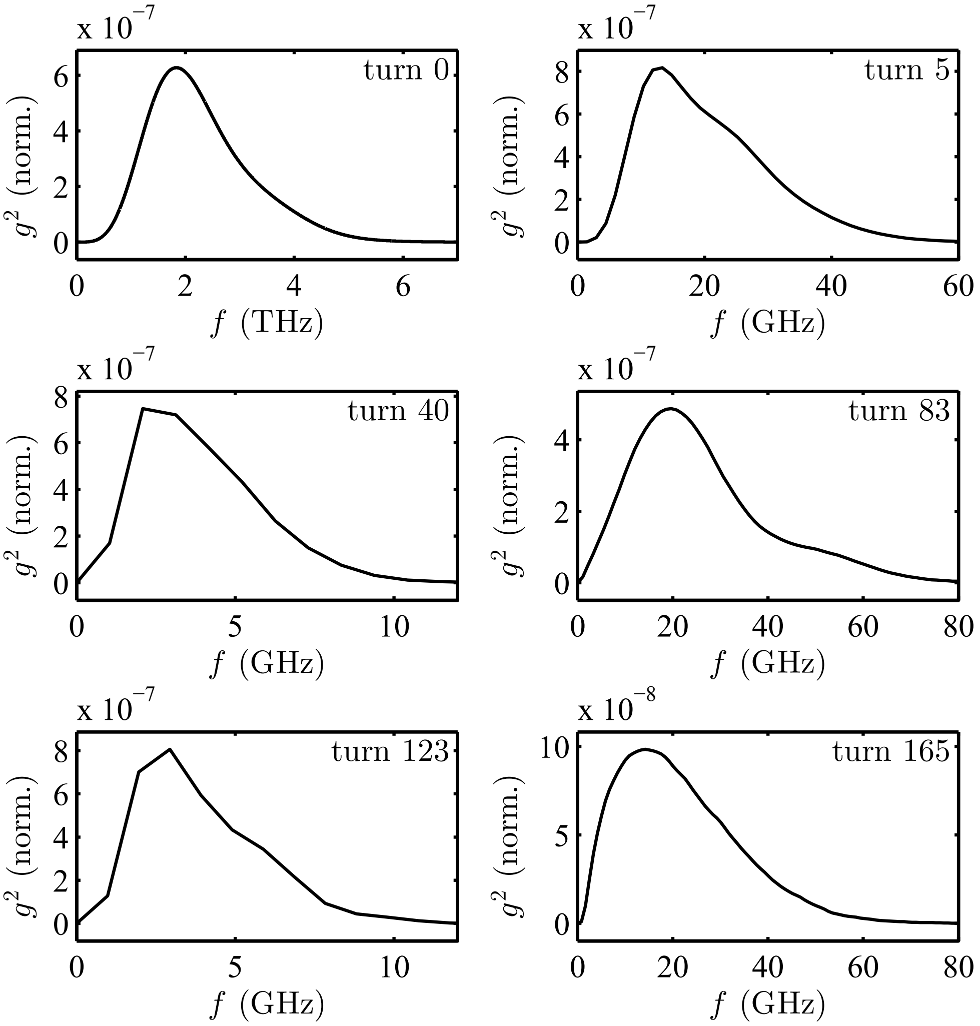

Figure 3.4.: Form factor $g^2(f) \propto \mathrm{FT}[\rho_\mathrm{l}(t)]^2$ for the same turns as shown in Figs. 3.2 and 3.3. Only the squared Fourier transform of the difference histogram is shown, while the normalization was performed using the squared Fourier transform of the total electron density (see text for details). Note the different scales.

with initial energy gain (red). Only after a complete synchrotron oscillation period (turn 165), all off-energy particles have experienced both sides of the asymmetric non-linear potential, leading again to a symmetric phase space distribution and histogram.

The normalization of $g^2(f)$ was performed using the Fourier transform $g^2_\mathrm{tot}(f)$ of the total histogram

$$\rho_\mathrm{l,tot}(t) = \rho_\mathrm{l}(t) + \rho_\mathrm{l,bunch}(t) \tag{3.1}$$

given by the difference histogram $\rho_\mathrm{l}(t)$ added to a properly scaled Gaussian bunch profile $\rho_\mathrm{l,bunch}(t)$. Now, the condition $g^2_\mathrm{tot}(f) = 1$ can be used, as all electrons radiate coherently for extremely low frequencies (see Eq. 2.107).

Using $g^2_\mathrm{tot}(f)$ and Eq. 2.107, the emission spectrum is shown for turn 0 to turn 10 in Fig. 3.5. Like the maximum of the form factor, the peak emission frequency decreases

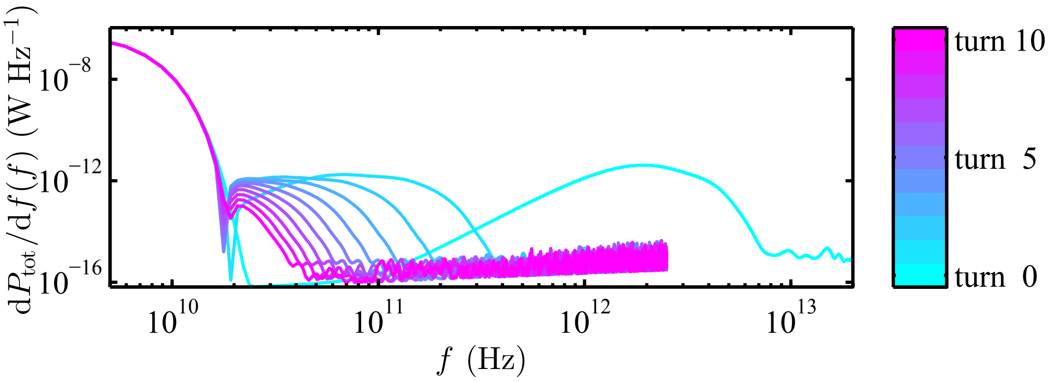

Figure 3.5.: Simulated spectra of laser-induced THz radiation for turn 0 to turn 10 (color-coded).

from turn to turn. The strong coherent emission below 20 GHz is caused by the finite bunch length and is not transmitted through the beamline.

3.2.2. Example 2: Chirped-Pulse Beating

As a second example, the results from a CPB simulation shall be presented. Here, the default setup (Tab. A.9) was modified to include a chirped pulse length of 11 ps FWHM (corresponding to a chirp parameter of $b = 3.15$ ps^{-2}) and a modulation frequency of 1 THz (corresponding to a Michelson-interferometer delay of $\tau = 0.997$ ps). Only the turn-0 evolution was simulated and the number of particles was increased to $2 \cdot 10^6$.

Due to the limited laser pulse energy of 8 mJ but increased pulse length of 11 ps FWHM, the peak electrical field is strongly reduced leading to a smaller energy mod-

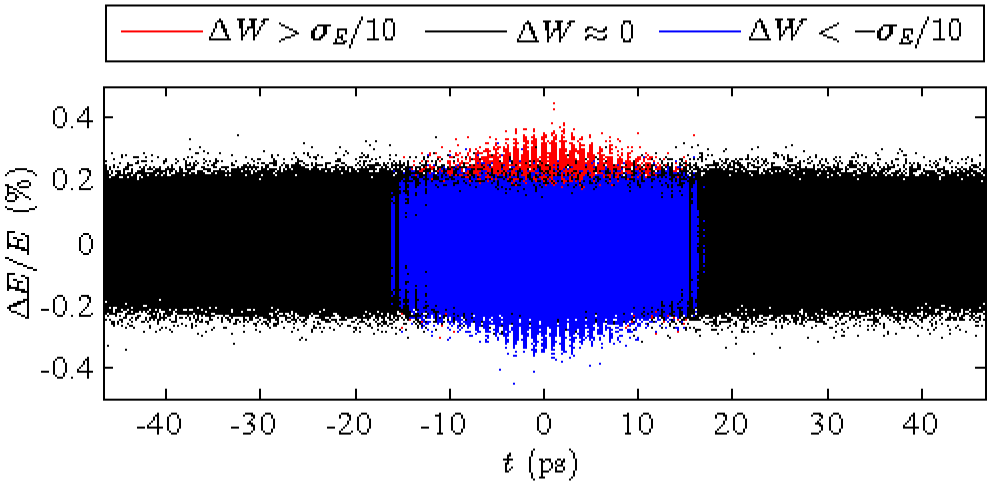

Figure 3.6.: Longitudinal phase space distribution of the generated particle slice after simulation of the energy modulation. As particles with negative energy deviation (blue) are plotted last, black and red dots are partially obscured due to the high number of macro-particles.

ulation amplitude (Fig. 3.6). The stripes no longer represent the sinusoidal energy modulation as in Fig. 3.1 (which is on a much shorter scale), but instead show the periodic energy modulation due to the intensity modulation of the laser pulse.

Caused by the reduced energy modulation amplitude, the path length differences are smaller as compared to turn 0 of the multi-turn simulation discussed above and the longitudinal density histogram is dominated by noise. Nevertheless, a Fourier transform reveals a form factor with a strong and narrow line at 1 THz with a bandwidth of about 58 GHz FWHM (Fig. 3.7, black). Compared to the bandwidth of about 1.8 THz FWHM for the turn-0 form factor based on an interaction with a short laser pulse (Fig. 3.4), the bandwidth is reduced by a factor of 30, while the peak power is increased by a factor of about 10. This makes the CPB principle attractive for THz radiation users who do not require ultrashort pulses but instead prefer a narrow spectrum and/or high spectral peak intensity at a still reasonably short pulse length of several picoseconds.

Using Eq. 2.24 (a quadratic chirp has not been included in this simulation run), a theoretical bandwidth of $\Delta f_{\mathrm{mod}} = 80.2$ GHz FWHM for the intensity modulation of the laser pulse is obtained. Assuming a linear dependence between laser intensity modulation and electron density modulation, the form factor $g^2(f)$ given by the *squared* Fourier transform of the density modulation introduces a factor of $1/\sqrt{2}$ in spectral width. Thus, a theoretical THz bandwidth of $\Delta f_{\mathrm{THz}} = \Delta f_{\mathrm{mod}}/\sqrt{2} = 56.7$ GHz is obtained, which is in good agreement with the numerical simulation result of (58.3 ± 0.4) GHz[1] (Fig. 3.7, black).

Figure 3.7 also shows the form factor resulting from a second simulation with a quadratic chirp $\alpha = 142\ \mathrm{ps}^{-3}$, which has been calculated based on the geometrical parameters of the amplifier-internal compressor at DELTA and assuming $\alpha = 0$ for shortest pulses. In Ch. 2.1.2, an increase of the intensity modulation bandwidth from 80.2 GHz to 163.9 GHz has been predicted taking into account this value of a quadratic chirp (Fig. 2.6). Including the factor of $1/\sqrt{2}$, a theoretical THz bandwidth of $163.9/\sqrt{2}$ GHz $= 115.9$ GHz is obtained, again in good agreement with the numerical result of (113.3 ± 1.9) GHz[1] (Fig. 3.7, red).

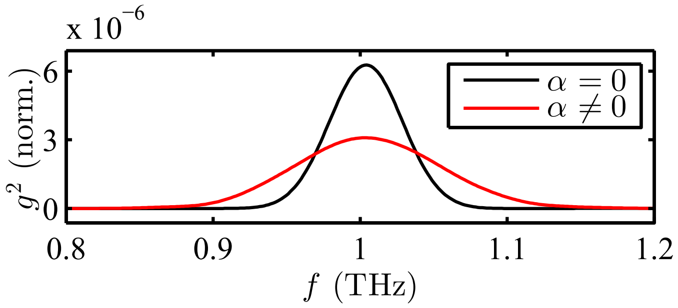

Figure 3.7.: Form factor $g^2(f) \propto \mathrm{FT}[\rho_l(t)]^2$ for the CPB simulations with and without a quadratic laser pulse chirp α.

---

[1] Mean and standard deviation of four independent simulation runs with unchanged parameters but new random particle distributions.

4. Laser-Induced THz Radiation at DELTA

The general layout and components of the entire short-pulse facility, including the laser system, laser beamline, and undulator section, have been described in Ch. 1.3.1. This chapter will give a more detailed overview of the THz-specific setup.

4.1. Setup and Properties of the THz Beamline

The dedicated THz beamline 'BL5a' at DELTA was designed, constructed, and commissioned in 2010 and 2011 as an integral part of the DELTA short-pulse facility in the course of two diploma theses [12, 13]. Based on a turn-0 simulation of the laser-induced THz generation (Ch. 3.1), the optimum position for the source point of the THz beamline was found to be inside the third dipole magnet following the undulator U250 (see Fig. 1.8).

A sketch of the beamline (as of 2011) is shown in Fig. 4.1. The vacuum chamber with beam port (1) is placed in the dipole magnet used as the radiation source (blue, semitransparent). The beam port, a round tube with an inner diameter of 38 mm, extends tangentially outwards to the first mirror chamber (M0). The chamber houses a plane gold-coated water-cooled copper mirror, which absorbs most of

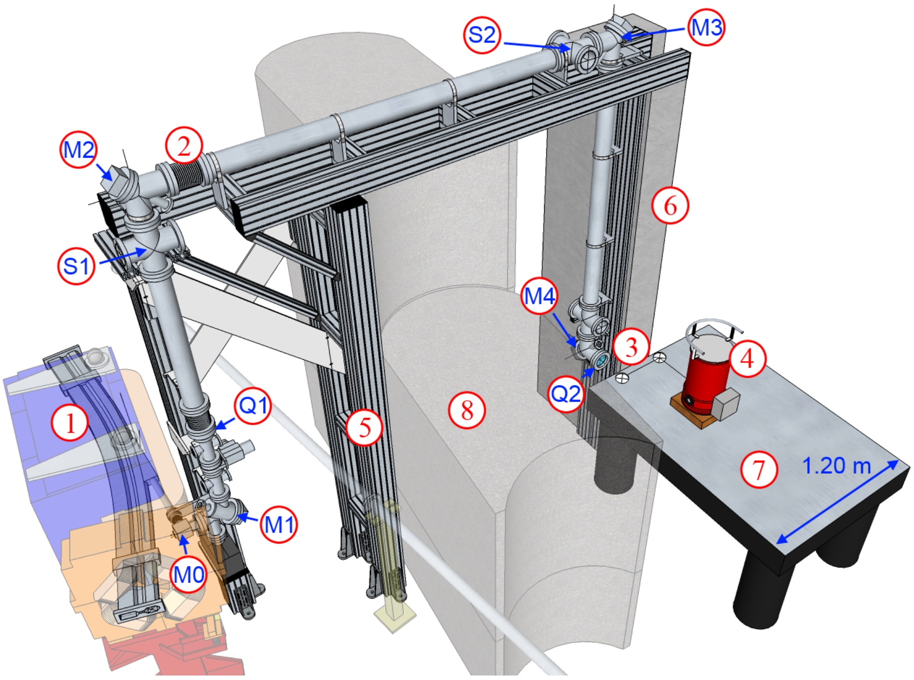

Figure 4.1.: Sketch of the DELTA THz beamline as of 2011 (see text for details).

the high-frequency spectrum of the synchrotron radiation and only reflects UV light and longer wavelengths. Up to a first z-cut quartz window (Q1), which separates the storage-ring UHV from the pre- to high vacuum conditions in the rest of the beamline, the inner diameter of the beamline tubing is 63 mm. The rest of the beamline (2) is based on 100-mm tubing, which partially features a 10-mm layer of an aluminium-foam absorber. Four remotely adjustable in-vacuum mirrors (M1–M4) based on uncoated aluminium machined into toroidal shape (Ch. 2.6.2) provide guidance and focusing for the THz beam. For alignment using the visible spectrum of the synchrotron radiation, two screens (S1, S2) equipped with cameras can be moved into the beam path, and the mirror chambers are equipped with additional cameras. A second z-cut quartz window (Q2, view diameter 89 mm) is followed by a short in-air section (3) with two additional aluminium mirrors leading to the InSb bolometer (4) used as a detector. The beamline is supported by a structure consisting of sand-filled aluminium profiles (5), a polymer-concrete column (6), and an optical table (7). A direct horizontal penetration of the radiation shielding wall (8) was already blocked by the adjacent BL5.

The following sections will describe modifications and upgrades designed and installed as part of this thesis, including a description of the complete beamline optics.

4.1.1. Extension of the Vacuum Beamline

In mid 2012, a vacuum FTIR spectrometer was installed at the THz beamline (Ch. 4.3). Due to the strong absorption lines caused by water vapor in the air (Ch. 1.1.1), the vacuum beamline was extended in the beginning of 2013 to provide an uninterrupted evacuated beam path from source to spectrometer.

A sketch of the modifications is shown in Fig. 4.2. The InSb bolometer (1) was moved to the front of the table. The FTIR spectrometer (2) was also placed at the front of the table, allowing for easy access of the sample compartment (light blue section with handle). The z-cut quartz window Q2 was removed from mirror chamber M4, and the vacuum beamline was extended to the FTIR spectrometer (2) using three new mirror chambers (M5–M7).

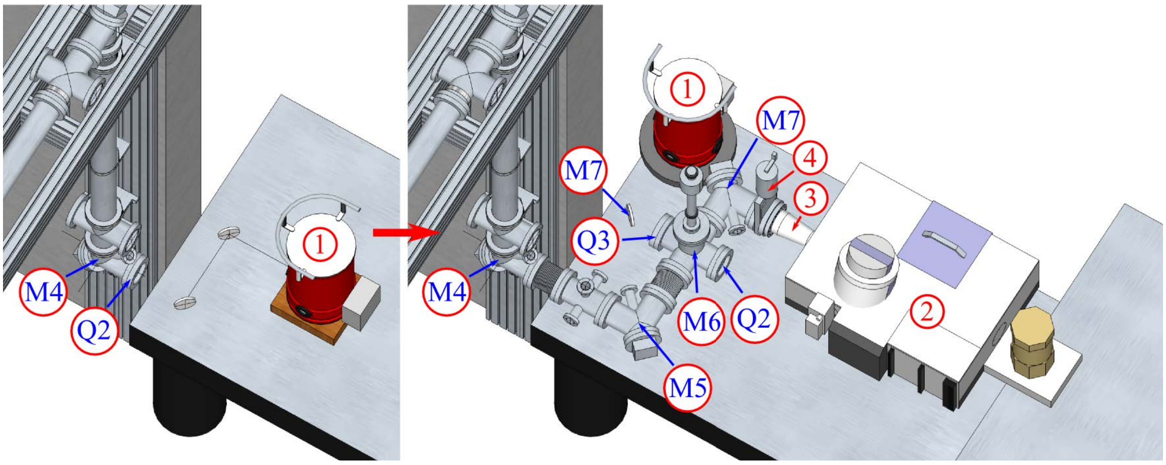

Figure 4.2.: Sketch of the existing BL5a setup (left) and the modifications installed in the beginning of 2013 (right, see text for details).

The adjustable mounts for M5 and M7 are similar to those of the original beamline existing since 2011 [13]. The four-way cross houses a plane mirror (M6) attached to a manual rotary-/linear-motion feedthrough. When M6 is retracted, radiation can pass through to the M7 chamber and the spectrometer. When M6 is lowered into the beam path, it directs the THz radiation either to the InSb bolometer (through the 63-mm z-cut quartz window Q3), or to the opposite direction (through the 89-mm window Q2) opening up a third beam path.

A reducer (3) was designed as an adapter from the CF flanges with copper gaskets used throughout the beamline to the proprietary flanges of the FTIR spectrometer (2) with elastomer gaskets. Beamline and spectrometer vacuum can be separated by a manual gate valve (4), e.g., for venting the spectrometer. The valve features a 43-mm viewport placed in the gate allowing visible synchrotron light to pass through in closed position. This way, the spectrometer can be vented and uncovered to adjust the beam path inside without having to vent the THz beamline.

The extended vacuum beamline includes two flexible bellows for individual alignment of the mirror chambers and all vacuum components are fixed to the optical table via adjustable mounts and standard optical posts/pedestals with fork clamps.

4.1.2. Modification of the THz Optics

The optics layout of the extended beamline is shown in Fig. 4.3; parameters are listed in Tab. 4.1. The positions and focal lengths of the existing in-vacuum mirrors M1–M4 remain unchanged. Both previous in-air mirrors (see Fig. 4.2, left) were removed. The positions and focal lengths of the new final two focusing mirrors (Fig. 4.2, right: M5 and M7; M6 is a plane mirror) were chosen to meet the following criteria:

- A third Gaussian telescope must be formed to achieve a frequency-independent final focus.
- The optics must match the mechanical design of the beamline extension.
- The final focus must be 26 mm in front of the FTIR spectrometer entrance to match its internal optics (see Ch. 4.3), or inside the InSb bolometer cryostat when M6 is lowered into the beam path.

Calculations were performed using a numerical code based on the equations from Chs. 2.1.3 (matrix formalism for the complex beam parameter) and 2.6.1 (initial waist based on beamline aperture).

Table 4.1.: Parameters of the current BL5a optics (all values in mm).

	M1	**M2**	**M3**	**M4**	**M5**	**M7**	**final focus**
distance z to source point	1422.5	3559.5	6304.5	8590.5	9230.5	9930.5	10329.5
distance to previous element	1422.5	2137.0	2745.0	2286.0	640.0	700.0	400.0
focal length f	894.5	1242.5	1931.2	354.8	340.0	360.0	-
beam radius at 1 THz	24.2	8.5	31.0	21.7	19.8	24.4	1.6

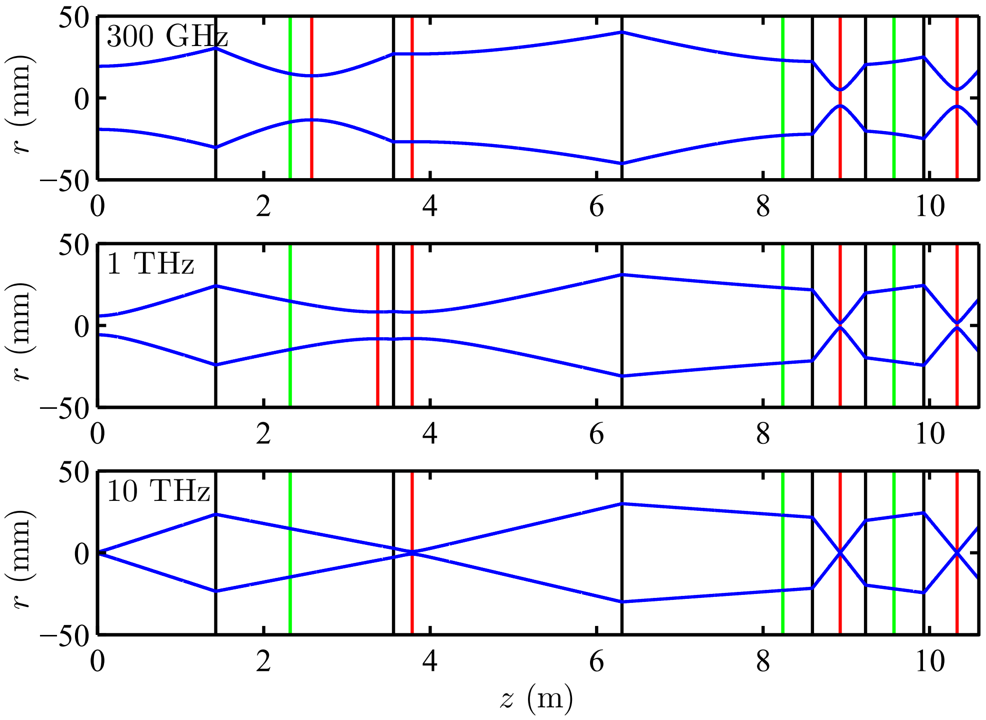

Figure 4.3.: Extended optics of BL5a showing the beam diameter (blue) for three different emission frequencies, the mirror positions (black), the focal lengths (distance between mirrors and green lines), and the waist positions (red).

4.1.3. General Improvements

The InSb bolometer used as the standard THz detector at DELTA (Ch. 4.2) is cooled with liquid nitrogen (LN2) and liquid helium (LHe). While the inner LHe reservoir in the detector cryostat has to be refilled only once every ten days, the LN2 in the outer shell/reservoir completely evaporates within 24 to 30 hours, requiring a manual LN2 refill once per day. For ease of operation, a system for the automated transfer of LN2 from a storage Dewar vessel to the cryostat was designed and installed in the beginning of 2012.

As is the case for several other beamlines at DELTA, the THz beamline BL5a was originally designed without a surrounding laboratory hutch. With the installation of the FTIR spectrometer and the future plan for laser-pump THz-probe experiments, new requirements have emerged:

- The FTIR spectrometer demands a maximum ambient temperature of 35°C with a temperature stability of ±1°C during a measurement and ±2°C per day.
- For opening the spectrometer (to adjust the beam path, change samples, etc.), a clean environment is required.
- Laser safety must be ensured.

To meet these demands, an air-conditioned hutch was designed and constructed at BL5a in August 2013.

4.2. Detectors for Time-Resolved Measurements

The general working principles of different THz detectors have been discussed in Ch. 1.1.4. In the following sections, the properties, positioning, and readout setup of the detectors employed at DELTA shall be presented.

4.2.1. The InSb Bolometer

The InSb bolometer is a hot-electron bolometer (HEB) based on a $5 \cdot 5$ mm^2 InSb detector chip on a quartz substrate (Fig. 4.4, left). The detector is mounted below the bottom plate of a LHe reservoir (4.2 K), which is surrounded by a 44-K helium gas shield and a 77-K shield connected to an LN2 reservoir (Fig. 4.4, center). The radiation enters through a high-density polyethylene (HDPE) window and additional 1 THz low-pass filters, which are embedded in the temperature shields to block radiation at MIR or higher frequencies, and is coupled to the detector chip using a Winston cone (Fig. 4.4, right). Attached to the cryostat are a bias source and an ultra-low noise amplifier switchable between a gain of 40 dB or 60 dB. Instead of a power socket, internal batteries can be used for low-noise operation. The bolometer offers a sensitivity range of 60 GHz to 500 GHz FWHM, an NEP of about $5 \cdot 10^{-13}$ W/$\sqrt{\mathrm{Hz}}$, and a temporal bandwidth of 1 MHz FWHM. Further parameters of the detector are specified in Tab. A.3.

The InSb bolometer has been permanently installed at the THz beamline since 2011 and still is the standard detector used for finding and optimizing the laser-electron overlap and for intensity-dependent measurements. However, due to the DELTA revolution frequency of 2.6 MHz, it is not fast enough to resolve turn-by-turn THz signals.

The bolometer is positioned in the final focus of the THz beamline optics (Fig. 4.3) following two z-cut quartz windows and a short in-air section (Fig. 4.2). Unless indicated otherwise during discussion of the corresponding results (Ch. 5), the output from the pre-amplifier is connected to a 1-GHz digital storage oscilloscope (DSO) via coaxial cable with BNC connectors. The oscilloscope is triggered on the rising edge of a potential-free 1-kHz signal, which is generated by a battery-driven photodiode looking at stray light within the Ti:sapphire laser amplifier in order to suppress noise

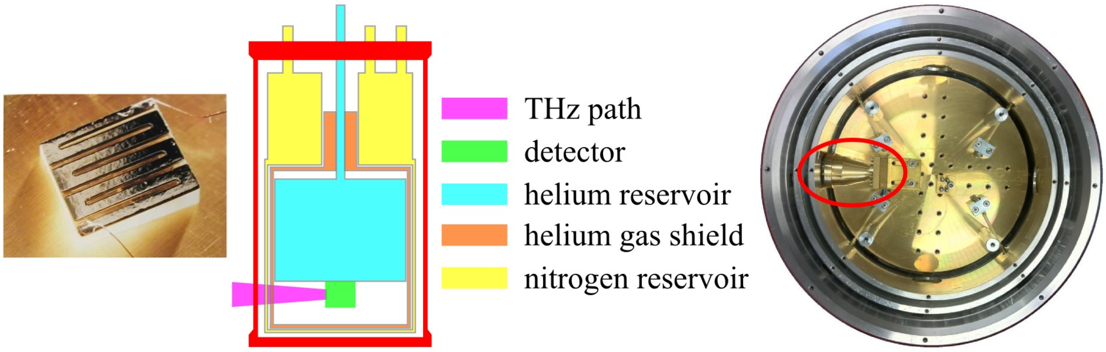

Figure 4.4.: InSb detector chip (left, source: [127]), sketch of the detector cryostat (center), and photograph of the LHe-reservoir bottom plate from below (right) showing the detector mounted behind a Winston cone (red circle). Courtesy of QMC Instruments Ltd., Cardiff, UK.

based on different electrical ground levels (Ch. 5.1.1). An averaging over five successive InSb signal traces is usually set in the oscilloscope software to partially suppress shot-to-shot fluctuations of the laser intensity or laser-electron overlap as well as further electronic noise. The amplitude of the averaged signal trace is calculated using the peak-to-peak function of the oscilloscope software. This adds a noise floor of the order of the high-frequency baseline noise, but effectively suppresses slow shifts of the entire baseline, e.g., due to noise from the power supplies at 50 Hz and harmonics thereof. The peak-to-peak values are read out by a Visual Basic script and stored in an EPICS record. A self-written MATLAB tool is then used to record the THz amplitude data as well as several parameters of the storage ring and the short-pulse facility, e.g., during a slow variation of the longitudinal laser-electron overlap. To exclude further sources of electronic noise, a local Ethernet-to-optical-fiber converter is employed for the network connection of the oscilloscope. Since the turn-0 THz spectrum is above the sensitivity range of the detector, the extracted peak-to-peak data is determined by the turn-1 radiation intensity (see Ch. 5.1.1 for details).

4.2.2. The NbN Bolometer

In 2012, an ultrafast NbN HEB [36, 37] was employed at DELTA during a four-day joint measurement with the ANKA THz group from KIT to study the turn-by-turn THz signals. It was developed in a cooperation between the Institute of Micro- and Nanoelectronic Systems (IMS) at KIT and the German Aerospace Center, Berlin, and offers a sensitivity range of 160 GHz to 3 THz, an NEP of $6 \cdot 10^{-9}$ W/$\sqrt{\text{Hz}}$, and a response time of less than 160 ps. The detector chip is embedded in a log-spiral antenna placed behind an elliptical silicon lens, and is mounted in a LHe cryostat. Further parameters are given in Tab. A.4.

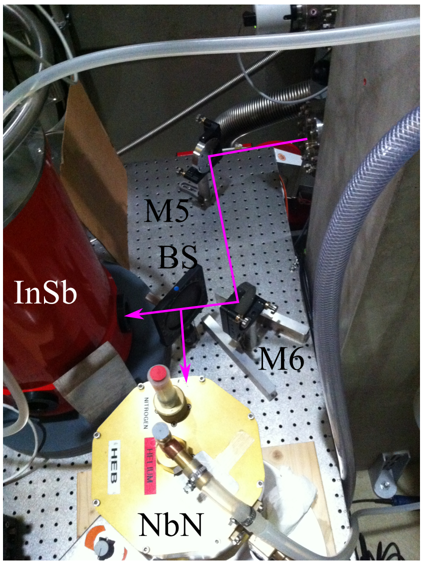

Figure 4.5.: Temporary setup of the NbN bolometer (bottom) near the InSb bolometer (left). A wire-grid polarizer (BS) was used as a variable beam splitter behind the two in-air mirrors M5 and M6.

The NbN bolometer was placed next to the InSb bolometer (old setup before beamline extension; Fig. 4.2 left) and a variable part of the THz radiation was sent to the NbN bolometer using a wire-grid polarizer on a rotary mount (Fig. 4.5). The output of the attached pre-amplifier was connected to a 4-GHz DSO, which was used to record single traces with variable averaging settings (Ch. 5). The same potential-free photodiode trigger as for the InSb bolometer was employed.

4.2.3. The YBCO Detector

The YBCO detector was developed at the Institute of Micro- and Nanoelectronic Systems (IMS) at KIT [38–40] and offers an ultrafast response time of less than 17 ps. A prototype was employed at DELTA during a test measurement in June 2013, and a nearly identical detector has been permanently installed since 2014.

The detector chip is based on a log-spiral antenna and co-planar readout line patterned into a gold-covered multilayer structure on a sapphire substrate. A µm-sized 'micro-bridge' in the antenna center, where only the gold film is removed, acts as the actual YBCO detector element (Fig. 4.6, right). The rear side of the substrate is glued to a silicon lens (thus, radiation passes through the substrate), which is mounted in a copper detector block. The gold readout line on the chip is bonded to a planar readout line in the detector block (Fig. 4.6, center). The detector block is mounted in a LN2 cryostat (Fig. 4.6, left), and coaxial connectors, semi-rigid cables, and feedthroughs (specified for transmission up to 65 GHz) are used to provide a readout port on top of the cryostat. Radiation enters the cryostat through a polyethylene window.

For the system permanently installed at DELTA, the detector block mounted in an LN2 cryostat was manufactured by the IMS together with a battery-powered bias source. Based on suggestions from the IMS, room temperature read out electronics including a 65-GHz bias tee, a 55-GHz 22-dB amplifier, and 67-GHz flexible coaxial cables were acquired. The prototype detection system employed in 2013 was based on similar components; however, the bias source allowed for the variation of more parameters. Figure 4.7 shows a sketch of the complete detection system. Further parameters are given in Tabs. A.5 and A.6. Due to the high sensitivity, measurements can also be performed connecting an oscilloscope directly to the bias tee without the

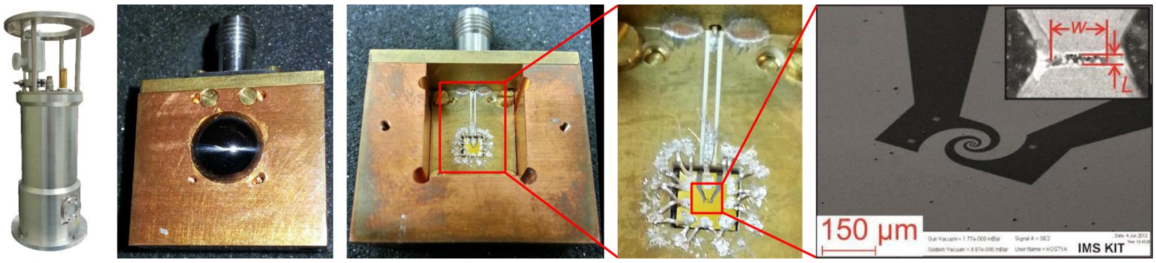

Figure 4.6.: From left to right: Cryostat of the YBCO detector, copper detector block (front) with silicon lens and coaxial connector, detector block (back, open), zoom to detector chip and indium bonds, and scanning electron microscope pictures (source: [82]) of the gold antenna (light gray) on the sapphire substrate (dark gray) and the YBCO micro-bridge (inset). Courtesy of the IMS at KIT, Karlsruhe, Germany.

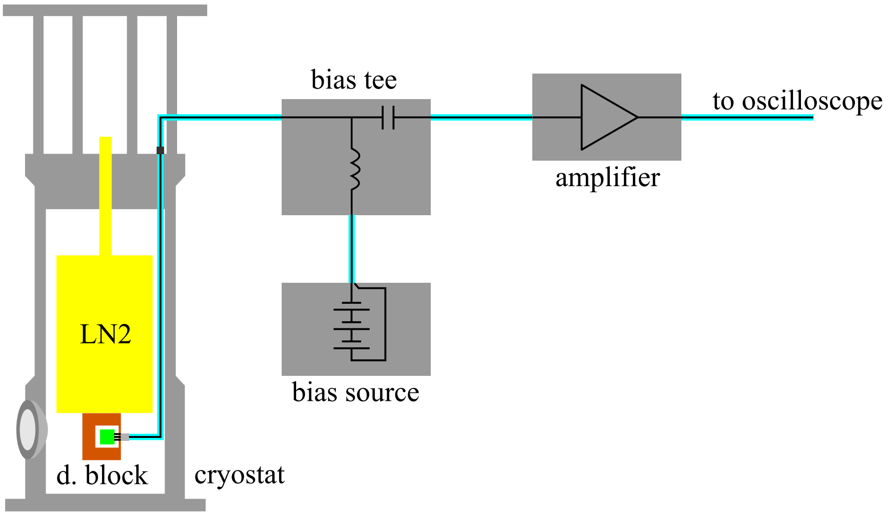

Figure 4.7.: Sketch of the YBCO detection system (see text for details).

amplifier. The bias-source output port can be shorted, allowing the zero-bias response (see Ch. 1.1.4) to be observed.

Due to the LN2-only cryostat, the YBCO detector offers a much shorter set-up time and low-effort maintenance as compared to the InSb or NbN bolometers. Also, with a dynamic range of about 30 db and a variable bias source, measurements can be performed over a huge range of signal intensities. However, as the connections to the µm-sized detection bridge are directly accessible on the cryostat without any integrated protection circuit or pre-amplifier (as it is the case for the InSb or NbN bolometers), a

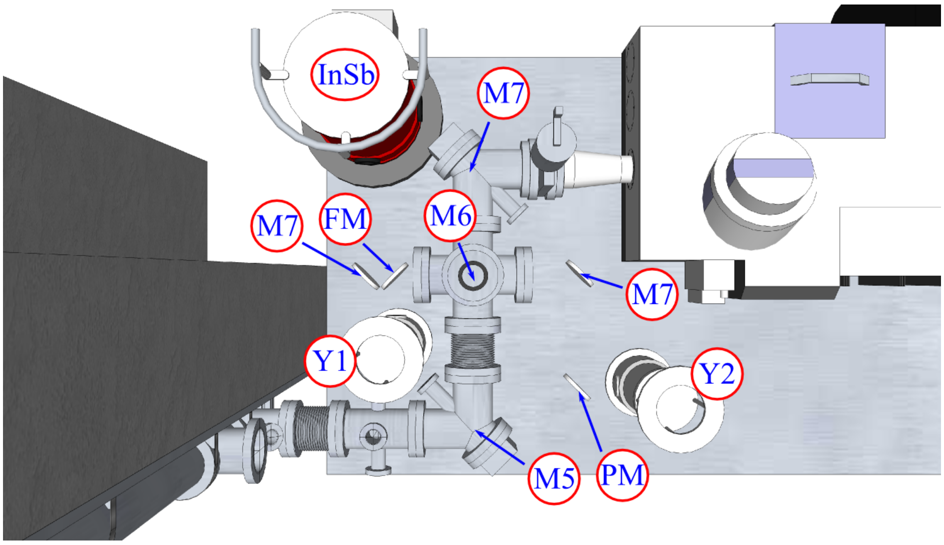

Figure 4.8.: Temporary setup of the prototype YBCO detector (Y1) behind a focusing mirror on a flip mount (FM) and position of the permanently installed YBCO detector (Y2) at the third beam path behind M7 and an additional plane mirror (PM). See Fig. 4.2 for a description of the remaining components.

very careful handling and high electrostatic discharge (ESD) protection standards are essential.

The positioning of the detector for the test measurement in 2013 and of the permanently installed detector is shown in Fig. 4.8. The data presented in Ch. 5 was recorded using different DSOs connected via a 0.5-m 67-GHz cable. A 6-GHz DSO is permanently available at DELTA. During the test measurement in 2013, a 32-GHz DSO with 80 GSa/s provided by KIT-IMS was employed. In September 2014, YBCO measurements were performed using a 63-GHz DSO with 160 GSa/s (Keysight Z-Series DSA-Z 634A) which was kindly provided by Keysight Technologies Deutschland GmbH.

4.2.4. The Schottky Diode

A commercial zero-bias Schottky-barrier diode (SBD) [41, 42, 128] provided by the ANKA THz group was employed at DELTA in 2015. The Schottky diode is embedded into a planar log-spiral antenna and placed behind a silicon lens. Limited only by the built-in amplifier, a 4-GHz electrical bandwidth, an NEP of $8.5 \cdot 10^{-10}$ W/$\sqrt{\text{Hz}}$ (at 1 THz), and a sensitivity range of 50 to 1200 GHz are provided. Further parameters are given in Tab. A.7.

During the measurements at DELTA, the SBD was positioned in the final focus of the third beam port (Fig. 4.8, Y2) instead of the YBCO detector. The signal was read out using a 6-GHz DSO triggered on the potential-free photodiode signal (see above).

Due to its high speed, compact design (about $7 \cdot 6 \cdot 4$ cm^3), and room-temperature operation, the Schottky diode is an easy to handle and maintenance-free detector. A permanent installation at DELTA is planned for the autumn of 2015. Following a test phase, the SBD might replace the InSb bolometer as the standard THz detector for every-day operation when a higher sensitivity or increased spectral range is not required.

4.3. The FTIR Spectrometer

A central part of this thesis was the installation and commissioning of a THz spectrometer at BL5a.

An FTIR-type spectrometer (Ch. 2.7) was chosen due to several advantages of this technique in the FIR regime as compared to diffractive or dispersive spectrometers:

- Signals from all frequencies reach a single detector simultaneously leading to an increased signal-to-noise ratio and/or reduced acquisition times (multiplex advantage). In a diffractive setup, the signal is split into a fan of frequencies with less intensity per frequency range.
- FTIR spectrometers do not require an entrance or exit slit, which determine the resolution of a diffractive spectrometer. This is particularly important due to the rather large beam waists in the THz regime (throughput advantage).
- FTIR spectrometers usually employ a helium-neon (HeNe) laser with a well-defined, stable, and narrow emission spectrum as a reference to measure the path length difference of the interferometer. This allows for a highly accurate calibration of every single interferogram and spectrum.

In principle, there are two types of FTIR spectrometers; one is based on a classical Michelson interferometer with an optical beam splitter, the other is based on a polarizing wire grid used as a beam splitter and roof-top mirrors used as retroreflectors – a so-called Martin-Puplett interferometer (MPI) [129].

After checking several alternatives, the Michelson-type ‘VERTEX 80v’ from Bruker Optics was selected. As will be shown in Ch. 5, it is well suited for the study of the turn-0 spectrum and future user experiments, but cannot be employed for the turn-1 and higher-turn signals due to its low-frequency limit at about 0.5 to 1 THz. For this purpose, an MPI-type spectrometer is currently under construction [83].

4.3.1. Description of the Spectrometer

The VERTEX 80v spectrometer is based on a single-piece machined aluminium body of about 850 x 700 x 300 mm^3 with segmented top covers (Fig. 4.9). THz radiation (magenta) either enters from the beamline (right) and passes over a vertical periscope, or is emitted by an internal MIR Globar (1). After optional filter and aperture wheels (2), the beam enters the interferometer block below the automated beam-splitter exchanger (3). Alternatively, radiation is coupled in from an external water-cooled Hg arc lamp (top). The beam splitter (green) is slightly tilted. Thus, half of the radiation is reflected to a fixed mirror in the back of the spectrometer, and half of the radiation passes over a 90° mirror to the movable reflector arm on an air bearing (4). After recombination, the radiation passes the sample compartment (5) with shutters for separate venting and evacuation, and with a central in-focus sample holder. The radiation is detected either by an MIR DLaTGS detector (6), an FIR DLaTGS detector (7, not installed when this photograph was taken), or a LHe-cooled Si bolometer (left). The control and readout electronics, vacuum control valves, and a HeNe reference laser are located in the back of the spectrometer (top). An external dry Roots pump allows a pressure of 2 to 3 mbar to be reached during operation (the air bearing presents a small leak in the vacuum system).

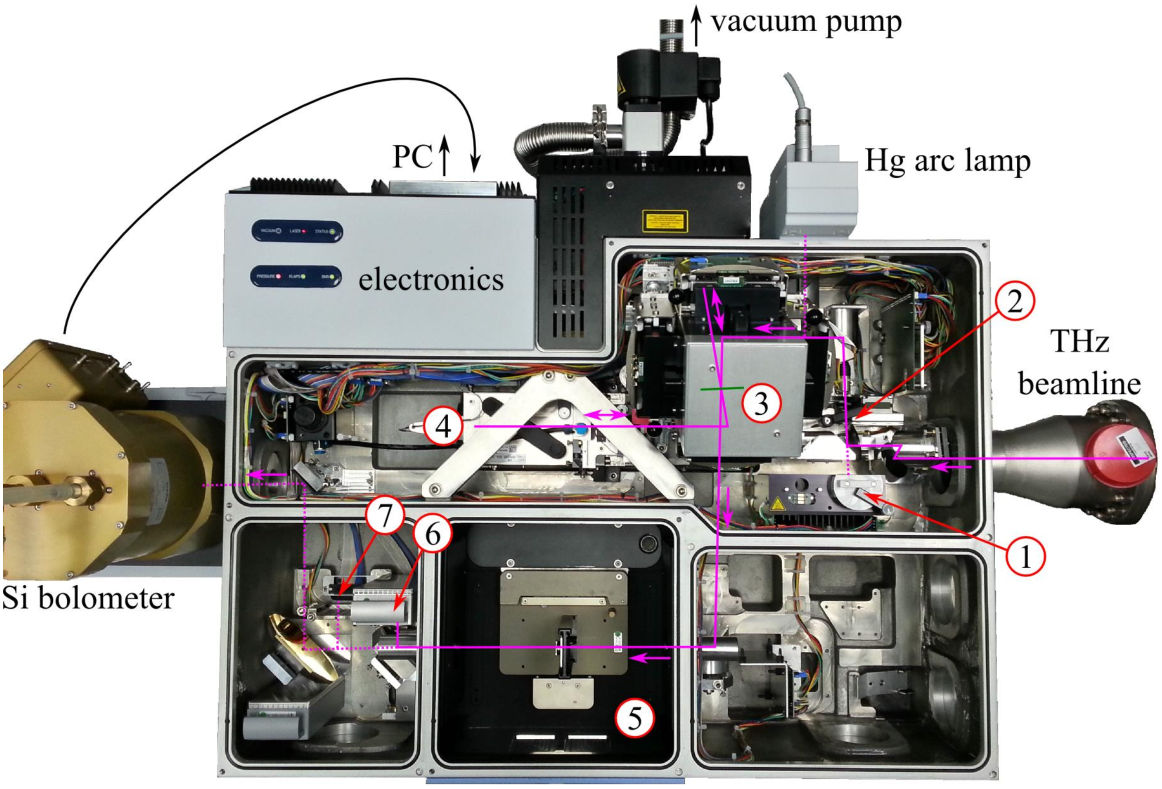

Figure 4.9.: Photograph of the VERTEX 80v (cover segments removed, see text for details). Courtesy of Bruker Optik GmbH, Ettlingen, Germany.

All components (wheels, mirrors on linear stages to switch between sources and detectors, the beam-splitter exchanger, etc.) are motorized and can be controlled via the spectroscopy software OPUS on an external PC. The software is also used to perform zero-filling, truncation, a phase correction and the Fourier transform (Ch. 2.7).

A full set of parameters can be found in Tab. A.8.

4.3.2. Installation of the Spectrometer Accessories and Extensions

After final positioning of the spectrometer and connection to the THz beamline, several accessories and extensions were installed to reach a fully operational status.

Four solenoid valves are integrated into the spectrometer back-plane to separately connect the sample compartment or the rest of the spectrometer either to the vacuum pump (via flexible steel tubing) or the ambient air for venting. The spectrometer is connected to an uninterruptible power supply (battery buffer), which would keep the valves to the pump open even in case of a power failure and the following shutdown and venting of the pump. Therefore, an external solenoid valve was added between the spectrometer and vacuum pump, which closes immediately in case of a power failure to protect the vacuum inside the spectrometer.

The manual valve between beamline and spectrometer (Fig. 4.2, 4) has to be opened during measurements, thereby connecting the beamline vacuum (usually 10^{-6} mbar) to the spectrometer vacuum (2 to 3 mbar due to the air bearing). Therefore, the air bearing is only operated with dry nitrogen gas in order to prevent contamination of the beamline with air. A manual valve was added in the nitrogen supply line to close off the air-bearing gas-inlet during idle time of the spectrometer, which prevents air from leaking in, e.g., when exchanging the gas cylinder.

For cooling the Hg arc lamp, a recirculating chiller was connected using flexible tubing. The lamp is switched manually at an external high-voltage power supply.

In order to transfer LHe to the Si bolometer, an adapter was designed which replicates the LHe reservoir neck of the InSb bolometer. This allows employing the same LHe transfer lines and connecting a helium gas return line. The helium return line in the BL5a hutch was extended to provide self-closing connectors for the Si bolometer and a storage Dewar vessel close to the spectrometer.

5. Experimental and Simulation Results

Unless indicated otherwise, all experimental results were obtained during single-bunch operation of the storage ring with a bunch revolution period of 384 ns. The laser-electron overlap occurs with the laser repetition period of 1 ms. Results obtained from numerical simulations with the computer code THzSMe (Ch. 3.2) will be shown in connection with corresponding experimental findings.

5.1. Characterization Measurements

5.1.1. Characterization of the Time-Resolving Detectors

The InSb Bolometer

Due to its high sensitivity (Tab. A.3), the InSb bolometer strongly responds to electrical noise. Systematic studies of the peak-to-peak noise level were performed, showing an increase from about 50 mV with nothing but the bolometer connected to the readout oscilloscope to about 200 to 500 mV when attaching electronic trigger lines or an Ethernet cable to the oscilloscope, or when providing a direct ground connection of the metallic bolometer cryostat. The noise is dominated by 50 Hz and accompanying odd harmonics resulting from different ground levels at the remote ends of the above-mentioned connections. As a consequence, a direct ground connection of the cryostat is avoided and the standard readout setup uses a potential-free trigger signal and an optical network connection (Ch. 4.2.1).

Significant influences were also observed during operation of the booster synchrotron and pulsed transfer-line components (sporadic voltage peaks), a nearby turbo pump system (noise at 1 kHz), and stepper motor drivers in a nearby electronics rack (noise at 21 kHz and accompanying harmonics), which are transmitted as electromagnetic waves or via the alternating current (AC) power connection of the oscilloscope. To reduce these influences, the turbo pump is usually operated at a reduced speed to avoid interference of its 1-kHz nominal speed with the repetition rate of the laser-induced signals. The stepper motor drivers are shut off during measurements requiring a high sensitivity and low noise level.

Figure 5.1 shows typical InSb oscilloscope traces[1] recorded during optimized laser-electron overlap conditions with a short laser pulse (about 40 fs FWHM). Due to the limited temporal detector bandwidth of 1 MHz, signals from single revolutions of the bunch cannot be clearly distinguished. Although similar storage ring and laser

---

[1] All traces from the InSb bolometer shown in this thesis were multiplied by -1, as the amplifier always provides a negative-polarity signal.

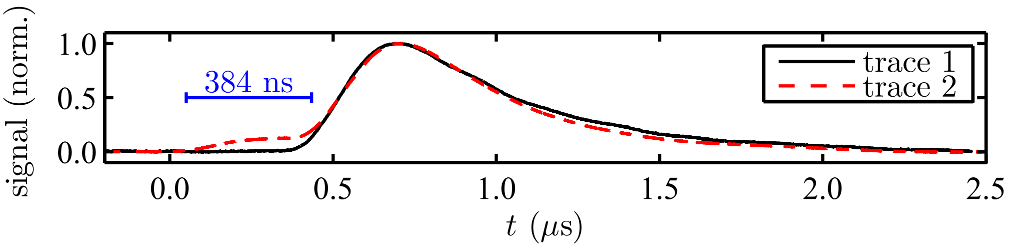

Figure 5.1.: Averaged InSb bolometer signals recorded during optimized laser-electron overlap conditions with a short laser pulse (about 40 fs FWHM) at two different dates but with similar storage ring and laser parameters.

parameters were set, the traces recorded at two different dates show a significant difference between 0 and 0.5 µs. Based on a consideration of signal propagation times, the strongest intensity at about 0.7 µs is found to be caused by the turn-1 radiation pulse, whereas the turn-0 pulse is not always detected (trace 1). This behavior is explained by the spectral sensitivity of the InSb bolometer only ranging up to about 500 GHz, which makes it almost blind for the turn-0 pulse with a maximum spectral intensity at about 2 THz (Fig. 3.4). The infrequent occurrence of a significant turn-0 response (trace 2) is assumed to be related to slight differences in laser pulse length, amplitude, overlap parameters, etc. and corresponding spectral shifts of the turn-0 THz pulse.

Depending on the intensity of the incoming THz radiation, the InSb bolometer shows a saturation effect [71]. For small intensities (Fig. 5.2 a, high-gain setting of the amplifier), the amplitude of the output voltage pulse changes, but the pulse shape remains similar to Fig. 5.1. For larger intensities resulting in output voltages of about 1 V and above (Fig. 5.2 b), a different behavior is observed. Deviations from expected signal amplitudes at other measurements, e.g., bunch profile studies (Ch. 5.3.1), showed

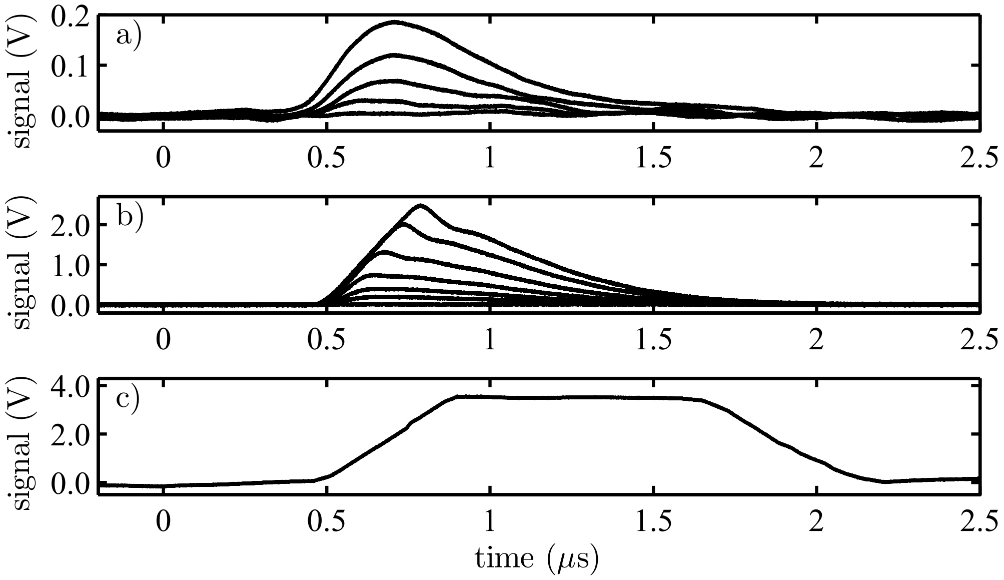

Figure 5.2.: Averaged laser-induced InSb bolometer signals recorded with the high-gain amplifier setting at different transverse laser-electron overlap conditions (see text for details). Note the different voltage scales.

that the amplitude of the output voltage is no longer linear to the incoming intensity in this regime. For even higher radiation intensities, the output signal is cut off by the pre-amplifier at about 3.5 V (Fig. 5.2 c). As a consequence, measurements depending on the linearity of the intensity scale should only be performed in the regime of output voltages below 1 V. For the low-gain setting of the amplifier similar limitations exist, but with the non-linear overshoot behavior appearing already at lower output voltages.

The NbN Bolometer and the Schottky Diode

Due to the limited operation time at DELTA in the course of one- or two-day joint measurements with groups from the Karlsruhe Institute of Technology (KIT), no detailed characterizations of the NbN bolometer or Schottky-barrier diode (SBD) were performed as part of this thesis, but are described in [36, 37, 41, 42, 128] and further references listed there.

The YBCO Detector

Studies of the different THz detection mechanisms in YBCO (Ch. 1.1.4) as well as detailed characterizations of improved YBCO detector systems are ongoing at the KIT-IMS [130]. Here, only results from a rough characterization of the YBCO detector permanently installed at DELTA shall be presented.

Figure 5.3 shows the pulse shape of the turn-0 and turn-2 signal recorded with a detector bias current of 7 mA (a) and with the bias source shorted (zero bias, b). With biasing, the turn-0 signal shows a strong bolometric component (slow exponential relaxation on a ns scale) which is not present in the turn-2 signal [76]. This is related to the different detection mechanisms in YBCO (Ch. 1.1.4). The turn-0 spectrum (Fig. 3.4) provides photon energies above the superconducting energy gap in the YBCO micro-bridge triggering a hot-electron bolometer (HEB) response. The turn-2 spectrum lies well below the superconducting energy gap, leaving only the vortex-based detection principle. Without biasing, the turn-0 signal no longer shows a bolometric component, which always requires a bias current. The remaining response is assumed to be caused by frequency components below the superconducting energy gap. The zero-bias turn-2

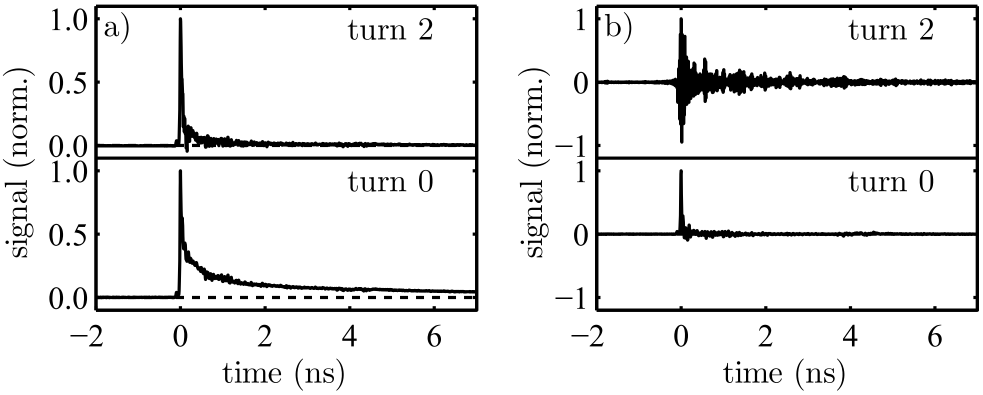

Figure 5.3.: Averaged laser-induced turn-0 and turn-2 YBCO detector signals with 7 mA bias current (a) and with zero bias (b). Each trace is normalized to a maximum amplitude of 1.

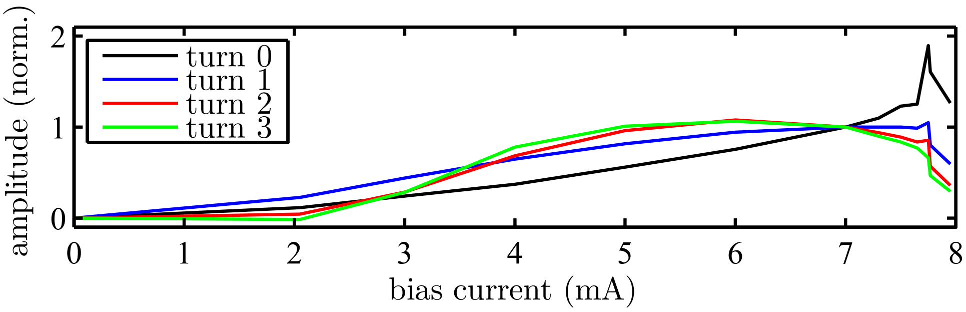

Figure 5.4.: Peak amplitude of the turn-0 to turn-3 pulses under variation of the YBCO detector bias current normalized to the amplitude at 7 mA (design bias current).

signal shows a bipolar response, which is assumed to be related to the electric field detection in the vortex regime as opposed to intensity detection in the HEB regime. Without bias, a bipolar response can be seen for all turn-1 and higher-turn signals.

Not only the pulse shape of the turn-0 signal depends on the bias current (Fig. 5.3 a), but also the pulse amplitude for signals from all turns detected (Fig. 5.4). With increasing bias current, the amplitude for all turns increases. At 6 mA, the amplitude for turn 2 and higher turns starts to decrease again. Usually, the detector is operated at its design bias current of 7 mA. At 7.75 mA, which is close to the upper superconducting transition current, a strong increase in the turn-0 response is observed, which gets weaker from turn to turn. This effect might also be related to the different detection mechanisms, as a superconducting HEB works best right at the transition current/temperature [14], whereas the vortex-based detection works best between the

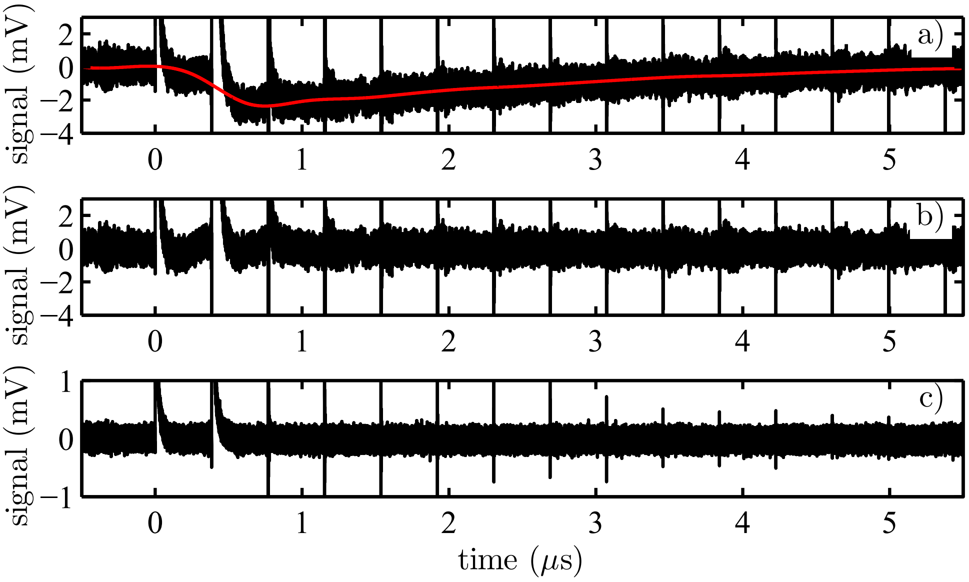

Figure 5.5.: Laser-induced YBCO detector signal (black) recorded with a 55-GHz amplifier employed (a) showing a baseline shift (red), the same data with the baseline shift corrected (b), and a signal recorded without amplifier showing no baseline shift (c).

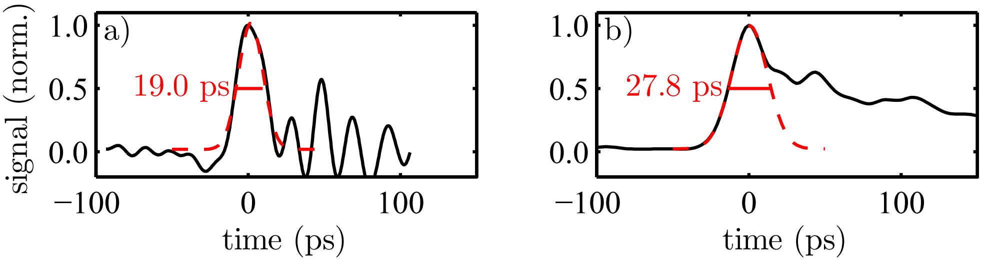

Figure 5.6.: Laser-induced turn-0 YBCO detector signals (black) recorded with a 63-GHz oscilloscope, and Gaussian least-squares fits (red) with corresponding FWHM values. The data was recorded with zero bias averaged over 16 sweeps (a) and with 7 mA bias current averaged over 4090 sweeps.

two critical currents of a type-II superconductor [40]. Above 7.75 mA, parts of the YBCO micro-bridge become normal-conducting, and the detector response decreases quickly.

The external 55-GHz amplifier is prone to a saturation effect in the form of a baseline shift following the strong turn-0 and turn-1 signals (Fig. 5.5 a). Without amplifier (c), the baseline shift does not occur, but signal intensities are quite low. For the multi-turn results presented in the following sections, which were recorded using the amplifier, the baseline is interpolated (Fig. 5.5 a, red line) and subtracted from the data to obtain a corrected signal trace (b).

The bandwidth during measurements with the YBCO detector is usually limited by the readout electronics, e.g., the 6-GHz oscilloscope available at DELTA. As shown in [38], the YBCO detection system (incl. bias tee, amplifier, and RF cabling) offers a minimum pulse length of less than 17 ps FWHM, and even this value is limited by the employed 63-GHz oscilloscope. During a demonstration measurement at DELTA with a 63-GHz oscilloscope kindly provided by Keysight Technologies Deutschland GmbH, a minimum turn-0 pulse length of 19 ps FWHM was observed (Fig. 5.6 a). For the standard settings of 7 mA bias current (Fig. 5.6 b), a pulse length of 27.8 ps FWHM was extracted from an oscilloscope trace averaged over 4090 sweeps. Here, the pulse lengthening is assumed to be related to the partially bolometric detection and a small jitter between single sweeps.

5.1.2. The FTIR Spectrometer

Unless indicated otherwise, the THz spectra presented within this thesis were all acquired using the VERTEX-80v spectrometer (Ch. 4.3). Although a direct extraction of a recorded interferogram followed by an offline Fourier transform is possible, the results presented here are all based on the spectra calculated by the spectrometer software OPUS with its optimized implementation of truncation, apodization, zero-filling, and phase correction (Ch. 2.7).

Background Spectrum

The detectors employed at the THz beamline only react to changes of the incoming intensity and are blind for CW signals like the thermal radiation from beamline compo-

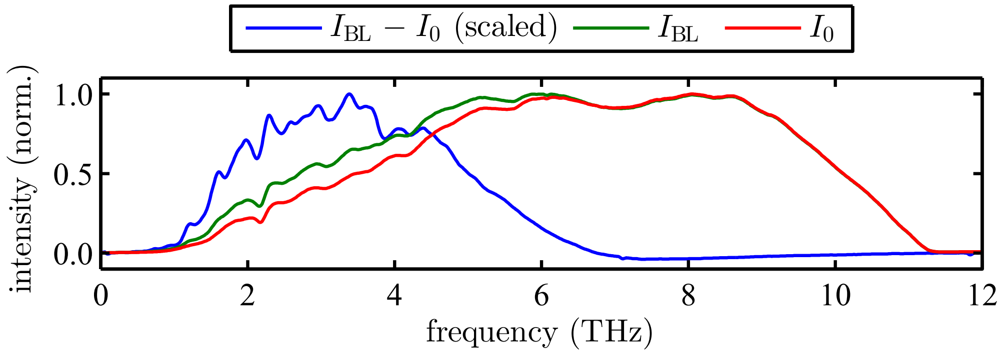

Figure 5.7.: Spectrum I_{BL} of radiation from the THz beamline during 100-mA mulibunch operation of the storage ring (green), thermal background spectrum I_0 recorded while the beamline was blocked by mirror M6 (red), and difference spectrum $I_{BL} - I_0$ (blue, scaled). The spectra were acquired with the Si bolometer and Mylar-multilayer beam splitter.

nents. This results in a background-free detection of the incoherent and laser-induced synchrotron radiation pulses during time-resolved measurements. However, any radiation passing through the spectrometer is modulated by the interferometer, which causes the CW thermal radiation to be detected. As the CW thermal radiation is much stronger than the weak incoherent synchrotron radiation at THz frequencies or the average power of laser-induced THz pulses occurring only with a duty cycle of below 10^{-9} (sub-ps pulses with 1 kHz repetition rate), this presents a huge background to all synchrotron-light-based measurements performed with the spectrometer. Measurements performed with the internal sources (Globar and Hg arc lamp) are less affected, as they provide a strong CW emission as well.

Figure 5.7 shows a spectrum of incoherent synchrotron radiation from the THz beamline (I_{BL}, green). The spectrum is dominated by background intensity which is still present when the beamline is blocked (I_0, red). Only the difference spectrum ($I_{BL} - I_0$,

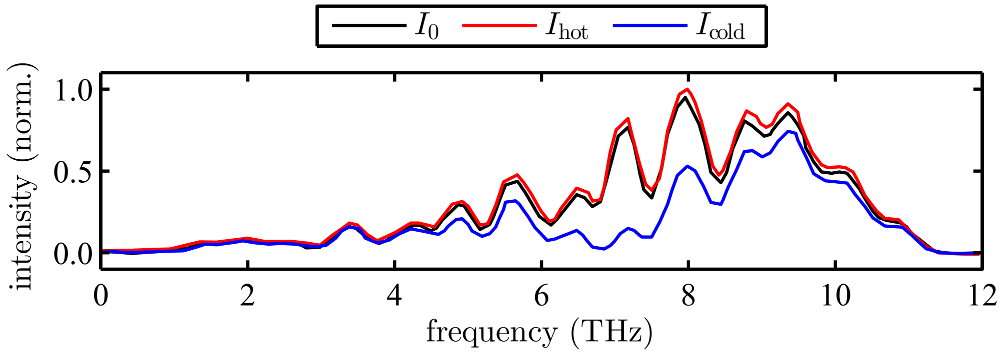

Figure 5.8.: Background spectrum I_0 recorded while the beamline was blocked (black), and spectra recorded with a heated (I_{hot}, red) or cooled (I_{cold}, blue) metal plate placed in the beam path. The spectra were acquired with the Si bolometer and Mylar-multilayer beam splitter. The general shape is attributed to the strong in-air absorption (the spectrometer was vented and opened) and low resolution set for this measurement.

blue) contains information about the synchrotron radiation (see below for a discussion of the spectral shape). Figure 5.8 confirms thermal radiation as the primary source for background intensity, as the background spectrum increases or decreases with a heated (via hot air gun) or cooled (via LN2) metal plate placed in the internal beam path.

For the spectral measurements of synchrotron radiation presented below, the background is either subtracted like in Fig. 5.7, a spectrum without laser-electron overlap is subtracted to obtain only the spectrum of the laser-induced radiation, or a lock-in amplifier is employed between the Si bolometer and the spectrometer readout electronics to directly extract the 1-kHz component caused by laser-induced THz pulses, for which the Si bolometer is just fast enough.

Detector, Beam-Splitter, and Source Characteristics

In order to characterize the cut-off frequencies of the spectrometer components, to compare these values to the manufacturer specifications (Tab. A.8), and to find suitable combinations for later measurements of the laser-induced THz radiation, spectral measurements were performed employing various combinations of sources, beam splitters, and detectors. The resulting spectral ranges are shown in Tab. 5.1. Here, the measured spectral range is defined as the section of a spectrum in which the corresponding emission, transmission, or sensitivity is above 10% of its maximum value without intermittent absorption lines. An inequality sign indicates that the value acquired is limited by another component employed during the corresponding measurement. The overall range of the entire spectrometer is limited by the Mylar 50-µm beam splitter (low-frequency cut-off at 0.5 THz) and the KBr beam splitter (high-frequency cut-off at 230 THz).

The Si bolometer should be combined with the Mylar-multilayer beam splitter, or with the Mylar 50-µm beam splitter for frequencies below 1 THz. The FIR-DLaTGS detector exceeds the upper limit of the Si bolometer and may be employed for the 10- to 20-THz regime in combination with the Mylar-multilayer beam splitter. Below 3 THz, an increase in noise of the FIR-DLaTGS signal was observed and the Si bolometer

Table 5.1.: Comparison of measured spectral ranges (see text for definition) of the spectrometer components to manufacturer specifications (all values in THz).

component	**specification**	**measurement**
Si bolometer	0.3 to 11.1	< 0.5 to 11.3
FIR-DLaTGS detector	0.3 to 21.0	< 0.5 to 20.9
MIR-DLaTGS detector	5.4 to 300	< 9 to > 230
KBr beam splitter	10.5 to 240	9.8 to 230
Mylar 50-µm beam splitter	0.8 to 1.8	0.5 to 1.7
Mylar-multilayer beam splitter	0.9 to 20.4	0.9 to 21.8
MIR source (Globar)	0.9 to 240	1.6 to 166
Hg arc lamp	0.1 to 30	< 0.5 to 85

should be used. For the MIR-DLaTGS detector, a useful combination is achieved with the KBr beam splitter.

The upper cut-off frequency of the Mylar 50-µm beam splitter is given by an absorption line at about 1.9 THz occurring due to a Fabry-Pérot-like interference in the single-layer Mylar foil, which is not present in the Mylar-multilayer beam splitter. Above 1.9 THz, the transmission rises again but provides additional absorption lines occurring with an average distance of $\Delta f \approx 1.9$ THz. With a refractive index of $n \approx 1.6$, the measured foil thickness amounts to

$$d = \frac{c}{2n\Delta f} \approx 49\ \mu\mathrm{m}, \tag{5.1}$$

which is close to the 50-µm specification.

The MIR source covers almost the entire range of all other spectrometer components and can be employed for calibration. An MIR spectrum is usually recorded before and after a sequence of other spectra for comparability of spectrometer conditions on a day-to-day basis. The Hg arc lamp is well-suited for table-top measurements in the sub- and low-THz regime and should be combined with the Mylar beam splitters and the Si bolometer or FIR-DLaTGS detector.

Noise and Signal Fluctuations

The time to record a single spectrum varies depending on the desired resolution (corresponding to the maximum excursion of the movable interferometer arm) and the optimum modulation speed for the employed detector (corresponding to the speed of the movable interferometer arm). For the measurements performed in the course of this thesis, the average recording time of a single spectrum was about 10 to 15 s. Therefore, each spectrum of the spontaneous incoherent synchrotron radiation is based on up to $4 \cdot 10^7$ revolutions of a single bunch or multi-bunch filling, and each spectrum of the laser-induced coherent radiation is based on up to $1.5 \cdot 10^4$ laser shots. In addition to, e.g., statistical noise of the detector affecting the entire spectrum, shot-to-shot fluctuations during the movement of the interferometer arm influence the shape of the spectrum. An averaging over 15 to 20 subsequent single spectra was set in the OPUS spectrometer software to suppress these fluctuations. The spectrometer uses both sides of the symmetrical interferogram and also the backwards motion of the interferometer arm to record four spectra with one forward-backward movement. Still, recording one averaged spectrum took several minutes depending on the detailed settings.

The characterization spectra shown above and the spectra in the following sections are always based on the internal averaging described above. Especially for the measurements based on difference spectra (beamline open/blocked to subtract thermal background; with/without laser-electron overlap to obtain only the coherent spectrum), the limited beam time allowed for only one averaged spectrum to be recorded for a certain set of storage ring and laser parameters, which does not provide any information about amplitude fluctuations or fluctuations of the spectral shape. Therefore, the spectra presented in this thesis are generally shown without error bars.

However, to gain a basic understanding of fluctuations and uncertainties in the spectral measurements, three data sets were recorded based on single spectra without averaging followed by an offline analysis to extract a mean spectrum and its rms spread. The measurements were performed during standard conditions of the storage ring and

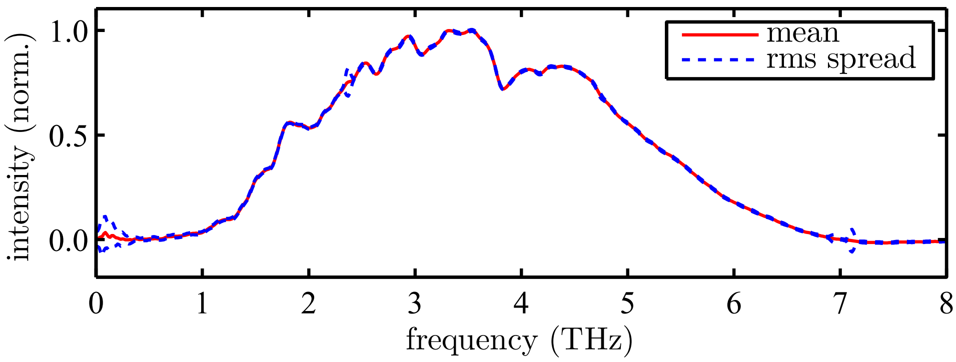

Figure 5.9.: Normalized mean spectrum (red) and mean spectrum plus/minus the rms spread (blue, dashed) based on 20 single spectra of spontaneous incoherent THz radiation (125 mA multi-bunch filling). Each single spectrum is based on the difference between a spectrum with open beamline and blocked beamline.

short-pulse facility and should provide a reasonable estimate also for the uncertainties in the spectra presented above or in the following sections. Here, only the noise characteristics are analyzed. Remarks on systematical errors or the general spectral shapes are given in the following sections.

Figure 5.9 shows the spectrum of incoherent THz radiation from a 125-mA multi-bunch filling of the storage ring. Except for the range below 0.5 THz and narrow features at 2.3 and 7.1 THz, the rms spread is below ±0.8% of the maximum intensity. For the spectrum of coherent laser-induced radiation based on the difference method (Fig. 5.10), an increased rms spread of up to ±4% (again except for several narrow features of even higher fluctuations) is observed. The increase of fluctuations in comparison to the incoherent spectrum from the multi-bunch filling is related to fluctuations of the transverse laser-electron overlap and to the decrease in absolute intensity. As shown below, the ratio between coherent and incoherent radiation $N_\mathrm{e}g^2(\nu)$ (Eq. 2.107) reaches values up to 10^3 to 10^4. However, with 2600 revolutions per laser shot and a

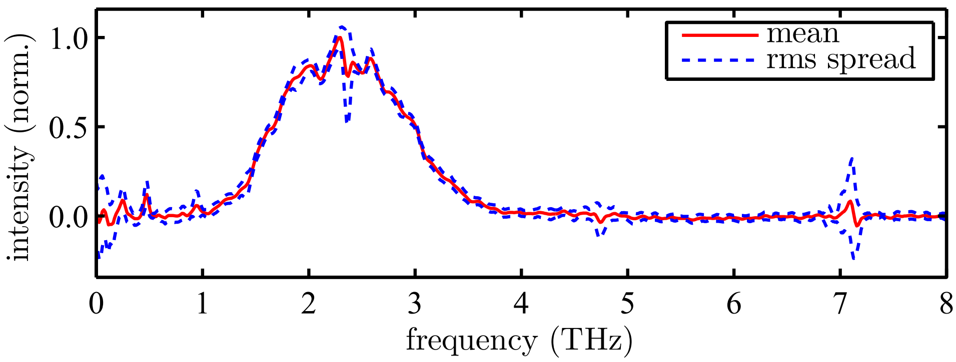

Figure 5.10.: Normalized mean spectrum (red) and mean spectrum plus/minus the rms spread (blue, dashed) based on 16 single spectra of laser-induced coherent THz radiation. Each single spectrum is based on the difference between a spectrum with and without laser-electron overlap.

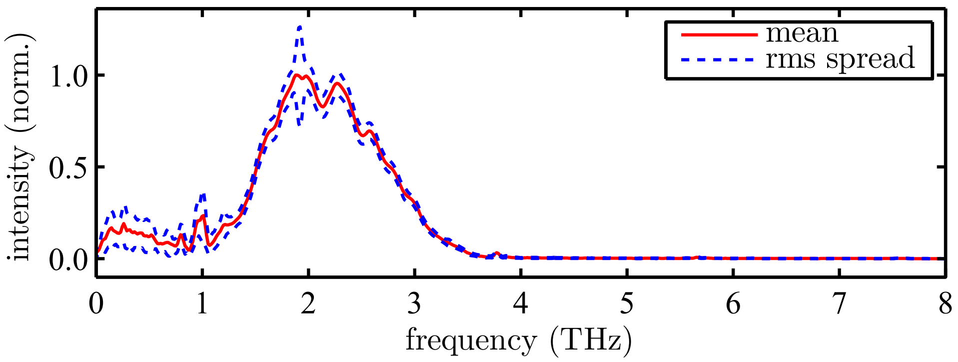

Figure 5.11.: Normalized mean spectrum (red) and mean spectrum plus/minus the rms spread (blue, dashed) based on 21 single spectra of laser-induced coherent THz radiation, which were recorded using a lock-in amplifier.

multi-bunch current of 125 mA as compared to a typical single-bunch current of 10 mA, the absolute peak intensity in Fig. 5.9 still is about 10 times higher than in Fig. 5.10. Finally, Fig. 5.11 shows a spectrum recorded using a lock-in amplifier to directly extract the coherent laser-induced radiation signal without the need for background subtraction. The rms spread is of the order of ±5%, but with a general increase of fluctuations below 1 THz. The narrow features of increased rms spread which are present in all three measurements are related to electronic noise in the detector signal at Hz and kHz frequencies. Appearing as a periodic modulation of the recorded interferograms, this electronic noise is translated into narrow spectral features at THz frequencies due to the Fourier transform and depending on the speed of the movable interferometer arm.

5.1.3. Characteristics of the THz Radiation

Current Dependence of the THz Radiation

A basic property of the laser-induced THz radiation is its quadratic dependence on the number of electrons affected by the laser, whereas the incoherent synchrotron radiation shows a linear dependence on the number of electrons in the beam (Eq. 2.107).

To check these dependencies, the incoherent THz radiation intensity was measured with the InSb bolometer during standard multi-bunch operation of the storage ring. As the InSb bolometer only responds to changes in radiation intensity, it does not react to the multi-bunch radiation appearing CW-like due to its 500-MHz repetition rate. Therefore, a chopper wheel operated at 27 Hz was placed in the in-air beam path section of the THz beamline and the bolometer was read out using an FFT analyzer. This data set was already presented in [13] and is shown here for the sake of completeness. The signal intensity in terms of the 27-Hz amplitude on the FFT analyzer versus the multi-bunch beam current is shown in Fig. 5.12 a. For each data point, the signal was recorded over a predefined measurement period and the error bars represent the standard deviation of the signal fluctuations during this period. Based on the result of a weighted linear least-squares fit (red), the baseline was subtracted and the curve was normalized to a value of 1 at 100 mA. A good agreement between the data and the linear fit confirms the expected dependency.

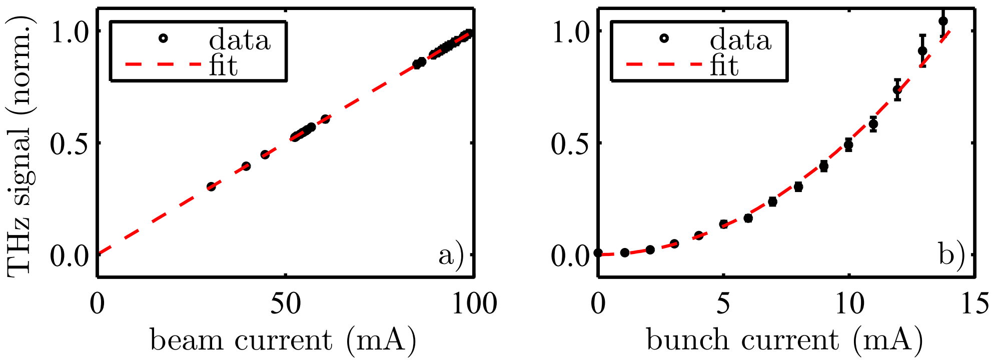

Figure 5.12.: Incoherent THz signal intensity versus multi-bunch beam current (a) and coherent laser-induced THz signal intensity versus single-bunch current (b). See text for details.

For the coherent laser-induced THz radiation, the signal intensity was measured based on the standard readout setup described in Ch. 4.2.1, i.e., the intensity was extracted from the peak-to-peak function of a DSO. In order to decrease the overall duration of the measurement and, thus, the risk of influencing the measurement by, e.g., slow drifts of the laser-electron overlap, the single-bunch current was gradually decreased by temporarily reducing the RF power. However, the bunch current cannot be measured directly, as the single bunch is usually accompanied by one or two low-current trailing bunches. Instead, the overall beam current was measured using the DCCT beam current monitor which was also employed for the multi-bunch measurement, and the single-bunch current was calculated using the averaged fill pattern (relative current per bucket) provided by a digitized BPM signal. The result of the laser-induced THz measurement is shown in Fig. 5.12 b with a quadratic least-squares fit. In comparison to a data set shown in [13], the single-bunch current-range was extended from 4.5 to 14 mA. Again, a good agreement between the data and the fit confirms the expected dependency.

Spectrum of Spontaneous Incoherent THz Radiation

As described in Ch. 5.1.2, spectra of the incoherent synchrotron radiation are based on the difference between a spectrum with open and blocked beamline to subtract the thermal background. The resulting difference spectra are shown in Fig. 5.13.

Comparing these spectra to the characterization measurements of the FTIR spectrometer (Ch. 5.1.2), structures like the low-frequency cut-off at about 0.5 THz, the absorption lines around 85 THz, and the slow decrease in intensity from 90 to 250 THz can be attributed to the spectrometer and its components. The complete absorption of synchrotron radiation between 7.5 and 62 THz is caused by the z-cut quartz windows employed in the THz beamline, which are – according to the manufacturer – opaque between approximately 7 and 70 THz.

Figure 5.14 shows again the measured synchrotron radiation spectrum between 0 and 10 THz (black). In addition, the theoretical synchrotron radiation spectrum (Eq. 2.101) is displayed (blue), which was scaled to result in a matching transmission (see below). The overall transmission (beamline and spectrometer, green) was calculated dividing the measured by the theoretical spectrum. The red curve represents a combination of

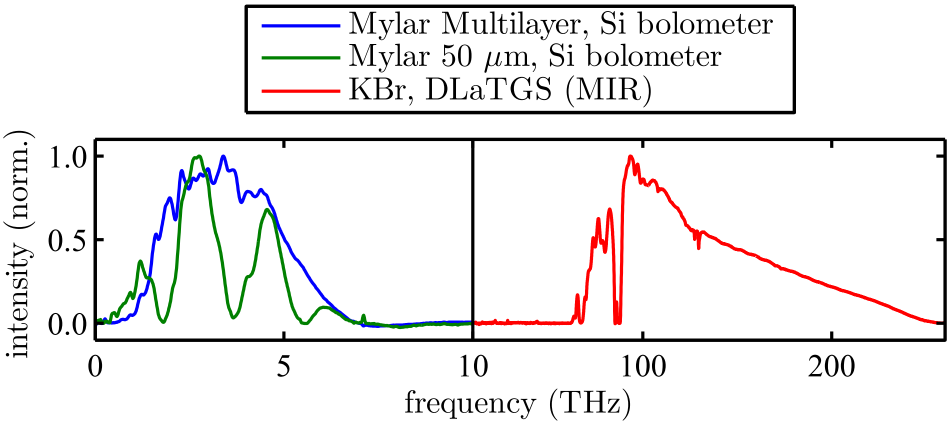

Figure 5.13.: Normalized difference spectra (thermal background subtracted) of incoherent synchrotron radiation employing different beam splitters and detectors (see legend). Note the change in frequency scale.

the theoretical z-cut quartz transmission (see Fig. 2.20) and the Mylar-multilayer transmission extracted from spectra of the Hg arc lamp. A reasonable agreement between the measured transmission (green) and the calculated Mylar and quartz transmission (red) is observed, which clearly marks these two components as the dominating contributors to the shape of the measured synchrotron radiation spectra.

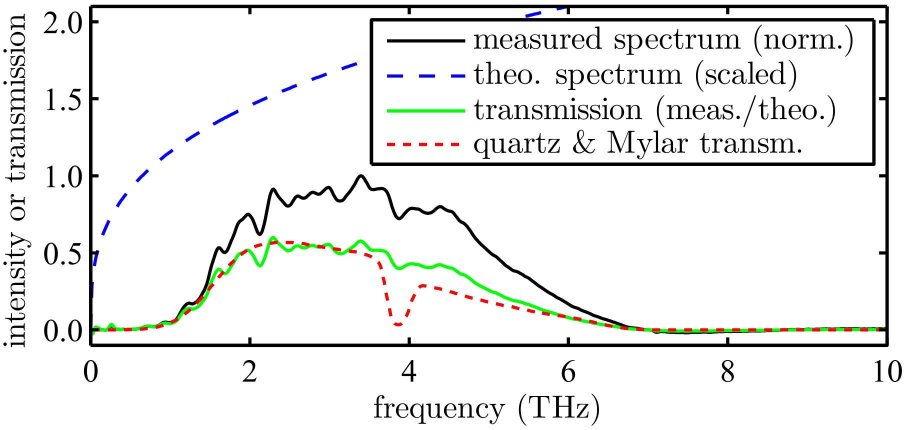

Figure 5.14.: Normalized difference spectrum of incoherent synchrotron radiation employing the Mylar-multilayer beam splitter and the Si bolometer (black). Furthermore, a theoretical synchrotron radiation spectrum (blue), the measured beamline and spectrometer transmission (green), and a theoretical Mylar and z-cut-quartz transmission (red) are shown. See text for details.

Spectrum of Laser-Induced THz Radiation

Due to the spectral range of the FTIR spectrometer reaching down to about 0.5 THz (Tab. 5.1), only the turn-0 spectrum of laser-induced coherent THz radiation can be observed (see Fig. 3.4). The first spectra were recorded in 2013, at which point seeding was only possible at a wavelength of 400 nm (via SHG unit). Since 2014, quick switching between 400 and 800 nm is possible, and spectra of coherent THz radiation seeded with 800 nm were recorded.

Figure 5.15 shows a data set recorded with 400-nm seeding [73]. The laser-induced spectrum I_{coh} (a, red) is given by the difference of a spectrum recorded during laser-electron overlap (I_{tot}, black) and without laser-electron overlap (I_{spon}, blue). For both, I_{tot} and I_{spon}, the thermal background was already subtracted. The form factor times the number of electrons in the bunch (b, black) is given by

$$N_{\mathrm{e}} \cdot g^2(\nu) = 2600 \left(\frac{I_{\mathrm{tot}}(\nu)}{I_{\mathrm{spon}}(\nu)} - 1 \right) . \tag{5.2}$$

This is a re-arrangement of Eq. 2.107 with the approximation $N_{\mathrm{e}} - 1 \approx N_{\mathrm{e}}$. Furthermore, the factor 2600 was introduced to account for the 2600 revolutions of the single bunch per laser shot. For regions where $I_{\mathrm{spon}}(\nu)$ is smaller than 10% of its maximum, the form factor was set to zero. Otherwise, the relative error of the spontaneous spectrum would cause arbitrarily large values of $g^2(\nu)$ due to the division by small numbers. A weighted least-squares fit of a Gaussian distribution (blue) provides a reasonable measure of the central frequency and FWHM, in this case 2.6 and 2.1 THz.

A data set recorded during 800-nm seeding [76] is shown in Fig. 5.16. The same steps were applied as in Fig. 5.15. The spectrum and form factor differ from the 400-nm seeding data in two aspects. Firstly, the intensity of the coherent spectrum is much stronger, and the corresponding form factor times the number of electrons in the bunch reaches a value of about 15000 as opposed to only 3300, although the 400-nm seeding was performed at a slightly increased bunch current of 13.3 mA as opposed to 11.1 mA during the 800-nm seeding. This might be related to an increased laser pulse energy of about 3 mJ at 800 nm (about 2.1 mJ at 400 nm) and a better laser-pulse quality, as

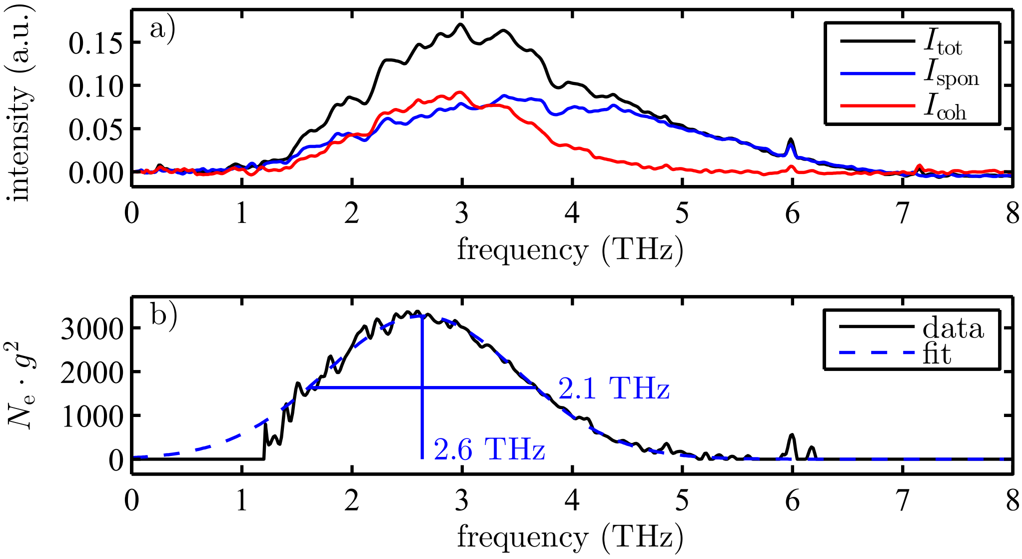

Figure 5.15.: Spectrum of laser-induced THz radiation (a) based on a seeding wavelength of 400 nm, and corresponding form factor times the number of electrons in the bunch (b). The spectrum was recorded using the Mylar-multilayer beam splitter and the Si bolometer. See text for details.

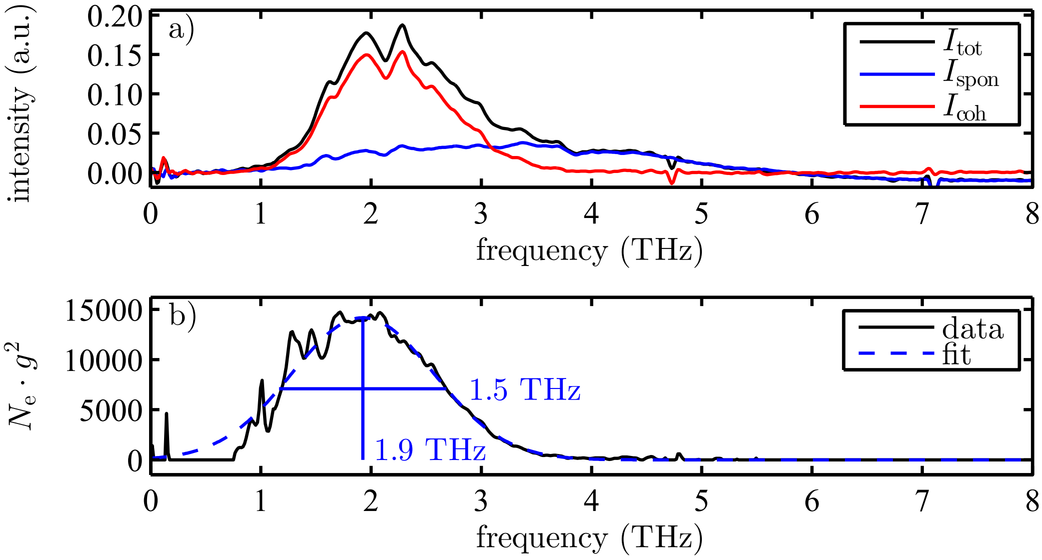

Figure 5.16.: Spectrum of laser-induced THz radiation (a) based on a seeding wavelength of 800 nm, and corresponding form factor times the number of electrons in the bunch (b). The spectrum was recorded using both Mylar beam splitters (to cover the sub-THz regime) and the Si bolometer. See text for details.

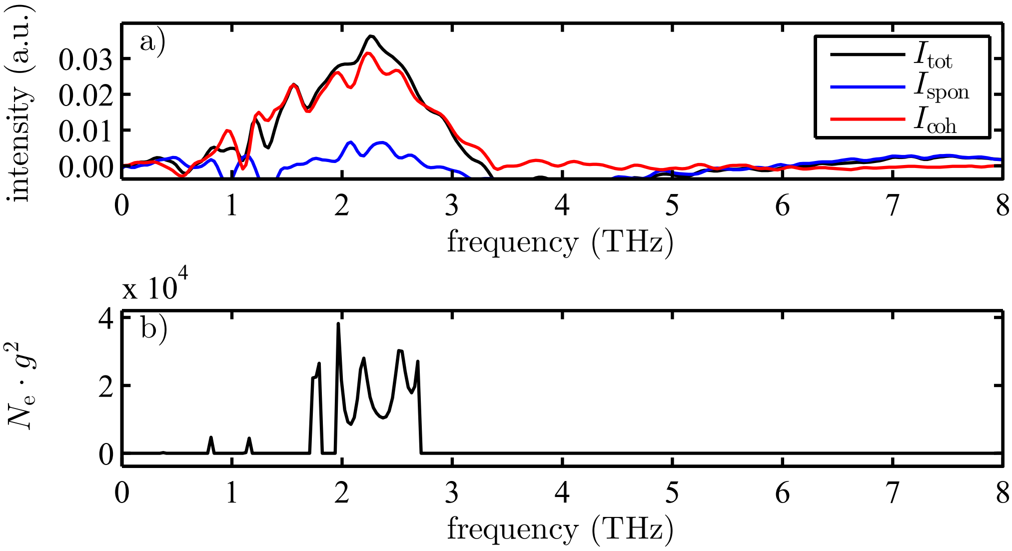

Figure 5.17.: Spectrum of laser-induced THz radiation (a) based on a seeding wavelength of 800 nm, and corresponding form factor times the number of electrons in the bunch (b). The spectrum was recorded using the Mylar-multilayer beam splitter and the FIR-DLaTGS detector. See text for details.

the properties of the pulses generated in the SHG unit are not well known. Secondly, the 800-nm-seeded spectrum is more narrow (1.5 THz FWHM) and shifted towards lower frequencies (1.9 THz). This is an indication for an increased width of the dip in the electron density (see Ch. 5.3.2 for a more detailed analysis), which might be caused by an increased laser pulse length. In general, only 800-nm laser pulses can be characterized using a FROG or SPIDER in the laser laboratory. These devices cannot be employed for the 400-nm pulses, and even the 800-nm pulses cannot be characterized reliably because they pass through a window and three lenses before interacting with the electrons, which changes the pulse shape and increases the pulse length (Ch. 2.1).

The FIR-DLaTGS detector can also be employed to measure the laser-induced coherent THz spectrum (Fig. 5.17 a, red). The shape and central frequency of I_{coh} (red) are in good agreement with the coherent spectrum shown in Fig. 5.16. However, the overall intensity is quite low, and the intensity of the spontaneous emission spectrum is dominated by noise, which prevents the calculation of a reasonable form factor (b).

An alternative method to recording spectra with and without overlap and looking at their difference/quotient is to employ a lock-in amplifier between the Si bolometer and read-out electronics locked to the 1-kHz repetition rate of the laser system. The lock-in amplifier acts as a phase-sensitive narrow-band filter centered at 1 kHz. The output of the lock-in amplifier then represents the interferogram of the laser-induced THz pulses only and no background spectrum has to be subtracted. A laser-induced spectrum recorded with the lock-in amplifier is shown in Fig. 5.18 (a, I_{coh}, red). A shape comparable to the difference spectrum I_{coh} in Fig. 5.16 is observed. Thus, the lock-in method allows for a more simple data recording with an overall decrease of measurement time and a direct view on the spectrum of the laser-induced THz pulses. However, as no spontaneous background is recorded, the form factor can only be calculated

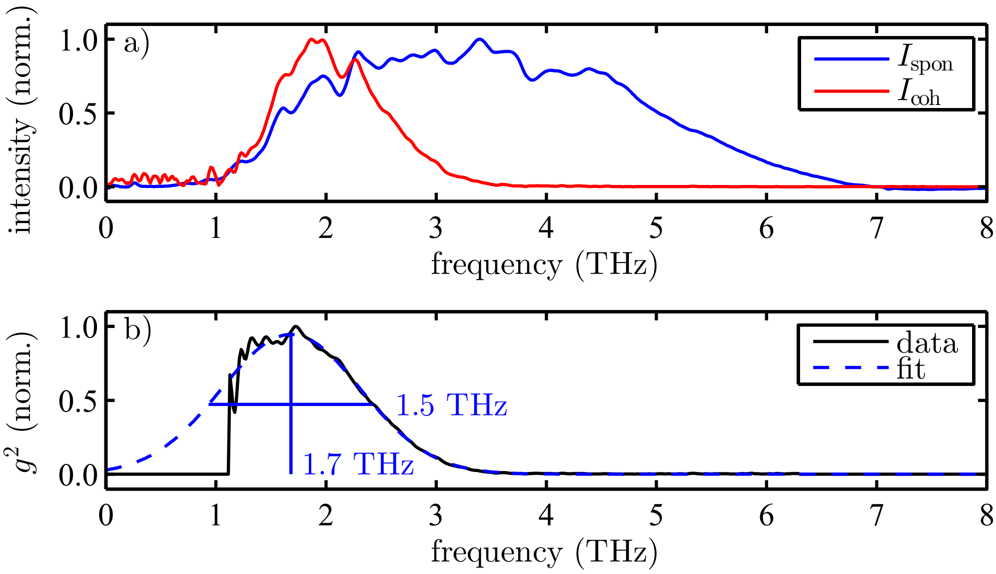

Figure 5.18.: Spectrum of laser-induced THz radiation (a) based on a seeding wavelength of 800 nm, and corresponding normalized form factor (b). The spectrum was recorded using the Mylar-multilayer beam splitter, the Si bolometer, and a lock-in amplifier. See text for details.

based on a spontaneous spectrum acquired independently without lock-in amplifier (Fig. 5.18 a, I_{spon}, blue). As a consequence, no absolute scale for the form factor (b) can be computed.

Pulse Energy and Photon Flux

An important parameter for future user experiments at the DELTA THz beamline is the achievable pulse energy or photon flux. As none of the employed detectors is calibrated for the absolute measurement of sub-ps pulse energies, the following consideration is based on an analytical calculation of the incoherent synchrotron radiation power spectrum $N_{\mathrm{e}} \cdot \mathrm{d}P_{\mathrm{e}}/\mathrm{d}\nu$ from a bending magnet (Eq. 2.101), the measured coherent amplification $N_{\mathrm{e}}g^2$ (form factor times the number of electrons in the bunch, see above), and the beamline transmission $T(\nu)$ (Fig. 5.14). The pulse energy is then given by the spectrally integrated power multiplied by the fraction of the revolution time (384 ns) it takes for the electrons to pass by the beamline with its opening angle of 33.5 mrad:

$$E_{\mathrm{pulse}} = \left[\int N_{\mathrm{e}} \frac{\mathrm{d}P_{\mathrm{e}}}{\mathrm{d}\nu}(\nu) \cdot N_{\mathrm{e}} g^2(\nu) \cdot T(\nu)\, \mathrm{d}\nu \right] \cdot \frac{33.5 \text{ mrad}}{2\pi \text{ rad}} \cdot 384 \text{ ns} = 5.9 \text{ nJ}. \tag{5.3}$$

With a repetition rate of 1 kHz, an average power of 5.9 μW is achieved, which translates to a photon flux of $4.7 \cdot 10^{15}\ \mathrm{s}^{-1}$ (at 1.9 THz).

These values are based on the turn-0 form factor from Fig. 5.16 (800-nm seeding) recorded at a bunch current of 11.1 mA. For future user operation, a single-bunch current of about 5 mA is more realistic, leading to a pulse energy of about 1 nJ and an average power of about 1 μW.

5.2. Diagnostics and Optimization of the Laser-Electron Overlap

A primary motivation for the construction of a dedicated THz beamline at DELTA was its use as a diagnostics tool for the laser-electron overlap at the short-pulse facility. The procedure for finding and optimizing the overlap always starts with finding a laser-induced THz signal. The parameters of the short-pulse facility are then optimized for maximum THz signal amplitude before starting to look for the CHG signal.

5.2.1. Variation of the Spatial Laser-Electron Overlap

For the longitudinal direction, the delay between the laser pulse and the electron bunch can be varied continuously using a so-called vector modulator – a digitally controlled phase shifter based on splitting the 500-MHz RF signal into two copies, introducing a 90° phase difference, and recombining both copies with variable relative amplitudes. The 40-fs laser pulse then acts as an ultrashort probe of the electron density in the 100-ps bunch – a technique described in detail in Ch. 5.3.1. A MATLAB tool was developed, which allows for an automatic variation of the delay (and several other parameters, see below) and for recording the turn-1 THz amplitude from the InSb bolometer (Ch. 4.2). A Gaussian fit is performed and the delay value with maximum THz amplitude is displayed, to which the vector modulator is then set for longitudinal optimization of the laser-electron overlap.

For the transverse directions, the last two mirrors M1 and M2 in the laser beamline BL3 (Fig. 1.8) are motorized allowing their horizontal and vertical angle to be adjusted in order to change the transverse position and angle of the laser pulse in the undulator U250. Using the MATLAB tool, the horizontal or vertical angle of each mirror can be varied automatically and the corresponding THz amplitude is recorded [71]. An example for this kind of measurement is shown in Fig. 5.19. Here, each data point was normalized to the squared mean bunch current during the individual measurement period to correct for the bunch current decrease occurring over the entire measurement, and the error bars represent the rms signal fluctuations. The width of the Gaussian profile is determined by the convolution of the horizontal laser pulse and electron bunch distribution.

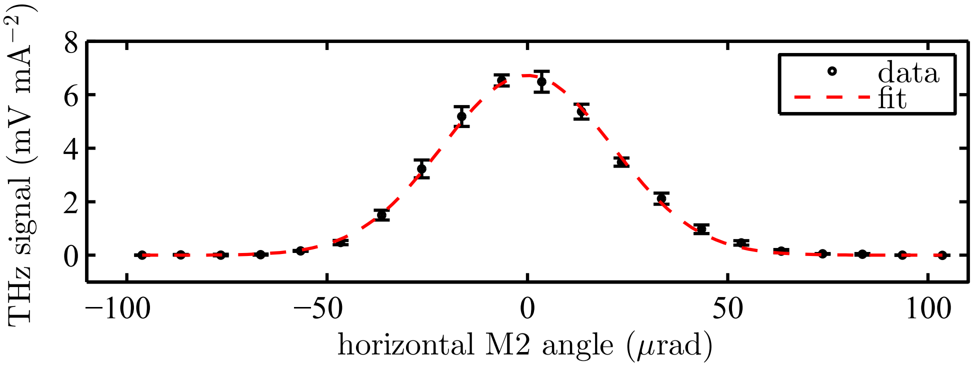

Figure 5.19.: THz signal intensity (turn-1 peak-to-peak data from InSb bolometer) versus relative horizontal angle of mirror M2 (black) [71]. See text for details.

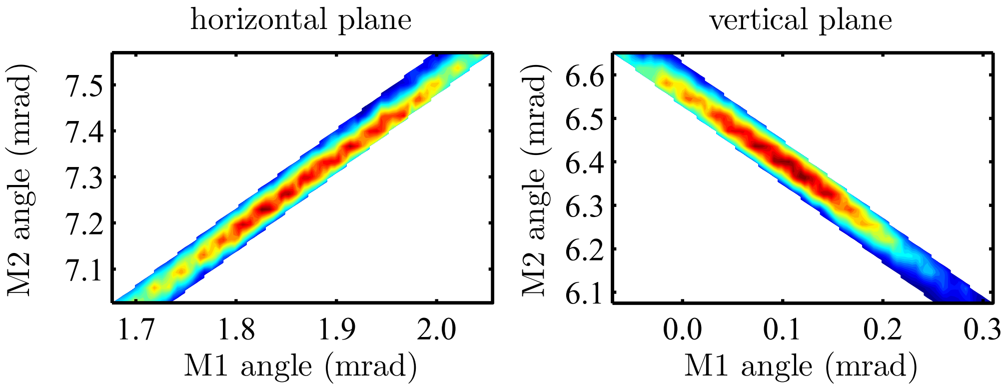

Figure 5.20.: Color-coded THz signal intensity (turn-1 peak-to-peak data from InSb bolometer) versus horizontal (left) and vertical (right) angles of mirrors M1 and M2. See text for details.

More important for an optimized transverse laser-electron overlap is a simultaneous variation of M1 and M2 in order to achieve the correct position and angle between laser and electron beam (a so-called 'beam walk'). For this purpose, the MATLAB tool allows M1 and M2 to be automatically tilted either horizontally or vertically covering a pre-defined area of the corresponding M1-M2 plane. An example of the resulting THz intensity distributions is shown in Fig. 5.20. The shape of these distributions is based on the fact that an offset introduced by M1 can be partially corrected by a corresponding movement of M2, resulting in a variation of the crossing angle between laser and electron beam. For an optimized spatial and angular overlap, the mirror axes have to be set to the centers of the horizontal and vertical distributions.

5.2.2. Variation of Laser Parameters

Figure 5.21 shows the dependence of the turn-1 THz signal on the laser pulse energy [71]. The data points are normalized to the squared bunch current and the error bars represent the rms signal fluctuations. The pulse energy was varied by rotating the laser polarization angle with a half-wave plate, which changes the projected electric

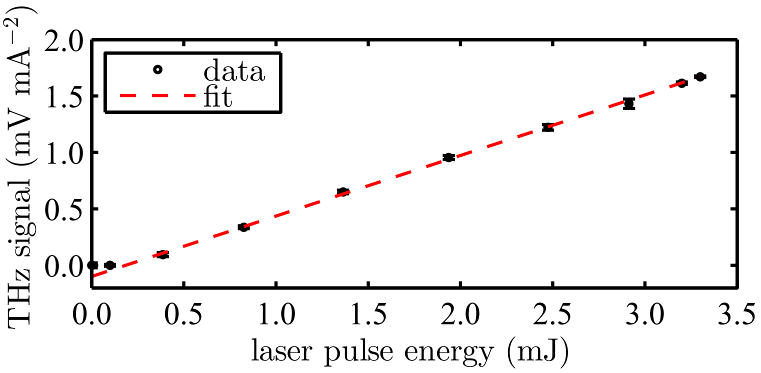

Figure 5.21.: THz signal intensity (turn-1 peak-to-peak data from InSb bolometer) versus effective laser pulse energy (black; see text for details) [71]. For the linear fit (red), the first two data points were excluded.

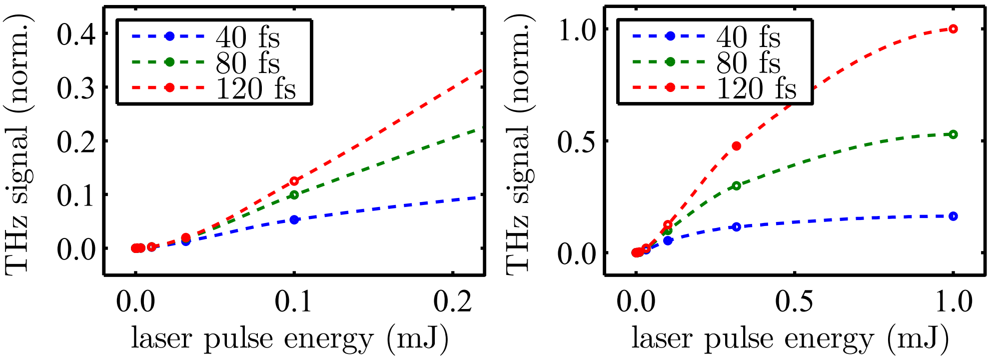

Figure 5.22.: Simulated InSb-THz signal (see text for details) versus laser pulse energy up to 0.2 mJ (left) and 1 mJ (right) for three different laser pulse lengths from 40 to 120 fs.

field in the horizontal undulator plane. A straight line fits all but the first two data points. In the limit of low laser peak powers, a quadratic increase of the THz intensity was predicted independent of the laser pulse shape [99]. This effect is confirmed by a simulation of the InSb-THz signal with THzSMe (Fig. 5.22), in which the detector response is calculated from the simulated spectrum integrated over the sensitivity range of the InSb bolometer. A quadratic increase for low laser powers, a region with linear dependence resembling the experimental result, and a saturation which occurs at different pulse energies depending on the pulse length are observed. The absence of saturation in the experimental data may indicate that the pulse energy arriving in the U250 at DELTA is below the pulse energy measured in the laser laboratory. Furthermore, some of the simulation parameters concerning the pulse length, focus size, Rayleigh length, etc. might deviate from the real parameters during the experiment.

The dependence of the turn-1 THz signal on the laser pulse length is shown in Fig. 5.23. The pulse length was varied moving the internal compressor in the laser amplifier, thereby introducing a GDD resulting in a chirp. No data point was recorded at zero GDD, which corresponds to the shortest pulse length < 50 fs in the laser laboratory. For a positive GDD, the laser pulse length exhibits a stronger increase

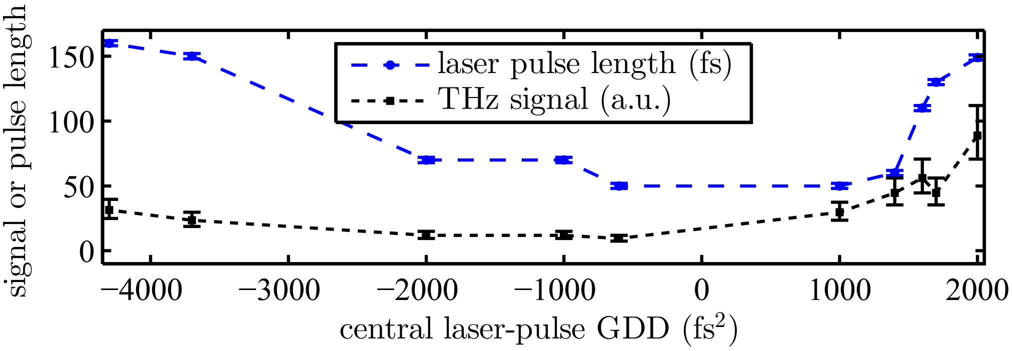

Figure 5.23.: Laser pulse length (blue; via SPIDER) and THz signal intensity (black; turn-1 amplitude via FFT analyzer, normalized to squared bunch current) versus central GDD of the laser pulse (via SPIDER). The error bars represent the signal fluctuations observed during each measurement.

than for negative GDD. This behavior cannot be explained by a linear chirp (Eq. 2.15) and is an indication for a higher-order chirp. The THz signal increases with the pulse length, however, the smallest amplitude is recorded for a GDD of about -650 fs^2. The rise in THz intensity with increasing pulse length is based on a complex dependence, which involves the decreasing laser peak power due to the constant pulse energy and a spectral shift (see below) more into the sensitivity range of the InSb bolometer. The asymmetry indicates that the laser pulse in the undulator is shortest for a GDD in the laser laboratory of about -650 fs^2. This can be explained by the previously mentioned lenses and window in the beam path. With a GVD of fused silica glass of 36.16 fs^2 mm^{-1} [131] and an overall material thickness of about 15 to 20 mm, the material introduces a GDD of about 540 to 720 fs^2. Thus, for a GDD of about -650 fs^2 measured with the SPIDER in the laser laboratory, the actual GDD in the undulator is close to zero and the pulse is shortest.

Employing the lock-in method (see Fig. 5.18), the dependence of the turn-0 spectrum on the 800-nm laser pulse length was also studied (Fig. 5.24). Due to difficulties with the corresponding equipment (FROG and SPIDER) during the experiment, the laser pulse length could not be measured directly, but a relative measure (0 for shortest pulse length, positive numbers for increased pulse length) is given based on the output power of the SHG unit, to which the pulses were sent before each spectral measurement, and which strongly depends on the pulse length. A clear influence of the pulse length on the central THz frequency is observed, although an interpretation is difficult due to the missing absolute measure of the laser pulse length. Performing a series of simulations with THzSMe using different laser pulse lengths from 40 to 300 fs, a similar behavior can be seen (Fig. 5.25) for the regime above 80 to 120 fs depending on the pulse energy. Here, the central frequency decreases with increasing pulse length, as the dip in the

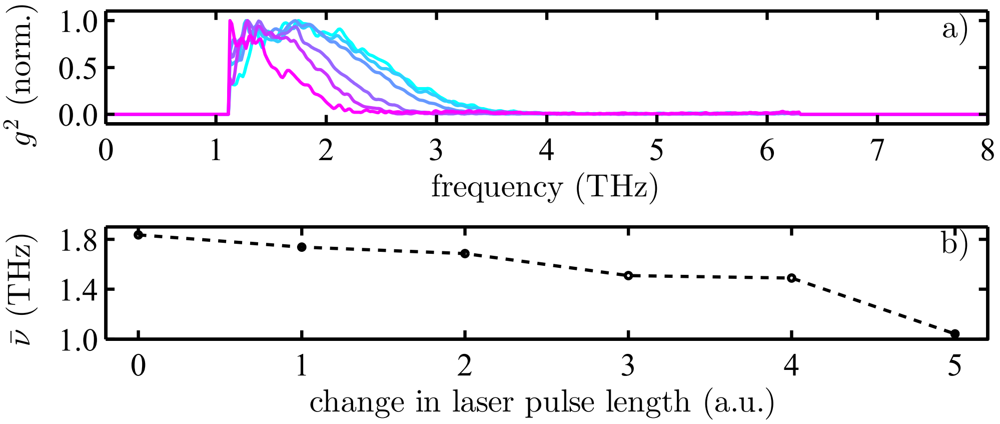

Figure 5.24.: Normalized form factors g^2 of laser-induced THz radiation during 800-nm seeding (a); and the dependence of the central frequency $\bar{\nu}$ on the laser pulse length (b). For a), the laser pulse length is color-coded (cyan/short to magenta/long). The form factors were recorded using the Mylar-multilayer beam splitter, the Si bolometer, and a lock-in amplifier. The cut-off at about 1.2 THz is due to the low transmission of the beam splitter. The central frequencies (b) were extracted from weighted fits of the form factors.

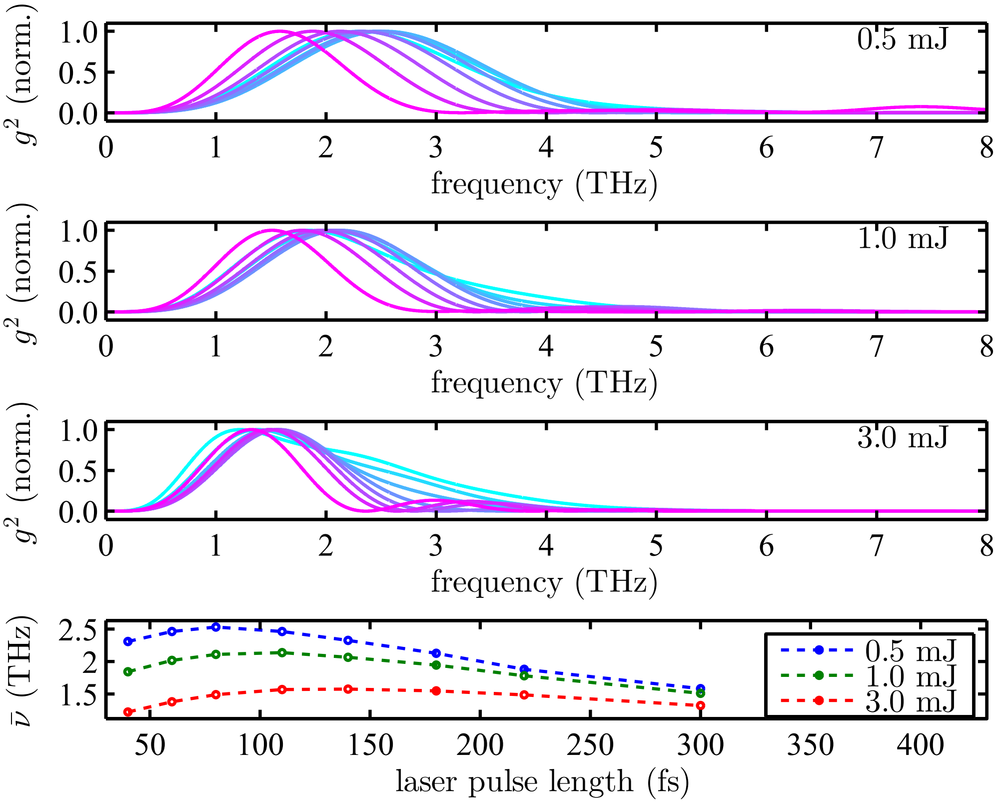

Figure 5.25.: Normalized simulated turn-0 form factors g^2 of laser-induced THz radiation (top) for different laser pulse energies and pulse lengths (color-coded; cyan/short to magenta/long), and the dependence of the central frequency $\bar{\nu}$ on the laser pulse length (bottom). Except for the pulse length and power, the standard settings from Tab. A.9 were used.

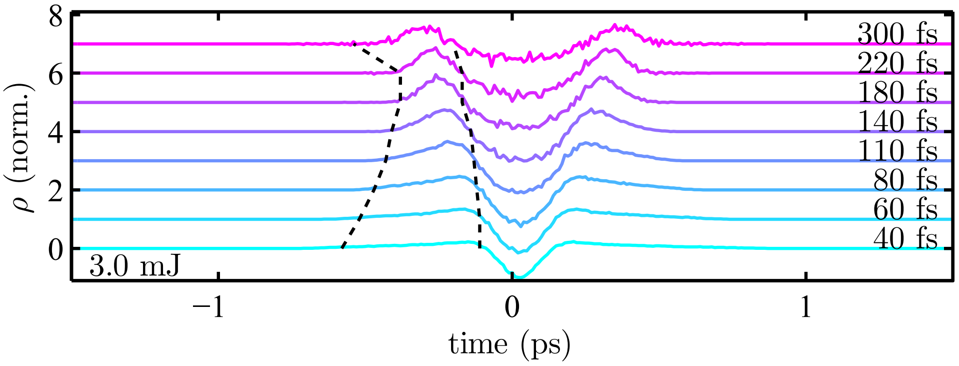

Figure 5.26.: Normalized simulated turn-0 density modulations ρ for different laser pulse lengths corresponding to the 3-mJ data in Fig. 5.25. The black dashed lines indicate the width of the left density maximum (full width at 5% of the density maximum).

electron density becomes broader and shallower (Fig. 5.26). Below 80 to 120 fs, the central frequency decreases with decreasing laser pulse length. In this regime, the higher laser peak power and corresponding amplitude of the energy modulation cause a broadening of the density maxima accompanying the dip (Fig. 5.26), which translates into a decrease of the central frequency despite the more narrow dip.

5.2.3. THz Signal in the Presence of an RF Phase Modulation

During standard user operation of DELTA, a periodic phase modulation with twice the synchrotron oscillation frequency is usually applied to the storage ring RF system to suppress coupled-bunch instabilities and to increase the beam lifetime [132]. With increasing amplitude of the phase modulation, this leads to a 'breathing' of the bunch in longitudinal phase space (the bunch gets longer and shorter, the energy spread smaller and larger) or to two or three 'islands' rotating in longitudinal phase space, which are seen as sub-bunches oscillating forth and back on the longitudinal axis (Fig. 5.27). For the operation of the short-pulse facility during standard user operation based on a hybrid filling-pattern with a high-current single bunch in the gap of a 3/4-multi-bunch pattern, this phase modulation presents a challenge. A general decrease of intensity and increase of fluctuations of the laser-induced THz and CHG signals is expected and observed (see, e.g., Fig. 5.31 vs. Fig. 5.32, or [133]).

A strategy was tested to counteract these challenges and even profit from the phase modulation [81, 134]. If the modulation frequency $f_\mathrm{m} \approx 2f_\mathrm{s}$ is tuned close to a harmonic n of the laser repetition rate $f_\mathrm{L} = 1$ kHz – the synchrotron frequency f_s can be changed accordingly by slight variations of the RF power – the laser hits the electron bunch at a slowly changing phase of the RF modulation. As a result, the laser-induced signals 'sample' the RF modulation on a time scale of several minutes corresponding to a frequency of $|f_\mathrm{m} - nf_\mathrm{L}|$ (Fig. 5.28).

As expected, the CHG signal is high for a high electron density (short bunch) and low for a low electron density (long bunch). However, the THz signal shows a counter-intuitive behavior with large amplitudes for long bunches and low amplitudes for short bunches. To understand this effect, a simulation with THzSMe was performed for sev-

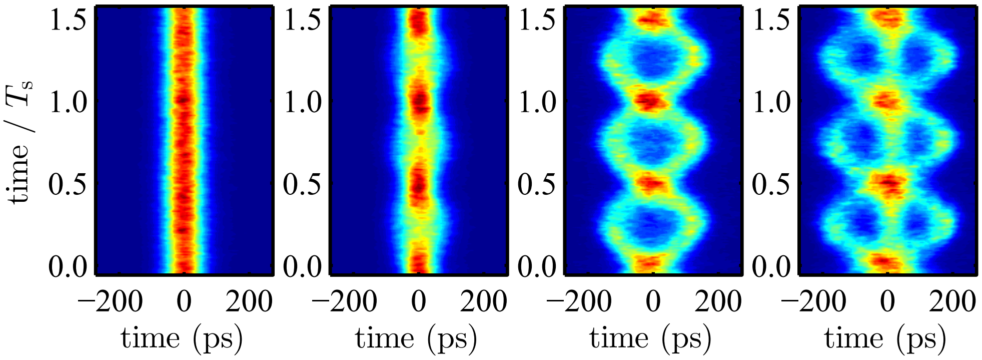

Figure 5.27.: Streak camera images showing the evolution of the longitudinal bunch profile (horizontal axis) over 1.5 synchrotron oscillation periods T_s (vertical axis) for an undisturbed beam (left) and in the presence of an RF phase modulation with increasing amplitude (left to right) [81].

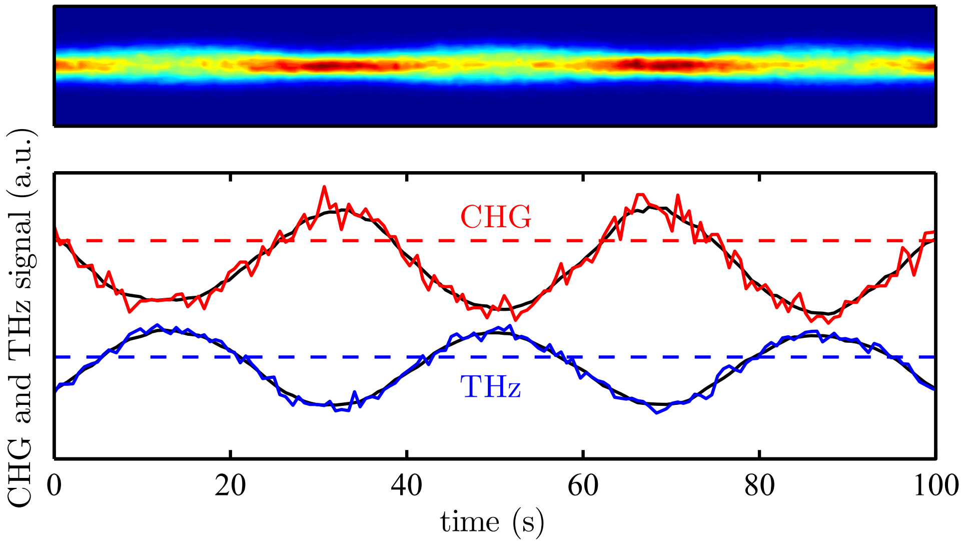

Figure 5.28.: Streak camera image (top, see Fig. 5.27) and laser-induced signals (bottom) in the presence of an RF phase modulation with $f_\mathrm{m} \approx nf_\mathrm{L}$ (see text for details) [81, 134]. The signal level with the RF phase modulation switched off is indicated by the dashed lines.

eral different energy spreads and corresponding bunch lengths. The resulting turn-1 density modulations and THz spectra are shown in Fig. 5.30. For increasing energy spread, the dip gets broader and shallower, and the spectrum is shifted to lower frequencies (with its amplitude increasing as more electrons are involved). By integrating the simulated spectrum over the sensitivity range of the InSb bolometer (indicated by red areas), the THz signal as seen by the InSb bolometer was calculated (Fig. 5.29). Although the simulated bunch length was decreased with increasing energy spread (as it is the case during the phase modulation) leading to an increased electron density, the THz signal decreases due to a reduced overlap between the emission spectrum and the sensitivity range of the detector. Thus, the InSb-THz signal is more sensitive to the energy spread than to the electron density, which explains the behavior seen in Fig. 5.28.

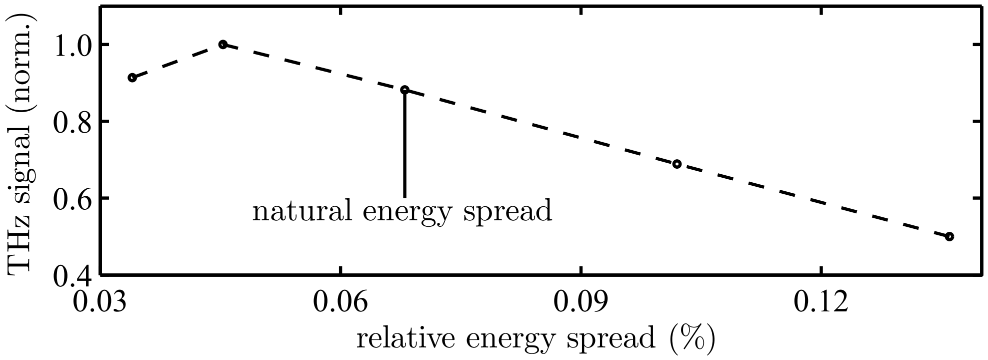

Figure 5.29.: Simulated InSb-THz signal (see text for details) versus energy spread of the electron bunch.

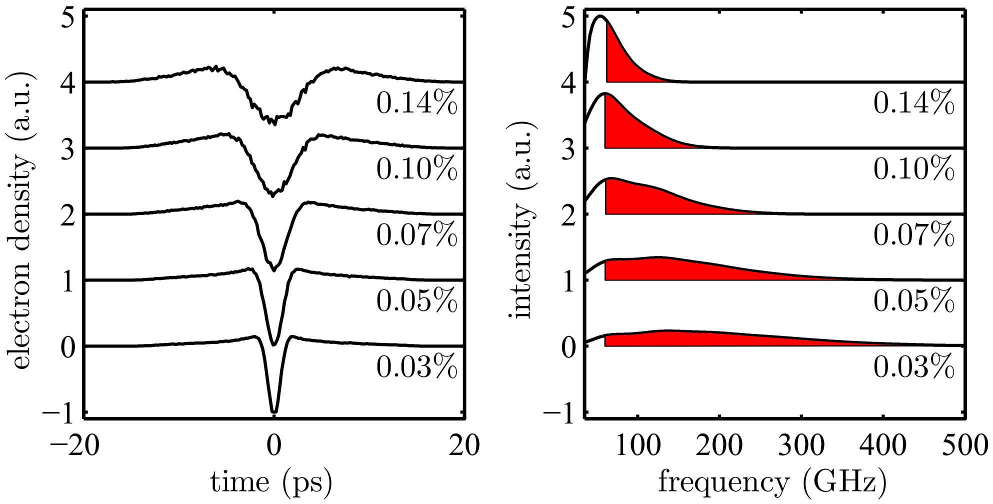

Figure 5.30.: Simulated turn-1 electron density modulation (left) and corresponding THz spectrum (right) for different energy spreads (given in %). The red areas indicate the sensitivity range of the InSb bolometer.

At certain phases of the RF modulation, the THz or CHG signals become even stronger than without modulation (dashed lines in Fig. 5.28), indicating a smaller bunch length (CHG) or smaller energy spread (THz) than it is the case for an undisturbed bunch. As a further step, the RF modulation was synchronized to the laser repetition rate f_{L}. A delay applied to the laser trigger allowed for choosing a phase of the RF modulation at which the signal level could then be kept constant for an arbitrary amount of time.

5.3. Studies of the Longitudinal Charge Distribution

5.3.1. Short-Pulse Laser Sampling

Used primarily for achieving and optimizing the longitudinal laser-electron overlap, the vector modulator (see above) can also be employed to systematically study the dependence of the laser-induced THz intensity on the longitudinal position of the laser pulse within the electron bunch [71].

Figure 5.31 shows the laser-induced THz signal intensity for several relative delays between the electron bunch and laser pulse. The data points are normalized to the squared bunch current and the error bars represent the rms signal fluctuations. The THz signal closely follows a Gaussian distribution function as indicated by the Gaussian fit (red). Due to the quadratic dependence of the THz signal on the number of electrons affected by the laser (Eq. 2.107, Ch. 5.1.3) and the almost negligible laser pulse length of about 40 fs as compared to the bunch length of about 100 ps, this curve represents the squared longitudinal charge distribution within the electron bunch. Thus, the FWHM bunch length is given by

$$\Delta t_\mathrm{b} = 2\sqrt{2\ln 2} \cdot \sqrt{2} \cdot \sigma_t = (103.3 \pm 0.7)\ \mathrm{ps} \tag{5.4}$$

with the rms width σ_t of the Gaussian least-squares fit weighted by the inverse standard deviations and the corresponding 1-σ confidence interval. This confidence interval only represents the statistical fluctuations during the measurement (e.g., a shot-to-shot variation of the laser pulse energy). Potential systematical errors include a jitter, non-linearity or inaccurate calibration of the vector modulator, a jitter of the RF or laser system, or a non-quadratic dependence of the turn-1 InSb bolometer signal on the number of electrons (e.g., due to slight shifts of the emission spectrum or detector saturation). Although a calibration of the vector modulator was performed on a few-ns level [135], non-linearities might cause local deviations on a 100-ps level, which have not been studied yet. Based on the observation of the shot-to-shot THz signal fluctuations while the laser pulse was placed on the slope of the bunch profile, the overall timing jitter is estimated to be below 20 ps. To avoid a non-linear bolometer response due to saturation, the signal voltage is kept below 1 V (for the high-gain setting of the attached

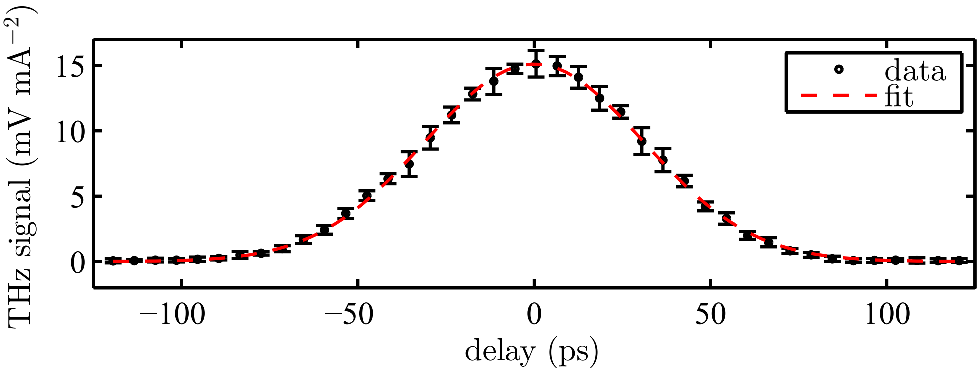

Figure 5.31.: THz signal intensity (black, turn-1 peak-to-peak data from InSb bolometer) and Gaussian fit (red) versus relative delay between electron bunch and laser pulse [71].

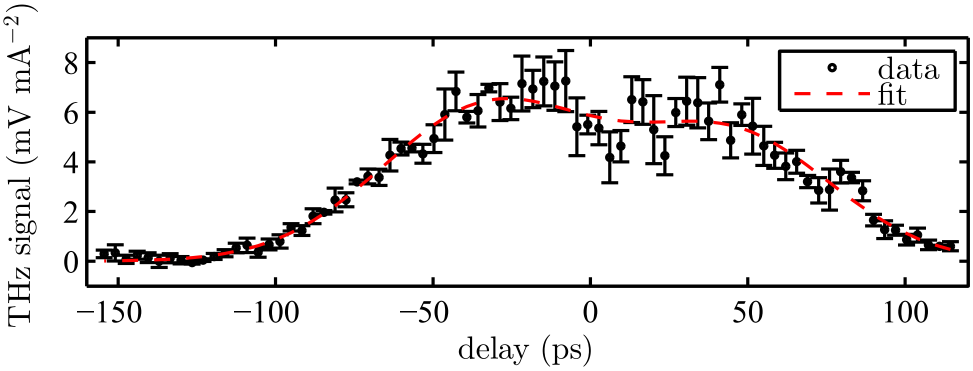

Figure 5.32.: THz signal intensity (black, peak-to-peak data from InSb bolometer) and double-Gaussian fit (red) versus relative delay between electron bunch and laser pulse during application of the RF phase modulation [71].

pre-amplifier). In conclusion, the THz-based bunch profile measurement provides a method to determine the bunch length with a low statistical uncertainty and within about 30 s to 5 minutes depending on the number of data points and the averaging time. However, due to limited knowledge of the system jitter and the calibration or linearity of the vector-modulator time scale, a dominating systematical uncertainty of the order of 10 to 20 ps must be assumed.

Figure 5.32 shows a longitudinal bunch profile recorded using the laser-induced THz signal while the previously mentioned phase modulation of the storage-ring RF was applied (without synchronization as discussed in Ch. 5.2.3). Due to the averaging of the InSb peak-to-peak data (see above), the bunch profile represents an averaged projection of the oscillation in longitudinal phase space with decreased peak intensity and strong fluctuations at the bunch center.

The bunch length also strongly depends on several storage ring parameters (see Eqs. 2.61 and 2.60). Figure 5.33 shows a measurement of the bunch length under variation of the RF power with the superconducting asymmetric wiggler (SAW) switched off and on. For comparison, the bunch length was not only measured via the THz signal as described above (black), but also via the CHG signal based on a similar analysis (blue), and by taking streak-camera images (green; independent of the laser-electron interaction). The function for the least-squares fits, weighted by the inverse 1-σ confidence intervals, is based on the analytical expression for the bunch length (see Eqs. 2.55 to 2.61)

$$\Delta t_{\mathrm{b}} \propto \sigma_z = \frac{c\alpha}{\Omega}\frac{\sigma_E}{E_0} = \frac{T_0 c}{\sqrt{2\pi}}\sqrt{-\frac{\alpha E_0}{qeV_0\cos\Psi_{\mathrm{s}}}}\frac{\sigma_E}{E_0} \tag{5.5}$$

$$\propto \sqrt{\frac{1}{eV_0\cos\Psi_{\mathrm{s}}}} \propto \sqrt{\frac{1}{eV_0\cos\{\arcsin[W/(eV_0)]\}}} \tag{5.6}$$

$$\propto \frac{1}{\sqrt[4]{(eV_0)^2 - W^2}} \propto \frac{1}{\sqrt[4]{P_{\mathrm{RF}} - C}} \tag{5.7}$$

with $C \equiv W^2/(2e^2R_{\mathrm{s}})$. Here, σ_z is the rms bunch length, c is the speed of light, α is the momentum compaction factor, Ω is the synchrotron oscillation frequency, σ_E/E_0 is the natural relative energy spread, T_0 is the revolution time, q is the harmonic number,

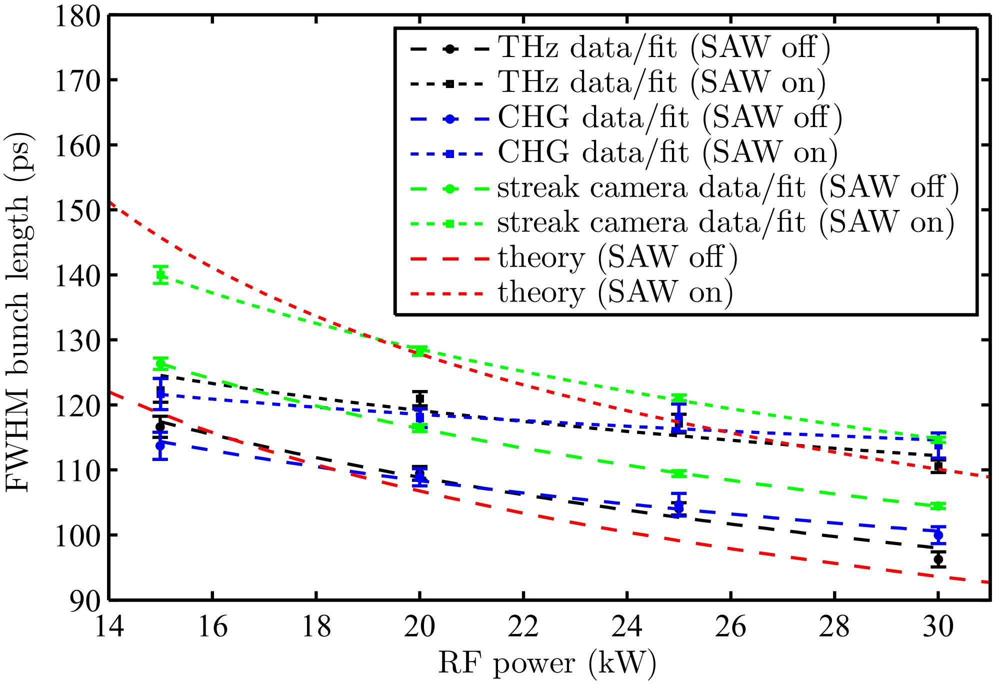

Figure 5.33.: Bunch length measured via the laser-induced THz (black) and CHG signal (blue) as well as streak-camera images (green) including fit-based 1-σ confidence intervals for several settings of the storage ring RF power and with the SAW switched off and on. See text for details about the fit functions.

V_0 is the effective accelerating RF voltage, Ψ_s is the synchronous phase, W are the synchrotron radiation losses per revolution, P_RF is the average RF power, and R_s is the shunt impedance.

Generally, a reasonable agreement between the THz and CHG data is observed. The bunch length also follows the theoretically expected increase with decreasing RF power, and the increase with the SAW switched on (which increases the energy spread). However, due to the previously mentioned systematical uncertainties, and the equally limited knowledge about storage ring parameters like the momentum compaction factor, the natural energy spread (both only known from simulations), or the absolute calibration of the RF power, deviations of the THz and CHG data from the streak camera measurements and the theoretical curve cannot be explained without independent experimental verification of these parameters.

Bunch length measurements based on the laser-sampling method were performed on more than 30 occasions over a period of four years (2011 to 2015) under various storage-ring and laser conditions. A significant dependence on the seeding wavelength or bunch current is not apparent, whereas an influence of an excitation using the longitudinal bunch-by-bunch feedback system is clearly visible (not shown here). For the standard RF power setting of 25 kW and without any deliberate excitations, an overall weighted mean of

$$\Delta \bar{t}_\mathrm{b} = (99.6 \pm 8.8)\ \mathrm{ps} \tag{5.8}$$

is calculated.

A theoretical calculation of the FWHM natural bunch length via Eqs. 2.55 to 2.61 using the parameters in Tab. 1.4, an RF voltage of 387 kV (based on a power of 25 kW, a shunt impedance of 3 MΩ [136], and a transit-time factor of 0.69), and a corresponding synchronous phase of 152.1°, leads to

$$\Delta t_{\mathrm{b,th.}} = (99.5 \pm 12.2)\ \mathrm{ps}. \tag{5.9}$$

Here, the error estimate is based on a propagation of uncertainties in the input parameters. Although this is a good match to the average experimental result, the same parameters and uncertainties lead to a theoretical synchrotron oscillation frequency of (12.8 ± 1.0) kHz, whereas the measured synchrotron frequency is about 16 kHz. This again emphasizes the need to independently verify the input parameters, which is beyond the scope of this thesis.

5.3.2. Reconstruction from Broad-Band THz Spectra

The laser-sampling technique can be employed to study the steady-state density profile of an undisturbed electron bunch, but not of the modulation introduced by the laser itself. Information about the laser-induced density modulation can instead be gained from a Fourier transform of the turn-0 coherent THz spectrum [73]. As an example, the turn-0 spectrum $I_{\mathrm{coh}}(\nu)$ and form factor times the number of electrons in the bunch $N_{\mathrm{e}}g^2(\nu)$ from seeding with 800 nm (Fig. 5.16) shall be used. After calculating the square root of the form factor $g(\nu)$ (Fig. 5.34 a), appending zeros ('zero-filling', not shown), and mirroring the data vector $\{g_i\} = g(\{\nu_i\})$ according to

$$[g_1, g_2, \ldots, g_{n-1}, g_n] \rightarrow [g_1, \ldots, g_{n-1}, g_n, g_{n-1}, \ldots, g_1] \tag{5.10}$$

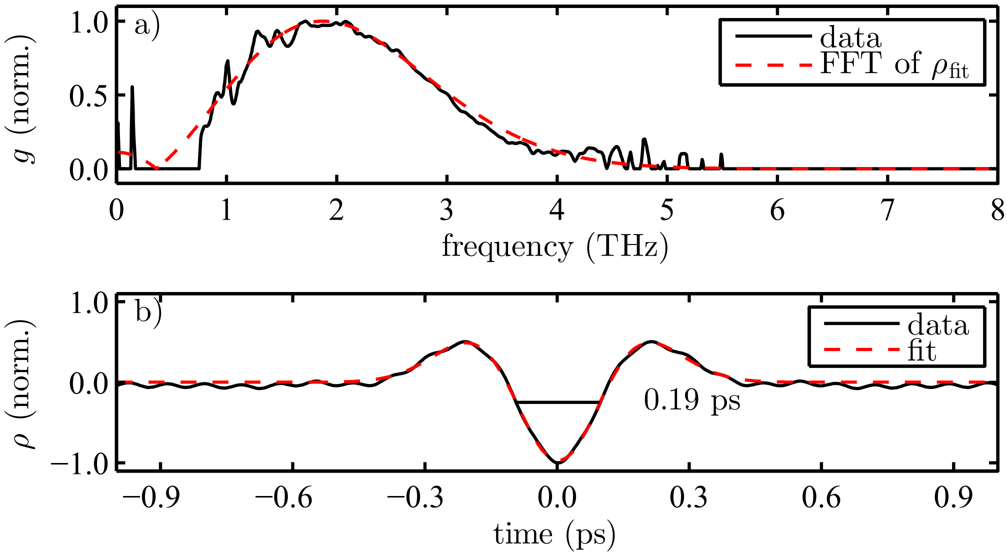

Figure 5.34.: Normalized square root of form factor (a) calculated from the turn-0 spectrum of laser-induced THz radiation recorded using 800-nm seeding (Fig. 5.16); and normalized turn-0 electron density (b) reconstructed from the form factor. A fit of the density modulation is again Fourier-transformed and shown in (a). See text for details.

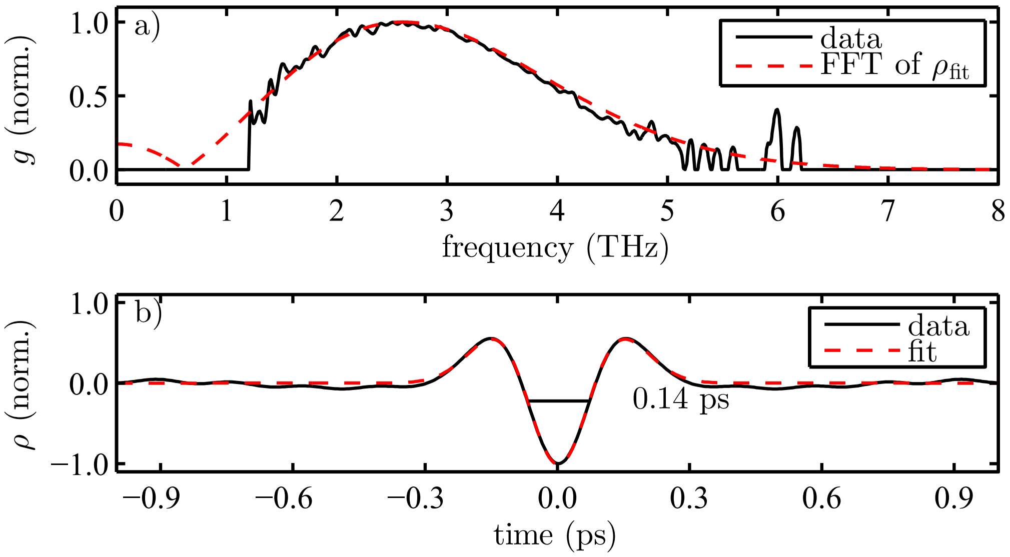

Figure 5.35.: Normalized square root of form factor (a) calculated from the turn-0 spectrum of laser-induced THz radiation recorded using 400-nm seeding (Fig. 5.15); and normalized turn-0 electron density (b) reconstructed from the form factor [73]. A fit of the density modulation is again Fourier-transformed and shown in (a). See text for details.

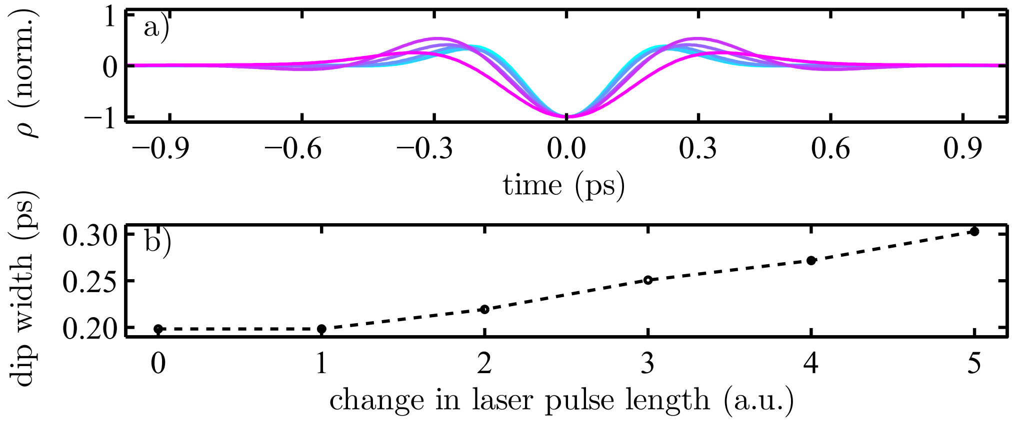

Figure 5.36.: Turn-0 electron density modulation for different laser pulse lengths reconstructed from the fitted form factors in Fig. 5.24 (a) and dependence of the dip width on the pulse length (b). For a), the laser pulse length is color-coded (cyan/short to magenta/long). See text for details.

(also not shown), an FFT is performed. The full information about the density modulation cannot be reconstructed knowing only the intensity spectrum or absolute value of g but not its phase. Instead, the density shown in Fig. 5.34 b) was calculated according to

$$\rho(t) = -\left|\mathrm{FT}[g(\nu)]\right| \cdot \mathrm{sgn}\{\mathrm{Re}(\mathrm{FT}[g(\nu)])\}, \quad t > 0. \tag{5.11}$$

The resulting curve was mirrored to $t < 0$ eliminating any asymmetries and presenting only one possible shape of the density modulation. However, the shape of the density modulation – a dip with two accompanying density maxima – is similar to the simulation result (turn 0 in Fig. 3.3), and an FFT of a double-Gaussian fit to the density modulation leads to a curve (a, red) closely matching the square root of the measured form factor (black). It is therefore assumed that $\rho(t)$ presents a close match to the actual laser-induced modulation of the longitudinal electron density. With a dip width of about 190 fs, it is also of the same order as the simulated turn-0 dip (Fig. 3.3).

A similar result is obtained for a spectrum recorded during seeding with 400 nm (Fig. 5.35). Here, the width of the dip is about 140 fs, corresponding to the increased central frequency of the 400-nm-induced THz spectrum.

For the reconstruction of the density modulation under variation of the laser pulse length from the spectra shown in Fig. 5.24, the cut-off at 1.2 THz requires to use a fit of the form factor g^2 rather than the data itself. The resulting electron densities are shown in Fig. 5.36. Corresponding to the decrease of central frequency in Fig. 5.24, the dip broadens with increasing laser pulse length as expected.

5.4. Studies of the Electron Beam Dynamics

5.4.1. Turn-By-Turn Observation of Laser-Induced THz Radiation

With its low temporal resolution and limited spectral range (Tab. A.3, Ch. 5.1.1), usually the turn-1 response is the only recognizable signal on the InSb bolometer (Fig. 5.37, black). However, during the chirped-pulse beating (CPB) experiments to generate narrow-band THz radiation with longer intensity-modulated pulses (see Ch. 5.5 for details), it was also possible to distinguish signals from several revolutions on the InSb bolometer (Fig. 5.37, red). Here, a CPB frequency in the sensitivity range of the InSb bolometer was set, and the corresponding density modulation seems to survive several revolutions in the storage ring. Still, a turn-0 response is not visible and the turn-2 and following signals appear only as small bumps on the slowly falling edge of the turn-1 response, which impedes the analysis of signal amplitudes.

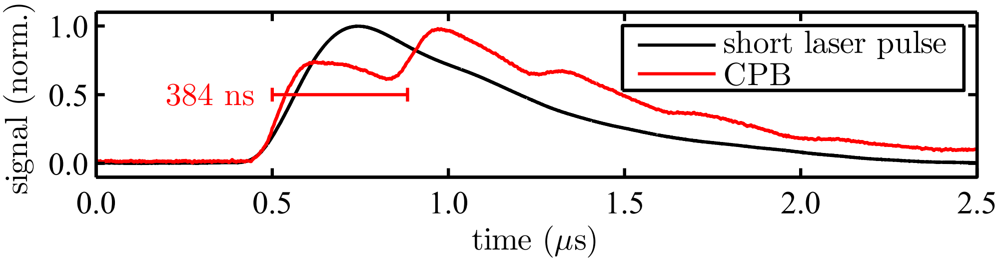

Figure 5.37.: Averaged oscilloscope traces of the InSb bolometer signal induced by a short laser pulse (about 40 fs FWHM, black) and by a long intensity-modulated pulse (via CPB, red).

Turn-by-turn-resolved studies of the THz pulses induced by a short laser pulse were made possible by employing the NbN bolometer (Tab. A.4) and YBCO detector (Tab. A.5). Figure 5.38 shows the response of both detector types and of the InSb bolometer for reference [73, 76]. Due to their high temporal resolution, the NbN and YBCO signals from single revolutions appear as sharp peaks and allow their amplitude to be extracted, e.g., for the studies presented below. Also the turn-0 signal is visible

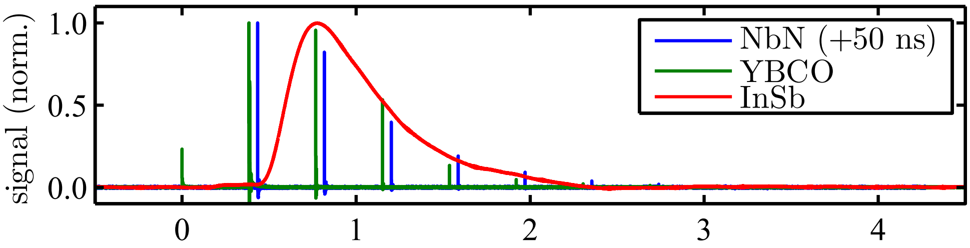

Figure 5.38.: Averaged oscilloscope traces of the NbN bolometer (blue), YBCO detector (baseline shift corrected, green), and InSb bolometer signal (red) induced by a short laser pulse [73, 76]. The NbN trace is shifted by 50 ns for better visibility.

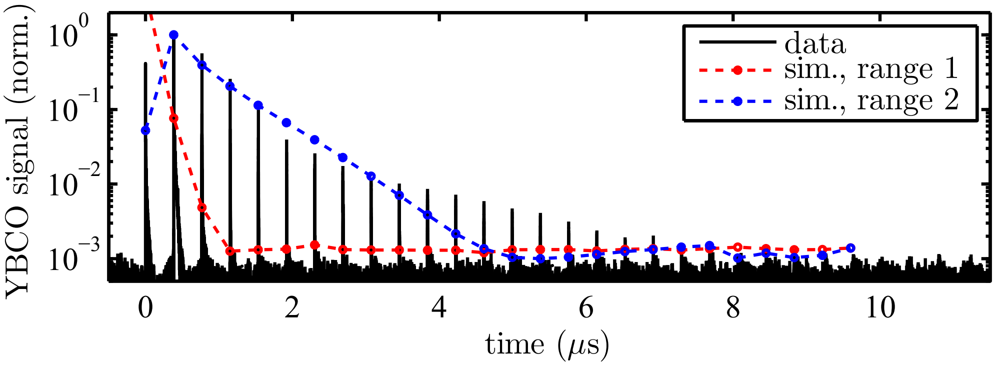

Figure 5.39.: Averaged oscilloscope trace of the YBCO signal induced by a short laser pulse (black) [137], and simulated YBCO response for a sensitivity range of 0.1 to 2.5 THz ('range 1', red) and for a sensitivity range of 20 to 500 GHz ('range 2', blue, see text for details).

on the YBCO response, but not on the NbN response due to the attenuator employed during this measurement, which blocked the turn-0 radiation frequencies in front of the detector. The exponential decay of signal intensities is related to the decreasing density modulation amplitude and the spectral shift to lower frequencies (Figs. 3.3 to 3.5).

Using a 63-GHz oscilloscope kindly provided by Keysight Technologies Deutschland GmbH, signals from up to 20 revolutions after the laser-electron interaction were observed (Fig. 5.39, black) [137]. Here, the increased temporal resolution of the read-out electronics in combination with the ultrafast YBCO response and its high dynamic range allowed detecting extremely weak signals and distinguishing them from the noise. A simulation of the turn-by-turn YBCO response based on an integration of the spectra from the THzSMe run described in Ch. 3.2.1 over the YBCO sensitivity range of 0.1 to 2.5 THz (red) shows a different behavior with only turn 0 to turn 2 visible above the noise level. With a decreased sensitivity range of 20 to 500 GHz (blue), the measured

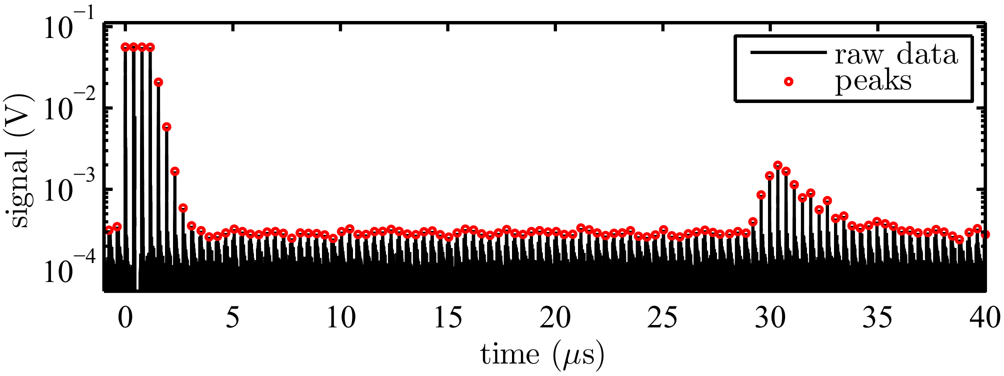

Figure 5.40.: Averaged oscilloscope trace of the SBD signal induced by a short laser pulse (black) and extracted peak amplitudes (red). The peaks of the first four coherent signals are cut off due to a reduced voltage scale set on the oscilloscope.

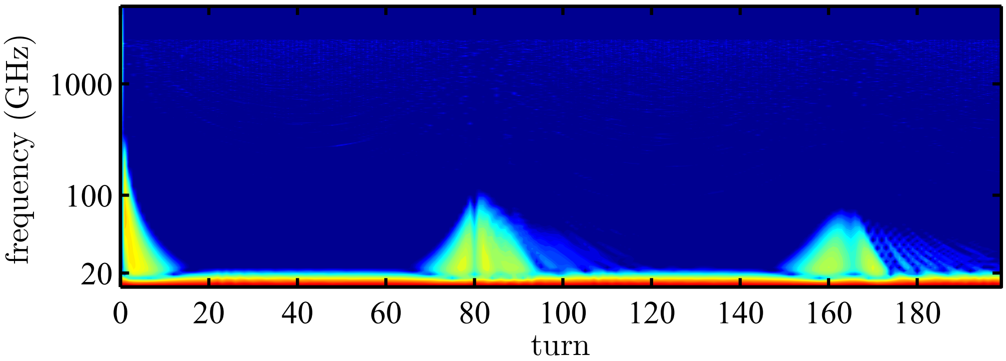

Figure 5.41.: Simulated spectral intensity (logarithmic, color-coded) versus turn number and frequency based on the THzSMe run described in Ch. 3.2.1.

response is reproduced more closely. This indicates that either the simulated spectra provide lower frequencies than the real spectra (e.g., due to different laser parameters during the measurement), or that the YBCO detector provides a significant sensitivity at frequencies below its nominal range. It should be mentioned that the detector sensitivity is a not well known function of the frequency and depends on the antenna design and YBCO properties, whereas a constant sensitivity curve (over the given range) was assumed for the simulation results.

The Schottky-barrier diode (SBD) also allows resolving single-turn signals [137]. In contrast to the measurements performed with the NbN bolometer or YBCO detector, the laser-induced signal re-appears after about 30 µs, corresponding to turn 79 (Fig. 5.40). This is related to the increase in central frequency after half a synchrotron oscillation period due to the rotation of the energy modulated electrons in longitudinal phase space by 180° (Fig. 3.2). Based on the THzSMe run described in Ch. 3.2.1, Fig. 5.41 shows the simulated emission spectrum for turns 0 to 199. The strong and constant intensity below 15 GHz is caused by the coherent emission of the entire bunch. After half a synchrotron oscillation period, the spectral content of the laser-induced intensity rises up to 100 GHz, and again after a full period to about 80 GHz. The fact that these signals only appear on the SBD, but have never been observed with the other

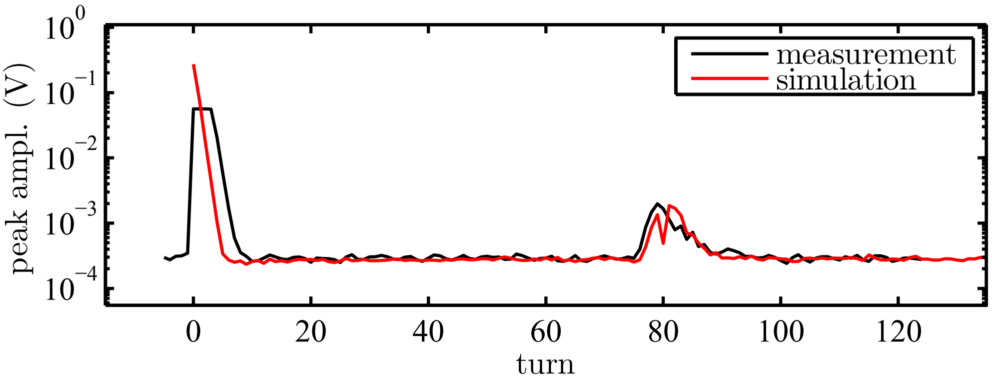

Figure 5.42.: Extracted peak amplitudes from Fig. 5.40 (black) and simulated SBD response (red, spectra from Fig. 5.41 integrated over the nominal SBD sensitivity range).

detector types, is attributed to the low-frequency sensitivity range of the SBD ranging from 50 GHz to 1.2 THz (Tab. A.7). The measured peak intensities and a simulated SBD response are shown in Fig. 5.42. The experimental data is well matched by the simulated curve.

5.4.2. Variation of the Laser-Electron Overlap and Storage Ring Parameters

The influence of several laser and storage ring parameters on the turn-1 signal detected by the InSb bolometer were discussed in Ch. 5.2. By extracting the peak amplitude of single revolution signals from oscilloscope traces of the NbN-bolometer and YBCO-detector response, it is also possible to study the influence of laser and storage ring parameters on the turn-0, turn-2, and higher-turn signals.

Variation of the Delay Between Laser Pulse and Electron Bunch

Figure 5.43 shows the THz signal of turns 0 to 4 under variation of the delay between laser pulse and electron bunch recorded using the NbN bolometer [73] and both, the prototype (1) and permanently installed (2) YBCO detectors. The selection of turn curves shown in each case depends on the attenuators employed (which might block the turn-0 signal due to a spectral cut-off) and the general signal strength during the measurement (which might cause higher-turn signals to be dominated by noise).

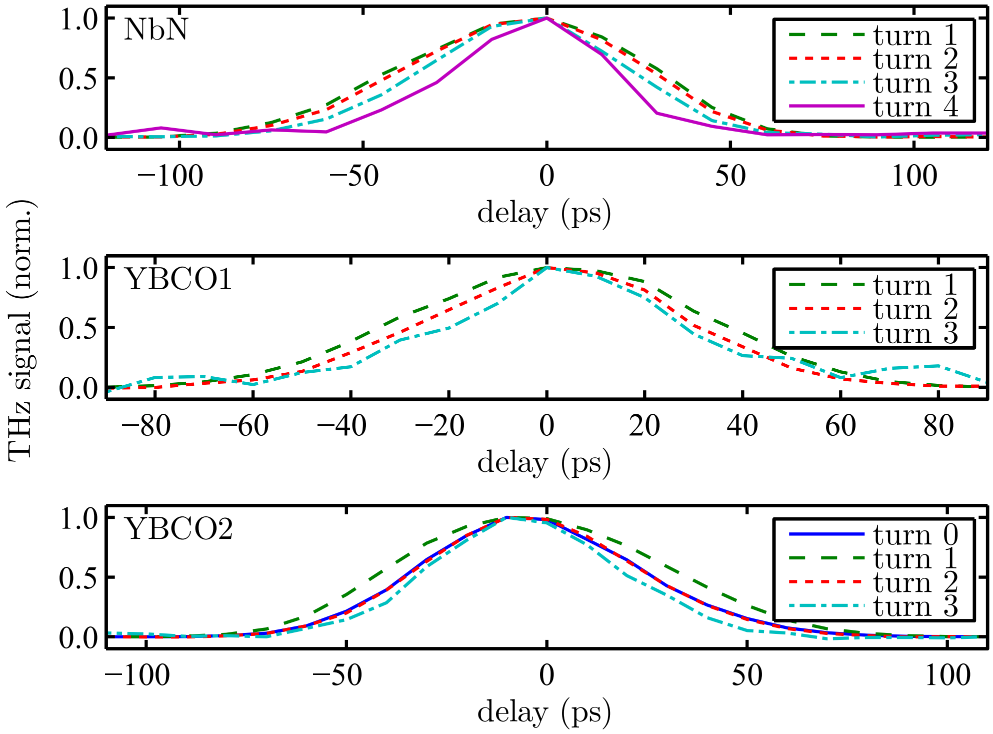

Figure 5.43.: Normalized turn-by-turn peak amplitudes extracted from oscilloscope traces of the NbN bolometer [73] and YBCO detectors (1: prototype, 2: permanently installed) under variation of the longitudinal overlap between laser pulse and electron bunch.

Compared to the turn-0, turn-2, and higher-turn profiles, all three measurements show an increased width of the turn-1 profile. The turn-0 and turn-2 profiles in the second YBCO measurement are almost identical, and for higher-turn profiles all of the three measurements show a further decrease in profile width. As described in Chs. 5.2 and 5.3.1, the general profile shape is given by the decreasing electron density when moving the laser pulse towards the head or tail of the electron bunch. Differences in the turn-by-turn profiles can only be caused by different decay rates of the turn-by-turn density modulation depending on its position inside the bunch, or by spectral changes in combination with the detector sensitivity ranges.

The increased width of the turn-1 profile shown in Fig. 5.43 is not reproduced by a THzSMe simulation (Fig. 5.44). Instead, the turn-1 and higher-turn profiles show an asymmetry between negative and positive delays. By looking at the simulated density modulations and form factors (not shown), the asymmetry of the simulated profiles can be attributed to the asymmetric RF potential (see Fig. 3.2), which smears out the density modulation stronger for positive laser-electron delays than for negative delays, resulting in weaker THz radiation intensities at positive delays especially for higher-turn signals. A weaker asymmetry is also present in the experimental results (Fig. 5.43), which can be explained by a weaker energy modulation amplitude during the experiment. This was verified by a second simulation with reduced laser pulse energy (not shown). A more detailed study with measurements and simulations of these turn-by-turn-resolved longitudinal bunch profiles under variation of several other parameters might give further insight into the longitudinal phase space dynamics, but this is beyond the scope of the thesis.

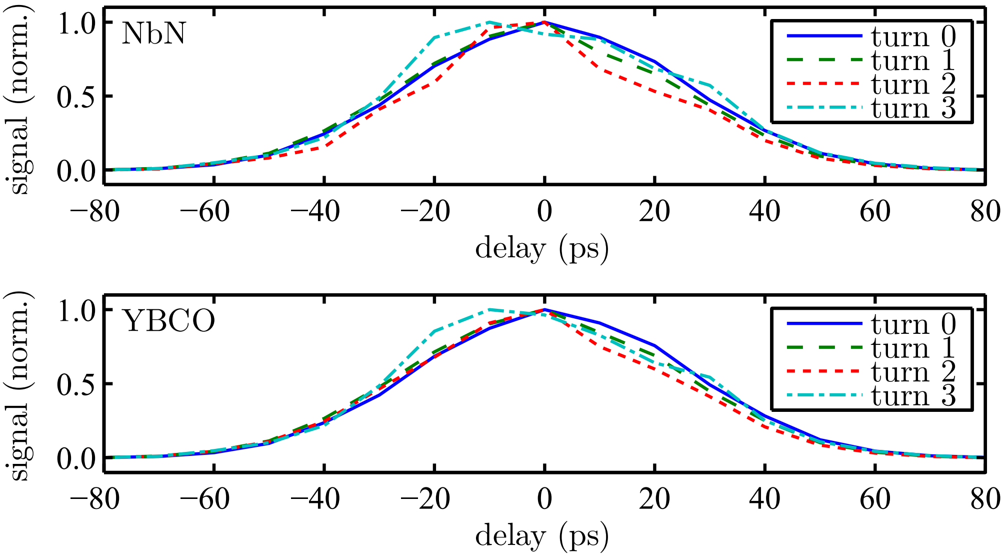

Figure 5.44.: Normalized turn-by-turn peak amplitudes extracted from a THzSMe simulation under variation of the longitudinal overlap between laser pulse and electron bunch, with the NbN-bolometer and YBCO-detector response based on the simulated spectra integrated over the corresponding nominal sensitivity ranges.

Variation of the Transverse Overlap

Under variation of the horizontal overlap between laser pulse and electron bunch by tilting the M2 mirror in BL3 horizontally, turn-by-turn-resolved profiles corresponding to the convolution between the horizontal laser-waist and electron-bunch size were recorded (Fig. 5.45). A significantly reduced width of the turn-0 profiles is observed, whereas the turn-1 and higher-turn profiles show a similar width. This is well reproduced by a corresponding THzSMe simulation (Fig. 5.46) and can be explained by a spectral shift of the form factors (not shown). From zero to an offset of, e.g., ±415 μm, the simulated central frequency of the turn-0 form factor increases from 1.8 to 2.3 THz, and of the higher-turn form factors accordingly. While the shift of the higher-turn form factors does not influence the detector signals, the turn-0 form factor is shifted beyond the upper sensitivity limit of the detectors for non-zero horizontal offsets, thereby reducing the relative signal intensity and profile width. The same behavior was observed for vertical offsets (not shown), only with a reduced general profile width due to the reduced vertical size of the electron bunch.

The spectral shift is motivated for turn 0 in Fig. 5.47 showing the simulated density modulations. The dominating effect is given by the reduced width and distance of the density maxima for a horizontal offset (left) or (much weaker) for a vertical offset (right), which leads to the increased central frequency of the form factor. The reduced width and distance of the density maxima is caused by a reduced energy modulation amplitude of the majority of the electrons in the center of the bunch, which experience a reduced electric field on the slope of the displaced laser pulse.

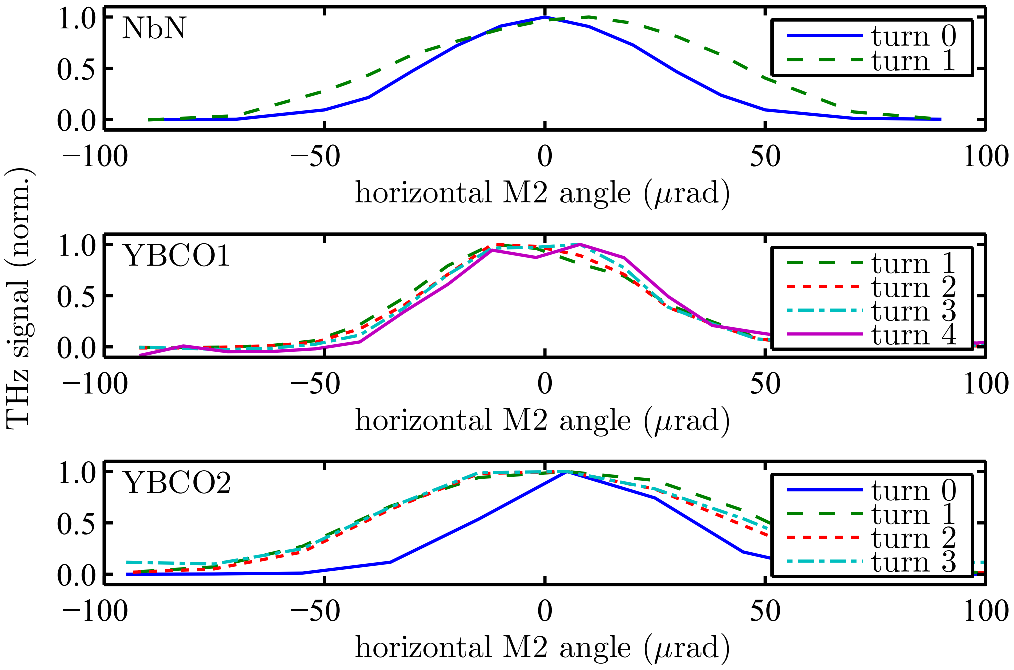

Figure 5.45.: Normalized turn-by-turn peak amplitudes extracted from oscilloscope traces of the NbN bolometer [73] and YBCO detectors (1: prototype, 2: permanently installed) under variation of the horizontal angle of BL3 mirror M2.

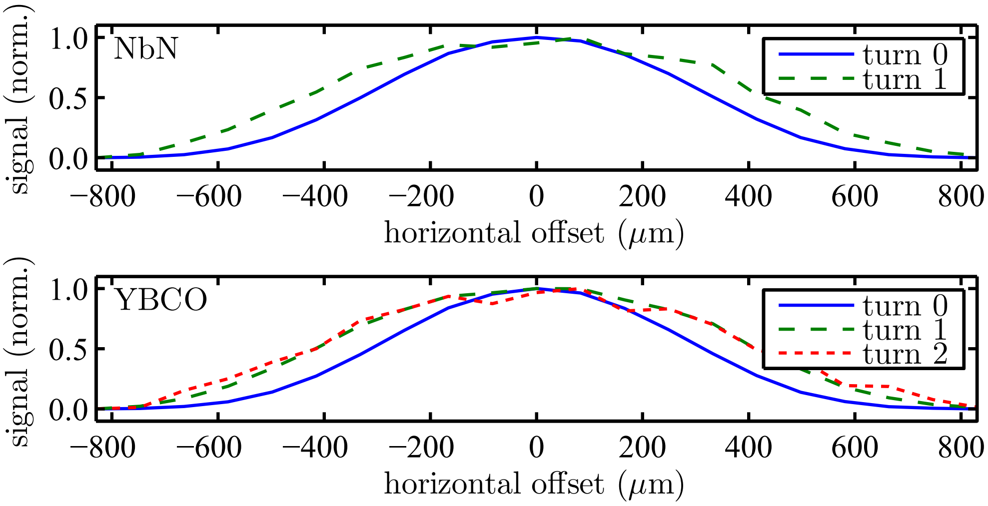

Figure 5.46.: Normalized turn-by-turn peak amplitudes extracted from a THzSMe simulation under variation of the horizontal overlap between laser pulse and electron bunch, with the NbN-bolometer and YBCO-detector response based on the simulated spectra integrated over the corresponding nominal sensitivity ranges.

This explanation is supported by the experimentally observed dependence of the turn-by-turn peak amplitudes on the laser pulse energy (Fig. 5.48). Here, the turn-0 signal also shows a stronger decrease with decreasing pulse energy than the higher-turn signals due to the same reduction in width and distance of the density-modulation maxima and the corresponding shift of the turn-0 form factor.

Figure 5.47 also shows an asymmetry of the density modulation depending on the horizontal laser offset. For example, the density maximum arriving first ($t < 0$) is more pronounced for a negative horizontal offset (blue). Here, the electrons closer to the storage ring center receive a stronger energy modulation and then move on an even shorter dispersion orbit, which leads to an enhancement of the density maximum arriving first.

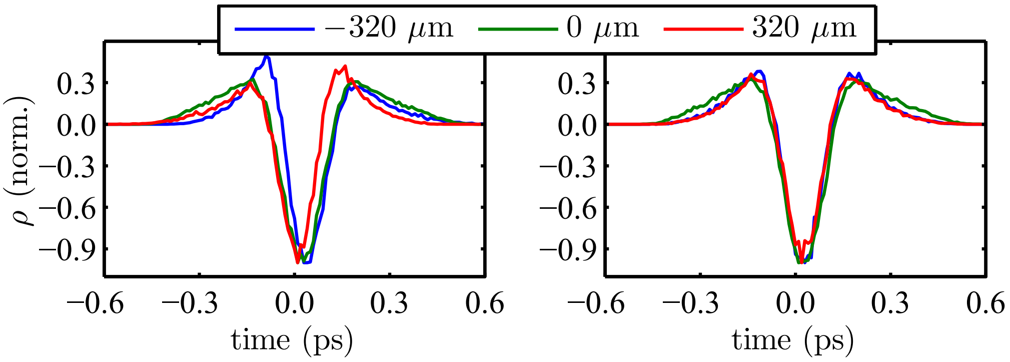

Figure 5.47.: Normalized turn-0 density modulation from a THzSMe simulation with a horizontal (left) and vertical (right) offset between laser pulse and electron bunch of −320 µm (blue), 0 µm (green), and +320 µm (red).

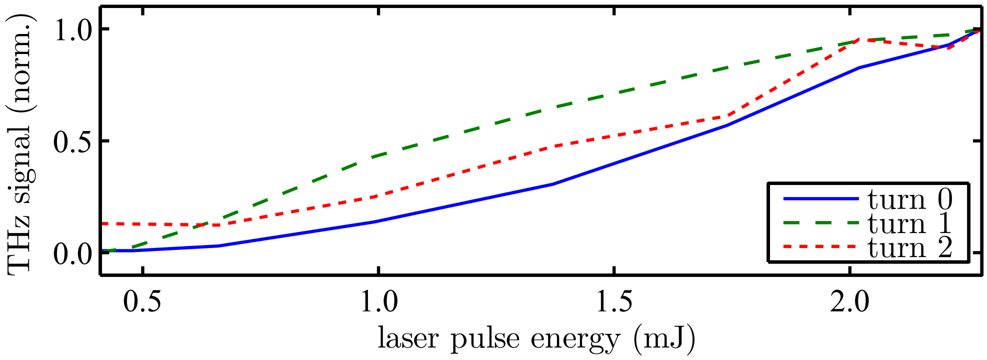

Figure 5.48.: Normalized turn-by-turn peak amplitudes extracted from oscilloscope traces of the NbN bolometer under variation of the laser pulse energy.

Use of the Radiator as a Second Modulator

The radiator (second half of the undulator U250) is usually tuned to a harmonic of the seeding wavelength for generation of VUV radiation based on the CHG principle. When tuned to the seeding wavelength, both sections of the U250 act as a modulator. The chicane now causes a variable phase shift between laser pulse and electron bunch due to the introduced longitudinal path length difference. Depending on the chicane current, the electron bunch lags behind the laser pulse by a variable distance, and the energy modulations in the first and second half of the U250 either add up or partially cancel, resulting in an intensity modulation of the laser-induced THz signal (Fig. 5.49). Although a slight phase shift between the turn-0 and both turn-1 signal oscillations is observed, which needs further analysis, all signals show the same number of about 8.5 oscillations between 300 and 700 A, corresponding to a phase advance of $8.5 \cdot 400$ nm $=$ 3.4 μm, which is close to the value determined independently by measurements of optical klystron spectra [77].

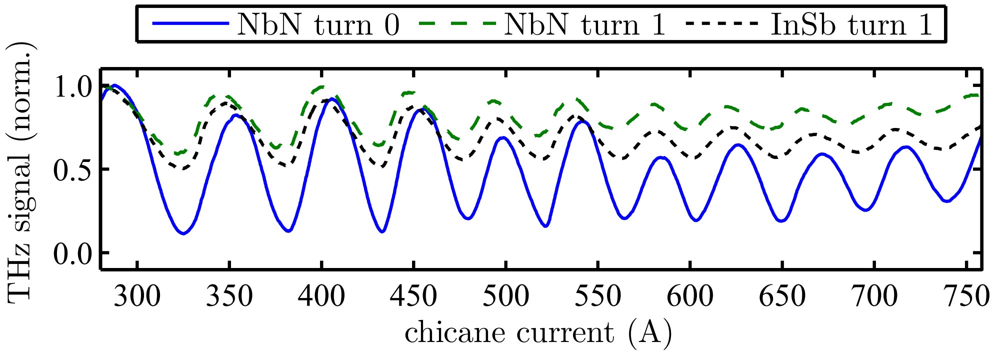

Figure 5.49.: Normalized turn-0 and turn-1 peak amplitudes extracted from oscilloscope traces of the NbN bolometer and signal from the InSb bolometer (also providing the turn-1 intensity) under variation of the chicane current. Both, modulator and radiator, were set to the seeding wavelength of 400 nm.

Variation of the Modulator Wavelength

The dependence of the turn-0 (blue) and turn-1 (green) THz signals on the resonant wavelength of the modulator (see [138]) is shown in Fig. 5.50 for a seeding wavelength of 400 nm. Next to the maximum at 400 nm, the typical sinc-function side lobes of the undulator spectrum (red, Eq. 2.79) appear in both revolution signals. However, the turn-1 response shows a reduced distance between the side lobes, which needs further examination.

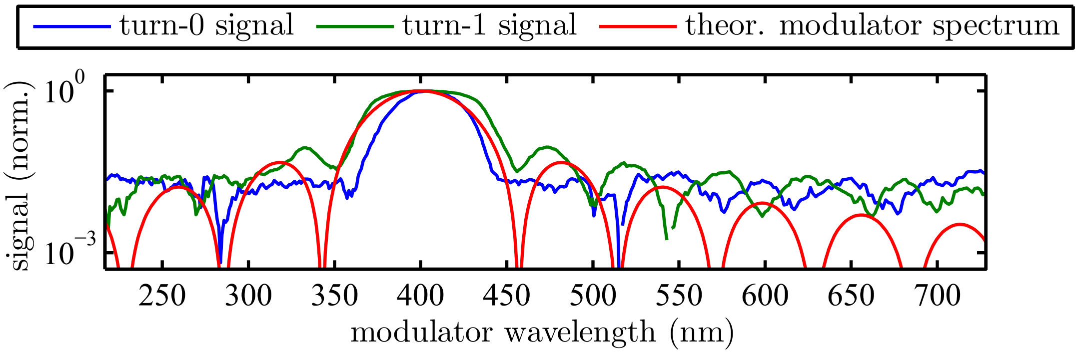

Figure 5.50.: Normalized turn-0 and turn-1 peak amplitudes extracted from oscilloscope traces of the NbN bolometer and theoretical spectrum of the modulator (Eq. 2.79) under variation of the modulator wavelength. The seeding wavelength was set to 400 nm.

Variation of the RF Power

Coming back to the Schottky-barrier diode (SBD)-based measurements discussed above, the re-appearance of the laser-induced THz signal after half a synchrotron oscillation period was also studied under variation of the storage-ring RF power P_{RF}. Figure 5.51 shows the peak amplitudes similar to Fig. 5.42, but for different RF powers between 14 and 30 kW. A shift of the reappearing signal to lower turn numbers is observed, corresponding to an increase of the synchrotron oscillation frequency Ω, which agrees well with the theoretical expression $\Omega \propto \sqrt[4]{P_{\mathrm{RF}} - C}$ (see Eqs. 2.60 and 5.7).

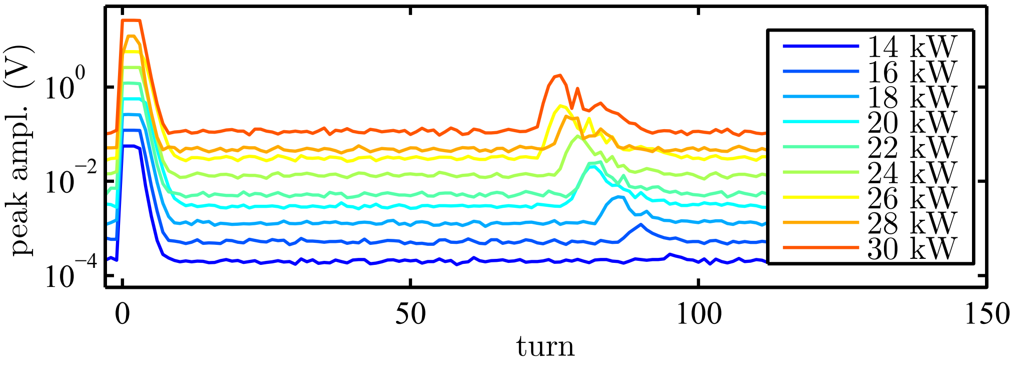

Figure 5.51.: Normalized peak amplitudes extracted from SBD measurements performed at different storage-ring RF powers (see legend).

5.5. Generation of Narrow-Band THz Radiation

5.5.1. Experimental Setup

Experiments based on chirped-pulse beating (CPB) were performed at DELTA in 2014 [76] in cooperation with a group from PhLAM at the University Lille 1, France, who temporarily provided essential components for the setup described below and, more importantly, shared their valuable knowledge and experience gained from employing CPB at UVSOR in Okazaki, Japan [98, 99].

Figure 5.52 shows a sketch of the optical table in the laser laboratory. During standard operation of the short-pulse facility, the internal compressor of the laser amplifier is set to full compression. From the outgoing 800-nm beam (red, solid), 10% are split off and sent to the pump-pulse beamline (green), and 90% bypass the reflective 400-nm telescope and enter BL3 with its refractive 800-nm telescope further downstream. Alternatively, the beam is reflected into the SHG unit (blue) and the generated 400-nm radiation is focused by the reflective telescope and then sent into BL3. For the CPB setup, the internal compressor of the amplifier was detuned (see below) and a temporary beam path (red, dashed) was established, sending the 800-nm pulses to a Michelson interferometer provided by PhLAM and then back to the original 800-nm path. After the Michelson interferometer, about 1% of the intensity was split off and sent to a far-field camera (camera in the focal point behind a lens) and an optical intensity-autocorrelator (see below), both also provided by PhLAM. The far-field camera is very sensitive to an angular offset and was used to (re-)adjust the optics especially within the Michelson interferometer, while the autocorrelator was employed to measure the pulse length and modulation frequency.

The Michelson interferometer and the autocorrelator are sketched in Fig. 5.53. Corner-cube retroreflectors are used to ease the adjustment and to provide the transverse offset necessary either to hinder the back-reflected beam from re-entering the amplifier using a beam block (5), or to have two parallel beams which can be focused (10)

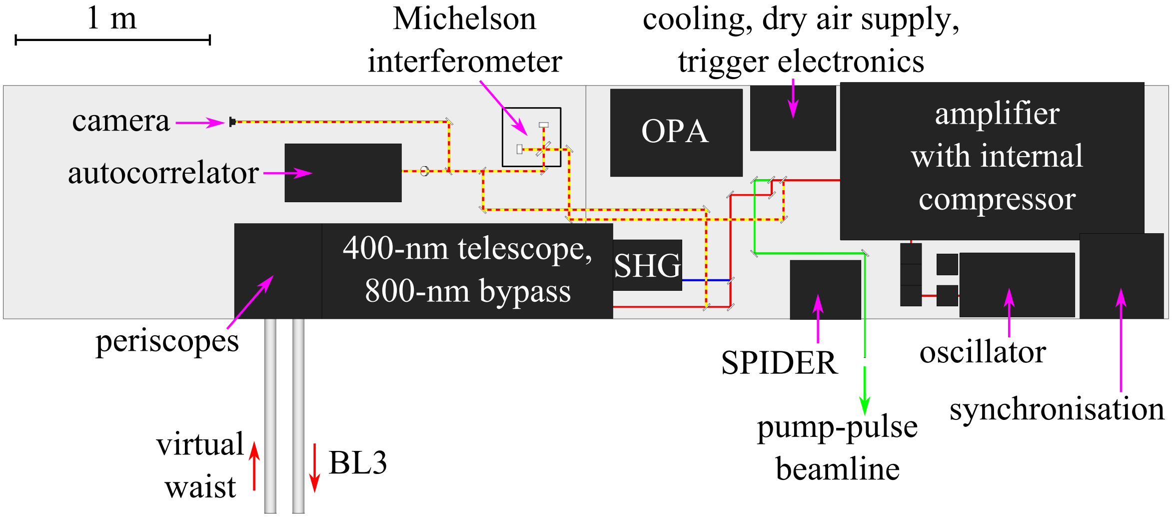

Figure 5.52.: Sketch of the optical table in the laser laboratory with the permanently installed components and the temporary CPB setup (Michelson interferometer, autocorrelator, and camera).

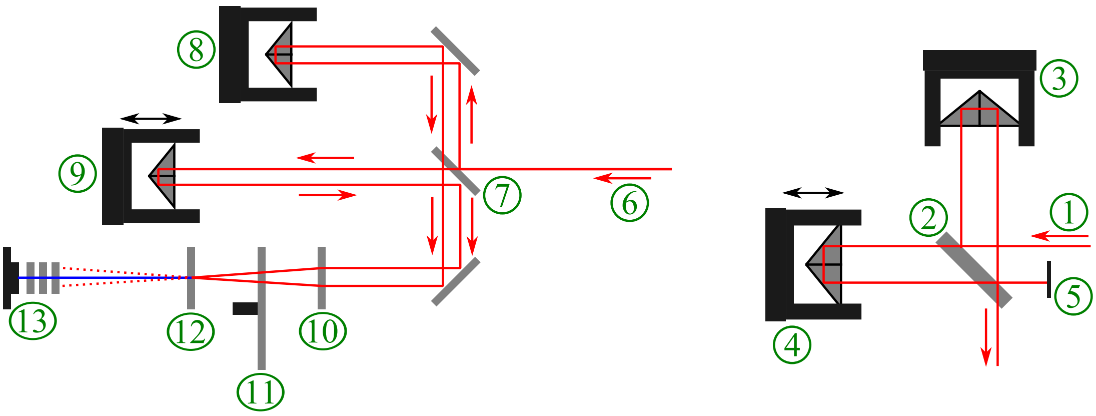

Figure 5.53.: Sketch of the autocorrelator (left) and Michelson interferometer (right) with the incoming beam from the amplifier (1), a 50:50 beam splitter (2), a fixed retroreflector (3), a retroreflector on a motorized linear stage (4), a beam stop (5), the incoming beam of the autocorrelator (6), a 50:50 beam splitter (7), a fixed retroreflector (8), a retroreflector on a motorized linear stage (9), a focusing lens (10), a variable attenuator (11), a BBO crystal (12), and a photodiode with additional attenuators (13).

to meet at the BBO crystal of the autocorrelator (12) with a crossing angle. The latter is the basis for optical intensity-autocorrelation. Here, the retroreflector on the linear stage (9) is continuously moved in order to slowly vary the delay τ_{ac} between both outgoing pulses with electrical fields $E(t)$ and $E(t-\tau_{\mathrm{ac}})$. In the BBO crystal, a second-harmonic signal is generated with an intensity proportional to

$$\begin{aligned} I_{\mathrm{SHG}} &\propto |E(t)+E(t-\tau_{\mathrm{ac}})|^2 = \left|E^2(t)\right|^2 + 2\,|E(t)E(t-\tau_{\mathrm{ac}})|^2 + \left|E^2(t-\tau_{\mathrm{ac}})\right|^2 && (5.12)\\ &\propto I^2(t) + 2I(t)I(t-\tau_{\mathrm{ac}}) + I^2(t-\tau_{\mathrm{ac}}). && (5.13)\end{aligned}$$

However, due to the crossing angle, only the signal proportional to $I(t)I(t-\tau_{\mathrm{ac}})$ is propagating on-axis to the photodiode, providing a background-free autocorrelation signal. The slow photodiode then records an integrated signal

$$I_{\mathrm{pd}}(\tau) \propto \int I(t)I(t-\tau_{\mathrm{ac}})\mathrm{d}t. \tag{5.14}$$

For an incoming Gaussian-shaped pulse, the autocorrelation signal $I_{\mathrm{pd}}(\tau)$ provides a Gaussian shape with a width of $\sqrt{2}$ times the incoming pulse length. Furthermore, the intensity modulation of a CPB pulse is reproduced allowing the modulation frequency to be measured.

5.5.2. Results and Discussion

Autocorrelator Measurements

An example for an autocorrelator measurement is shown in Fig. 5.54. For the abscissa, the slow time scale t_{pd} of the photodiode signal (based on the slow movement of the retroreflector on the linear stage) is converted to the delay of the internal Michelson

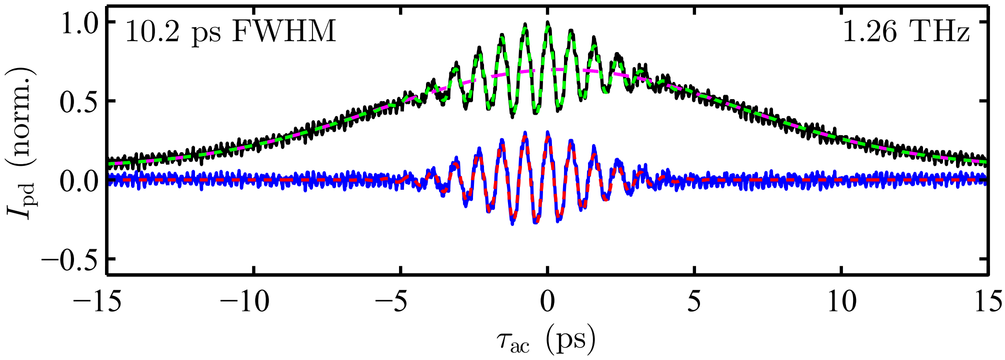

Figure 5.54.: Autocorrelator trace (black), modulation trace (blue, original trace minus Gaussian pulse shape), and corresponding fit functions (dashed). See text for details.

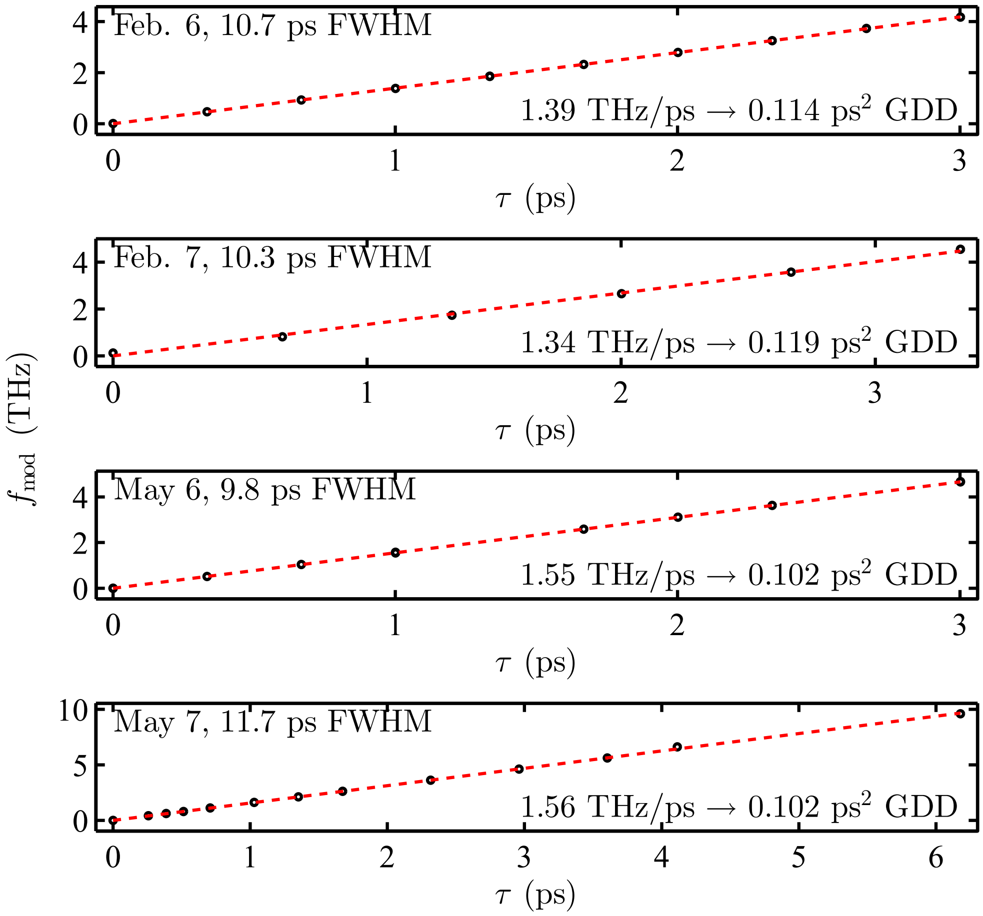

Figure 5.55.: Dependence of the modulation frequency f_{mod} on the delay τ introduced by the Michelson interferometer. The day of the experiment (all in 2014) and the mean pulse length extracted from all autocorrelator traces are indicated in each plot, as are the slope of a linear fit and the resulting GDD calculated via Eq. 5.17.

interferometer according to

$$\tau_{\mathrm{ac}} = 2\frac{t_{\mathrm{pd}} \cdot v_{\mathrm{lin}}}{c} \tag{5.15}$$

with the speed of the linear stage $v_{\mathrm{lin}} = 2$ mm/s, the speed of light c, and the factor 2 accounting for the double path to the mirror and back. The pulse length is extracted from a Gaussian fit (magenta) to the trace (black). After subtraction of the Gaussian pulse shape, only the oscillation caused by the periodic intensity modulation of the laser pulse remains (blue), and a function proportional to

$$\exp\left[-\frac{1}{2}\left(\frac{\tau_{\mathrm{ac}} - \tau_{\mathrm{ac},0}}{\sigma_{\tau,\mathrm{ac}}}\right)^2\right] \cdot \sin(f_{\mathrm{mod}}\tau_{\mathrm{ac}} + \phi_0) \tag{5.16}$$

is used for fitting (red) and extraction of the modulation frequency f_{mod}.

Based on this approach, the pulse lengths Δt and modulation frequencies f_{mod} for several delay settings τ of the main Michelson interferometer were calculated and are shown in Fig. 5.55 for four independent measurements. Due to slightly different settings of the compressor in the laser amplifier, the pulse length varies from day to day. A linear dependence between τ and f_{mod} is observed in accordance with (see Eq. 2.23)

$$f_{\mathrm{mod}} \approx \frac{\tau}{2\pi|D_2|}, \tag{5.17}$$

which allows the group delay dispersion D_2 to be extracted from a fit (red). With $\Delta t = 10.6$ ps and $D_2 = 0.11$ ps^2 (average from all four measurements), the Fourier-limited pulse length of the laser system is (see Eq. 2.15)

$$\Delta t_{\mathrm{min}} = \frac{\sqrt{2}\zeta}{\sqrt{\sqrt{\Delta t^4 - 4\zeta^2} + \Delta t^2}} = 28.8 \text{ fs} \quad \text{with} \quad \zeta \equiv 4D_2 \ln 2, \tag{5.18}$$

which is even shorter than the previously assumed value of 40 fs.

THz Spectra and Gain Curve

Spectra of the narrow-band THz radiation were recorded using the FTIR spectrometer in combination with the Mylar-multilayer beam splitter, the Si bolometer, and the lock-in amplifier (Ch. 5.1.3). Each spectrum was normalized to the squared bunch current during the measurement and divided by a separately measured spectrum of the incoherent synchrotron radiation. The resulting form factors from independent sweeps of the target frequencies performed on three different days in 2014 are shown in Figs. 5.56 to 5.58 (top) together with the extracted gain curves (bottom, see Eq. 2.91 and Fig. 2.15). The following conclusions can be drawn from these results:

- Spectral widths (FWHM) between about 210 GHz (May 7) and 450 GHz (February 6) at 3 THz central frequency were achieved. As compared to a width of 1.5 THz for the coherent spectrum induced by an ultrashort laser pulse (Fig. 5.16), the goal of generating narrow-band THz radiation was fulfilled.
- The individual target frequencies resulting from the autocorrelation measurements are well matched by the corresponding form factors, indicating a correct calibration of all components and a general agreement with the underlying theory.

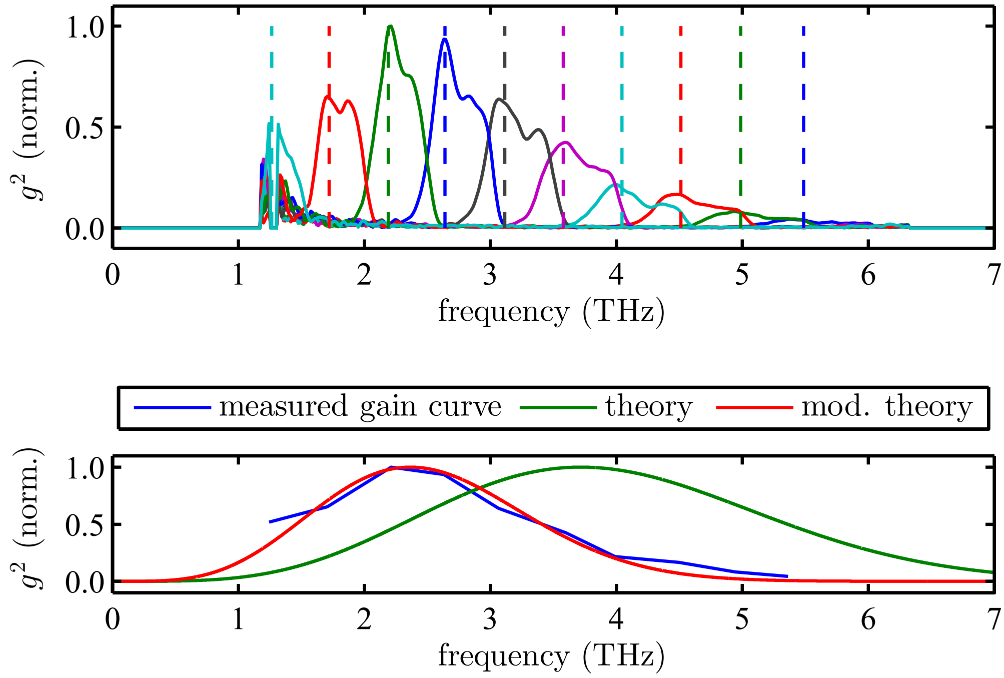

Figure 5.56.: Top: Form factors (solid) based on narrow-band THz spectra recorded on February 6 via the lock-in method for different target frequencies (dashed) [76]. Each spectrum was normalized to the corresponding squared bunch current and divided by a separately measured spectrum of incoherent synchrotron radiation to retain the form factor. Bottom: Gain curve extracted from the measured form factors (blue), theoretical turn-0 gain curve (green, see Fig. 2.15), and theoretical gain curve with modified parameters (red, 105% increase of $r_{56} \cdot \sigma_E$).

- Due to the dispersive properties of the DELTA magnet lattice resulting in a high-frequency turn-0 form factor, narrow-band THz radiation could be generated at up to 5.5 THz. Previous experiments performed at UVSOR could only be performed in the sub-THz range [98, 99].
- The spectral width increases with increasing target frequency, which was predicted for the case of a quadratic chirp of the laser pulse (Fig. 2.6).
- Considering the May-6 measurement, the spectral width increases from about 160 GHz at 1.6 THz to 380 GHz at 5.5 THz. With the numerical simulation for Fig. 2.6 predicting bandwidths of 170 and 555 GHz (including the factor of $1/\sqrt{2}$ discussed in Ch. 3.2.2), the effect of third-order dispersion is much smaller in the measurement as compared to the numerical prediction.
- The form factors display a double- or triple-peak shape which cannot be explained by the theory discussed in Ch. 2.1.2. A possible explanation is given below.
- The gain curves extracted from the combination of all corresponding form factors (blue) do not match the theoretical prediction given by Eq. 2.91 (green). Instead, the experimental gain curves are well matched assuming a 105% increase (factor of 2.05) of the transport matrix element r_{56} times the natural energy spread σ_E for the measurement in February, and a 70% increase (factor of 1.7) of $r_{56} \cdot \sigma_E$ for the measurement in May (red).

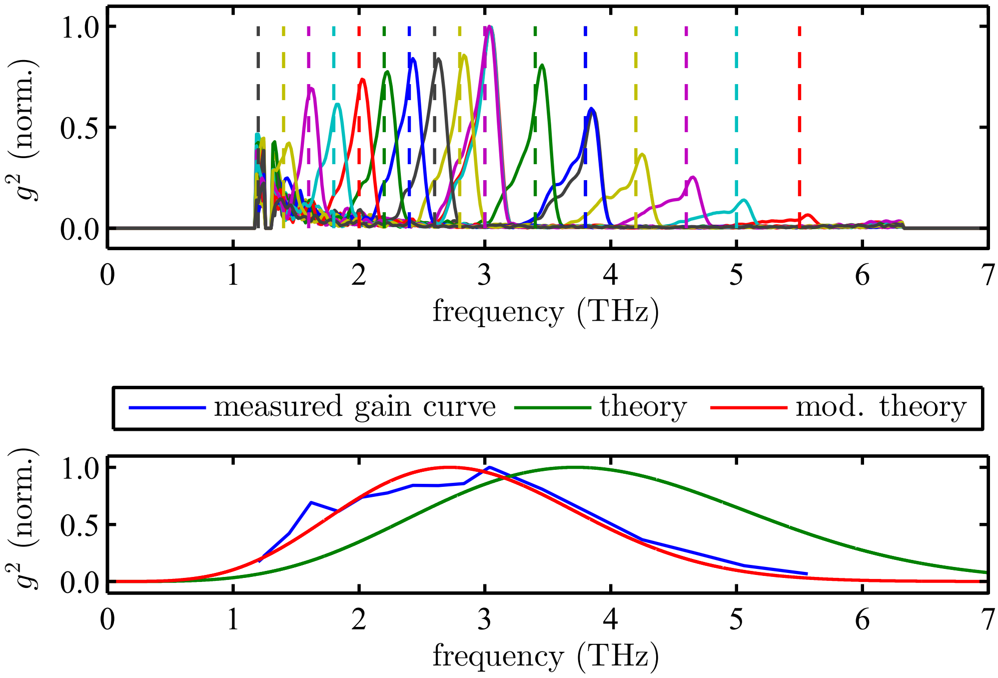

Figure 5.57.: Top: Form factors (solid) recorded on May 6 for different target frequencies (dashed). Bottom: Measured gain curve (blue), theoretical turn-0 gain curve (green), and modified gain curve (red, 70% increase of $r_{56} \cdot \sigma_E$).

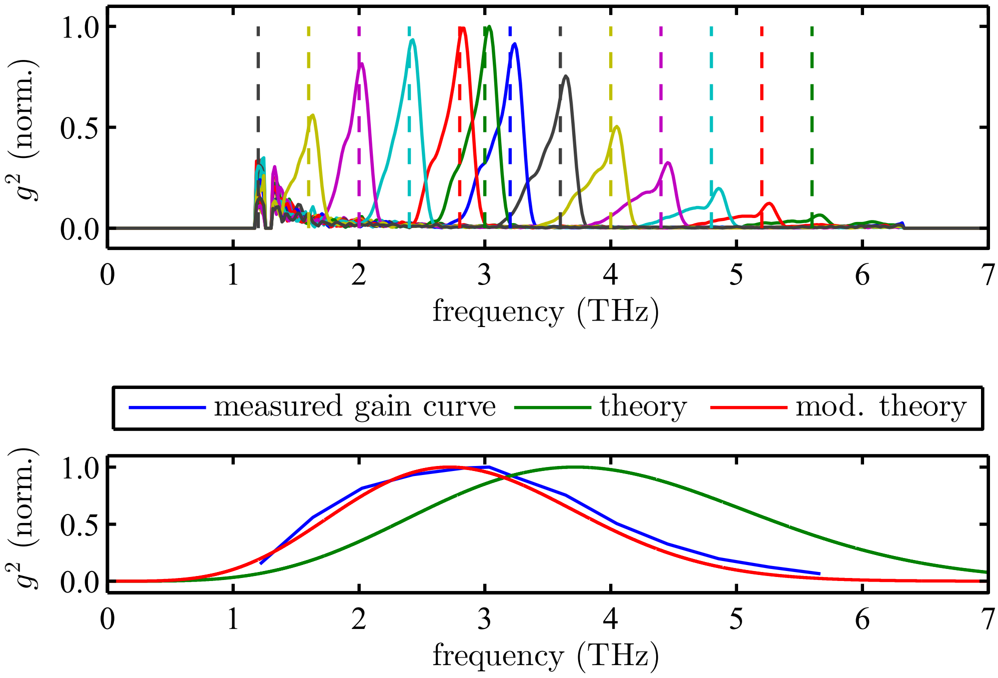

Figure 5.58.: Top: Form factors (solid) recorded on May 7 for different target frequencies (dashed). Bottom: Measured gain curve (blue), theoretical turn-0 gain curve (green), and modified gain curve (red, 70% increase of $r_{56} \cdot \sigma_E$).

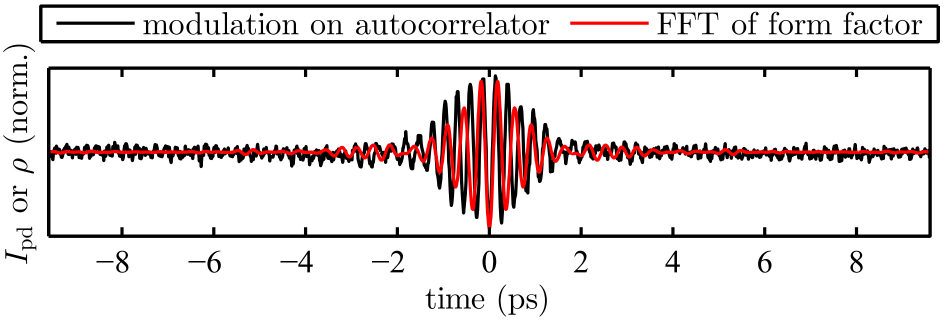

Figure 5.59.: Intensity modulation of the laser pulse as seen on an autocorrelator trace (black, similar to Fig. 5.54) and electron density modulation based on an FFT of the form factor at 2.6 THz in Fig. 5.56 (red).

One possible explanation for the deviations from the theoretical gain curve is that either the r_{56} value, the natural energy spread σ_E, or a combination of both were underestimated due to a mismatch between the model of the magnetic lattice and the actual storage ring. Similar discrepancies were already discussed in Ch. 5.3.1. Another possibility is that the form factors were systematically underestimated at frequencies above 3 or 4 THz due to the decreasing transmission of the quartz window (Ch. 5.1.3). Finally, the theoretical gain curve is based on several assumptions (see Ch. 2.4.2), particularly infinitely long laser pulses and electron bunches and no quadratic chirp.

To understand the multiple-peak shape of the form factors mentioned above, the density modulation for one exemplary form factor was calculated based on an FFT (see Ch. 5.3.2) and is shown in Fig. 5.59 together with the corresponding intensity modulation from an autocorrelation measurement of the laser pulse. The multiple peaks in the spectra are caused by the beating behavior of the density modulation which is also present in the autocorrelation data. Therefore, the non-Gaussian shape of the measured form factors is believed to be unrelated to a possibly unknown effect involved in the laser-electron interaction, beam dynamics, or THz emission, but is instead already present in the laser pulse. A more detailed study of the laser-pulse properties is recommended for future CPB experiments; e.g., to always measure the laser spectrum.

First Application

Together with the second CPB experiment in May 2014, a first user experiment was performed at the DELTA short-pulse facility. Here, the narrow-band THz pulses were employed by a group from IMS at KIT to characterize the transition between both detection mechanisms in YBCO. Being able to arbitrarily choose and continuously vary the emission frequency from the sub-THz regime up to more than 5 THz, a more detailed and frequency-resolved study was possible in comparison to previous measurements based solely on broad-band THz pulses. Depending on the bias current and temperature, the transition between ultra-fast vortex-based detection and the slower bolometric detection appeared between 1.4 and 1.6 THz. As a first conclusion, the observed transition photon energy of about 6 meV lies well below the expected value of the superconducting energy gap in YBCO of almost 12 meV [82]. The studies of the detection mechanisms and their transition frequency continue [130].

6. Conclusion and Outlook

6.1. Summary and Conclusion

The goals of this thesis have been the extension of generation and detection schemes for laser-induced THz radiation at the DELTA short-pulse facility as well as the optimization of the laser-electron overlap, the study of the longitudinal charge distribution of the electron bunches, and the study of the beam dynamics in the storage ring.

With the NbN bolometer, the prototype YBCO detector, and the Schottky-barrier diode (SBD), recently developed technologies for ultrafast detection of THz pulses were tested at DELTA and could be employed to gain information about the turn-by-turn evolution of the laser-induced density modulation. A YBCO detector is now permanently installed, allowing these studies to be continued on a regular basis. The installation of a commercial FTIR spectrometer enabled first spectral studies of the laser-induced THz pulses at DELTA, and may now be used for future studies and user experiments. Detailed characterization measurements of the beamline, spectrometer, detectors, and general THz radiation properties were performed, providing a knowledge base for future experiments and indicating possibilities for further improvements.

With THzSMe, a powerful and fast simulation code was created, which helped to understand experimental observations within the scope of this thesis, and which may also be used in the future for more extensive studies regarding the influence of several laser and storage ring parameters on the properties of the laser-induced VUV and THz radiation.

Studies of the dependence of the THz signal on the laser pulse energy indicated that some of the pulse energy might be lost between the laser laboratory and the undulator U250. A variation of the laser pulse length showed an asymmetric dependence on the GDD introduced by the compressor indicating strong higher-order dispersion, and an influence of the dispersion introduced by the window and lenses in BL3 was observed. Future measurements would benefit from a more regular and extensive determination of the laser pulse properties, e.g., the pulse shape and emission spectrum. The counter-intuitive influence of an RF phase modulation on the THz signal was explained by the spectral shift due to the change in energy spread, and with a hybrid filling pattern and the synchronization of the phase modulation to the laser system it is possible to operate the short-pulse facility in parallel to the standard user operation.

Applying the laser sampling method (delay scans), detailed studies of the longitudinal charge distribution with small statistical uncertainties are possible. The influences of the RF phase modulation and of the RF power were analyzed and showed a general agreement with theoretical expectations. Systematical uncertainties have been pointed out, e.g., in the calibration of the vector modulator and streak camera, or in the knowledge of storage ring parameters like the natural energy spread, the momentum compaction factor, or the calibration of the RF power measurement. The sub-picosecond modulation of the longitudinal charge distribution was studied using an FFT of the measured THz spectra, and the influence of, e.g., the laser pulse length was shown.

Turn-by-turn-resolved measurements of the laser-induced THz intensity were performed using different detectors. Here, the occurrence of coherent THz pulses for more than one revolution after a single laser-electron interaction, the general decrease of intensity with turn number, and the re-appearance after half a synchrotron oscillation period in accordance with theoretical expectations were observed for the first time at DELTA. The turn-by-turn dependence of the THz signal on a variation of laser, storage ring, and overlap parameters could partially be reproduced by corresponding numerical simulations and assumptions on the detector sensitivity ranges. Some effects, e.g., occurring during a variation of the longitudinal overlap or the modulator wavelength, require more detailed studies.

With the generation of narrow-band THz radiation pulses up to 5.5 THz, first CPB experiments were successfully performed and the frequency range compared to previous experiments at UVSOR was extended significantly. With a first application in the study of detection mechanisms in YBCO, this method already proved to be beneficial for future user experiments. Effects of higher-order dispersion and non-Gaussian pulse shapes were observed and indicate that the full potential of this method has yet to be exploited.

6.2. Future Upgrades and Outlook

The construction of a Martin-Puplett interferometer (MPI) is almost completed [83]. It will allow studying spectra of higher-revolution THz pulses and enable a more detailed analysis of the beam dynamics and influence of laser and storage ring parameters.

A fiber laser system [139] was recently acquired and will shortly be installed at DELTA. It will be used for electro-optical measurements of the electric field (intensity and phase) of the THz pulses. A future near-field electro-optical setup directly in the vacuum chamber of the storage ring is also intended.

A Schottky-barrier diode (SBD) for permanent usage at the THz beamline and possible replacement of the InSb bolometer as the standard THz detector was ordered and will arrive shortly. More extensive studies based on the signal re-appearance after half a synchrotron oscillation period will be possible on a regular basis, also in combination with the MPI.

By the design and construction of a permanent CPB setup, the shape and bandwidth of the narrow-band THz spectra will be optimized further and the regular generation of narrow-band spectra will be possible. Additional diagnostics equipment like a permanent optical autocorrelator would also be of general benefit to the short-pulse facility.

Preparations for a modification of the northern straight section of DELTA to implement the echo-enabled harmonic generation (EEHG) principle have begun [87]. The THz beamline will remain the most important diagnostics tool for both laser-electron interactions involved in EEHG. With three undulators and two new chicanes, more extensive studies based on combinations of laser-electron interactions, on hitting the bunch at different longitudinal positions simultaneously, and on a change of the energy-dependent path length due to the additional chicane strength will be possible. Seeding both undulators with a slightly different wavelength might even enable an alternative method to generate narrow-band THz radiation [140].

A. Appendices

A.1. Devices & Parameters of the Short-Pulse Facility

A.1.1. Laser Laboratory

Table A.1.: Parameters of the Ti:sapphire laser oscillator.

parameter	**value**
manufacturer	Coherent, Inc.
model	Micra-5
type	broadband ultrafast Ti:sapphire oscillator (mode-locked)
pump laser	Coherent Verdi Nd:YVO_4 (integrated)
synchronization	Coherent Synchro-Lock AP
central wavelength (typ.)	800 nm
bandwidth (typ.)	100 nm
repetition rate	83 MHz
power (typ.)	350 mW

Table A.2.: Parameters of the Ti:sapphire laser amplifier.

parameter	**value**
manufacturer	Coherent, Inc.
model	Legend Elite Duo HP
type	high-power Ti:sapphire chirped-pulse amplifier, regenerative (multi-pass) + single-pass stage
pump laser	Coherent Evolution-HE Nd:YLF (integrated)
central wavelength (typ.)	800 nm
pulse length (typ.)	40 fs
repetition rate	1 kHz
power (typ.)	8 W

A.1.2. THz Beamline

Table A.3.: Parameters of the InSb bolometer installed at DELTA.

parameter	value
manufacturer	QMC Instruments Ltd. [127]
model	QFI/3
amplifier model	ULN95
optical[1] responsivity	> 2.5 kV/W (at 275 GHz; 1 kHz modulation)
optical NEP	< 750 fW $\mathrm{Hz}^{-1/2}$ (at 275 GHz; 1 kHz modulation)
frequency range	60 GHz to 500 GHz FWHM
temporal bandwidth	1 MHz FWHM
output impedance	50 Ω
cryostat model	TK1840
LHe reservoir (hold time)	4.5 L (10 days)
LN2 reservoir (hold time)	4.3 L (24–30 hours)
filters	HDPE window plus 1-THz low pass filer

Table A.4.: Parameters of the NbN bolometer [36, 37].

parameter	value
manufacturer	IMS at KIT and German Aerospace Center, Berlin
optical responsivity	5 V/W (at 0.8 THz CW)
optical NEP	6 nW $\mathrm{Hz}^{-1/2}$ (at 0.8 THz CW)
frequency range	160 GHz to 3 THz
response time	< 160 ps
cryostat	HDL-5 (Infrared Laboratories, Inc.)
LHe reservoir (hold time)	1.2 L (> 6 hours)
LN2 reservoir	0.8 L
filters	polyethylene window

---

[1] The optical responsivity and NEP are measured for the detector system including a potential antenna gain and coupling, filters, etc.. The electrical responsivity and NEP describe the actual detection element only.

Table A.5.: Parameters of the prototype YBCO detectors [38–40].

parameter	**value**
manufacturer	IMS at KIT
response time	< 17 ps
max. optical responsivity	≈ 89 V/W (at 0.65 THz CW) (for a 0.9 µm x 0.3 µm micro-bridge), ≈ 76 V/W (at 0.65 THz CW) (for a 4.7 µm x 2.0 µm micro-bridge)
min. optical NEP	12 pW $\text{Hz}^{-1/2}$ (at 0.65 THz; 10 kHz modulation) (for a 0.9 µm x 0.3 µm micro-bridge), 16 pW $\text{Hz}^{-1/2}$ (at 0.65 THz; 10 kHz modulation) (for a 4.7 µm x 2.0 µm micro-bridge)
available antenna frequency ranges	30 GHz to 1 THz 100 GHz to 2.5 THz 1 THz to 5 THz

Table A.6.: Parameters of the YBCO detector permanently installed at DELTA [38–40].

parameter	**value**
manufacturer	IMS at KIT
micro-bridge dimensions	30 nm x 4.5 µm x 2 µm (film thickness x width x length)
antenna frequency range	100 GHz to 2.5 THz
cryostat manufacturer	IMS at KIT
LN2 reservoir (hold time)	0.85 L (> 12 hours)
filters	polyethylene window
bias tee	SHF Communication Technologies AG ‘BT65’ 50 kHz to 65 GHz
amplifier	SHF Communication Technologies AG ‘804 TL’ 200 kHz to 55 GHz 22 dB
flexible cables	Totoku Electric Co., Ltd. ‘TCF219’ 0 to 67 GHz

Table A.7.: Parameters of the Schottky-barrier diode (SBD) [41, 42, 128].

parameter	**value**
manufacturer	ACST GmbH
model	2DL 12C LS 1200 A2
optical responsivity	463 V/W (at 70 GHz), 15 V/W (at 1 THz)
optical NEP	24.2 pW $\mathrm{Hz}^{-1/2}$ (at 70 GHz), 850 pW $\mathrm{Hz}^{-1/2}$ (at 1 THz)
frequency range	50 GHz to 1.2 THz
temporal bandwidth	4 GHz

Table A.8.: Parameters (according to data sheet, quote, or OPUS software) of the Bruker VERTEX 80v FTIR spectrometer installed at DELTA.

parameter	**value**
manufacturer	Bruker Optik GmbH
model	VERTEX 80v
spectral range	10 cm^{-1} to 8000 cm^{-1} 0.3 THz to 240 THz
beam splitters	KBr (380 cm^{-1} to 10000 cm^{-1}) Mylar multilayer (30 cm^{-1} to 680 cm^{-1}) Mylar 50 µm (10 cm^{-1} to 60 cm^{-1}) automated in-vacuum beam-splitter exchanger
internal sources	Globar (30 cm^{-1} to 8000 cm^{-1}) Hg arc lamp (3 cm^{-1} to 1000 cm^{-1})
detectors	DLaTGS (180 cm^{-1} to 10000 cm^{-1}) DLaTGS (10 cm^{-1} to 700 cm^{-1}) Si bolometer (10 cm^{-1} to 370 cm^{-1})
resolution	$< 0.06\ \mathrm{cm}^{-1}$ (1.8 GHz)
vacuum	external multi-stage Roots pump < 3 mbar

A.2. Mathematical Derivations

A.2.1. Chirped-Pulse Beating

Derivation of Eq. 2.21

$$
\begin{aligned}
I_{\text{tot}} &\propto \frac{1}{2}\left|E_{\text{out}}\left(t+\frac{\tau}{2}\right)+E_{\text{out}}\left(t-\frac{\tau}{2}\right)\right|^2 && \text{(A.1)}\\
&= \frac{E_0^2}{2}\frac{\Delta t_{\text{in}}}{\Delta t_{\text{out}}}\\
&\cdot \left\{\left[e^{-a_{\text{out}}\left(t+\frac{\tau}{2}\right)^2}\cdot e^{i\omega_0\left(t+\frac{\tau}{2}\right)+ib_{\text{out}}\left(t+\frac{\tau}{2}\right)^2}+e^{-a_{\text{out}}\left(t-\frac{\tau}{2}\right)^2}\cdot e^{i\omega_0\left(t-\frac{\tau}{2}\right)+ib_{\text{out}}\left(t-\frac{\tau}{2}\right)^2}\right]\right.\\
&\cdot \left.\left[e^{-a_{\text{out}}\left(t+\frac{\tau}{2}\right)^2}\cdot e^{-i\omega_0\left(t+\frac{\tau}{2}\right)-ib_{\text{out}}\left(t+\frac{\tau}{2}\right)^2}+e^{-a_{\text{out}}\left(t-\frac{\tau}{2}\right)^2}\cdot e^{-i\omega_0\left(t-\frac{\tau}{2}\right)-ib_{\text{out}}\left(t-\frac{\tau}{2}\right)^2}\right]\right\} && \text{(A.2)}\\
&= \frac{E_0^2}{2}\frac{\Delta t_{\text{in}}}{\Delta t_{\text{out}}}\left[e^{-2a_{\text{out}}\left(t+\frac{\tau}{2}\right)^2}+e^{-2a_{\text{out}}\left(t-\frac{\tau}{2}\right)^2}\right.\\
&\left.+\,e^{-2a_{\text{out}}\left(t^2+\frac{\tau^2}{4}\right)}\cdot e^{i\omega_0 t+2ib_{\text{out}}t\tau}+e^{-2a_{\text{out}}\left(t^2+\frac{\tau^2}{4}\right)}\cdot e^{-i\omega_0 t-2ib_{\text{out}}t\tau}\right] && \text{(A.3)}\\
&= \frac{E_0^2}{2}\frac{\Delta t_{\text{in}}}{\Delta t_{\text{out}}}\left[e^{-2a_{\text{out}}\left(t+\frac{\tau}{2}\right)^2}+e^{-2a_{\text{out}}\left(t-\frac{\tau}{2}\right)^2}+2e^{-2a_{\text{out}}\left(t^2+\frac{\tau^2}{4}\right)}\cdot\cos(\omega_0\tau+2b_{\text{out}}\tau t)\right]\\
& && \text{(A.4)}\\
&= \frac{E_0^2}{2}\frac{\Delta t_{\text{in}}}{\Delta t_{\text{out}}}e^{-2a_{\text{out}}\left(t^2+\frac{\tau^2}{4}\right)}\left[e^{-2a_{\text{out}}\tau t}+e^{2a_{\text{out}}\tau t}+2\cos(\omega_0\tau+2b_{\text{out}}\tau t)\right] && \text{(A.5)}\\
&= E_0^2\frac{\Delta t_{\text{in}}}{\Delta t_{\text{out}}}e^{-2a_{\text{out}}\left(t^2+\frac{\tau^2}{4}\right)}\left[\cosh(2a_{\text{out}}\tau t)+\cos(\omega_0\tau+2b_{\text{out}}\tau t)\right] && \text{(A.6)}
\end{aligned}
$$

Derivation of Eq. 2.23

$$
\begin{aligned}
\Delta t_{\text{in}}\Delta t_{\text{out}} &= \Delta t_{\text{in}}^2\sqrt{1+\frac{z^2}{z_0^2}} && \text{(A.7)}\\
&\approx \Delta t_{\text{in}}^2\frac{|z|}{z_0}\quad \text{for } \Delta t_{\text{out}} \gg \Delta t_{\text{in}} && \text{(A.8)}\\
&= \Delta t_{\text{in}}^2\frac{4|D_2|\ln 2}{\Delta t_{\text{in}}^2} && \text{(A.9)}\\
&= 4|D_2|\ln 2 && \text{(A.10)}
\end{aligned}
$$

A.2.2. Emission of THz Radiation

Derivation of Eq. 2.107

$$
\begin{aligned}
P_{\mathrm{tot}}(\omega,t) &= P_{\mathrm{e}}(\omega)\left|\sum_k e^{i(\omega t+\varphi_k)}\right|^2 && \text{(A.11)}\\
&= P_{\mathrm{e}}(\omega)\sum_k\sum_l e^{i(\omega t+\varphi_k)}e^{-i(\omega t+\varphi_l)} && \text{(A.12)}\\
&= P_{\mathrm{e}}(\omega)\sum_k\sum_l e^{i(\varphi_k-\varphi_l)} && \text{(A.13)}\\
&= P_{\mathrm{e}}(\omega)\left[N_{\mathrm{e}}+\sum_k\sum_{l\neq k} e^{i(\varphi_k-\varphi_l)}\right] && \text{(A.14)}\\
&= P_{\mathrm{e}}(\omega)\left[N_{\mathrm{e}}+\sum_k e^{i\omega\frac{z_k}{c}}\sum_{l\neq k} e^{-i\omega\frac{z_l}{c}}\right] && \text{(A.15)}\\
&= P_{\mathrm{e}}(\omega)\left[N_{\mathrm{e}}+\int N_{\mathrm{e}}\rho(z)e^{i\omega\frac{z}{c}}\mathrm{d}z\int (N_{\mathrm{e}}-1)\rho(z)e^{-i\omega\frac{z}{c}}\mathrm{d}z\right] && \text{(A.16)}\\
&= P_{\mathrm{e}}(\omega)\left[N_{\mathrm{e}}+N_{\mathrm{e}}(N_{\mathrm{e}}-1)\left|\int \rho(z)e^{i\omega\frac{z}{c}}\mathrm{d}z\right|^2\right] && \text{(A.17)}\\
&= P_{\mathrm{e}}(\omega)\left[N_{\mathrm{e}}+N_{\mathrm{e}}(N_{\mathrm{e}}-1)\left|\int \rho(t)e^{i\omega t}\mathrm{d}t\right|^2\right] && \text{(A.18)}
\end{aligned}
$$

A.3. Simulation Parameters

Table A.9.: General list of input parameters for THzSMe (Ch. 3.2).

parameter name	**default value**	**unit**	**description**
`latticeFile`	`del008_9233` `_THzSMe.lte`		modified `elegant` lattice file; see readme.txt for required content
`storageRingLength`	`-1.00e+00`	`m`	length of storage ring; set negative to extract from lattice file
`harmonicNumber`	`1.92e+02`		harmonic number; should match `elegant` lattice
`beamEnergy`	`1.49e+09`	`eV`	central beam energy
`relativeEnergySpread`	`6.80e-04`		natural relative energy spread; set negative to calculate from lattice
`horizontalEmittance`	`1.50e-08`	`m rad`	horizontal electron beam emittance; set negative to calculate from lattice
`verticalEmittance`	`1.50e-09`	`m rad`	horizontal electron beam emittance; set negative coupling (`eps_y/eps_x`) to calculate from lattice
`horizontalBetaFunction`	`-1.00e+00`	`m`	horizontal beta function at modulator start; set negative to calculate from lattice
`verticalBetaFunction`	`-1.00e+00`	`m`	vertical beta function at modulator start; set negative to calculate from lattice
`horizontalAlphaFunction`	`0.00e+00`		horizontal alpha function at modulator start; calculated from lattice if beta function set negative
`verticalAlphaFunction`	`0.00e+00`		vertical alpha function at modulator start; calculated from lattice if beta function set negative
`horizontalDispersion`	`0.00e+00`	`m`	horizontal Dispersion function at modulator start; calculated from lattice if beta function set negative
`horizontalDispersionAngle`	`0.00e+00`		horizontal dispersion angle at modulator start; calculated from lattice if beta function set negative
`rmsBunchDuration`	`3.37e-11`	`s`	rms bunch length in time; should match energy spread and cavity in lattice (see `calcTwiss` output)
`singleBunchCurrent`	`1.00e-02`	`A`	single bunch current

`laserWavelength`	8.00e-07	m	central laser wavelength
`FwhmLaserPulseDuration`	4.00e-14	s	laser pulse duration (FWHM, without chirp)
`FwhmChirpedPulseDuration`	0.00e+00	s	chirped laser pulse duration (FWHM); set >rmsLaserPulseDuration or <(-rmsLaserPulseDuration) to introduce a chirp
`quadraticChirpAlpha`	0.00e+00	s^-3	third order dispersion / quadratic chirp parameter α in $E \propto \exp(i\alpha t^3)$
`CpbFrequency`	0.00e+00	Hz	chirped pulse beating frequency; set >0 to introduce laser intensity modulation
`laserPulseEnergy`	1.00e-03	J	laser pulse energy
`horizontalLaserWaistRadius`	4.67e-04	m	horizontal laser waist radius '`w_0`' at focus
`verticalLaserWaistRadius`	4.67e-04	m	vertical laser waist radius '`w_0`' at focus
`mSquared`	1.50e+00		M^2 parameter of the laser beam
`horizontalLaserPosition`	0.00e+00	m	horizontal offset between laser pulse and electron bunch
`verticalLaserPosition`	0.00e+00	m	vertical offset between laser pulse and electron bunch
`horizontalLaserAngle`	0.00e+00	rad	horizontal crossing angle between laser pulse and electron bunch at laser waist
`verticalLaserAngle`	0.00e+00	rad	vertical crossing angle between laser pulse and electron bunch at laser waist
`longitudinalLaserOffset`	0.00e+00	s	longitudinal offset between laser pulse and electron bunch
`undulatorK`	1.02e+01		undulator parameter 'K'
`undulatorPeriodLength`	2.50e-01	m	undulator period length
`modulatorPeriods`	7.00e+00		number of modulator periods; should match modulator length in lattice file
`nParticles`	5.00e+03		number of particles to simulate
`simulatedSliceDuration`	0.00e+00	s	length of slice in time to simulate; set negative for complete bunch or zero for 10x rms laser pulse length
`energyModSteps`	1.00e+03		number of discrete time steps for simulation of energy modulation
`revolutions`	3.00e+00		number of revolutions to track with `elegant`
`plotPhaseSpace`	1.00e+00		flag (1 for yes, 0 for no) if longitudinal phase space plots shall be created for each revolution

`plotHistograms`	1.00e+00		flag (1 for yes, 0 for no) if longitudinal histogram plots shall be created for each revolution
`plotFormFactor`	1.00e+00		flag (1 for yes, 0 for no) if form factor plots shall be created for each revolution
`plotSpectrum`	1.00e+00		flag (1 for yes, 0 for no) if emission spectrum plots shall be created for each revolution
`longHistogramRange`	-1.00e+00	s	range in time for calculation of longitudinal density profiles; set negative for 10x rms bunch length
`longHistogramTempResolutionRev1`	1.00e-14	s	temporal resolution of longitudinal density profiles for first revolution
`longHistogramTempResolution`	2.00e-13	s	temporal resolution of longitudinal density profiles for following revolutions
`thzBendingRadius`	3.34e+00	m	bending radius of dipole magnet used as THz source
`deleteTempFiles`	1.00e+00		flag (1 for yes, 0 for no) if temporary files (e.g., single particle position) shall be deleted

References

[1] A. J. Liebeskind, *Palmblätter. Erlesene morgenländische Erzählungen für die Jugend*, volume 1, 1st edition (Akademische Buchhandlung, Jena, 1786).

[2] F. R. Elder et al., *Radiation from Electrons in a Synchrotron*, Phys. Rev. 71, 829 (1947).

[3] D. Iwanenko and I. Pomeranchuk, *On the Maximal Energy Attainable in a Betatron*, Phys. Rev. 65, 343 (1944).

[4] J. Schwinger, *On the Classical Radiation of Accelerated Electrons*, Phys. Rev. 75, 1912 (1949).

[5] A. L. Robinson, *History of Synchrotron Radiation*, in *X-Ray Data Booklet*, edited by A. C. Thompson and D. Vaughan, 3rd edition (Lawrence Berkeley National Laboratory, Berkeley, 2009).

[6] G. A. Schott, *Electromagnetic radiation and the mechanical reactions arising from it: being an Adams prize essay in the University of Cambridge* (Cambridge University Press, Cambridge, 1912).

[7] E. Wiechert, *Elektrodynamische Elementargesetze*, in *Archives néerlandaises des sciences exactes et naturelles*, volume 5, 549–573 (Martinus Nijhoff, The Hague, 1900).

[8] A.-M. Liénard, *Champ électrique et magnétique produit par une charge électrique concentrée en un point et animée d'un mouvement quelconque*, L'Éclairage Électrique 16, 5 (1898).

[9] J. Larmor, *A Dynamical Theory of the Electric and Luminiferous Medium. Part III. Relations with Material Media*, Philosophical Transactions of the Royal Society of London. Series A, Containing Papers of a Mathematical or Physical Character 190, 205 (1897).

[10] D. H. Tomboulian and P. L. Hartman, *Spectral and Angular Distribution of Ultraviolet Radiation from the 300-Mev Cornell Synchrotron*, Phys. Rev. 102, 1423 (1956).

[11] *Lightsources of the World*, `http://www.lightsources.org/regions` (2013), [accessed October 9, 2014].

[12] M. Höner, *Optical Design and Construction of a Dedicated THz Beamline at DELTA and Study of Laser-Electron Interaction*, diploma thesis, Technische Universität Dortmund (2011).

[13] P. Ungelenk, *A New THz Beamline at DELTA: Tracking Simulations, Mechanical Design, Assembly, and First Measurements*, diploma thesis, Technische Universität Dortmund (2011).

[14] E. Bründermann et al., *Terahertz Techniques*, 1st edition (Springer, Heidelberg, 2012).

[15] X.-C. Zhang and J. Xu, *Introduction to THz Wave Photonics*, 1st edition (Springer, New York, 2010).

[16] International Organization for Standardization, Geneva, Switzerland, *ISO21348:2007: Space environment (natural and artificial) – Process for determining solar irradiances*, 1st edition (2007).

[17] H. Rubens and E. F. Nichols, *Heat Rays Of Great Wave Length*, Phys. Rev. (Series I) 4, 314 (1897).

[18] D. Emerson, *The work of Jagadis Chandra Bose: 100 years of mm-wave research*, in *1997 IEEE MTT-S International Microwave Symposium Digest*, volume 2, 553–556 (Denver, 1997).

[19] C. Kübler et al., *Coherent Structural Dynamics and Electronic Correlations during an Ultrafast Insulator-to-Metal Phase Transition in* VO_2, Phys. Rev. Lett. 99, 116401 (2007).

[20] E. Jaeschke et al., *Lattice Design for the 1.7-GeV Light Source BESSY II*, in *Proceedings of the 15th Particle Accelerator Conference*, 1474–1476 (Washington, D.C., 1993).

[21] G. Wüstefeld et al., *Simultaneous Long and Short Electron Bunches in the BESSY II Storage Ring*, in *Proceedings of the 2nd International Particle Accelerator Conference*, 2936–2938 (San Sebastián, 2011).

[22] G. Stupakov and S. Heifets, *Beam instability and microbunching due to coherent synchrotron radiation*, Phys. Rev. ST Accel. Beams 5, 054402 (2002).

[23] J. M. Byrd et al., *Observation of Broadband Self-Amplified Spontaneous Coherent Terahertz Synchrotron Radiation in a Storage Ring*, Phys. Rev. Lett. 89, 224801 (2002).

[24] V. Judin et al., *Studies of Bursting CSR in Multi-bunch Operation at the ANKA Storage Ring*, in *Proceedings of the 5th International Particle Accelerator Conference*, 225–227 (Dresden, 2014).

[25] K. Holldack et al., *Femtosecond Terahertz Radiation from Femtoslicing at BESSY*, Phys. Rev. Lett. 96, 054801 (2006).

[26] V. Schlott et al., *THz Diagnostic for the Femtosecond Bunch Slicing Project at the Swiss Light Source*, in *Proceedings of the 10th European Particle Accelerator Conference*, 1229–1231 (Edinburgh, 2006).

[27] J. M. Byrd et al., *Tailored Terahertz Pulses from a Laser-Modulated Electron Beam*, Phys. Rev. Lett. 96, 164801 (2006).

[28] N. Stojanovic and M. Drescher, *Accelerator- and laser-based sources of high-field terahertz pulses*, Journal of Physics B: Atomic, Molecular and Optical Physics 46, 192001 (2013).

[29] A. P. Potylitsyn et al., *Diffraction Radiation from Relativistic Particles*, 1st edition (Springer, Berlin, 2010).

[30] E. Chiadroni et al., *The THz Radiation Source at the SPARC Facility*, Journal of Physics: Conference Series 359, 012018 (2012).

[31] S. J. Smith and E. M. Purcell, *Visible Light from Localized Surface Charges Moving across a Grating*, Phys. Rev. 92, 1069 (1953).

[32] M. J. E. Golay, *A Pneumatic Infra-Red Detector*, Review of Scientific Instruments 18, 357 (1947).

[33] Bruker Optics Inc., Billerica, MA, USA, *Guide for Infrared Spectroscopy* (2011).

[34] E. H. Putley, *Indium Antimonide Submillimeter Photoconductive Detectors*, Appl. Opt. 4, 649 (1965).

[35] *Indium antimonide (InSb) hot electron bolometer*, `http://www.terahertz.co.uk/index.php?option=com_content&view=article&id=215&Itemid=594` (2011), [accessed January 28, 2015].

[36] A. Semenov et al., *Monitoring coherent THz-synchrotron radiation with superconducting NbN hot-electron detector*, in *34th International Conference on Infrared, Millimeter, and Terahertz Waves, 2009. IRMMW-THz 2009.*, 1–2 (2009).

[37] A.-S. Müller et al., *Observation of Coherent THz Radiation from the ANKA and MLS Storage Rings with a Hot Electron Bolometer*, in *Proceedings of the 23rd Particle Accelerator Conference*, 1153–1155 (Vancouver, 2009).

[38] P. Thoma et al., *Real-time measurement of picosecond THz pulses by an ultra-fast* $YBa_2Cu_3O_{7-d}$ *detection system*, Applied Physics Letters 101, 142601 (2012).

[39] P. Thoma et al., *High-Speed Y-Ba-Cu-O Direct Detection System for Monitoring Picosecond THz Pulses*, IEEE Transactions on Terahertz Science and Technology 3, 81 (2013).

[40] P. Thoma, *Ultra-fast* $YBa_2Cu_3O_{7-x}$ *direct detectors for the THz frequency range*, Ph.D. thesis, Karlsruher Institut für Technologie (2013).

[41] A. Semenov et al., *Application of Zero-Bias Quasi-Optical Schottky-Diode Detectors for Monitoring Short-Pulse and Weak Terahertz Radiation*, Electron Device Letters, IEEE 31, 674 (2010).

[42] ACST GmbH, Hanau, *Product Flyer – UWB Quasi-optical Detectors up to 2THz* (2014).

[43] D. Schirmer, *Synchrotron radiation sources at DELTA*, DELTA Int. Rep. 001-05, Institute of Acceleratorphysics and Synchrotronradiation, University of Dortmund (2009).

[44] D. Nölle et al., *Status of the Dortmund Electron Test Accelerator Facility*, in *Proceedings of the 6th European Particle Accelerator Conference*, 611–613 (Stockholm, 1998).

[45] G. Schmidt et al., *Status of the synchrotron light source DELTA*, in *Proceedings of the 8th European Particle Accelerator Conference*, 745–747 (Paris, 2002).

[46] M. Tolan et al., *DELTA: Synchrotron light in nordrhein-westfalen*, Synchrotron Radiation News 16, 9 (2003).

[47] D. Schirmer et al., *Status of the Synchrotron Light Source DELTA*, in *Proceedings of the 9th European Particle Accelerator Conference*, 2296–2298 (Lucerne, 2004).

[48] T. Weis, *Space Charge Effects in Particle Sources, RFQs and Rings*, `http://www.delta.tu-dortmund.de/cms/de/Studium/Homepage_Weis/Vortraege/VortragRiezlern2006.pdf`, [accessed January 29, 2015], (presented at the Winterseminar Beschleunigerphysik of the Goethe University Frankfurt am Main, Riezlern, 2006).

[49] S. Khan, *Status of DELTA: Light Source and Short-Pulse Facility*, `http://www.anka.kit.edu/downloads/ESLS2013_Delta_status.pdf`, [accessed January 29, 2015], (presented at the European Synchrotron Light Source XXI Workshop, Karlsruhe, 2013).

[50] A. Jankowiak et al., *Reconstruction of the 75 MeV Linac of the DELTA Synchrotron Radiation Facility*, in *Proceedings of the 7th European Particle Accelerator Conference*, 634–636 (Vienna, 2000).

[51] K. Wille, *Initial Experience with DELTA*, in *Proceedings of the 5th European Particle Accelerator Conference*, 95–99 (Barcelona, 1996).

[52] H. Huck et al., *Past and Future of the DELTA Free-Electron Laser*, in *Proceedings of the 32nd International Free Electron Laser Conference*, 310–313 (Malmö, 2010).

[53] M. Grewe, *SVD-basierte Orbitkorrektur am Speicherring Delta*, Ph.D. thesis, Universität Dortmund (2005).

[54] M. Höner et al., *Investigation of Beam Instabilities at DELTA using Bunch-by-bunch Feedback Systems*, in *Proceedings of the 5th International Particle Accelerator Conference*, 3486–3488 (Dresden, 2014).

[55] M. Höner, *Investigation of Transient Processes at the DELTA Electron Storage Ring Using a Digital Bunch-by-Bunch Feedback System*, Ph.D. thesis, TU Dortmund (2015).

[56] Argonne National Laboratory, *Experimental Physics and Industrial Control System*, `http://www.aps.anl.gov/epics/about.php` (2011), [accessed January 29, 2015].

[57] H. Huck et al., *Coherent Harmonic Generation at the DELTA Storage Ring*, in *Proceedings of the 33rd International Free Electron Laser Conference*, 5–8 (Shanghai, 2011).

[58] S. Khan et al., *Coherent Harmonic Generation at DELTA: A New Facility for Ultrashort Pulses in the VUV and THz Regime*, Synchrotron Radiation News 24, 18 (2011).

[59] R. Coisson and F. de Martini, *Free-Electron Coherent Relativistic Scatterer for UV Generation*, in *Free-Electron Generators of Coherent Radiation*, edited by S. F. Jacobs et al., volume 9 of *Physics of Quantum Electronics*, 1st edition (Addison-Wesley Publishing Company, Massachusetts, 1982), based on lectures of the Office of Naval Research sponsored workshop 1981, Sun Valley, Idaho.

[60] R. Prazeres et al., *Coherent harmonic generation in the vacuum ultraviolet spectral range on the storage ring ACO*, Nuclear Instruments and Methods in Physics Research Section A: Accelerators, Spectrometers, Detectors and Associated Equipment 272, 68 (1988).

[61] G. De Ninno et al., *Generation of Ultrashort Coherent Vacuum Ultraviolet Pulses Using Electron Storage Rings: A New Bright Light Source for Experiments*, Phys. Rev. Lett. 101, 053902 (2008).

[62] M. Labat et al., *Coherent Harmonic Generation experiments on UVSOR-II storage ring*, Nuclear Instruments and Methods in Physics Research Section A: Accelerators, Spectrometers, Detectors and Associated Equipment 593, 1 (2008).

[63] T. Schulte-Eickhoff, private communication (2014).

[64] C. Iaconis and I. A. Walmsley, *Spectral phase interferometry for direct electric-field reconstruction of ultrashort optical pulses*, Opt. Lett. 23, 792 (1998).

[65] R. Trebino, *Frequency-resolved optical gating : the measurement of ultrashort laser pulses* (Kluwer Academic, Boston, 2000).

[66] M. Czerny and A. F. Turner, *Über den Astigmatismus bei Spiegelspektrometern*, Zeitschrift für Physik 61, 792 (1930).

[67] M. Höner et al., *A Dedicated THz Beamline at DELTA*, in *Proceedings of the 2nd International Particle Accelerator Conference*, 2939–2941 (San Sebastián, 2011).

[68] A. Schick et al., *Ultrashort VUV and THz Pulse Generation at the DELTA Storage Ring*, in *Proceedings of the 2nd International Particle Accelerator Conference*, 2942–2944 (San Sebastián, 2011).

[69] M. Zeinalzadeh et al., *Temporal and Spatial Alignment of Electron Bunches and Ultrashort Laser Pulses for the CHG Experiment at DELTA*, in *Proceedings of the 2nd International Particle Accelerator Conference*, 2945–2947 (San Sebastián, 2011).

[70] A. Schick et al., *Recent Results from the Short-Pulse Facility at the DELTA Storage Ring*, in *Proceedings of the 3rd International Particle Accelerator Conference*, 1617–1619 (New Orleans, 2012).

[71] P. Ungelenk et al., *Recent Developments at the DELTA THz Beamline*, in *Proceedings of the 3rd International Particle Accelerator Conference*, 768–770 (New Orleans, 2012).

[72] H. Huck et al., *Status of the DELTA Short-Pulse Facility*, in *Proceedings of the 34th International Free Electron Laser Conference*, 401–404 (Nara, 2012).

[73] P. Ungelenk et al., *Temporal and Spectral Observation of Laser-Induced THz Radiation at DELTA*, in *Proceedings of the 4th International Particle Accelerator Conference*, 94–96 (Shanghai, 2013).

[74] M. Huck, *Characterization of VUV Pulses from the Short-Pulse Facility at DELTA and Steps towards Pump-Probe Experiments*, Ph.D. thesis, Technische Universität Dortmund (2015).

[75] A. Schick et al., *Status Report of the Short-Pulse Facility at the DELTA Storage Ring*, in *Proceedings of the 35th International Free Electron Laser Conference*, 642–645 (New York, 2013).

[76] P. Ungelenk et al., *Studies of Ultrashort THz Pulses at DELTA*, in *Proceedings of the 5th International Particle Accelerator Conference*, 1936–1939 (Dresden, 2014).

[77] R. Molo et al., *Investigation of the Magnetic Chicane of the Short-Pulse Facility at the DELTA Storage Ring*, in *Proceedings of the 4th International Particle Accelerator Conference*, 1889–1891 (Shanghai, 2013).

[78] M. Huck et al., *Experimental Characterisation of the Coherent Harmonic Generation Source at the DELTA Storage Ring*, in *Proceedings of the 4th International Particle Accelerator Conference*, 2132–2134 (Shanghai, 2013).

[79] M. Huck et al., *Ultrashort and Coherent Radiation for Pump-Probe Experiments at the DELTA Storage Ring*, in *Proceedings of the 5th International Particle Accelerator Conference*, 1848–1851 (Dresden, 2014).

[80] S. Khan et al., *Generation of Ultrashort and Coherent Synchrotron Radiation Pulses at DELTA*, Synchrotron Radiation News 26, 25 (2013).

[81] A. Meyer auf der Heide et al., *Coherent Harmonic Generation at the DELTA Storage Ring: Towards User Operation*, in *Proceedings of the 36th International Free Electron Laser Conference*, 556–560 (Basel, 2014).

[82] J. Raasch et al., *Tunable narrowband THz radiation for the investigation of the frequency-dependent picosecond response of YBCO detectors*, in *Proceedings of the 10th DELTA User Meeting*, 5–6 (Dortmund, 2014).

[83] C. Mai, *Design and Construction of a Polarizing Interferometer for the DELTA Terahertz Beamline*, master's thesis, TU Dortmund (2015).

[84] D. Xiang and G. Stupakov, *Echo-enabled harmonic generation free electron laser*, Phys. Rev. ST Accel. Beams 12, 030702 (2009).

[85] R. Molo et al., *Echo-Enabled Harmonic Generation at DELTA*, in *Proceedings of the 2nd International Particle Accelerator Conference*, 3074–3076 (San Sebastián, 2011).

[86] R. Molo et al., *Conceptual Layout of a New Short-Pulse Radiation Source at DELTA Based on Echo-Enabled Harmonic Generation*, in *Proceedings of the 33rd International Free Electron Laser Conference*, 219–222 (Shanghai, 2011).

[87] R. Molo et al., *EEHG and Femtoslicing at DELTA*, in *Proceedings of the 35th International Free Electron Laser Conference*, 594–597 (New York, 2013).

[88] S. Hilbrich et al., *Upgrade Plans for the Short-Pulse Facility at DELTA*, in *Proceedings of the 36th International Free Electron Laser Conference*, 255–259 (Basel, 2014).

[89] S. M. Hilbrich, *Studies of the DELTA Lattice in View of a Future Short-Pulse Facility Based on Echo-Enabled Harmonic Generation*, master's thesis, TU Dortmund (2015).

[90] Coherent, Inc., Santa Clara, CA, USA, *Operator's Manual – Micra-5 Modelocked Titanium:Sapphire Laser System* (2009).

[91] S. Khan, *Instruments of Modern Physics – A Primer to Lasers, Accelerators, Detectors and all that*, lecture notes, TU Dortmund University, `http://www.delta.tu-dortmund.de/cms/de/Studium/Homepage_Khan/Lehre/Instrumente_SS2014/index.html` (2014), [accessed March 24, 2015].

[92] M. Eichhorn, *Laserphysik*, 1st edition (Springer, Berlin, 2013).

[93] T. Brabec et al., *Kerr lens mode locking*, Opt. Lett. 17, 1292 (1992).

[94] Coherent, Inc., Santa Clara, CA, USA, *Operator's Manual – Coherent Legend Elite Ultrafast Amplifier Laser Systems* (2010).

[95] G. Vaillancourt et al., *Operation of a 1-kHz pulse-pumped Ti:sapphire regenerative amplifier*, Opt. Lett. 15, 317 (1990).

[96] A. S. Weling et al., *Generation of tunable narrow-band THz radiation from large aperture photoconducting antennas*, Applied Physics Letters 64, 137 (1994).

[97] A. S. Weling and D. H. Auston, *Novel sources and detectors for coherent tunable narrow-band terahertz radiation in free space*, J. Opt. Soc. Am. B 13, 2783 (1996).

[98] S. Bielawski et al., *Tunable narrowband terahertz emission from mastered laser–electron beam interaction*, Nature Physics 4, 390 (2008).

[99] C. Evain et al., *Laser-induced narrowband coherent synchrotron radiation: Efficiency versus frequency and laser power*, Phys. Rev. ST Accel. Beams 13, 090703 (2010).

[100] E. Treacy, *Optical pulse compression with diffraction gratings*, IEEE Journal of Quantum Electronics 5, 454 (1969).

[101] I. Christov and I. Tomov, *Large bandwidth pulse compression with diffraction gratings*, Optics Communications 58, 338 (1986).

[102] The MathWorks, Inc., *MATLAB*, `http://www.mathworks.com/products/matlab/` (2015), [accessed May 21, 2015].

[103] K. Wille, *The Physics of Particle Accelerators – an introduction*, 1st edition (Oxford University Press, Oxford, 2000).

[104] H. Wiedemann, *Particle Accelerator Physics*, 3rd edition (Springer, Berlin, 2007).

[105] E. Courant and H. Snyder, *Theory of the alternating-gradient synchrotron*, Annals of Physics 3, 1 (1958).

[106] H. Klingbeil et al., *Theoretical Foundations of Synchrotron and Storage Ring RF Systems*, 1st edition (Springer, Cham, 2015).

[107] M. Sands, *The Physics of Electron Storage Rings: An Introduction*, SLAC-121, SLAC National Accelerator Laboratory, Menlo Park (1970).

[108] T. Shintake, *Real-time animation of synchrotron radiation*, Nuclear Instruments and Methods in Physics Research Section A: Accelerators, Spectrometers, Detectors and Associated Equipment 507, 89 (2003), proceedings of the 24th International Free Electron Laser Conference and the 9th Users Workshop.

[109] *Shintake Radiation2D*, `http://www.shintakelab.com/en/enEducationalSoft.htm` (2008), [accessed May 5, 2015].

[110] E. Hagen and H. Rubens, *On some relations between the optical and the electrical qualities of metals*, Philosophical Magazine (Series 6) 7, 157 (1904).

[111] M. Naftaly and R. Dudley, *Terahertz reflectivities of metal-coated mirrors*, Appl. Opt. 50, 3201 (2011).

[112] *THz Materials*, `http://www.tydexoptics.com/products/thz_optics/thz_materials/` (2015), [accessed May 17, 2015].

[113] *Quartz Crystal (SiO2)*, `http://www.crystran.co.uk/optical-materials/quartz-crystal-sio2` (2012), [accessed May 17, 2015].

[114] F. Hinterberger, *Physik der Teilchenbeschleuniger und Ionenoptik*, 2nd edition (Springer, Berlin, 2008).

[115] Universität Münster, Institut für Physikalische Chemie, Münster, *Apparatives Praktikum: FT-IR-Spektroskopie* (2006).

[116] H. Nyquist, *Certain Topics in Telegraph Transmission Theory*, American Institute of Electrical Engineers, Transactions of the 47, 617 (1928).

[117] C. Shannon, *Communication in the Presence of Noise*, Proceedings of the IRE 37, 10 (1949).

[118] Bruker Optics Inc., Billerica, MA, USA, *Introduction to FT-IR Spectroscopy* (2011), [interactive tutorial delivered with the OPUS software package].

[119] *ChemWiki: The Dynamic Chemistry E-textbook – FTIR: Computational*, `http://chemwiki.ucdavis.edu/Analytical_Chemistry/Instrumental_Analysis/Spectrometer/How_an_FTIR_instrument_works`, [accessed May 18, 2015].

[120] A. Terebilo, *Accelerator Modeling with MATLAB Accelerator Toolbox*, in *Proceedings of the 19th Particle Accelerator Conference*, 3203–3205 (Chicago, 2001).

[121] Wolfram Research, Inc., *Mathematica*, `http://www.wolfram.com/mathematica/` (2015), [accessed May 21, 2015].

[122] L.-G. Böttger, *Simulation der Entstehung kohärenter Terahertzstrahlung am Speicherring DELTA*, bachelor's thesis, TU Dortmund (2013).

[123] M. Borland, *elegant: A Flexible SDDS-Compliant Code for Accelerator Simulation*, Advanced Photon Source LS-287, Argonne National Laboratory, Argonne (2000).

[124] R. Soliday, *Home of Accelerator Operations & Physics Software Package Source Code*, `http://www.aps.anl.gov/Accelerator_Systems_Division/Accelerator_Operations_Physics/software.shtml#elegant` (2015), [accessed June 3, 2015].

[125] R. Molo, *Echo-Enabled Harmonic Generation at FLASH and DELTA*, Ph.D. thesis, in preparation, TU Dortmund (2015).

[126] D. Schirmer and K. Wille, *DELTA Optics*, in *Proceedings of the 14th Particle Accelerator Conference*, 2859–2861 (San Francisco, 1991).

[127] *QMC Instruments Ltd. and Thomas Keating Toolmaking Ltd.*, `http://www.terahertz.co.uk/` (2015), [accessed June 7, 2015].

[128] ACST GmbH, Hanau, *Manual and Specification – Detector model 2DL 12C LS 1200 A2* (2013).

[129] D. Martin and E. Puplett, *Polarised interferometric spectrometry for the millimetre and submillimetre spectrum*, Infrared Physics 10, 105 (1970).

[130] J. Raasch, Ph.D. thesis, in preparation, Karlsruhe Institute of Technology.

[131] *The Effect of Dispersion on Ultrashort Pulses*, `http://www.newport.com/The-Effect-of-Dispersion-on-Ultrashort-Pulses/602091/1033/content.aspx`, [accessed July 17, 2015].

[132] S. Khan et al., *Studies and Control of Coupled-bunch Instabilities at DELTA*, in *Proceedings of the 1st International Particle Accelerator Conference*, 2755–2757 (Kyoto, 2010).

[133] M. Höner et al., *Bunch-by-Bunch Feedback Systems at the DELTA Storage Ring used for Beam Diagnostics*, in *Proceedings of the 3rd International Beam Instrumentation Conference*, 703–706 (Monterey, 2014).

[134] S. Khan et al., *Diagnostics of and with Laser-Induced Energy Modulation at the DELTA Storage Ring*, in *Proceedings of the 3rd International Beam Instrumentation Conference*, 202–208 (Monterey, 2014).

[135] A. Nowaczyk, private communication (2012).

[136] R. G. Heine, *Untersuchung der Wechselwirkung intensiver Elektronenstrahlen mit höheren Resonatormoden an Delta*, Ph.D. thesis, Universität Dortmund (2006).

[137] C. Mai et al., *Observation of Coherent Pulses in the Sub-THz Range at DELTA*, in *Proceedings of the 6th International Particle Accelerator Conference*, 823–826 (Richmond, 2015).

[138] K. Holldack and A. Zholents, *Energy Modulation of the Electrons by the Laser Field in the Wiggler Magnet: Analysis and Experiment*, in *Proceedings of the 28th International Free Electron Laser Conference*, 725–727 (Berlin, 2006).

[139] F. L. Müller, *Electro-Optical Bunch Length Measurements at the Swiss Light Source*, Ph.D. thesis, University of Bern (2011).

[140] M. Dunning et al., *Generation of Narrow-Band Coherent Tunable Terahertz Radiation using a Laser-Modulated Electron Beam*, in *Proceedings of the 3rd International Particle Accelerator Conference*, 1146–1148 (New Orleans, 2012).

Acknowledgement

First of all I would like to thank Prof. Shaukat Khan for giving me the opportunity to prepare this thesis and continue my work on the THz beamline at DELTA. His valuable input and ideas about new topics to study and methods to employ, as well as his close interest in each experiment performed and result obtained have been a great support and motivation. I am grateful for his trust and the opportunities he granted me to present not only my own results but also our group efforts related to the short-pulse facility at local, national, and international workshops and conferences, and for the possibility to join the CPB experiments at UVSOR in Japan.

I would also like to thank Prof. Anke-Susanne Müller from KIT for preparing the second assessment of this thesis with her expert knowledge on generation and detection of THz radiation at electron storage rings, and Prof. Metin Tolan for preparing the third assessment.

This work has been funded by the Federal Ministry of Education and Research (BMBF) under contract numbers 05K10PEB and 05K13PEC, by the German Research Foundation (DFG) under contract number INST 212/236-1 FUGG, the Federal State of North Rhine-Westphalia (NRW), and by the TU Dortmund University.

To Detlev Schirmer my thanks go for proofreading and providing content-related as well as moral support during the sometimes tedious work of preparing this thesis.

I would like to extend my gratitude to the colleagues in our group. Markus Höner, with whom I had the pleasure of designing and constructing the THz beamline in the scope of our diploma theses, has continued to be a close friend and a valuable support in all questions related to the THz beamline, our common projects at DELTA as well as in private matters. Carsten Mai, who has joined the THz beamline in 2013 to prepare his master's thesis about an MPI, has been a great colleague from the first day on and I am very grateful for our fruitful discussions and his scientific and technical support in the experiments we have performed since then. I would like to thank all former and present members of our group, especially Fin Bahnsen, Svenja Hilbrich, Holger Huck, Maryam Huck, Andre Nowaczyk, Arne Meyer auf der Heide, Robert Molo, Helge Rast, Andreas Schick, and Gholamreza Shayeganrad, for the mutual respect, support, and all the fun we had during our time at DELTA.

My thanks also go to all members of the DELTA machine and administration teams, who have been a great support in all scientific, technical, and administrative questions. My work at DELTA has always been very pleasant due to the friendly atmosphere and mutual respect. Furthermore, I would like to thank my colleagues from the DELTA user community and the other groups and workshops from the Faculty of Physics for their support, our fruitful discussions, and the exchange of equipment and manpower if help was needed.

A big word of thanks goes to my colleagues from KIT, especially Prof. Anke-Susanne Müller, Nicole Hiller, Vitali Judin, Michael Nasse, Miriam Brosi, Benjamin Kehrer, Patrik Schoenfeldt, Paul Schütze, and Sophie Walther from ANKA, and Prof. Michael

Siegel, Petra Thoma, Juliane Raasch, Matthias Arndt, Konstantin Ilin, and Artem Kuzmin from IMS. I have very much enjoyed our exchange of visits, our joined experiments, and the scientific, technical, and moral support that I have received from them. The same applies to my colleagues from PhLAM, namely Serge Bielawski, Clément Evain, Eléonore Roussel, and Christophe Szwaj, who provided their expert knowledge and equipment for the CPB experiments at DELTA, and with whom it has always been an enjoyable collaboration.

For their support during the decision phase, procurement and commissioning of the FTIR spectrometer I would like to thank Karsten Holldack from BESSY and Volker Schlott and Gerhard Ingold from the SLS.

To Andreas Siegert and Thomas Kirchner from Keysight Technologies Deutschland GmbH I am grateful for providing the 160 GSa/s DSO and joining our test measurement in 2014.

I would like to thank Katoh-sensei, Adachi-san, Konomi-san, and Hagiwara-san for their very warm welcome, their valuable time, and the exchange of knowledge during my visit to UVSOR. For inviting me to a visit of the new Aichi Synchrotron Radiation Center my thanks go to Hosaka-san. I would also like to thank Eléonore and Christophe for being my guides during my first visit to Japan.

Finally, my thanks go to my family, especially my parents, who have been a great moral support and have always respected my busy schedule, especially during the final months of my thesis work.